Imperial College London

Minimal Nonlinear Modal Aeroelastic Descriptions for Highly Flexible Aircraft Control

Marc Artola

Supervised by
Dr. Andrew Wynn and Prof. Rafael Palacios

Imperial College London
Department of Aeronautics

Submitted in partial fulfilment of the requirements for the degree of
Doctor of Philosophy in Aeronautics and
the Diploma of Imperial College London, August 2021

Declaration

I hereby declare that the contents of this dissertation are original and genuine product of my own work. This thesis has only been submitted to the Imperial College London in partial fulfilment of the requirements for the degree of Doctor of Philosophy in Aeronautics. Other people's work, used to support or contextualise the results of this work, is fully acknowledged.

The copyright of this thesis rests with the author. Unless otherwise indicated, its contents are licensed under a Creative Commons Attribution-Non Commercial 4.0 International Licence (CC BY-NC).

Under this licence, you may copy and redistribute the material in any medium or format. You may also create and distribute modified versions of the work. This is on the condition that: you credit the author and do not use it, or any derivative works, for a commercial purpose.

When reusing or sharing this work, ensure you make the licence terms clear to others by naming the licence and linking to the licence text. Where a work has been adapted, you should indicate that the work has been changed and describe those changes.

Please seek permission from the copyright holder for uses of this work that are not included in this licence or permitted under UK Copyright Law.

Marc Artola

Abstract

The increase in aircraft structural flexibility, resulting from the use of slender wings and composite light-weight materials, to improve aerodynamic efficiency, poses a severe control problem. The dynamics of these vehicles, described by nonlinear mathematical models, are complex, with large wing deformations that significantly affect the vehicle flight mechanics and make them vulnerable to disturbances or adverse atmospheric conditions. Therefore, advanced control methodologies capable of accounting for the nontrivial dynamics of such aircraft are required to improve their manoeuvrability and ensure their structural integrity.

We propose a control framework that employs a model predictive controller and its dual moving horizon estimator. These strategies are highly suitable to address this challenge, since they rely on solving optimal control problems which are constrained by arbitrary nonlinear dynamics and can explicitly account for state and actuator constraints. With available proofs on stability and algorithmic improvements to enable real-time application, the focus of this work is placed on deriving efficient characterisations that encapsulate the relevant dynamics of these complex systems for successful control.

The conceived internal models for control build upon a recently developed geometrically-exact beam description, known as the intrinsic formulation. It uses velocities and strains as main variables, which leads to a compact mathematical model, amenable to efficient *nonlinear* model-order reduction using the structural modes of vibration. These are also used to project the typically high-dimensional inputs and outputs of a linearised unsteady vortex lattice formulation onto lower dimensional subsets. This enables efficient model-order reduction of its state-space representation and establishes a common fluid-structure interface facilitating the aeroelastic coupling. Finally, data-driven modelling is explored to improve known limitations of the coupled aeroelastic models and further optimise their size for control.

The resulting framework, able to operate in the nonlinear regime, allows for exploration of unconventional control and stabilisation mechanisms as shown in the numerical examples, which would be unattainable with traditional control methods.

Acknowledgements

I would like to start by thanking my supervisors Andrew Wynn and Rafael Palacios for betting on me from the beginning and for giving me the opportunity to pursue a PhD programme under their supervision. Even though it is a formality in the acknowledgements section of every PhD dissertation, my acknowledgements are truly genuine and I am deeply grateful for their continued support and guidance. They have created a very comfortable environment from day one and I can say I have enjoyed our weekly discussions, which have undeniably enriched me and which I will most surely miss.

What I am missing already are the fun moments at the office, which helped in raising the spirits especially during the stressful moments of the life as a PhD student, and which were suddenly taken away from our daily routines when the pandemic first struck, precisely one year ago as I write this. I am grateful for those lunches where we would have the most varied and colourful chats, for the (not necessarily) Friday pints, but especially for our *meriendas*, truly an institution in our office corner. Thank you guys! I am also particularly grateful to Norberto and Arturo, for showing me the ropes with SHARPy.

I would not like to forget the members of the ConFlex project, both students and investigators, with whom I have shared unforgettable moments in our network meetings and also during my visits to the University of Twente in the Netherlands and to FAU in Germany. I personally enjoyed our discussions and learned a lot from their more mathematical approach to life! As part of ConFlex, my PhD has been funded by the European Union Horizon 2020 research and innovation programme under the Marie Sklodowska-Curie grant agreement No 765579, which is gratefully appreciated and acknowledged.

Finally, I would like to thank my family, especially my parents and my sister, who have been unconditionally supporting me from the beginning of my studies and whose help one usually takes for granted. Special thanks go to a little recent addition to my life, Melissa, for her moral support and for brightening my days, especially the even greyer days of lockdown in London. I also want to thank my friends in London, with whom we have many pending celebrations, and my friends in Barcelona, who always await impatiently for my holiday returns.

‘Everything should be made as simple as possible, but no simpler.’

Albert Einstein

Contents

Abstract **3**

Acknowledgements **7**

Nomenclature **25**

1 Introduction **31**

1.1 Research Motivation 31

1.2 State-of-the-Art in Aeroservoelasticity of Very Flexible Aircraft 34

1.2.1 Geometrically-Exact Beam Formulations 35

1.2.2 Unsteady Aerodynamics 39

1.2.3 Aeroelasticity of Very Flexible Aircraft 42

1.2.4 Low-Order Modelling and Control 43

1.3 Research Questions 47

1.4 Thesis Outline and Publications 48

2 Underlying Structural and Aerodynamic Models 53

2.1 Intrinsic Beam Formulation 54

2.1.1 Frames of Reference 54

2.1.2 Original Intrinsic Beam Equations 55

2.1.3 Damped Intrinsic Beam Equations 57

2.1.4 Intrinsic Beam Equations with Linearised Damping 60

2.1.5 Displacements and Finite Rotations 63

2.2 Unsteady Vortex Lattice Method 64

2.2.1 Spatial Discretisation and UVLM Formulation 65

2.2.2 Linearised UVLM Formulation 67

3 Nonlinear Modal Aeroelastic Description 69

3.1 Structural Linear Normal Modes 70

3.1.1 Single Beam Case 70

3.1.2 Network of Beams 71

3.1.3 Concentrated Masses 73

3.1.4 Modes Computation 76

3.2 Modal Aeroelastic Description 79

3.2.1 Nonlinear Intrinsic Equations in Modal Coordinates 80

3.2.2 Displacements and Finite Rotations 82

3.2.3 Modal Aerodynamic Description 86

3.2.4 Coupled Aeroservoelastic System 91

3.3 Data-Driven Model Fitting 92

3.3.1 Gravity Forcing 95

3.3.2 Aerodynamic Forcing 96

3.3.3 Training Data Acquisition 96

4 Control and Estimation Framework 101

4.1 Model Predictive Control 101

4.2 Moving Horizon Estimation 109

4.3 Optimal Problem Solution 110

4.3.1 Sequential Quadratic Programming 110

4.3.2 Internal Model Time Integration 111

4.3.3 Sensitivity Analysis 113

5 Numerical Examples I: Proofs of Concept 117

5.1 Analysis of Damped Intrinsic Beam Equations 118

5.1.1 Damping Model Verification 118

5.1.2 Response of a Damped Highly Flexible Hinged Beam 122

5.2 Swinging Pendulum Optimal Control Problem 127

5.2.1 Model Convergence Studies 128

5.2.2 Solution to Optimal Problem Parameterised by Multiple Shooting . 131

5.2.3 Computational Cost of Sensitivity Analysis 135

5.3 Nonlinear Control of a Very Flexible Inverted Pendulum 136

5.3.1 2D Clamped Case 137

5.3.2 3D Clamped Case 139

5.3.3 3D Case on a Moving Base with Gravity Effects 142

6 Numerical Examples II: Realistic Configurations 147

6.1 Aeroelastic Control of Very Flexible Clamped Wings 147

6.1.1 Gust Load Alleviation of a High Aspect Ratio Very Flexible Wing . 148

6.1.2 Flutter Suppression of a Pazy Wing Model 157

6.2 Aeroelastic Control of a Very Flexible HALE Concept Aircraft 166

6.2.1 Rigid and Flexible Trim Solutions 166

6.2.2 Stabilisation After Payload Drop 170

6.3 Data-Driven Enhanced Aeroelastic Model for Control 176

6.3.1 Training Data and Model Regression 177

6.3.2 Open-Loop Improvements 182

6.3.3 Effect on MPC/MHE Performance 184

7 Conclusions 195

7.1 Summary of Achievements 195

7.1.1 Structural Damping for Geometrically-Nonlinear Beams 195

7.1.2 Theoretical MPC Results for the Intrinsic Description of Geometrically Nonlinear Structures 196

7.1.3 Nonlinear Low-Order Internal Models for Control 197

7.1.4 Application of Data-Driven Methods in Aeroelasticity Modelling . . 198

7.1.5 Applications of the Framework 199

7.2 Recommendations for Future Work 200

7.2.1 Improvements to the Nonlinear Low-Order Control Models 200

7.2.2 Algorithmic Improvements Towards Real-Time Deployment 202

7.2.3 Physics-Informed Data-Driven Modelling 203

Bibliography **205**

A NMPC Convergence Proofs **221**

B Relation of Intrinsic Equations to Standard Beam Formulations **225**

C FE Implementation of the Damped Intrinsic Beam Equations **229**

List of Figures

1.1 Airbus' A350-1000 (left) [8] and Boeing's 787-Dreamliner (right) [24] first flights. 31

1.2 Airbus' ZEROe turbofan configuration [7]. 32

1.3 Aurora Flight Sciences (Boeing) HAPS prototype Odysseus [18]. 33

1.4 NASA's Helios prototype [109]. 33

2.1 Inertial frame of reference (black) and local frame of references at $s = 0$ (blue) and at an arbitrary location s (red) in an unconstrained beam configuration. Elastic axis displayed in thick, solid, black line. 55

2.2 Continuous vortex distribution to model lifting surfaces and wake. 65

3.1 Example of a three beam network interconnected by a ball joint. 72

3.2 Example of a three beam rigid joint with a lumped mass at a distance $\boldsymbol{r}_l$. Dashed line represents an infinitely rigid link. 75

3.3 First six Chebyshev polynomials. 78

3.4 Sparsity of an example A_{cheb} matrix from an 8 beam and one lumped mass assembly. 78

3.5 Block diagram description of the aerodynamic system with modal inputs and outputs projected onto modal coordinates. (Adapted and reproduced here with the permission of N. Goizueta) 88

3.6 Training data acquisition scheme. 98

5.1 Setup of the beam subjected to pre-stress caused by an axial compressive force Q and excited with a moving harmonic force $P(t)$. 119

5.2 Mid-beam displacement for damping coefficients of (a) $\eta = 0.0001\,\mathrm{s}$, (b) $\eta = 0.001\,\mathrm{s}$ and (c) $\eta = 0.01\,\mathrm{s}$. Markers (+) and (×) in (b) refer to linear and nonlinear reference results of [141], respectively. 120

5.3 Setup of the three-dimensional highly-elastic hinged beam subject to two following point torque inputs $u(t)$ applied at the free end. 122

5.4 Total energy (kinetic + potential) of the beam as a function of time for the three different damping coefficients considered. Thick line corresponds to full nonlinear damping, thin line to linearised damping. 123

5.5 Total energy rate $\dot{\epsilon}$ and damping dissipation rate $\dot{\epsilon}_\eta$ for the three different damping coefficients (colour code follows Fig.5.4) for the linearised (top) and the full nonlinear damping cases (bottom). 124

5.6 Snapshots of the beam every 0.1 s for the linearised damping case and $\eta = 0.001\,\mathrm{s}$, including the projection on a horizontal plane of the tip displacement trace. Shade darkens with time and (a) $t \in [0, 5]\,\mathrm{s}$, (b) $t \in [5, 10]\,\mathrm{s}$, (c) $t \in [10, 15]\,\mathrm{s}$. 125

5.7 Snapshots of the beam every 0.1 s for the full nonlinear damping case and $\eta = 0.001\,\mathrm{s}$, including the projection on a horizontal plane of the tip displacement trace. Shade darkens with time and (a) $t \in [0, 5]\,\mathrm{s}$, (b) $t \in [5, 10]\,\mathrm{s}$, (c) $t \in [10, 15]\,\mathrm{s}$. 126

5.8 Sketch of the the swinging pendulum optimal problem. The pendulum is vertical and straight in its equilibrium position. 128

5.9 RMS error (a) and last mode energy contribution (b) vs N_m. 129

5.10 Control signal used for the open loop convergence studies. 130

5.11 Axial stiffness EA (a) and number of modes N_m convergence studies (b). Above, the pendulum tip x-coordinate, below, its z-coordinate. 131

5.12 Bending moment (a), quaternion norm (b), quaternion scalar component ξ_0 (c) and quaternion second vector component $\xi_{v,2}$ (d) spatial distributions. Results at $t = 1.83\ s$. 132

5.13 Number of optimisation iterations (a), execution time (b) and execution time per iteration (c) vs multiple shooting intervals. 133

5.14 Optimal control input (a). Snapshots (grey) of the pendulum trajectory at a rate of 25 fps for $t \in [0, 0.72]$ (b), $t \in [0.72, 1.60]$ (c) and for $t \in [1.60, 2]$ (d). The black line represents the initial configuration of the shown interval and the grey, dashed, one the tip path. 135

5.15 Execution time per time step of the forward (solid line) and sensitivity (dashed line) problems, with dotted lines showing the +2 and +3 slopes. . 136

5.16 (a) Control input comparison for the *nominal* case of all the linear and converged MPC controllers and (b) snapshots every 0.2 s of the control action of the *NMPC* controller (with resultant applied force in green). . . . 138

5.17 Control input comparison of all the three controllers acting on the *true* system. 139

5.18 Target position for the less flexible (thin stroke) and more flexible (thicker stroke) beams, where projections onto each plane have been included and where the width of the beam specifies the direction of higher stiffness. . . . 140

5.19 Control input comparison of *LMPC* and *NMPC* for the *nominal* case for a torsion stiffness of (a) $GJ = 0.67EI$ and of (b) $GJ = 0.33EI$. 141

5.20 Control input comparison of the three controllers on the *true* system for the more flexible beam case. 141

5.21 Control input in the *nominal* case using the present *NMPC* design for $\delta = 0.0001$. 143

5.22 Fifteen snapshots for $t \in [0.1, 6]$ s, with logarithmic spacing in time, of the controlled pendulum in the (a) 1-2 and the (b) 1-3 planes, with shade darkening for increasing time. 143

5.23 Control input for both the (a) spline and the (b) modal finite-dimensional approximations for the quaternions applied to the *true* system. 144

5.24 Control input on the *true* system using the present *NMPC* design for $\delta =$ 0.0001 and constraint on vertical base displacement. 145

5.25 Fifteen snapshots for $t \in [0.1, 10]$ s, with logarithmic spacing in time, of the controlled pendulum in the (a) 1-2 and the (b) 1-3 planes, with shade darkening with time for the vertical displacement constrained case. 145

6.1 3D, top and front views of the nonlinear aeroelastic equilibrium deformation. Displayed the local frames of reference x-red, y-green and z-blue. (By N. Goizueta) 149

6.2 Dynamic response (left) of the wing release at three different free stream velocities. Steady state values against velocity squared shown on the right. (SHARPy results by N. Goizueta) 151

6.3 Comparison of the dynamic response of the wing to external gust and aileron inputs with SHARPy nonlinear reference. (SHARPy results by N. Goizueta) 153

6.4 Normalised wing tip vertical displacement (left) and root bending moment (right). 155

6.5 Aileron deflection rate (control input) and deflection angle. 156

6.6 Pazy wing experimental model. 157

6.7 Stability analysis of the wing with (a) stability plot at two non-zero angles of attack and (b) root locus diagram. (Figures by N. Goizueta) 159

6.8 Wing flutter instability regions. (Figure by N. Goizueta) 159

6.9 Normalised wing tip displacement and aileron deflection vs time for the flutter suppression direct actuation mechanism. 161

6.10 (a) Normalised wing tip displacement, aileron deflection and rate for the deformation-control-based mechanism and (b) 3D view of the initial and final wing configurations. 163

6.11 Time history of the vertical displacement of the Pazy wing for the open-loop and control cases. 164

6.12 Time history of the flap deflection for the two considered control cases. . . 164

6.13 Pazy wing (a) at 0.5s in flutter prior to control actuation and (b) at 1.5s once the controller increases the wing deflection to suppress flutter, with the open loop counterpart shown in dark shade. (Figures by N. Goizueta) . 165

6.14 3-view schematic of HALE aircraft [44], displaying the body-attached frame of reference A. 167

6.15 Normalised trim parameters as a function of the linearisation angle of attack. 169

6.16 Wing loading and deformation changes before and after the mass drop in open loop. (Figure by N. Goizueta) 171

6.17 Payload drop open-loop results. (SHARPy results by N. Goizueta) 172

6.18 Open-loop vs. MPC closed-loop response comparison. (Open-loop simulation by N. Goizueta) 174

6.19 Normalised control inputs and estimated mass. 175

6.20 Trajectory of the controlled HALE aircraft in blue over 30s, shown at 2.5s intervals, alongside the open-loop trajectory in grey. (Figure by N. Goizueta) 176

6.21 Open loop response comparisons. Payload drop case (top) and elevator input case (bottom). 183

6.22 Estimates of the disturbance magnitude for gust perturbations of span (a) 10 m (b) 20 m and (c) 40 m. MPC closed-loop responses with the data-driven (▪▪▪▪▪) and linear ROM (——) UVLM models. 186

6.23 Estimates of the $\boldsymbol{q}_2$ state components (first bending in colour ■, second bending in ■) for gust perturbations of span (a) 10 m (b) 20 m and (c) 40 m for the data-driven (▪▪▪▪▪) and linear ROM (——) UVLM internal models. Actual components from SHARPy closed-loop MPC simulations corresponding to the data-driven (▪▪▪▪) and linear ROM (▬) UVLM internal models. 187

6.24 U, α and θ for gust perturbations of span (a) 10 m (b) 20 m and (c) 40 m, with open loop (——) and MPC closed-loop responses using the data-driven (- - - - -) and the linear ROM (——) UVLM models. 188

6.25 Normalised control inputs: elevator rate $\dot{\delta}$ (—), deflection δ (—) and thrust T (—) for gust perturbations of span (a) 10 m (b) 20 m and (c) 40 m. MPC closed-loop responses with the data-driven (- - - - -) and linear ROM (——) UVLM models. 189

6.26 Estimates of the disturbance magnitude for the payload mass releases of (a) 25 kg (b) 35 kg and (c) 45 kg. MPC closed-loop responses with the data-driven (- - - - -) and linear ROM (——) UVLM models. 191

6.27 Estimates of the $\boldsymbol{q}_2$ state components (first bending in colour ■, second bending in ■) for the payload mass releases of (a) 25 kg (b) 35 kg and (c) 45 kg for the data-driven (- - - - -) and linear ROM (——) UVLM internal models. Actual components from SHARPy closed-loop MPC simulations corresponding to the data-driven (▪▪▪▪) and linear ROM (▬) UVLM internal models. 192

6.28 U, α and θ for the payload mass releases of (a) 25 kg (b) 35 kg and (c) 45 kg with open loop (——) and MPC closed-loop responses using the data-driven (- - - - -) and the linear ROM (——) UVLM models. 193

6.29 Normalised control inputs: elevator rate $\dot{\delta}$ (—), deflection δ (—) and thrust T (—) for the payload mass releases of (a) 25 kg (b) 35 kg and (c) 45 kg. MPC closed-loop responses with the data-driven (- - - - -) and linear ROM (——) UVLM models. 194

C.1 Five first interpolating quadratic shape functions for a beam discretisation of $L = 1$ using 10 nodes (5 elements). 231

C.2 Local nodes and shape functions within an element. 232

List of Tables

5.1 Beam structural properties of the test case [141] 119

6.1 High aspect ratio, flexible wing properties 149

6.2 Beam model stiffness matrix. 157

6.3 Beam model mass and geometrical properties. 158

6.4 Wing tip rod mass and inertia properties. 158

6.5 SHARPy model of HALE aircraft numerical discretisation 173

6.6 Gravity modal forcing 181

6.7 Low-order aerodynamic states dynamics 181

6.8 Aerodynamic forces output equation 182

Nomenclature

Acronyms

FE	Finite Element
GEB(T)	Geometrically Exact Beam (Theory)
HALE	High-Altitude Long-Endurance
HAPS	High-Altitude PseudoSatellites
LMI	Linear Matrix Inequality
LPV	Linear Parameter Varying
(N)MHE	(Nonlinear) Moving Horizon Estimation
(N)MPC	(Nonlinear) Model Predictive Control
NLP	Nonlinear Program
ODE	Ordinary Differential Equation
PDE	Partial Differential Equation
ROM	Reduced Order Model
SQP	Sequential Quadratic Programming
UAV	Unmanned Aerial Vehicle
UVLM	Unsteady Vortex Lattice Method
VFA	Very Flexible Aircraft

Sub-/Superscripts

$(\bullet)^*$	Complex conjugate
$[\bullet]_i$	ith entry of a vector/matrix

$(\hat{\bullet})$	Error with respect to a reference point or solution $(\bar{\bullet})$
$(\breve{\bullet})$	Normalised/scaled variables
$(\bar{\bullet})$	Reference/equilibrium state/solution
$(\bullet)'$	Partial derivative with respect to spatial coordinate s
$\widetilde{(\bullet)}$	Cross-product matrix operator
$(\bullet)^\top$	Matrix transpose
$(\bullet)^n$	Value of variable at discrete time instance n
$(\dot{\bullet})$	Partial derivative with respect to time

Notation

$\mathbb{C}^n$	Set of complex numbers in n dimensions
I_n	Identity matrix in $\mathbb{R}^n$
$\delta(\bullet)$	Linear perturbation variables
$\mathbb{R}^n$	The set of real numbers in n dimensions
$\mathbb{R}_+$	The set of positive real numbers
$\mathcal{S}^n_{++}$	The set of symmetric positive definite matrices in $\mathbb{R}^n$
$\mathcal{S}^n_{+}$	The set of symmetric positive semi-definite matrices in $\mathbb{R}^n$

Symbols

(A, B, C, D)	Discrete-time state-space representation of the full-order linearised UVLM
(A_q, B_q, C_q, D_q)	Continuous-time state-space representation of the reduced-order linearised UVLM
$\alpha(t)$	Aircraft angle of attack
$\boldsymbol{\beta}$	Data-driven model coefficients
$C(s)$	Compliance mass matrix

$C_\tau(s)$	Damping matrix
$\boldsymbol{\delta}(t)$	Control surface deflection vector
$D_0(s)$, $D_1(s)$, $D_2(s)$	Linear damping matrices
s_∂	Spatial coordinate of any of the two beam boundaries
$\epsilon(t)$	Total structural energy (kinetic and elastic potential)
$\epsilon_q(t)$	Total energy (kinetic and elastic potential) of the modal low-order structural model
$\boldsymbol{\eta}_g(t), \boldsymbol{\eta}_a(t), \boldsymbol{\eta}_e(t)$	Projection of gravity, aerodynamic and other external forces onto modal space
$\boldsymbol{e}_i^*$, $i = \{1, 2, 3\}$	Canonical vectors of the inertial frame of reference
$\boldsymbol{e}_i(s,t)$, $i = \{1, 2, 3\}$	Canonical vectors of the local frame of reference
$E(s)$	Initial curvatures matrix
$\boldsymbol{f}(s,t)$	Local force sectional resultant
$\boldsymbol{f}_g(s,t), \boldsymbol{f}_a(s,t), \boldsymbol{f}_e(s,t)$	Gravity, aerodynamic and other external forces and moments
$\Gamma_1, \Gamma_2, \Gamma_g, \Gamma_\xi$	Modal matrices describing the quadratic nonlinearities
$\boldsymbol{\gamma}(s,t)$	Local strains vector
$\boldsymbol{\Gamma}_b(t), \boldsymbol{\Gamma}_w(t)$	UVLM bound and wake panel circulation intensities
$\boldsymbol{g}$	Acceleration due to gravity
$\boldsymbol{h}(s,t)$	Local angular momentum
$\boldsymbol{\kappa}(s,t)$	Local curvatures vector
L	Beam arc-length
$\boldsymbol{m}(s,t)$	Local moment sectional resultant

$\mu(s)$	Beam linear density
$M(s)$	Sectional mass matrix
N_c, N_e	Number of MPC and MHE sub-intervals
N_m	Number of structural modes
$\boldsymbol{\phi}_1(s), \boldsymbol{\phi}_2(s), \boldsymbol{\phi}_\xi(s)$	Mode shapes for the velocity, force and quaternion modes
$\boldsymbol{p}(s,t)$	Local linear momentum
P_c, P_e	Final state penalty and arrival cost for the control/estimation problems
$\boldsymbol{q}_0(t), \boldsymbol{q}_1(t), \boldsymbol{q}_2(t), \boldsymbol{q}_\xi(t), \boldsymbol{q}_\Gamma(t)$	Displacement, velocity, force, quaternion and aerodynamic modal coordinates
q_∞	Dynamic pressure of the free stream
Q_c, Q_e, R_c	Control/estimation stage cost weights
$\boldsymbol{r}(s,t)$	Displacements
$\boldsymbol{r}_{cg}(s)$	Distance of the cross sectional centre of mass with respect to elastic axis
ρ	Free stream density
Σ	Structural damping matrix in modal coordinates
s	Spatial coordinate
Δt	Time step of the discrete-time system
τ_s, τ_c, τ_e	Control sampling period and control/estimation horizons
$\theta(t)$	Aircraft pitch
t	Time coordinate
$T(s,t)$	Transformation matrix from the local to the global frame of reference
t_∞	Free stream time scale
$\boldsymbol{u}$	MPC control input vector

$U(t)$	Aircraft flight velocity
U_∞	Free stream velocity
$\boldsymbol{v}(s,t)$	Local translational velocity
$\boldsymbol{\omega}(s,t)$	Local angular velocity
$\boldsymbol{w}$	MHE external disturbance vector
Ω	Modal structural linear matrix containing the natural frequencies of vibration
ω	Natural frequency of vibration
w_g	Perturbation velocity to free flow due to vertical gust
$\boldsymbol{\xi}(s,t)$	Rotation quaternions
$\boldsymbol{x}_1(s,t)$	Intrinsic velocity variable: Local translational and angular velocities vector
$\boldsymbol{x}_2(s,t)$	Intrinsic force/moment variable: Local sectional force and moment resultants vector
$\boldsymbol{\zeta}_b(t), \boldsymbol{\zeta}_w(\mathrm{t})$	UVLM grid nodes coordinates of the bound and wake panels

Chapter 1

Introduction

1.1 Research Motivation

Driven by economic and, more recently, environmental factors, aircraft manufacturers are striving to design a new generation of more efficient airliners that further reduce fuel consumption, hence reducing harmful emissions. Amidst global warming concerns, which have recently seen numerous countries declaring a climate emergency [1], it is expected that in the foreseeable future new and stricter measures on the use of fossil fuels and restrictions on carbon emissions will increase the pressure on the aviation industry to shift towards greener and more efficient technologies. Examples of these incipient changes in a rather slow-paced industry are the latest developments of the two largest manufacturers: Boeing's 787 Dreamliner and Airbus' A350 XWB (Fig. 1.1), whose determined bid for composite materials in the aircraft architecture sets a precedent for next-generation aircraft designs.



Figure 1.1: Airbus' A350-1000 (left) [8] and Boeing's 787-Dreamliner (right) [24] first flights.

Slender wings and overall aircraft weight reduction, achieved by employing lighter com-

posite materials for instance, is a design solution which allows for more efficient configurations. Both measures aim to reduce the thrust required to maintain flight by minimising the induced drag, which is a consequence of finite-span wings and proportional to the lift squared. On the one hand, slender wings are aerodynamically more efficient, meaning that for a given lift, less induced drag is generated. On the other hand, weight reduction implies a decrease in the required overall lift. These structural improvements go hand in hand with the efforts by the engine manufacturers to conceive more efficient engines by using unprecedentedly high bypass ratios or alternative energy sources. This change of paradigm in the commercial aircraft industry is exemplified by Airbus' ZEROe concepts, aimed to be put into service by 2035, which rely on efficient high-ratio wing configurations and hydrogen-powered engines (Fig. 1.2).



Figure 1.2: Airbus' ZEROe turbofan configuration [7].

On the other end of the aircraft manufacture spectrum we find the faster-paced, more dynamic environment of experimental aircraft such as High-Altitude Long-Endurance UAV or High-Altitude Pseudosatellite concepts. The latter are the latest expression of HALE aircraft, often employed for terrestrial reconnaissance or atmospheric exploration, with the ultimate aim to remain airborne perpetually. These vehicles are usually powered by electric engines which use batteries or fuel cells, and solar cell arrays mounted along the aircraft lifting surfaces (Fig. 1.3). It is clear that, for these vehicles, low energy consumption (for high endurance) is the main design criterion and hence extremely slender wings and light-weight configurations are usually the norm. The identification of a promising market niche in the telecommunications sector, where these aircraft can be employed to provide wireless internet connection to remote, isolated areas, together with the maturity level that this concept of aircraft is reaching is motivating most aerospace manufacturers to conceive their own prototypes.

The immediate consequence of slender wing configurations and the use of composite materials, usually less rigid than conventional aluminium or other metal alloys, is increased flexibility in the structures that conform the airframes, leading to large deflections and rotations even at nominal range of operation. This translates into non-negligible



Figure 1.3: Aurora Flight Sciences (Boeing) HAPS prototype Odysseus [18].

geometrically-nonlinear effects, importantly the stiffening effect, the follower-force effect and the change in the global inertia properties. The first of them refers to the gain in rigidity due to stress reorientation in the deformed configuration of the structure, which produces a restoring internal force resultant. The follower force effect, by which external forces and moments keep their relative orientation with respect to the structure while it undergoes deformation, is an essential characteristic of pressure forces such as aerodynamic loads. Finally, the deformation-driven change in the inertia distribution of the structure is especially pertinent in the case of unconstrained or free flying structures, displaying rigid-body motions, since the natural frequencies of the elastic modes experience a drop due to the increase in flexibility and couplings with flight-mechanics modes become stronger.

While nonlinear models to describe the fundamentally more complex dynamics of fluid motion are standard use in aircraft modelling for design and analysis, with a range of varying fidelity models (from less computationally demanding potential flow theories to highly-resolved computational fluid dynamics simulations), application of structural geometrically-nonlinear formulations is only now starting to gain more relevance. To date, the relative rigidity of the airframes justified the use of linear structural models. However, the aforementioned new trend in aircraft design brings about an entirely new paradigm, where structural geometrical nonlinearities not only entail design and control challenges but also offer exploration of unprecedented design spaces and control mechanisms.



Figure 1.4: NASA's Helios prototype [109].

Precisely, control of these highly-flexible vehicles still remains an open challenge and is a known concern of HALE and HAPS manufacturers, with NASA's Helios prototype

(Fig. 1.4) being the archetypal — though not the only one — example of the difficulties these aircraft face; most tested concepts, including Airbus' Zephyr [143] or Google's Solara [54], have suffered similar unfortunate fates. These repeated failures in off-design operations, such as low-altitude flight or the critical landing and take-off manoeuvres, have exposed the necessity to devise new control mechanisms, which should be able to accurately predict and manage arbitrarily large deflections in real time. Besides, any investigation breakthrough in the challenging realm of control of highly flexible aircraft has the potential to enlarge the design space of next-generation commercial airliners, relying more confidently on flexible concepts and thus boosting the ongoing transition to a greener aviation industry. NASA's X-56A prototype [93] is an example of a flexible-wing test aircraft that aims to transfer control-centred design and technologies to future airliners with highly flexible, light-weight wings.

1.2 State-of-the-Art in Aeroservoelasticity of Very Flexible Aircraft

In this section a brief review on the developments and the state-of-the art methods used in the modelling, analysis and control synthesis of very flexible aircraft is given, focusing the attention on HALE or HAPS aircraft concepts. General approaches relying on highly resolved discretisations of the underlying three dimensional solid mechanics and fluid dynamics equations, usually reserved to solve static problems more representative of advanced design stages such as multidisciplinary/topology aeroelastic optimisation, are left out of the scope of this review. Instead, the focus is placed on the more tractable and efficient methodologies to tackle the dynamic problem developed and broadly used by the aeroelastics community and which leverage the typical characteristics of very flexible aircraft, namely slender structural components and slow, subsonic flight speeds. Hence, resting on these assumptions there exists extensive literature on appropriate beam models, aimed at handling the large displacements and rotations to which very flexible aircraft are subject, and on potential flow solutions, which offer a good trade-off between model fidelity and computational complexity for the typical operational speeds. These simplified models facilitate faster and more efficient modelling, simulation and analysis.

First, a review on the modelling of flexible, slender beams which capture geometrical-nonlinearities is given, together with the different approaches taken to account for the large rigid-body motions that unconstrained structures, such as free-flying vehicles, undergo. A brief account on the employed damping models in the context of geometrically-exact

beams is also given. Second, the different methodologies to compute the aerodynamic loads, based on potential flow solutions, are presented. A short section on relevant aeroelastic studies of very flexible aircraft follows, which describes how the previous methods have been combined in the state-of-the-art dynamic simulation tools for VFA. Subsequently, an overview of the diverse order-reduction methods employed to transform the usually high-dimensional systems, arising from typical finite-dimensional realisations of very flexible aircraft models, into more tractable analysis- and control-oriented low-order systems is given. Finally, existing control implementations and examples are also discussed.

1.2.1 Geometrically-Exact Beam Formulations

Justified by the typical high slenderness of the diverse structural components, the use of beam theories to describe the structural dynamics is common practice in dynamic aeroelasticity of very flexible aircraft. The beam definition implies prominence of a particular dimension over the remaining ones, which allows splitting the original three-dimensional problem into separate analysis of the two-dimensional cross sections and a chosen (one-dimensional) reference line. This treatment of the structural three-dimensional kinematics offers very reasonable agreement with higher-fidelity methods in applications of our interest.

First, a cross-sectional analysis of the three-dimensional material properties of the beam must be performed to obtain averaged effective sectional properties (e.g., inertia, stiffness) of the possibly anisotropic and non-homogeneous material distributions [33], which might vary along the principal dimension of the structure too [30, 87, 111, 113]. This beam characterisation, which aims to select appropriate coefficients for the corresponding constitutive relationships, is typically done experimentally for small-amplitude tests or numerically employing full finite element models, where linear theory holds [50, 99].

However, for the case of very flexible structures large overall deflections and rotations can be expected during the nominal range of operation, invalidating thus the assumptions on which linear beam theories rely. Hence, to analyse the motion of the one-dimensional reference line, geometrically-exact (nonlinear) beam models are used, so called because they allow for arbitrary large displacements and rotations. This is not at odds with assuming that deformations remain within the linear elastic regime (small local strains and curvatures), which is a common engineering practice since maximum loads and safety factors are usually computed to prevent the structure from undergoing plastic deforma-

tion, in the case of metallic alloys, or failure mechanisms in composite materials such as delamination, fiber-matrix debonding or fibre buckling.

Several approaches in the presentation of geometrically-exact beam formulations exist in the literature in terms of the chosen primary variables. An illustrative example is found in [114], where the starting point in the derivation of the geometrically-exact beam formulations is Hamilton's Principle written in weak (or variational form), where a set of kinematic and constitutive relationships must also be considered. It is shown that from this initial statement, three different descriptions are obtained all using different sets of variables: the classical displacement-based formulation, an alternative description that uses velocities and sectional forces resultants and one which solely uses strains. These and other alternative formulations are discussed next.

The most conventional closed description of geometrically-exact beams is written in terms of displacements and finite-rotations, expressed through a rotation matrix according to Cosserat's model of a rigid cross section whose orientation varies along the possibly initially twisted and curved reference line [37]. This GEB model consists of a set of six second-order-in-time partial differential equations, with strong nonlinearities. It stems from the incipient works of Reissner, who initially described the dynamics and kinematics of plane beams subject to large displacements [125, 126], and subsequent generalisations of Simo and Vu-Quoc [135, 136] that extended the formulation to the three-dimensional scenario.

The main nuisance of such description is the treatment of the rotation matrix, whose parametrisation has seen several approaches. Euler angles were first used by Reissner [125], which have the known difficulty of presenting a singularity. Later, the singularity-free alternative that quaternions offer was employed by Simo and Vu-Quoc in their generalisation to the three-dimensional case [135, 136]. Finally, Cardona and Géradin introduced a three-variable parametrisation of the finite-rotations using the Cartesian rotation vector [29, 58].

The usual approach in displacement-based formulations to account for rigid-body motions is to track the motion of a particular point in the structure, with respect to which all the elastic deformations are expressed. Then, the resulting six ordinary differential equations governing the rigid equations of motion are coupled to the GEB system and depend on the instantaneous inertia distribution of the structure [137, 138]. A known concern is the invariance of the solutions to rigid-body motions when approximations on the rotation field are introduced (i.e., via spatial discretisation) [38], but this difficulty is usually addressed by considering sufficiently fine spatial resolutions.

An equivalent strong-form description which avoids the necessity of finite-rotation parameterisation is the intrinsic description of Hodges [75], so called since the energy-conjugate variables — local translational and angular velocities and local strains and curvatures — are chosen as primary variables. The cost is a doubling in the number of partial differential equations. Nonetheless, this allows us to express compactly the dynamics of geometrically exact beams using only first-order time and space derivatives, and quadratic nonlinearities. The result is a semi-linear hyperbolic set of partial differential equations, which facilitates the analysis and can be cast under the form of a first-order infinite dimensional port-Hamiltonian system [98], proven useful for analysis and control purposes [97, 129]. Another feature of the formulation is that it is invariant to rigid-body motions, which are extended into the infinite-dimensional description, since rigid translations and rotations are inherently contained in the solution (velocity) space.

Another alternative is the strain-based variational formulation of Su and Cesnik [145], which considers nodal strains as independent variables. This has the advantage of presenting a constant stiffness matrix, which has clear beneficial computational implications. A final example is Hodges' mixed variational formulation [74], which writes the geometrically-nonlinear beam dynamics using local velocities, strains and rotations as primary variables. The large number of variables that this formulation implies, since it is a three-field vector solution, is compensated by less complex equations, which also require of less spatial refinement for convergence.

Damping Modelling in Geometrically Exact Beams

Theoretical analysis of damping in structural dynamics is a notable challenge and often two more practical and approximate strategies to damp oscillations and dissipate energy are employed: the first one relies on the assumption of proportional/viscous damping while the second one introduces an *ad hoc* numerical damping.

The first approach has been, undoubtedly, the most commonly used ever since Rayleigh introduced the idea of viscous damping [124] and it builds on the physical concept that forces arising to damping oppose velocity. The classical (finite-dimensional) description of structural dynamics $M\ddot{\boldsymbol{x}} + K\boldsymbol{x} = \boldsymbol{0}$ describes the vibrations of undamped structures, where the vector $\boldsymbol{x}$ gathers all the structural degrees of freedom and M and K are the mass and stiffness matrices (with both M and/or K possibly $\boldsymbol{x}$-dependent to account for nonlinear effects). Subsequently, damping is introduced by adding a term $D\dot{\boldsymbol{x}}$ to the previous equation, where it is assumed that $D = \alpha M + \beta K$, with $\alpha, \beta \geq 0$. This is not only a simple way to model damping but it also offers remarkable analysis advantages

as, for instance, modal analysis is facilitated [31]. However, damping in real structures arise from more complex mechanisms and hence viscous/proportional damping can fail to accurately predict its real effect on the overall dynamics. Significant effort is still put in the quest for identifying both viscous [94] and non-viscous [4] mechanisms experimentally.

With the second approach, damping is added artificially in the equations simulations by employing certain time-marching integration schemes, as it is usually done with the Newmark-β scheme [70, 73]. However, this methodology does not build on any kind of physical mechanism but is a mere numerical artefact employed to stabilise solvers, hence dismissing any attempt on understanding the role of damping in the dynamics.

As opposed to viscous/proportional damping, where the source of damping is assumed external (e.g., friction with surrounding fluid), structural damping is an internal energy dissipation mechanism (e.g., friction between atomic particles that make up the structure). Hence, modelling of structural damping requires a deeper understanding of the damping mechanisms. It has been found that in linear elastic materials a generic model can be often utilised by means of the following constitutive law [90], which defines the characteristics of a viscoelastic material by relating the temporal derivatives of both stresses (σ) and strains (ϵ)

$$\sum_{n=0}^{N} a_n \frac{\partial^n \sigma}{\partial t^n} = \sum_{m=0}^{M} b_m \frac{\partial^m \epsilon}{\partial t^m}, \tag{1.1}$$

with constant coefficients $a_n,\ b_m$. Different analytical models stem from this constitutive law, such as the strain-rate based damping (Kelvin-Voigt, where $N = 0$ and $M = 1$ are chosen) or time-hysteretic damping models, accounting for past loading time-histories. Spatial-hysteretic models can also be obtained by considering spatial derivatives in (1.1). An early thorough study of the four most common physical damping mechanisms is found in [20], although damping modelling remains still an active field of research, with a recent comprehensive study addressing the identification [3] and analysis of non-viscous [2] damping mechanisms. All these analytical models, based on physical principles, have been used alongside linear beam models [21, 28, 152], for the complexity of the resulting system is still amenable to mathematical manipulation and theoretical analysis.

As described in the introduction, recent advances in lightweight composite materials and the ongoing quest for improving aerodynamic efficiency of aircraft and wind turbine blades have led to a dramatic increase in slenderness, and hence, flexibility. Design and control of such aerostructures demands the use of geometrically nonlinear models in order to capture nonlinear effects due to the large deflections and rotations arising from the increased flexibility. Many are the reasons why theoretical analysis of damping within the

field of three dimensional dynamics of highly flexible structures is disregarded and more practical strategies such as proportional damping or numerical dissipation are considered. A fundamental reason is the complexity of the underlying equations of motion, which are nonlinear. In the particular area of aeroelasticity [41, 81, 160], another motivation leading to the underestimation of more realistic structural damping models is the fact that aerodynamic damping plays a much more significant role in the overall dynamics. However, this reasoning is based on linear assumptions and its extension to the nonlinear scenario remains still of unclear validity.

Due to the aforementioned lack of analysis, understanding of the physical mechanisms of damping within the large-deflections realm is yet very limited; models are often limited to axial vibrations [36, 133] or two-dimensional nonlinear models [141]. A very recent work addressing geometrically nonlinear beams [69] shows how the Kelvin-Voigt model is introduced in the last variational formulation described in the previous section: the three-dimensional mixed-formulation (based on strains, velocities and displacements) of [74], which results from the combination of a variational asymptotic method, which effectively condenses the sectional dynamics using the beam centreline, and a GEB formulation.

1.2.2 Unsteady Aerodynamics

Typical flight velocities of very flexible aircraft concepts such as HALE or HAPS lie well within the subsonic range, meaning that compressibility effects can be safely neglected without significantly compromising the accuracy of the predictions. Although HAPS nominally operate in stratospheric flight conditions, where the characteristic Reynolds numbers are significantly low (very low air density) and appropriate aerodynamic models are scarce (rarefied atmosphere), the challenges faced by these vehicles are more numerous in tropospheric flight (especially in takeoff/landing manoeuvres). This justifies the need for accurate modelling at these lower-altitude (higher-Reynolds number) settings, where we place our focus. At low-altitude flight, the corresponding Reynolds numbers are sufficiently large so that viscous effects remain confined to a very thin, incipient boundary layer, which implies that the airflow away from the fluid-structure contact surfaces is almost unaffected by viscous effects. These reasons justify the use of aerodynamic models based on potential flow tools to evaluate the aerodynamic loads exerted on these vehicles.

The methods that have been most widely used in aeroelasticity of very flexible aircraft are (two-dimensional) thin-strip models, lifting line, doublet-lattice and vortex-lattice methods, in increasing order of model complexity. Unsteady versions of all these methods

can be obtained, which model the dynamic evolution of the aerodynamic loads by means of a set of aerodynamic (or lag) states. These account for the unsteady effect caused by the variation of circulation of the lifting surfaces due to changes in their geometry and kinematics. Following Kelvin's theorem [86], which states that the total circulation must be constant in an inviscid flow, the variation of circulation in the lifting surfaces is shed generating a wake, which is subsequently convected following the background flow and the circulation-induced velocities.

Thin-strip modelling relies on the splitting of the lifting surfaces into separate, independent segments. Therefore, the three-dimensional mechanism of circulation shedding due to a variation in the circulation distribution along the span is neglected. A particular consequence is that tip-loss effects are lost, and each of the segments is assumed to be of infinite-length. This problem becomes less relevant in high aspect ratio configurations, however, correction factors are usually employed to modify the resulting aerodynamic force distribution. Although it has the potential to allow for arbitrary kinematics, the accuracy of the method is compromised in the case of very flexible wings or wings subject to large rotational motions, where each of the segments perceives very different apparent flow velocities resulting in substantial variations in the circulation distribution.

In essence, the thin-strip model considers a continuous vortex distribution along the chord (airfoil) of a given wing segment and assumes a flat wake, both generating an induced velocity field following the Biot-Savart law. By imposing the non-permeability (non-penetration) boundary conditions along the airfoil the vortex distributions can be found. Using a truncated solution expansion typically results in a few aerodynamic states subject to a first-order time evolution involving the kinematics of the segment in consideration [120]. Other approaches rely directly on either time- or frequency-domain closed-form solutions of the problem. A typical time-domain alternative considers Wagner's lift response to a step angle of attack input, to define the unsteady lift as a convolution integral (Duhamel's formula) of the instantaneous quasi-steady angle of attack, dependent on the kinematics of the segment [92]. Similarly, but on the frequency domain, Theodorsen's lift deficiency function is considered to express the aerodynamic lift and moment as a function of the linear and angular velocities of the segment [157]. Both assume a Padé approximant to the closed-form solutions to obtain compact state-space representations of the aerodynamic states.

Lifting-line methods attempt to model the aerodynamics in a lifting surface by substituting it by a vortex line. The idea was first introduced by Prandtl [122], who found an analytical solution for the steady case. However, the solution was limited to straight wings and the generalisation to more complex geometries has been an active research field

[46, 68]. Extension of the method to the unsteady case was first considered in the frequency domain for small-amplitude oscillating plates [5, 76, 80], and later time-domain formulations were devised [45]. Current research efforts try to account for arbitrary kinematics and large rigid-body motions [22, 79]. At a notable higher computational complexity than early lifting-line methods, they enable a more accurate description of the aerodynamics for (unconstrained) highly flexible structures.

Panel or vortex-lattice methods are the most widely employed potential-flow based tools in aeroelastic simulation and analysis. At a fundamental level, these methods split the lifting surfaces into discrete panels, to which singular (elementary) solutions are assigned. The magnitude of each singular solution is found upon solution of a system of algebraic equations resulting from the non-penetration boundary conditions at defined control points [55]. VLM methods are especially attractive in aeroelasticity for its ability to reproduce complex geometries and account for arbitrary kinematics. After the development of steady formulations and due to the prohibitive cost of explicit unsteady VLM implementations, an unsteady extension based on harmonic solutions gave birth to the doublet-lattice method [10, 60, 83], widely used in industrial and commercial software for aerodynamic loads computation. With advances in computational power, time-domain unsteady vortex-lattice methods, as described in detail in [86], have seen a surge in its applications in aircraft aeroelasticity and flight dynamics [108].

An important limitation of all the aforementioned methods is that they rely on linearised aerodynamic potential theory, which assume thin airfoils and neglect all viscous-effects, including drag and flow separation or stall. While thickness of the airfoils can be readily accounted for in both doublet- and vortex-lattice methods by distributing the singular solutions along the actual airfoil profile instead of reducing it to its camber line [85], viscosity-driven effects require of rather *ad hoc* correction techniques. Large wing excursions due to increased flexibility, which justify the need of more accurate wake prediction (given naturally by unsteady VLM formulations), can lead precisely to dynamic stall and flow-separation. In an attempt to extend the potential-flow-based implementations into regimes characterised by non-negligible viscous effects (post-stall regimes, dynamic stall) empirical 2D data from higher-fidelity methods is usually employed to devise appropriate correction factors [51, 115, 159].

1.2.3 Aeroelasticity of Very Flexible Aircraft

In the previous two sections, the different methods used to account for the geometrically nonlinear dynamics of flexible beam-like structures and for the unsteady aerodynamic loads from potential flow assumptions have been described. Yet, it remains to give an overview of the integrated frameworks, engineered by the aeroelastics community, that describe the coupled aeroelastic and flight dynamics of very flexible aircraft.

ASWING [52] was one of the first developed aeroelastic frameworks conceived to analyse and perform preliminary studies of aircraft with flexible airframes. In such formulation, geometrically nonlinear beams, that undergo only bending and torsion deformations, are employed to model each of the airframe components. The structural equations are then coupled to a compressible lifting-line method. This formulation enables rapid nonlinear static, dynamic and frequency-domain analysis and was used to demonstrate the distinct feature of highly flexible aircraft: the coupling between elastic and rigid-body modes, which might lead to body freedom flutter [96], an especially critical instability in low-altitude operation.

Concurrently to ASWING, the University of Michigan's framework UM/NAST (The University of Michigan's Nonlinear Aeroelastic Simulation Toolbox) was developed. It employs the strain-based geometrically nonlinear beam description of [145] and a strip theory to model the unsteady aerodynamics. This framework has been comprehensively validated against experimental data in [147] and recently in [127], in the context of clamped very flexible wings. The software was used to identify the cause of body freedom flutter in a HALE aircraft [144]: the coupling between an elastic bending mode and the rigid short period mode. Furthermore, they observed that a nonlinear aerodynamic model was necessary to accurately capture the phugoid rigid body mode. The authors used UM/NAST to design and develop an experimental test aircraft [34], representative of very flexible HALE aircraft, with which they aim to correlate UM/NAST's numerical simulations in the free-flight scenario [82].

Another important contribution to the aeroelastic modelling and simulation of very flexible aircraft is NATASHA (Nonlinear Aeroelastic Trim and Stability of HALE Aircraft), a computational framework proposed by Patil and Hodges [35, 118]. At its core, it solves an implementation of the intrinsic geometrically nonlinear beam equations [75] coupled to a two-dimensional incompressible unsteady strip theory [119]. Simulations using this formulation have found very good agreement with well-established results [142] and consistency between time- and frequency-domain gust-response analyses [116]. This framework was used to reveal important implications of engine positioning in very flexible HALE aircraft

stability properties [103–105].

NANSI (Nonlinear Aerodynamics/Nonlinear-Structure Interaction) is an aeroelastic framework [159] that uses the geometrically nonlinear intrinsic beam equations [75] coupled to an unsteady vortex lattice method [107] with a stall model. It has been benchmarked with commercial software and with NATASHA, and it has been useful to identify how shear deformation plays an important role in the stability of HALE aircraft against gust excitation.

SHARPy (Simulation of High-Aspect Ratio aeroplanes in Python) is a dynamic aeroelastic simulation toolbox developed at Imperial College London [41] and, in contrast to the previously introduced computational tools, it is available under open-source distributions. It solves for a finite element implementation of a displacement-based geometrically exact beam model [70], tightly coupled to an unsteady vortex lattice formulation [108]. A significant contribution using this framework is the consistent linearisation of the underlying equations, which preserves the coupling between rigid-body and structural elastic degrees of freedom, improving analysis and prediction of loads around nonlinear reference aircraft configurations [73]. With no available/reliable experimental data of free-flying very flexible aircraft to benchmark the framework, a code-to-code comparison with UM/NAST was performed. The dynamic response of the X-HALE aircraft model against gust perturbations showed very good agreement in the longitudinal case, however, a non-negligible discrepancy in the lateral dynamics was detected [43]. A compelling insight on the effect of turbulence on the aeroelasticity of very flexible aircraft was given in [44] using this framework, which shows its potential to simulate realistic atmospheric conditions.

1.2.4 Low-Order Modelling and Control

Control of highly flexible aircraft still remains a challenge, and numerous examples of the difficulties these vehicles face have been directly observed in real flight conditions. The most relevant control application is load alleviation in the presence of gusts or other external disturbances, and in manoeuvring or trajectory tracking, in order to prevent these highly flexible structures from undergoing excessively large deformations which may compromise their integrity and increase fatigue. The fundamental complexity in devising appropriate control mechanisms lies with the highly-dimensional and markedly (geometrically) nonlinear systems that arise from typical state space representations of very flexible aircraft. In order to employ these models for control, a reduction in its complexity via order reduction or simplification of the underlying models must be sought and the different

alternatives that have been considered in the literature are discussed next.

To date, the most commonly used strategy is the linearisation of the underlying state-space realisations, with or without further model order reduction techniques, to employ well-established linear control theory results. For instance, in [117], the system is linearised around a reference configuration to then apply static output feedback, where a coarse spatial discretisation is used to obtain a system of manageable size. In [48], the authors linearise the state-space representation of the aeroelastic system around a reference configuration and a balanced truncation model-order reduction is sought to apply linear-quadratic-Gaussian (LQG) regulation while [71, 139] employ linearised state-space models to underpin a model predictive control strategy for gust-load alleviation. In [134] a rigid-body based controller is applied to the linearised flexible aircraft equations, further decoupling the rigid modes from the elastic motions, which makes obvious the loss of performance for large deflections. The more recent contribution of [65] uses two control loops based on a linearised state-space representation too, with the inner loop employing a linear quadratic regulator (LQR) to stabilise the elastic degrees of freedom while the outer loop makes use of robust $\mathcal{H}_\infty$ control theory to track the rigid-body kinematics.

These approaches are limited to small perturbations around the (nonlinear) reference state and are susceptible to failure and loss of authority when these become excessively large. In an attempt to improve control performance in these cases, while still relying on linear theory, successive linearisation or model updating is employed. It consists of replacing the internal model underpinning the control strategy at fixed time instants, or when large excursions from the reference, linearisation point are detected, for one linearised at the instantaneous configuration as done in [158].

To reduce the complexity of geometric nonlinearities without turning to plain linearisation of the underlying nonlinear equations, other strategies rely on its manipulation to obtain suitable systems for conventional control methods: for instance, the case of [49], where proportional-integral-derivative control (PID) or LQG strategies are used after a nonlinear transformation of the original nonlinear system is applied. A hybrid, more sophisticated strategy is often employed upon identification of a variable or set of variables most influential in the underlying system dynamics. It is the case of parameter varying systems, as the example in [59], where adaptive control is latter applied.

The construction of linear parameter-varying (reduced-order) models starts with building a library of different linear reduced order models for fixed values of the considered parameters leading to different equilibria of the nonlinear system, and an interpolation strategy is then sought to obtain the corresponding *seamless* system. This is of particular

interest in aeroservoelasticity, since increased flexibility translates into larger variations of the vehicle geometry for changing flight conditions and vehicle configurations, which needs to be accounted for by the controller in a fast manner. This is an active field of research, and parametric models are being sought to cover much of the typical aircraft flight envelopes, where common parameters are flight velocity [9, 63], weight configuration [56, 121], or angle of attack [102]. A key requirement in the construction of such systems is appropriate interpolation to obtain a consistent state space across the different systems that define the library [11].

Regarding control, linear control theory can be applied to each of the linear models in the library. Then, a family of linear controllers is obtained with which gain-scheduling [130] can be applied to obtain a control law valid throughout all the interpolated state space. Moreover, the most computationally demanding task of obtaining the library of different linearised systems can be performed offline, leaving only the interpolation step to be computed online, which alleviates the computational burden facilitating hence real-time control. However, the validity of linear parameter-varying systems is largely influenced by the choice of relevant parameters and confined to the vicinity of the corresponding linearisation points, hence being compromised for moderate to large excursions of the system away from these reference (equilibrium) configurations.

To overcome the limitations of linear approximations the much more complex quest of obtaining *nonlinear* reduced order models is starting to gain relevance over the last few years. In contrast to linear reduced-order modelling, where well-established and mature methods abound, rather *ad hoc* approaches must be sought instead when considering model reduction in the nonlinear scenario. Recent contributions focus on the structural dynamics of geometrically-exact beams and the main idea behind most of them is to consider global basis functions to span the solution space, such as the structural linear normal modes, with the expectation that they carry more representative information of the physics and, hence, less states are needed for convergence. This is in contrast to local solution bases, such as typical linear or quadratic interpolating functions employed in finite element implementations, which typically result in high-dimensional state-space representations, rather impractical for control.

A first example of this nonlinear model-order reduction is [106]. Starting from a modal approximation to the displacement field, and after substitution into the infinitesimal equations of motion, they write the governing equations with quadratic and cubic stiffness contributions, which are then identified using solutions obtained from finite element simulations. Similarly, [150] ends up with quadratic and cubic stiffness contributions by expanding the displacement field using quadratic products of the linear normal modes,

while [128] considers quadratic modes in the force-displacement relationships and expands the higher order terms of the elastic potential energy and the displacement field with a Taylor series up to fourth order. Linear normal modes are also used to get to a modal formulation of the strain-based geometrically exact beam [146] and of the intrinsic GEB formulation of Hodges [157]. The latter results in a compact first-order-in-time system of ordinary differential equations with quadratic nonlinearities. Other basis functions than linear normal modes have been explored, for instance in [77], where Chebyshev polynomials are employed to construct approximate solutions to a GEB formulation written in generalised coordinates.

The latest trend in model-order reduction (or rather, direct identification of low-order models) is to employ artificial intelligence tools, such as neural networks or other data-driven model-fitting techniques. As opposed to the previously described methods, where the systems are obtained from direct manipulation of mathematical models derived from first principles, they rely on the availability of a large quantity of data, obtained either through experimentation or through simulation of highly-resolved models, to obtain sensible and accurate models. A renowned data-driven method is dynamic mode decomposition [132, 149], from which a linear, low-order state-space representation is recovered building upon proper orthogonal decomposition of the obtained system data. It has found useful applications mainly in fluid dynamics problems [26, 91]. To extend the framework to the nonlinear case, linear-parameter varying systems are analogously used to interpolate across different data-driven linear models (see [57, 78] for application of different LPV strategies to aeroelasticity, where the performance of the obtained models as part of a model predictive control algorithm are also shown).

However, these data-driven techniques are now powerful enough to endeavour the more challenging task of finding *nonlinear* reduced order models fitted to existing data. Useful tools are sparsity-promoting regression algorithms, which have been successful at recovering well-established nonlinear low-order models, such as the Lorentz attractor, and at identifying coherent structures and symmetries in reduced nonlinear dynamics of fluid mechanics problems [27]. A known difficulty of purely data-driven approaches is obtaining models which preserve the structure of the underlying physics (e.g., energy or passivity preservation, dissipativity). Failure in capturing these structures exactly can potentially lead to unstable or nonphysical systems. Recent research focuses on the integration of some of these *a priori* known physical properties into a constrained model-fitting algorithm [95] to obtain, by construction, more accurate and physically-sensible models. Another strategy is to incorporate model-fitting or neural-network modelling into first-principles-based modelling, where the algebra or analysis becomes unmanageable, as

exemplified in [53].

Up until now, the different model-order reduction techniques used in aeroelasticity of very flexible aircraft have been described, alongside fitting or appropriate control methodologies. To conclude this section, model predictive control deserves a special mention. This control strategy, consisting of solving *online* open-loop optimal control problems repetitively at fixed time instants, is experiencing a growing interest for aeroelastic applications. This is explained because of its versatility, since it can be used both in regulation (e.g., disturbance rejection, load alleviation) and tracking (e.g., motion planning, trajectory tracking) problems, and for its ability to explicitly employ model nonlinearities [123, ch. 2]. The latter feature makes the approach particularly compelling for the control of highly flexible aircraft, since all the geometrically nonlinear effects (namely geometrical stiffening, global changes of inertia and follower force effects) are captured. Failing to do so has been attributed as the cause of the numerous unsuccessful flights of very flexible aircraft prototypes. Another advantage of MPC is the direct handling of state hard constraints, which are typical in many flexible structure application problems (e.g., maximum allowable stresses to alleviate fatigue, maximum allowable displacements to prevent collision of flexible components).

Nonetheless, model predictive control strategies have not yet been fully exploited in the nonlinear context of very flexible aircraft control due to its hitherto prohibitive computational cost. As an example, the classical approach of modelling highly flexible geometrically-nonlinear structures with displacement and rotations as primary variables typically requires markedly nonlinear models with $\mathcal{O}(10^3)$ states for simple geometries [114] to accurately capture the underlying dynamics, while typical unsteady aerodynamic models can have up to $\mathcal{O}(10^5)$ states. This has restricted MPC approaches to employ linearisations of the discretised state-space representations of aeroelastic systems about a reference steady state or a sequential linearisation about the instantaneous configuration, as seen in the application examples in gust and manoeuvre load alleviation [40, 71, 139] and in trajectory tracking [158] problems. Solving the constrained optimal control problems is also computationally expensive, and strategies to alleviate the associated burden in the setting of control of highly flexible aircraft is an active line of investigation [39].

1.3 Research Questions

Following the presented literature review, several research questions arise and potential gaps in the literature have been identified. These are summarised below.

- Capturing geometrical nonlinearities is paramount for an accurate prediction of the dynamics of highly flexible structures. Besides, the flight dynamics of very flexible aircraft are strongly influenced by the non-negligible couplings between elastic and rigid-body motions. A first question that arises is, how can a minimal description of the coupled flight dynamics/equations of motion be obtained, capable to retain the main geometrically nonlinear effects? Which are the most suitable mathematical models, describing both the structural dynamics and the aerodynamics, for this modelling synthesis endeavour?

- Control of very flexible aircraft remains, to date, still an open problem, with numerous and notorious examples justifying the need for new, unconventional control strategies. Traditional control methods have been shown to be rather vulnerable in off-design manoeuvres or under adverse meteorological conditions, which might potentially drive the system away from the region in which a nominal linear controller is accurate. Then, is it possible to devise a control framework that enlarges the range of operation of conventional control strategies and has authority in the nonlinear regime? What is a suitable choice of controller to handle nonlinear systems appropriately? Is this controller able to operate in real time? If not, how far is it currently from real-time operation or which alterations can be done towards achieving this goal?

- In the context of applicability of the control framework further questions arise. How can the framework be made as flexible as possible regarding control applications (e.g., gust load alleviation, manoeuvre alleviation, flutter suppression)? How can the devised methodology be as general as possible and easily adapted to different aircraft configurations or models? What are possible implementation difficulties and constraints for on-board deployment?

1.4 Thesis Outline and Publications

This dissertation aims to answer most of the questions risen above. In this section, the structure and order in which this work will be presented is outlined, where the different publications which have originated from each of the research pieces are also given. These are listed at the end of this section together with the labels used in the following lines.

Chapter 2. This initial chapter introduces the chosen underlying mathematical models to describe both the structural dynamics and the unsteady aerodynamics, upon which

the developed control framework is built. These consist of a set of partial differential equations (structure) and a highly resolved finite-dimensional formulation (aerodynamics) which form the theoretical backbone of the presented work.

To model the dynamics of highly flexible beam-like structures in three dimensions the intrinsic geometrically-exact beam equations are employed and a brief account of the original formulation is given. The extension of the Kelvin-Voigt damping model to the intrinsic, nonlinear framework is one of the novel contributions of the presented work (AIAAJ 2020). This is described in this rather introductory chapter devoted to background theories to portray a complete picture of the structural model. Regarding the model for the aerodynamics, an unsteady vortex lattice method is chosen, which arises from spatial discretisation of potential flow solutions.

Chapter 3. Here, the methods to obtain *nonlinear* low-order aeroelastic models amenable to control synthesis are presented. The keystone is the use of the structural normal modes of vibration (also referred to as linear normal modes, structural eigenfunctions or simply mode shapes) to construct a basis for an approximate, low-order solution. These not only play a pivotal role in the order-reduction of both structural and aerodynamic models, but also bring about a common basis with which the coupling of both subsystems is eased. It is found that typically, the first few modes of vibration carry enough physical information for successful control.

The chapter starts by introducing a systematical way to obtain the structural mode shapes for an arbitrary network and configuration of beams, directly from the intrinsic equations ((IFAC 2020) gives some details for the case of jointed structures). Later, it is described how these are used to construct a finite-dimensional nonlinear description of the intrinsic geometrically exact beam equations. Subsequently, it is shown how these mode shapes are further used to reduce the input/output dimensionality of unsteady vortex lattice models to then apply efficient model order-reduction techniques.

Data-driven techniques that have the potential to assist in the reduced-order modelling effort are also explored. In this chapter we discuss how these can be used to improve known limitations of the first-principles modal-based reduction approach.

Relevant details on the construction of such models can be found in all listed publications except for (AIAAJ 2020).

Chapter 4. This chapter introduces the chosen control strategy, a nonlinear model predictive control framework, which is underpinned by the low-order model described in Chapter 3. It builds upon an optimal control framework which was initially introduced

in (ECC 2019). Stability and convergence results are also presented. These, have been established for the typical systems that arise from structural models based on the intrinsic formulation, results which were shown in (IEEE TAC 2021). A nonlinear moving horizon estimation is also described, which has been implemented together with the control counterpart and its application to aeroelastic problems has been shown in (AIAAJ 2021) and (SciTech 2020, SciTech 2021).

Chapter 5. This chapter presents the numerical examples where the previously described methods are applied on fundamental (proof of concept) cases. The first numerical case is an illustrative example of the effect of Kelvin-Voigt damping in the nonlinear dynamics of the intrinsic beam equations, results that are shown in detail in (AIAAJ 2020). Focusing on the main topic of the dissertation, the next example shows the effectiveness and efficiency of the modal-based nonlinear structural models to solve optimal control problems concerning very flexible structures (ECC 2019). This nonlinear, optimal control framework is used to construct an efficient model predictive control implementation (IEEE TAC 2021), which is shown to be successful in the control of very flexible structures with very concise model descriptions. Besides, the performance of the novel MPC scheme, tailored to the *partially* stabilisable descriptions resulting from the necessity to compute finite-rotation or displacement fields in addition to the intrinsic equations, is shown.

Chapter 6. This chapter presents three numerical cases, where the conceived control framework, validated and showcased with canonical examples in the previous chapter, is put to the test with now full aeroelastic examples, where the moving-horizon estimator is also introduced. The first considers the case of clamped wings (AIAAJ 2021, SciTech 2021), which shows the controller leverage of the nonlinear dynamics to explore unconventional control mechanisms. The second considers the case of a free-flying high-altitude long-endurance concept aircraft to be stabilised after a sudden change in the aircraft payload configuration. Finally, the last example is used to show the potential advantages of combining data-driven modelling with the presented physical-based modelling methods, including its effect on open-loop simulations and on closed-loop control and estimation performance.

Chapter 7. In this summarising chapter, the main conclusions of the thesis are given, outlining the novel contributions of the presented work and presenting potential applications of the described methods. Future lines of investigation and recommendations for future work are also provided.

The different conference and journal publications that have arisen from this work are listed below:

Conference Publications.

(ECC 2019) M. Artola, A. Wynn and R. Palacios, "A Nonlinear Modal-Based Framework for Low Computational Cost Optimal Control of 3D Very Flexible Structures", 2019 18th European Control Conference (ECC), Naples, Italy, Jun 2019, pp. 3836-3841. https://doi.org/10.23919/ECC.2019.8796151

(IFAC 2020) M. Artola, A. Wynn and R. Palacios,"Modal-Based Model Predictive Control of Multibody Very Flexible Structures", IFAC-PapersOnline, Vol. 53, Num. 2, pp. 7472-7478. https://doi.org/10.1016/j.ifacol.2020.12.1302

(SciTech 2020) M. Artola, N. Goizueta, A. Wynn and R. Palacios, "Modal-Based Nonlinear Estimation and Control for Highly Flexible Aeroelastic Systems", AIAA Scitech 2020 Forum, Orlando, FL, Jan 2020. https://doi.org/10.2514/6.2020-1192

(SciTech 2021) M. Artola, N. Goizueta, A. Wynn and R. Palacios, "Proof of Concept for a Hardware-in-the-Loop Nonlinear Control Framework for Very Flexible Aircraft", AIAA Scitech 2021 Forum, Nashville, TN, Jan 2021. https://doi.org/10.2514/6.2021-1392

Journal Publications.

(AIAAJ 2020) M. Artola, A. Wynn and R. Palacios, "Generalized Kelvin-Voigt Damping Model for Geometrically-Nonlinear Beams", AIAA Journal, Vol. 59, Num. 1, pp. 356-365. https://doi.org/10.2514/1.J059767

(IEEE TAC 2021) M. Artola, A. Wynn and R. Palacios, "Modal-Based Nonlinear Model Predictive Control for 3D Very Flexible Structures", IEEE Transactions on Automatic Control, Vol. 67, Num. 5. (Scheduled for publication) https://doi.org/10.1109/TAC.2021.3071326.

(AIAAJ 2021) M. Artola, N. Goizueta, A. Wynn and R. Palacios, "Aeroelastic Control and Estimation with a Minimal Nonlinear Modal Description", AIAA Journal, Vol. 59, Num.7, pp. 2697-2713. https://doi.org/10.2514/1.J060018

In the papers listed above, co-authored with N. Goizueta, the contributions are as follows. All models, analyses and simulations obtained with Imperial College open-source aeroelasticity software (SHARPy) are N. Goizueta's work. The models, analyses and simulations referring to the control framework as well as other control-related implementations are M. Artola's work. Wherever joint results are presented in this dissertation, originating from combined contributions, a clear remark is made.

Chapter 2

Underlying Structural and Aerodynamic Models

In this chapter we describe the chosen structural and aerodynamic mathematical models which are the backbone of our control-oriented modelling framework. These are presented here in its original form; prior to any model-order reduction or aeroelastic coupling, matter that is addressed in Chapter 3.

To model the arbitrarily large three-dimensional motions of highly flexible beam-like structures we use the more recent *intrinsic* formulation of geometrically-exact beam formulation, which is based on strains and velocities. This is a Hamiltonian description of the geometrically nonlinear structural dynamics where the use of the energy-conjugate pair velocities-strains as main variables leads to a compact mathematical model. Due to its structure, analytical manipulation is facilitated, in particular, *nonlinear* low-order reduction. This is key in enabling efficient model-order reduction, as extensive evidence has suggested that the resulting low-order models typically necessitate of much lower number of states to capture the relevant geometrically nonlinear dynamics, when compared to conventional discretisations of displacement-based formulations, which is essential for control purposes. We also include here a novel contribution of our work to present the complete mathematical model describing the structural dynamics: the generalisation of structural Kelvin-Voigt damping model to the geometrically nonlinear, intrinsic setting. An insight of its dissipative effect on the solutions is studied in the case where the nonlinear terms arising from this damping model are fully retained and in the case where they are linearised.

To describe the unsteady aerodynamics we employ unsteady vortex lattice methods, due

to their ability to account for arbitrarily large deflections and rotations on attached flows, including large rigid-body motions. Besides, its state-space representation is naturally expressed in time-domain, which eases the coupling with the structural counterpart and it allows for consistent linearisation, which promotes efficient model-order reduction methods to be employed.

2.1 Intrinsic Beam Formulation

The dynamics of slender composite beams are described by the intrinsic, geometrically-exact beam theory of Hodges. The equations were initially derived from Hamilton's principle using a mixed formulation: generalised strains and curvatures were used to express the beam elastic potential energy and generalised linear and angular momenta coordinates to describe the kinetic energy [74]. The closed form of the equations, which needs constitutive relationships between generalised momenta coordinates and sectional linear and angular velocities and between generalised strains and force/moment sectional resultants, is given in [75]. Under small strain assumptions, these constitutive laws are linear and, by appropriate choice of coefficients (typically done experimentally for small-amplitude tests), they can also account for sectional warping effects.

2.1.1 Frames of Reference

Prior to introducing the mathematical model that describes the intrinsic beam formulation, it is convenient to present the two different frames of reference that are used in the following.

The first, referred to as *material* or *local* frame of reference, is defined locally (i.e., at each location along the spatial domain), with origin at the *centreline* (or *reference* line) of the beam and which moves together with the beam cross section, and defines the set of local coordinates. The generality of the formulation allows for freedom in the choice of reference line and the orientation of the local axes. However, for convenience, the beam *elastic* axis is chosen as a reference line, whose tangent direction defines the first local axis and the remaining two are chosen to coincide with the cross-sectional principal axes of inertia. As explained later, these choices allow for simplified constitutive relationships in the case of isotropic material properties. The second frame of reference is an *inertial* or *fixed* frame of reference, with respect to which displacements and finite-rotations are expressed. Both frames are depicted in Fig.2.1.

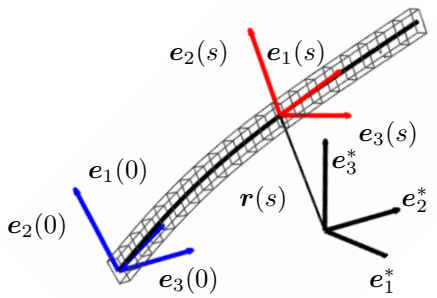


Figure 2.1: Inertial frame of reference (black) and local frame of references at $s = 0$ (blue) and at an arbitrary location s (red) in an unconstrained beam configuration. Elastic axis displayed in thick, solid, black line.

2.1.2 Original Intrinsic Beam Equations

This formulation, following the notation introduced in [112], uses two vector states, with components in local coordinates, namely the linear and angular inertial velocities vector $\boldsymbol{x}_1(s,t) := (\boldsymbol{v}^\top \boldsymbol{\omega}^\top)^\top : [0,L] \times \mathbb{R}_+ \to \mathbb{R}^6$ and the force and moment sectional resultants vector $\boldsymbol{x}_2(s,t) := (\boldsymbol{f}^\top \boldsymbol{m}^\top)^\top : [0,L] \times \mathbb{R}_+ \to \mathbb{R}^6$. The curvilinear spatial coordinate is denoted by s, which defines the beam elastic axis, origin of the local coordinates, and t is used to denote time. The arc-length of the undeformed and unloaded structure is L. Using prime $(\bullet)'$ and dot $(\dot{\bullet})$ superscripts to denote partial derivatives with respect to s and t, respectively, the equations read

$$M\dot{\boldsymbol{x}}_1 - \boldsymbol{x}_2' - E\boldsymbol{x}_2 + \mathcal{L}_1(\boldsymbol{x}_1)M\boldsymbol{x}_1 + \mathcal{L}_2(\boldsymbol{x}_2)C\boldsymbol{x}_2 = \boldsymbol{f}_e, \tag{2.1}$$

$$C\dot{\boldsymbol{x}}_2 - \boldsymbol{x}_1' + E^\top \boldsymbol{x}_1 - \mathcal{L}_1^\top(\boldsymbol{x}_1)C\boldsymbol{x}_2 = \boldsymbol{0}, \tag{2.2}$$

together with natural boundary conditions (i.e., no boundary forcing)

$$x_{1i}(0,t)x_{2i}(0,t) = 0, \quad x_{1i}(L,t)x_{2i}(L,t) = 0, \qquad i = 1,\dots,6, \tag{2.3}$$

where, for example, x_{1i} denotes the i^{th} entry of the vector $\boldsymbol{x}_1$ (that is, at a given boundary, either a velocity or force component can be prescribed to be zero). Matrices $M(s) : \mathbb{R} \to \mathcal{S}^6_{++}$ and $C(s) : \mathbb{R} \to \mathcal{S}^6_{+}$ are the mass and compliance matrices ($\mathcal{S}^6_{++}$ and $\mathcal{S}^6_{+}$ are used to denote the set of symmetric, positive definite and semidefinite matrices, respectively, in $\mathbb{R}^6$). These matrices define the aforementioned linear relationships between the intrinsic variables and the generalised linear and angular momenta $\boldsymbol{p}$, $\boldsymbol{h} \in \mathbb{R}^3$ and generalised

strains and curvatures $\boldsymbol{\gamma}$, $\boldsymbol{\kappa} \in \mathbb{R}^3$ as follows:

$$\begin{pmatrix} \boldsymbol{p} \\ \boldsymbol{h} \end{pmatrix} = M \begin{pmatrix} \boldsymbol{v} \\ \boldsymbol{\omega} \end{pmatrix} = M\boldsymbol{x}_1, \qquad \begin{pmatrix} \boldsymbol{\gamma} \\ \boldsymbol{\kappa} \end{pmatrix} = C \begin{pmatrix} \boldsymbol{f} \\ \boldsymbol{m} \end{pmatrix} = C\boldsymbol{x}_2. \tag{2.4}$$

As previously introduced, following our choice of local axes origin and orientation, for an isotropic material the mass and compliance matrices have the following structure

$$M = \begin{pmatrix} \mu I_3 & -\mu\widetilde{\boldsymbol{r}_{cg}} \\ \mu\widetilde{\boldsymbol{r}_{cg}} & \mathbb{I} \end{pmatrix}, \qquad C = \mathrm{diag}(EA, GA_2, GA_3, GJ, EI_2, EI_3)^{-1}, \tag{2.5}$$

where μ is the mass per unit length, $\mathbb{I}$ is the cross-sectional inertia (diagonal) matrix and $\boldsymbol{r}_{cg}$ is the relative distance between the sectional centre of mass and the elastic axis[1]. Regarding the stiffness terms, E and G denote the Young and shear moduli of the structure (material properties), and A, A_2, A_3, J, I_2 and I_3 are the area, the shear areas, the torsion constant and the second moments of area of the cross-section with respect to the local axes (geometrical properties). In the case of anisotropy in the material properties (for instance in structures formed by alternating composite material layers), the compliance matrix would display off-diagonal nonzero entries to account for the corresponding stiffness couplings [32]. The introduced tilde superscript $\widetilde{\boldsymbol{a}}$ denotes the vector product matrix operator, defined as $\widetilde{\boldsymbol{a}}\boldsymbol{b} = \boldsymbol{a} \times \boldsymbol{b}$, for $\boldsymbol{a}, \boldsymbol{b} \in \mathbb{R}^3$. This is,

$$\widetilde{\boldsymbol{a}} = \begin{pmatrix} 0 & -a_3 & a_2 \\ a_3 & 0 & -a_1 \\ -a_2 & a_1 & 0 \end{pmatrix}. \tag{2.6}$$

The matrix $E(s) : \mathbb{R} \to \mathbb{R}^{6\times 6}$ gathers information on the initial curvature and pre-twist $\boldsymbol{\kappa}_0 \in \mathbb{R}^3$ (i.e., for beams with curvature in an unloaded configuration, such as arched structures)

$$E = \begin{pmatrix} \widetilde{\boldsymbol{\kappa}}_0 & 0 \\ \widetilde{\boldsymbol{e}}_1 & \widetilde{\boldsymbol{\kappa}}_0 \end{pmatrix}, \tag{2.7}$$

where $\boldsymbol{e}_1 = (1, 0, 0)^\top$ is the first vector of the local frame of reference (whose origin is at the beam elastic axis and in which all variables and matrices are expressed), tangent to

[1]The sectional centre of mass is the point of the beam cross section in which the gravity resultant force is applied (i.e., depends on the density distribution of the cross section), while the elastic axis is the application point of the resultant elastic forces (i.e., the point in which applied linear forces do not generate torques). For uniform cross sections with two symmetry axes both points coincide, but they do not in U-shaped sections or conventional aircraft wing sections, for instance.

the beam elastic axis. The linear operators $\mathcal{L}_1, \mathcal{L}_2 : \mathbb{R}^6 \to \mathbb{R}^{6\times 6}$ are defined as

$$\mathcal{L}_1(\boldsymbol{x}_1) = \begin{pmatrix} \widetilde{\boldsymbol{\omega}} & 0 \\ \widetilde{\boldsymbol{v}} & \widetilde{\boldsymbol{\omega}} \end{pmatrix}, \qquad \mathcal{L}_2(\boldsymbol{x}_2) = \begin{pmatrix} 0 & \widetilde{\boldsymbol{f}} \\ \widetilde{\boldsymbol{f}} & \widetilde{\boldsymbol{m}} \end{pmatrix}. \tag{2.8}$$

External forces and moments per unit length, acting along the structure (e.g., aerodynamic or gravitational forces), are gathered in the vector $\boldsymbol{f}_e : [0, L] \times \mathbb{R}_+ \to \mathbb{R}^6$. Prescribed motions or forces at a boundary are enforced as $x_{1i}(s_\partial, t) = u(t)$ or $x_{2i}(s_\partial, t) = u(t)$, with $u(t) : \mathbb{R}_+ \to \mathbb{R}$ a function of time and $s_\partial \in \{0, L\}$.

The total energy (kinetic and potential) of the system is given by

$$\epsilon(t) = \frac{1}{2} \langle \boldsymbol{x}_1, M\boldsymbol{x}_1 \rangle + \frac{1}{2} \langle \boldsymbol{x}_2, C\boldsymbol{x}_2 \rangle . \tag{2.9}$$

Differentiating (2.9) with respect to time and substituting (2.1)–(2.2), the nonlinear terms vanish due to the skew-symmetric properties of the $\mathcal{L}_1$ and $\mathcal{L}_2$ operators and the energy rate is found to be

$$\dot{\epsilon}(t) = \langle \boldsymbol{x}_1, \boldsymbol{f}_e \rangle + \boldsymbol{x}_1^\top \boldsymbol{x}_2 \big|_0^L , \tag{2.10}$$

where $\langle \cdot, \cdot \rangle$ denotes the $L^2([0, L])^6$-inner product. We note that, provided boundary conditions (2.3) are satisfied and there is no external forcing $\boldsymbol{f}_e$, energy is conserved.

2.1.3 Damped Intrinsic Beam Equations

Now, we describe the novel contribution of our work to the modelling of the three-dimensional dynamics of geometrically-exact beams, namely, the generalisation of Kelvin-Voigt damping to the recently presented nonlinear intrinsic equations.

As it is suggested by (2.4), any (linear) modification to the constitutive relationship between forces and strains to account for damping has a significant effect on the internal force/moment distribution. Moreover, new nonlinear terms arise within the intrinsic formulation, due to couplings of cross-product nature (as dictated by (2.8)) between the extra forces coming from damping and the rest of elastic forces. The relevance of these higher order terms to the overall dynamics to obtain an accurate description of highly flexible structures is studied for the first time here. Specifically, we investigate the energy decay rates and the resulting equilibrium solutions imposed by the addition of structural damping in the full geometrically nonlinear scenario and in the case where these higher order terms involving damping are neglected.

We start by rewriting the equations of motion (2.1) prior to the introduction of the linear strain-force relationship (2.4), which expresses the dynamics of geometrically exact beams using velocities, $\boldsymbol{x}_1$, strains and curvatures $\boldsymbol{\gamma}$, $\boldsymbol{\kappa}$, and sectional force and moment resultants $\boldsymbol{f}$, $\boldsymbol{m}$:

$$M\dot{\boldsymbol{x}}_1 - \begin{pmatrix}\boldsymbol{f}\\ \boldsymbol{m}\end{pmatrix}' - E\begin{pmatrix}\boldsymbol{f}\\ \boldsymbol{m}\end{pmatrix} + \mathcal{L}_1(\boldsymbol{x}_1)M\boldsymbol{x}_1 + \mathcal{L}_2\left(\begin{pmatrix}\boldsymbol{f}\\ \boldsymbol{m}\end{pmatrix}\right)\begin{pmatrix}\boldsymbol{\gamma}\\ \boldsymbol{\kappa}\end{pmatrix} = \boldsymbol{f}_e. \tag{2.11}$$

Note that the compatibility equations (2.2) remain unaffected since they do not depend on constitutive relations. Then, the strain-force constitutive law in (2.4), which closes the problem, is modified according to the Kelvin-Voigt model of damping [21], where the stresses (here force/moment resultants, due to the sectional condensation) receive an additional contribution proportional to the time-derivative of the strains:

$$\begin{pmatrix}\boldsymbol{f}\\ \boldsymbol{m}\end{pmatrix} = C^{-1}\begin{pmatrix}\boldsymbol{\gamma}\\ \boldsymbol{\kappa}\end{pmatrix} + C_\tau C^{-1}\frac{\partial}{\partial t}\begin{pmatrix}\boldsymbol{\gamma}\\ \boldsymbol{\kappa}\end{pmatrix} = \boldsymbol{x}_2 + C_\tau\frac{\partial \boldsymbol{x}_2}{\partial t} \tag{2.12}$$

for a suitable choice of damping matrix C_τ, whose entries should be determined by a sectional condensation exercise similar to that required to obtain sectional inertia and compliance properties M and C. Some insight on how to proceed to obtain such matrices is given in [69]. Note that for convenience the definition of $\boldsymbol{x}_2$ is restricted now to refer uniquely to the product $\boldsymbol{x}_2 = C^{-1}\left(\begin{smallmatrix}\boldsymbol{\gamma}\\ \boldsymbol{\kappa}\end{smallmatrix}\right)$, contrarily to the original case, where $\boldsymbol{x}_2$ referred both to the force/moment sectional resultants $\left(\begin{smallmatrix}\boldsymbol{f}\\ \boldsymbol{m}\end{smallmatrix}\right)$ and to the product $C^{-1}\left(\begin{smallmatrix}\boldsymbol{\gamma}\\ \boldsymbol{\kappa}\end{smallmatrix}\right)$, since a one-to-one relationship was established between the instantaneous forces/moments and generalised strains. Here, it is further assumed that $C_\tau C^{-1} \in \mathcal{S}^6_+$, where C_τ is the damping coefficients matrix. As deduced from (2.12), C_τ has dimensions of time, which gives time scales that characterise the damping of the viscoelastic material. By replacing the force and moment terms in (2.11) using the modified constitutive law (2.12), the damped version of the geometrically nonlinear intrinsic beam equations is

$$M\dot{\boldsymbol{x}}_1 - (\boldsymbol{x}_2 + C_\tau\dot{\boldsymbol{x}}_2)' - E(\boldsymbol{x}_2 + C_\tau\dot{\boldsymbol{x}}_2) + \mathcal{L}_1(\boldsymbol{x}_1)M\boldsymbol{x}_1 + \mathcal{L}_2(\boldsymbol{x}_2 + C_\tau\dot{\boldsymbol{x}}_2)C\boldsymbol{x}_2 = \boldsymbol{f}_e, \tag{2.13}$$

$$C\dot{\boldsymbol{x}}_2 - \boldsymbol{x}_1' + E^\top\boldsymbol{x}_1 - \mathcal{L}_1^\top(\boldsymbol{x}_1)C\boldsymbol{x}_2 = \boldsymbol{0}. \tag{2.14}$$

We emphasise that the compatibility equation (2.14) remains unchanged by the new constitutive law, since no force/moment terms are present. The methodology in [69] is to substitute, instead, the strain/curvature terms in the variational form using the time-integrated version of (2.12), hence maintaining the forces/moments as main variables. With our approach, which directly accounts for the modified strain-force relationship (2.12) in the full PDEs, we expect to obtain a compact expression of damped geometrically

exact beams which facilitates the analysis and reveals the effect of damping on the three-dimensional dynamics.

In the damped case, natural boundary conditions (2.3) are replaced by

$$x_{1i}(s_\partial, t)\left[\boldsymbol{x}_2(s_\partial, t) + C_\tau(s_\partial)\dot{\boldsymbol{x}}_2(s_\partial, t)\right]_i = 0, \qquad i = 1, \ldots, 6, \quad s_\partial \in \{0, L\}, \tag{2.15}$$

since the addition of structural damping modifies the force and moment distributions. Similarly to the undamped case, if velocity is prescribed at any of the boundaries, then $x_{1i}(s_\partial, t) = u(t)$. Alternatively, if force is prescribed, we have $[\boldsymbol{x}_2 + C_\tau\dot{\boldsymbol{x}}_2]_i|_{s_\partial} = u(t)$, where $[\bullet]_i$ denotes the ith entry of the vector.

Energy Rate

Under this damping model, we now proceed to evaluate the new energy rate (2.10) for the case where neither external forces nor boundary forcing are present (i.e., $\boldsymbol{f}_e = \boldsymbol{0}$ and boundary conditions (2.15) hold). Differentiating (2.9) and using (2.13)–(2.14),

$$\begin{aligned}\dot{\epsilon} &= \langle \boldsymbol{x}_1, M\dot{\boldsymbol{x}}_1\rangle + \langle \boldsymbol{x}_2, C\dot{\boldsymbol{x}}_2\rangle = \\ &\left\langle \boldsymbol{x}_1, (\boldsymbol{x}_2 + C_\tau\dot{\boldsymbol{x}}_2)'\right\rangle + \langle \boldsymbol{x}_1, E\left(\boldsymbol{x}_2 + C_\tau\dot{\boldsymbol{x}}_2\right)\rangle - \langle \boldsymbol{x}_1, \mathcal{L}_1(\boldsymbol{x}_1)M\boldsymbol{x}_1 + \mathcal{L}_2\left(\boldsymbol{x}_2 + C_\tau\dot{\boldsymbol{x}}_2\right)C\boldsymbol{x}_2\rangle \\ &+ \langle \boldsymbol{x}_2, \boldsymbol{x}_1'\rangle - \left\langle \boldsymbol{x}_2, E^\top\boldsymbol{x}_1\right\rangle + \left\langle \boldsymbol{x}_2, \mathcal{L}_1^\top(\boldsymbol{x}_1)C\boldsymbol{x}_2\right\rangle.\end{aligned}$$

Leveraging the skew-symmetric properties of E, $\mathcal{L}_1$ and $\mathcal{L}_2$, it can be easily shown that, for any $\boldsymbol{x}_1, \boldsymbol{x}_2 \in \mathbb{R}^6$, the following results hold

$$\langle \boldsymbol{x}_1, E\boldsymbol{x}_2\rangle - \left\langle \boldsymbol{x}_2, E^\top\boldsymbol{x}_1\right\rangle = 0, \tag{2.16}$$

$$\boldsymbol{x}_1^\top\mathcal{L}_1(\boldsymbol{x}_1) = 0, \tag{2.17}$$

$$\boldsymbol{x}_2^\top\mathcal{L}_1^\top(\boldsymbol{x}_1) - \boldsymbol{x}_1^\top\mathcal{L}_2(\boldsymbol{x}_2) = 0. \tag{2.18}$$

Consequently,

$$\begin{aligned}\dot{\epsilon} &= \left\langle \boldsymbol{x}_1, (\boldsymbol{x}_2 + C_\tau\dot{\boldsymbol{x}}_2)'\right\rangle + \langle \boldsymbol{x}_1, EC_\tau\dot{\boldsymbol{x}}_2\rangle - \langle \boldsymbol{x}_1, \mathcal{L}_2\left(C_\tau\dot{\boldsymbol{x}}_2\right)C\boldsymbol{x}_2\rangle + \langle \boldsymbol{x}_2 + C_\tau\dot{\boldsymbol{x}}_2, \boldsymbol{x}_1'\rangle - \langle C_\tau\dot{\boldsymbol{x}}_2, \boldsymbol{x}_1'\rangle \\ &= \boldsymbol{x}_1^\top\left(\boldsymbol{x}_2 + C_\tau\dot{\boldsymbol{x}}_2\right)\big|_0^L + \langle \boldsymbol{x}_1, EC_\tau\dot{\boldsymbol{x}}_2\rangle - \langle \boldsymbol{x}_1, \mathcal{L}_2\left(C_\tau\dot{\boldsymbol{x}}_2\right)C\boldsymbol{x}_2\rangle - \langle C_\tau\dot{\boldsymbol{x}}_2, \boldsymbol{x}_1'\rangle.\end{aligned}$$

Using boundary conditions (2.15), substituting $\boldsymbol{x}_1'$ using (2.14), and employing again the

properties of the E and $\mathcal{L}$ operators (2.16)–(2.18) we arrive at

$$\dot{\epsilon} = -\langle C_\tau \dot{\boldsymbol{x}}_2, C\dot{\boldsymbol{x}}_2 \rangle \leq 0, \tag{2.19}$$

where the final inequality holds since we only consider $C_\tau C^{-1} \in \mathcal{S}^6_+$.

Unforced Equilibrium Solutions

The solutions to (2.13)–(2.14) without external forcing (neither distributed nor boundary forcing) are obtained using a Lyapunov stability argument. We use the energy of the system ϵ (Eq. (2.9)) as our Lyapunov candidate function, since we note that $\epsilon > 0$ for all $\boldsymbol{x}_1 \neq \mathbf{0}$ and $\boldsymbol{x}_2 \neq \mathbf{0}$ and $\dot{\epsilon} \leq 0$. Assuming now $C_\tau C^{-1} \succ 0$ and $\boldsymbol{f}_e = \mathbf{0}$, we have that $\dot{\epsilon} < 0$ for any $\dot{\boldsymbol{x}}_2 \neq \mathbf{0}$, and using LaSalle's Invariance Principle [89], which states that trajectories converge to the largest invariant set in $\{\boldsymbol{x}_1, \boldsymbol{x}_2 \mid \dot{\epsilon} = 0\}$, solutions to (2.13)-(2.15) converge to trajectories given by

$$\dot{\boldsymbol{x}}_2 = \mathbf{0} \quad \Rightarrow \quad \boldsymbol{x}_1' = E^\top \boldsymbol{x}_1 - \mathcal{L}_1^\top(\boldsymbol{x}_1) C \boldsymbol{x}_2. \tag{2.20}$$

Solutions described by (2.20) are rigid-body type steady trajectories (i.e., $\dot{\boldsymbol{x}}_2 = \mathbf{0}$ implies no variation of the elastic deformations) with constant energy ϵ, where the structure is allowed to have some remaining stress distribution due to gyroscopic forces appearing from steady rotations. Furthermore, if one of the boundaries is clamped (i.e., $\boldsymbol{x}_1(s_\partial) = \mathbf{0}$), then by spatial integration of (2.20) it is implied that $\boldsymbol{x}_1(s,t) \to \mathbf{0}$ at every s as $t \to \infty$, that is, the structure is asymptotically brought to a rest state.

We also note that, when the nonlinear terms arising from damping forces are retained, solutions to the damped intrinsic equations remain invariant with rigid body motions (solutions to the original intrinsic equations are invariant due to the main variables being vector fields): by (2.19) no dissipation occurs and by (2.12) the solution is unaffected when the motions are purely rigid, which are characterised precisely by $\dot{\boldsymbol{x}}_2 = \mathbf{0}$, that is, strains and curvatures remain constant with time.

2.1.4 Intrinsic Beam Equations with Linearised Damping

Here, we describe a linearised version of the damped intrinsic beam equations (2.13)–(2.14) which is of interest to us for the subsequent order-reduction step, as the complexity introduced in (2.13) by the extra nonlinear terms, involving time-derivatives of the states,

is avoided. Then, the original geometrically nonlinear terms are kept intact but those arising from damping are neglected. As it will be shown, this linearised damping produces solutions which are still energy-dissipative, even when coupled with the geometrically nonlinear structural model. We proceed by taking a first order expansion of the strain-rate dependent force $C_\tau \dot{\boldsymbol{x}}_2$ in (2.12) using the linear terms in (2.2)

$$C_\tau \dot{\boldsymbol{x}}_2 = C_d C \dot{\boldsymbol{x}}_2 \approx C_d(\boldsymbol{x}_1' - E^\top \boldsymbol{x}_1), \tag{2.21}$$

where we have introduced the matrix $C_d = C_\tau C^{-1}$. Now, the geometrically nonlinear intrinsic beam equations with linearised damping contribution read

$$M\dot{\boldsymbol{x}}_1 - \boldsymbol{x}_2' - E\boldsymbol{x}_2 + \boldsymbol{\mathcal{L}}_1(\boldsymbol{x}_1)M\boldsymbol{x}_1 + \boldsymbol{\mathcal{L}}_2(\boldsymbol{x}_2)C\boldsymbol{x}_2 = D_0\boldsymbol{x}_1 + D_1\boldsymbol{x}_1' + D_2\boldsymbol{x}_1'' + \boldsymbol{f}_e, \tag{2.22}$$

$$C\dot{\boldsymbol{x}}_2 - \boldsymbol{x}_1' + E^\top \boldsymbol{x}_1 - \boldsymbol{\mathcal{L}}_1^\top(\boldsymbol{x}_1)C\boldsymbol{x}_2 = \boldsymbol{0}, \tag{2.23}$$

with boundary conditions

$$x_{1i}(s_\partial, t)\left[\boldsymbol{x}_2(s_\partial, t) + C_d(s_\partial)\left(\boldsymbol{x}_1'(s_\partial, t) - E(s_\partial)^\top \boldsymbol{x}_1(s_\partial, t)\right)\right]_i = 0, \tag{2.24}$$

where the index i and s_∂ are as before and where substitution of (2.21) into (2.13) has led to the appearance of the linearised damping matrices

$$D_0 = -(C_d E^\top)' - EC_d E^\top, \qquad D_1 = C_d' - C_d E^\top + EC_d, \qquad D_2 = C_d. \tag{2.25}$$

As revealed by (2.22), linear Kelvin-Voigt damping is naturally written in terms of the material velocities and its spatial derivatives. This is a consequence of the compatibility equation between strains/curvatures and translational/angular velocities in the intrinsic formulation (2.23). For the particular case in which structural properties (i.e., C and C_τ) are constant in space, C_d is block diagonal and therefore written as $C_d = \mathrm{diag}(C_f, C_m)$ and there is no initial curvature ($\boldsymbol{\kappa}_0 = \boldsymbol{0}$), the matrices (2.25) reduce to

$$D_0 = \begin{pmatrix} 0 & 0 \\ 0 & \widetilde{\boldsymbol{e}}_1 C_f \widetilde{\boldsymbol{e}}_1 \end{pmatrix}, \; D_1 = \begin{pmatrix} 0 & C_f \widetilde{\boldsymbol{e}}_1 \\ \widetilde{\boldsymbol{e}}_1 C_f & 0 \end{pmatrix}, \; D_2 = \begin{pmatrix} C_f & 0 \\ 0 & C_m \end{pmatrix}, \tag{2.26}$$

where $D_0 \in \mathcal{S}_-^6$, $D_2 \in \mathcal{S}_+^6$ and D_1 is skew-symmetric.

Finally, if forces are prescribed at any of the boundaries, now $\left[\boldsymbol{x}_2 + C_d\left(\boldsymbol{x}_1' - E^\top \boldsymbol{x}_1\right)\right]_i\big|_{s_\partial} = u(t)$ holds.

Energy Rate

With this linearised damping model we compute the new energy rate (2.10), under the same previous assumptions: no external forces nor boundary control are present (that is, $\boldsymbol{f}_e = \mathbf{0}$ and (2.24) hold). We start by using the result (2.10), which gives now

$$\dot{\epsilon} = \boldsymbol{x}_1^\top \boldsymbol{x}_2\big|_0^L + \langle \boldsymbol{x}_1, D_0\boldsymbol{x}_1 + D_1\boldsymbol{x}_1' + D_2\boldsymbol{x}_1''\rangle\,. \tag{2.27}$$

Expanding each of the terms in the expression above

$$\begin{aligned}
\boldsymbol{x}_1^\top \boldsymbol{x}_2\big|_0^L &= -\,\boldsymbol{x}_1^\top C_d\left(\boldsymbol{x}_1' - E^\top \boldsymbol{x}_1\right)\big|_0^L\,, && (2.28)\\
\langle \boldsymbol{x}_1, D_0\boldsymbol{x}_1\rangle &= -\left\langle \boldsymbol{x}_1, EC_dE^\top \boldsymbol{x}_1\right\rangle + \left\langle \boldsymbol{x}_1', C_dE^\top \boldsymbol{x}_1\right\rangle + \left\langle \boldsymbol{x}_1, C_dE^\top \boldsymbol{x}_1'\right\rangle \\
&\quad - \boldsymbol{x}_1^\top C_dE^\top \boldsymbol{x}_1\big|_0^L\,, && (2.29)\\
\langle \boldsymbol{x}_1, D_1\boldsymbol{x}_1'\rangle &= \langle \boldsymbol{x}_1, C_d'\boldsymbol{x}_1'\rangle - \left\langle \boldsymbol{x}_1, C_dE^\top \boldsymbol{x}_1'\right\rangle + \langle \boldsymbol{x}_1, EC_d\boldsymbol{x}_1'\rangle\,, && (2.30)\\
\langle \boldsymbol{x}_1, D_2\boldsymbol{x}_1''\rangle &= -\langle \boldsymbol{x}_1, C_d'\boldsymbol{x}_1'\rangle - \langle \boldsymbol{x}_1', C_d\boldsymbol{x}_1'\rangle + \boldsymbol{x}_1^\top C_d\boldsymbol{x}_1'\big|_0^L\,. && (2.31)
\end{aligned}$$

The boundary conditions (2.24) have been taken into account to arrive at (2.28) and integration by parts has been performed to get (2.29) and (2.31). Substituting (2.28)–(2.31) into (2.27) results in

$$\dot{\epsilon} = -\left\langle \begin{pmatrix}\boldsymbol{x}_1\\ \boldsymbol{x}_1'\end{pmatrix}, \begin{pmatrix} EC_dE^\top & EC_d\\ C_dE^\top & C_d\end{pmatrix}\begin{pmatrix}\boldsymbol{x}_1\\ \boldsymbol{x}_1'\end{pmatrix}\right\rangle \leq 0, \tag{2.32}$$

since $C_d \in \mathcal{S}_+^6$ and

$$\begin{pmatrix} EC_dE^\top & EC_d\\ C_dE^\top & C_d\end{pmatrix} = \begin{pmatrix} 0 & -EC_d^{\frac{1}{2}}\\ 0 & C_d^{\frac{1}{2}}\end{pmatrix}\begin{pmatrix} 0 & -EC_d^{\frac{1}{2}}\\ 0 & C_d^{\frac{1}{2}}\end{pmatrix}^\top \in \mathcal{S}_+^{12}. \tag{2.33}$$

Unforced Equilibrium Solutions

Using the same Lyapunov argument as before, we see that solutions to (2.22)-(2.24) now converge to

$$\boldsymbol{x}_1' = E^\top \boldsymbol{x}_1, \tag{2.34}$$

since we note that (2.34) forms the null space of the positive-semidefinite matrix appearing in (2.32): the positive semi-definiteness is given by the product of two transpose matrices with nonzero rank, as shown in (2.33), while if we expand these matrix products we obtain $\dot{\epsilon} = \int_0^L \left\| C_d^{1/2}(-E^\top \boldsymbol{x}_1 + \boldsymbol{x}_1')\right\|^2 ds$, for which (2.34) is a zero. In this case, these

are rigid-body type steady trajectories with constant energy ϵ, however limited to pure translational and/or rotation about the longitudinal axis (where no initial curvature is present, i.e., $\boldsymbol{\kappa}_0 = \mathbf{0}$). That is, solutions are rigid-body motions which do not cause any gyroscopic force. Similarly to the full geometrically nonlinear case, if one of the boundaries is clamped the structure is completely brought to rest (zero velocity and unstressed configuration).

2.1.5 Displacements and Finite Rotations

Displacements and rotations appear as secondary variables in the intrinsic formulation and, unless the external forcing $\boldsymbol{f}_e$ depends on them (e.g., gravity), they are not needed to solve (2.1) and (2.2). For the cases where finite-rotations are required, a transformation matrix $T(s,t) : [0,L] \times \mathbb{R}_+ \to \mathbb{R}^{3\times 3}$ from the local to the inertial frame ($\boldsymbol{e}_1^*$, $\boldsymbol{e}_2^*$, $\boldsymbol{e}_3^*$ in Fig. 2.1) is defined and quaternions are employed to parametrise rotations $\boldsymbol{\xi}(s,t) = (\xi_0, \boldsymbol{\xi}_v^\top)^\top : [0,L] \times \mathbb{R}_+ \to \mathbb{R}^4$, with $\xi_0 \in \mathbb{R}$ and $\boldsymbol{\xi}_v \in \mathbb{R}^3$. They satisfy [72, ch. 26]:

$$\frac{\partial \boldsymbol{\xi}}{\partial s} = \mathcal{U}(\boldsymbol{\kappa} + \boldsymbol{\kappa}_0)\boldsymbol{\xi}, \tag{2.35}$$

$$\frac{\partial \boldsymbol{\xi}}{\partial t} = \mathcal{U}(\boldsymbol{\omega})\boldsymbol{\xi}, \tag{2.36}$$

where $\boldsymbol{\kappa}$ is the vector of curvatures and twist (i.e., the three last components of the product $C\boldsymbol{x}_2$) and $\mathcal{U}$ is the skew-symmetric operator

$$\mathcal{U}(\boldsymbol{a}) = \frac{1}{2}\begin{pmatrix} 0 & -\boldsymbol{a}^\top \\ \boldsymbol{a} & -\widetilde{\boldsymbol{a}} \end{pmatrix}, \qquad \boldsymbol{a} \in \mathbb{R}^3. \tag{2.37}$$

Given quaternions $\boldsymbol{\xi}$, the corresponding coordinate transformation matrix is [72, ch. 6]

$$T(\boldsymbol{\xi}) = (\xi_0^2 - \|\boldsymbol{\xi}_v\|^2)I_3 + 2\boldsymbol{\xi}_v\boldsymbol{\xi}_v^\top + 2\xi_0\widetilde{\boldsymbol{\xi}}_v, \tag{2.38}$$

where I_3 is the identity matrix in $\mathbb{R}^3$. The displacement field $\boldsymbol{r}$ can be computed similarly by solving either of the equations

$$\frac{\partial \boldsymbol{r}}{\partial s} = T(\boldsymbol{e}_1 + \boldsymbol{\gamma}), \tag{2.39}$$

$$\frac{\partial \boldsymbol{r}}{\partial t} = T\boldsymbol{v}, \tag{2.40}$$

where $\boldsymbol{\gamma}$ is the strain vector (i.e., the three first components of $C\boldsymbol{x}_2$).

Gravity Forces

Gravitational forces are an example of an orientation-dependent forcing term, which requires the evolution equation for the quaternions (2.36) to be added to the intrinsic equations. The contribution in the momentum balance equation (2.13) would read

$$\boldsymbol{f}_g(s,t) = \mu(s) \begin{pmatrix} I_3 \\ \widetilde{\boldsymbol{r}}_{cg}(s) \end{pmatrix} T(s,t)^\top \boldsymbol{g} = M_v T(s,t)^\top \boldsymbol{g}, \tag{2.41}$$

where $M_v \in \mathbb{R}^{6\times 3}$ gathers the three first columns of the mass matrix M, that is, the part of M that gives the linear and angular sectional momentum produced by translational velocities. The constant vector $\boldsymbol{g}$ is the gravity acceleration, which is expressed in the global frame of reference.

2.2 Unsteady Vortex Lattice Method

Starting from the incompressible Navier-Stokes equations governing the motion of a Newtonian fluid it can be shown that the velocity field past a solid object can be obtained from a potential function φ, with fluid velocity $\boldsymbol{u} = \nabla\varphi$, if viscosity effects are negligible and the fluid flow is irrotational [86, ch.2]. This is typically the case for flight regimes of very flexible aircraft, where typical Reynolds numbers are high enough (at least, in the flight phases of interest, i.e., where they are shown to be vulnerable to atmospheric disturbances and need accurate predictive models and control) so that viscosity effects remain confined within a thin boundary layer and its effect on the global flow field is negligible.

It can be further demonstrated that the general solution of the incompressible, potential flow equations can be built using *singular* or *elemental* solutions that are distributed along the boundaries of solid objects and the wake they generate. Thus, solving for the flow field $\boldsymbol{u}$ is reduced to finding the appropriate singularity elements that comply with the non-penetration condition $\boldsymbol{u}\cdot\boldsymbol{n} = 0$ at the fluid-structure interface (i.e., the flow velocity must be tangent to the solid surface, with normal vector $\boldsymbol{n}$). The forces can be obtained *a posteriori* by integrating the pressure field, given by the unsteady Bernoulli equation, over the body surfaces [86, ch.3]. In the case of finite, three-dimensional wings [86, ch. 4] a continuous two-dimensional distribution of vortex lines over the wing mean surface in the two transverse directions with intensities (i.e., circulation per unit surface) γ_x^b and γ_y^b, and over the wake, γ_x^w and γ_y^w, as shown in Fig. 2.2, is a particularly convenient choice in

view of numerical implementation, as will be described next.

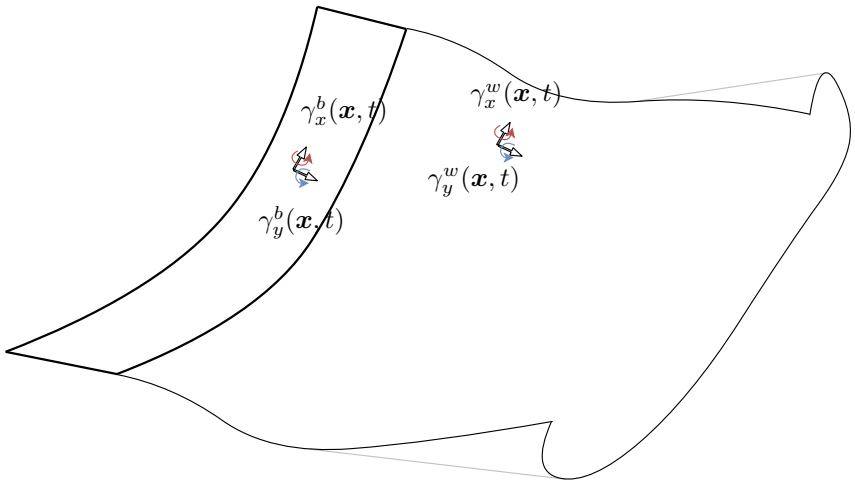


Figure 2.2: Continuous vortex distribution to model lifting surfaces and wake.

The intensity of the bound vortex distribution is found upon enforcement of the non-penetration conditions, which inherently introduces nonlinearity in the problem since the aerodynamic solution depends on the instantaneous geometry and kinematics of the lifting surfaces along with the shape of the wake. The Kutta condition, a physical constraint consisting of imposing the trailing edges as stagnation points, is required to give uniqueness of the solution [86, ch. 4]. By Kelvin's circulation theorem, which states that the total circulation within a region of inviscid flow [86, ch. 2] remains constant in time, any variation on the bound circulation must be shed from the lifting surfaces, which is the phenomenon that initially gives rise to the wake: the shed circulation is convected by the local velocity (incoming flow plus perturbation or circulatory velocity, induced by the singularities distribution) generating a continuous vortex sheet which starts at the trailing edge and extends infinitely with time.

2.2.1 Spatial Discretisation and UVLM Formulation

A straightforward discretisation of the problem follows from splitting the surfaces used to model the wing and the wake into a finite number of smaller surfaces, called panels. Then, the continuous distribution of two-dimensional vortex lines is substituted by rings of vorticity linked to each panel [86, ch. 13]. The potentially infinite wake is truncated to a manageable number of streamwise panels, noting that the velocity induced by vortex segments is inversely proportional to the distance squared (following Biot-Savart's law) and hence wake panels which are far away from the lifting surface have negligible effect on

the solution. Both the spanwise and streamwise discretisations and the wake extension are chosen following a convergence exercise.

For the present work, the aerodynamic model will be based on the unsteady vortex lattice formulation of [108]. As described in detail in the reference, the UVLM equations can be expressed by the following nonlinear discrete-time state-space system

$$\boldsymbol{f}_A\left(\boldsymbol{x}_A^{n+1}, \boldsymbol{u}_A^{n+1}\right) = \boldsymbol{g}_A\left(\boldsymbol{x}_A^{n}, \boldsymbol{u}_A^{n}\right), \tag{2.42}$$

$$\boldsymbol{y}_A^{n} = \boldsymbol{h}_A\left(\boldsymbol{x}_A^{n}, \boldsymbol{u}_A^{n}\right), \tag{2.43}$$

where the state and input vectors are

$$\boldsymbol{x}_A = \begin{pmatrix} \boldsymbol{\Gamma}_b \\ \boldsymbol{\Gamma}_w \\ \dot{\boldsymbol{\Gamma}}_b \\ \boldsymbol{\zeta}_w \end{pmatrix}, \quad \boldsymbol{u}_A = \begin{pmatrix} \boldsymbol{\zeta}_b \\ \dot{\boldsymbol{\zeta}}_b \end{pmatrix}. \tag{2.44}$$

That is, the state vector of the formulation consists of the circulation intensities of the vortex rings associated to bound and wake panels $\boldsymbol{\Gamma}_b$, $\boldsymbol{\Gamma}_w$, together with the time derivative of the former, which are added in the state-space only because they are required to compute the unsteady component of the aerodynamic forces. It also includes the grid coordinates of the wake panels, $\boldsymbol{\zeta}_w$. The input to the system are the coordinates and velocities of the grid nodes of the bound panels, $\boldsymbol{\zeta}_b$ and $\dot{\boldsymbol{\zeta}}_b$. Note that the input, defined in terms of grid coordinates and velocities, can account not only for displacements or *non-circulatory* velocities (i.e., velocities that are not induced by the vortex rings) arising from elastic motions, but also from rigid-body motions or deployment of control surfaces. Moreover, external wind or gust disturbances can be easily added to the set of UVLM inputs.

As detailed in [108], the method is time-marched so that at each time step, dictated by the mappings $\boldsymbol{f}_A$ and $\boldsymbol{g}_A$, the bound circulation intensities are obtained from enforcing the non-penetration boundary conditions at a grid of defined control points. The vorticity of the trailing edge panel is passed on to the first wake panel, from one step to the next, while the rest of the wake circulations are convected one panel streamwise. The shape of the wake, given by the set of coordinates $\boldsymbol{\zeta}_w$, is updated by convecting each of the wake grid points with the local velocity. Note that the equations describing the method require the input at the future time step $(\bullet)^{n+1}$. This is to account for the elliptic nature of the underlying equations, where any disturbance in the flow field has an immediate effect on the solution. The aerodynamic forces at each point in the bound grid is given

by the output equation $\boldsymbol{h}_A$, which accounts for the evaluation of the unsteady Bernoulli equation.

As shown in [108], the described UVLM formulation can be straightforwardly coupled to one-dimensional geometrically-exact beam models, with the only assumption that the cross-sections rotate rigidly. Besides, the spanwise UVLM and beam discretisations are forced to coincide, avoiding thus the need for interpolation. Therefore, mappings linking directly the geometry and kinematics of the beam centreline to the shape and motion of the surface grid, that gives the wing its form, can be defined. The forces and moments generated at each of the bound panels grid can be analogously mapped into equivalent forces and moments applied to the elastic axis of the beam. These two mappings define the required fluid-structure interaction to obtain a fully-coupled aeroelastic system.

2.2.2 Linearised UVLM Formulation

A feature of the described UVLM formulation, which will play an important role in the construction of efficient models for control, is the possibility to obtain a linearisation of the system around arbitrary reference geometries. These can be either (deformed) static or trim solutions or rigid-body orientations. As stated in the previous section, the method is nonlinear in the sense that the solution depends on the instantaneous configuration and kinematics of the lifting surfaces and on the wake geometry. Therefore, the linearisation is performed around a fixed, frozen (with zero grid velocities) geometry of both lifting surfaces and wake. Then, the non-penetration boundary conditions translate into constant *aerodynamic influence coefficients* which determine the intensity of the bound circulations, while the wake vortex intensities are passed on from one panel to the (streamwise) adjacent one subsequently at each time step in an invariant wake geometry.

Therefore, the linearised UVLM system can be written, in terms of perturbations $\delta(\bullet)$ to the reference solution $(\bar{\bullet})$, as a linear time-invariant difference equation such as

$$\begin{aligned} \delta\boldsymbol{x}_A^{n+1} &= A\delta\boldsymbol{x}_A^n + B\delta\boldsymbol{u}_A^{n+1}, \\ \delta\boldsymbol{y}_A^n &= C\delta\boldsymbol{x}_A^n + D\delta\boldsymbol{u}_A^n, \end{aligned} \tag{2.45}$$

where the used states and inputs are

$$\delta \boldsymbol{x}_A^n = \begin{pmatrix} \delta \boldsymbol{\Gamma}_b^n, \\ \delta \boldsymbol{\Gamma}_w^n, \\ \Delta t \delta \dot{\boldsymbol{\Gamma}}_b^n \\ \delta \boldsymbol{\Gamma}_b^{n-1} \end{pmatrix}, \quad \delta \boldsymbol{u}_A = \begin{pmatrix} \delta \boldsymbol{\zeta}_b \\ \delta \dot{\boldsymbol{\zeta}}_b \end{pmatrix}. \tag{2.46}$$

Full details on the structure and the entries of the discrete linear time-invariant representation (A, B, C, D) of the linearised UVLM are given in [101, 102, 108]. We note the disappearance of the wake grid coordinates from the linear UVLM state, which follows from the assumption of frozen wake geometry, and the appearance of $\delta \boldsymbol{\Gamma}_b^{n-1}$, which is only required if a second-order scheme to numerically approximate the time derivative $\delta \dot{\boldsymbol{\Gamma}}_b$ is used. The quantity Δt is the time-step size of the discrete-time system.

Chapter 3

Nonlinear Modal Aeroelastic Description

In this chapter we introduce the main building-blocks of the control-oriented modelling framework. These are the natural modes of vibration of the structure and they play a dual role in the construction of compact aeroelastic descriptions amenable to control: first, they are used to assist in the model order reduction of both structural and aerodynamics subsystems and, second, they introduce a common basis that serves as a natural coupling interface to obtain the final coupled aeroelastic models. This methodology takes into the nonlinear domain the standard modal analysis approach used in linear aeroelasticity.

We start the chapter by presenting the definition of these modes, based on the infinite-dimensional description of the geometrically-exact beams, and we introduce a numerical strategy to compute them directly from the intrinsic formulation. This is done, first, for the case of a single beam and extended later to networks of beams with lumped components, which are essential to reproduce aircraft-like structures. Later, we show how the modes are employed to construct low-order *nonlinear* aeroelastic descriptions for very flexible aircraft: while the use of this set of modes in the structural mathematical model enables direct state-order reduction, in the aerodynamic model it serves the purpose of reducing the input/output dimensionality of a linearised UVLM description; a first necessary step for subsequent efficient model-order reduction. Finally, the chapter is concluded with some directions on how data-driven modelling techniques can be employed to enhance the modal-based descriptions resulting from the described physics-based manipulation of the underlying equations.

3.1 Structural Linear Normal Modes

The linear normal modes (LNMs) of the structure, also referred to as *natural modes of vibration* or simply *mode shapes*, are the eigenfunctions of the linearised intrinsic beam equations (2.1)–(2.2) without external forcing or damping. Without loss of generality, we choose the origin (i.e., $\boldsymbol{x}_1 = \mathbf{0}$ and $\boldsymbol{x}_2 = \mathbf{0}$) to perform the linearisation since the obtained modes lead to more favourable, energy-preserving reduced-order models, as shown in [164]. Defining the linear perturbations around the origin as $\delta\boldsymbol{x}_1$ and $\delta\boldsymbol{x}_2$, the linearised equations read

$$\begin{pmatrix} M & 0 \\ 0 & C \end{pmatrix} \frac{\partial}{\partial t} \begin{pmatrix} \delta\boldsymbol{x}_1 \\ \delta\boldsymbol{x}_2 \end{pmatrix} + \begin{pmatrix} 0 & -E - \frac{\partial}{\partial s} \\ E^\top - \frac{\partial}{\partial s} & 0 \end{pmatrix} \begin{pmatrix} \delta\boldsymbol{x}_1 \\ \delta\boldsymbol{x}_2 \end{pmatrix} = \mathbf{0}. \tag{3.1}$$

3.1.1 Single Beam Case

We start focusing on obtaining solutions to the previous linear partial differential equation (3.1) for an isolated beam (i.e., a single beam with either clamped or free-end boundary conditions) with length L. They can be obtained turning to Fourier space for the temporal coordinate t, where it is easy to see that solutions to (3.1) can be sought in the form

$$\delta\boldsymbol{x}_1(s,t) = \sum_{k=-\infty}^{\infty} a_k \boldsymbol{\Phi}_{1k}(s) e^{i\omega_k t}, \tag{3.2}$$

$$\delta\boldsymbol{x}_2(s,t) = \sum_{k=-\infty}^{\infty} a_k \boldsymbol{\Phi}_{2k}(s) e^{i\omega_k t}, \tag{3.3}$$

for real constants $a_k \in \mathbb{R}$, which would be obtained from Fourier decomposition of hypothetical initial conditions $\delta\boldsymbol{x}_1(s,0)$ and $\delta\boldsymbol{x}_2(s,0)$ to (3.1), and complex vector variables $\boldsymbol{\Phi}_{1k}(s), \boldsymbol{\Phi}_{2k}(s) : [0,L] \to \mathbb{C}^6$ with associated frequencies $\omega_k \in \mathbb{R}$. The latter satisfy $\boldsymbol{\Phi}_{1k} = \boldsymbol{\Phi}^*_{1(-k)}$, $\boldsymbol{\Phi}_{2k} = \boldsymbol{\Phi}^*_{2(-k)}$, where $(\bullet)^*$ denotes the complex conjugate and $\omega_k = -\omega_{(-k)}$, since the underlying fields $\boldsymbol{x}_1$ and $\boldsymbol{x}_2$ are real. It is then easy to show that nontrivial solutions for (3.1) can be sought by considering real solutions of the form

$$\delta\boldsymbol{x}_1(s,t) = \sum_{k=-\infty}^{\infty} a_k \boldsymbol{\phi}_{1k}(s) \sin(\omega_k t), \tag{3.4}$$

$$\delta\boldsymbol{x}_2(s,t) = \sum_{k=-\infty}^{\infty} a_k \boldsymbol{\phi}_{2k}(s) \cos(\omega_k t), \tag{3.5}$$

leading to the eigenvalue problem

$$\omega_k \begin{pmatrix} M & 0 \\ 0 & -C \end{pmatrix} \begin{pmatrix} \boldsymbol{\phi}_{1k} \\ \boldsymbol{\phi}_{2k} \end{pmatrix} + \begin{pmatrix} 0 & -E - \frac{\partial}{\partial s} \\ E^\top - \frac{\partial}{\partial s} & 0 \end{pmatrix} \begin{pmatrix} \boldsymbol{\phi}_{1k} \\ \boldsymbol{\phi}_{2k} \end{pmatrix} = \mathbf{0}, \tag{3.6}$$

subject to the boundary conditions

$$\phi_{1i}(0)\phi_{2i}(0) = 0, \quad \phi_{1i}(L)\phi_{2i}(L) = 0, \qquad i = 1, \ldots, 6, \tag{3.7}$$

where, similarly to (2.3), the subscript i denotes the i^{th} component, meaning that at each boundary, either a velocity or force component can be prescribed to be zero. Equivalently, the set of boundary conditions (3.7) can be rewritten as a matrix-vector expression

$$G_{bc} \begin{pmatrix} \boldsymbol{\phi}_{1k}(0) \\ \boldsymbol{\phi}_{2k}(0) \\ \boldsymbol{\phi}_{1k}(L) \\ \boldsymbol{\phi}_{2k}(L) \end{pmatrix} = \mathbf{0}, \tag{3.8}$$

notation that will be useful to define the constrained eigenvalue problem. The constraint matrix has dimensions $G_{bc} \in \mathbb{R}^{12\times 24}$ with $\operatorname{rank}(G_{bc}) = 12$. Solution to (3.6)–(3.7) provides $\operatorname{Im}(\boldsymbol{\Phi}_{1k}(s)) = \boldsymbol{\phi}_{1k}$ and $\operatorname{Re}(\boldsymbol{\Phi}_{2k}(s)) = \boldsymbol{\phi}_{2k}$. Nontrivial solutions to (3.1) could alternatively be sought by swapping the trigonometric functions in (3.5), leading to a similar eigenvalue problem to (3.6), but with signs interchanged between matrices M and C, whose solution would give $\operatorname{Re}(\boldsymbol{\Phi}_{1k}(s))$ and $\operatorname{Im}(\boldsymbol{\Phi}_{2k}(s))$.

Therefore, solutions to (3.1) are fully characterised by the spatial functions $\boldsymbol{\phi}_{1k}(s), \boldsymbol{\phi}_{2k}(s) : [0, L] \to \mathbb{R}^6$, i.e., the *mode shapes*, and the corresponding natural frequencies of vibration $\omega_k \in \mathbb{R}_{>0}$.

3.1.2 Network of Beams

We now generalise the idea of mode shapes to networks of beams, formed by joining together the ends of multiple beams together. The constraints imposed by the joints/attachments between the diverse structures of the network restrain some of the degrees of freedom of the structure, and shall be translated into the velocity and force/moment variables of the intrinsic formulation. Constraints in displacements or rotations are directly imposed on linear or angular velocities, respectively, noting that these variables are expressed in a body-attached, local frame of reference. For instance, continuity in velocities across a joint (either fixed or allowing rotations) has to account for the change in rela-

tive orientation between the joined structures. Constraints for the sectional force/moment are not continuity constraints, as with velocities, but obtained by a force/moment balance at the joint.

The case of a ball joint, where only translational degrees of freedom are constrained leaving all three-dimensional rotations free, with three participating beams (labelled a, b and c, of lengths L_a, L_b, L_c) is portrayed in Fig. 3.1 as an illustrative example. The constraints imposed on translational velocities are

$$T_a \boldsymbol{v}_a|_{L_a} = T_b \boldsymbol{v}_b|_0 = T_c \boldsymbol{v}_c|_0 \,, \; t > 0, \tag{3.9}$$

where T is the transformation matrix (2.38) from the local to a common, inertial frame of reference, and the subscripts denote each of the diverse beams in the network (see Fig. 3.1). The evaluation notation $(\bullet)|$ is performed on the spatial variable and is introduced here to alleviate notation. The force constraint is obtained by a force balance around the joint, that is,

$$T_a \boldsymbol{f}_a|_{L_a} - T_b \boldsymbol{f}_b|_0 - T_c \boldsymbol{f}_c|_0 = \boldsymbol{0}, \; t > 0. \tag{3.10}$$

Note that in (3.10) the positive direction defined for the spatial coordinate s marks the sign of the force in the balance, as shown in Fig. 3.1, and also marks the spatial evaluation (0 or end L) of the velocity/force vector of each beam in (3.9)–(3.10). In the case of a rigid joint between two or more structures, constraints (3.9)–(3.10) shall also be equally applied to the angular counterparts $\boldsymbol{\omega}$ and $\boldsymbol{m}$.

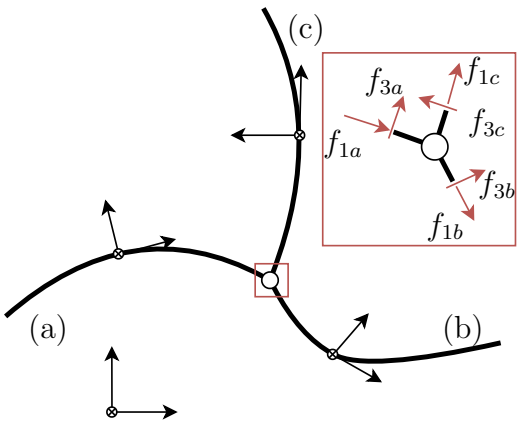


Figure 3.1: Example of a three beam network interconnected by a ball joint.

Therefore, to obtain the global mode shapes for networked configurations, one eigenvalue problem (3.6) for each of the participating beams needs to be defined which will have to be solved simultaneously. Moreover, the constraint equations introduced by the joints such as (3.9) and (3.10) need to be linearised and added to the set of constraints for the nodes

that are not part of any of the network joints (3.7). Note that the linearisation needs to be performed around the origin, and hence, translates into *frozen*[1] joint configuration at the linearisation point ($\overline{\bullet}$)

$$\begin{aligned} \overline{T}_a \boldsymbol{\phi}_{vk}^{(a)}\Big|_{L_a} &= \overline{T}_b \boldsymbol{\phi}_{vk}^{(b)}\Big|_0 = \overline{T}_c \boldsymbol{\phi}_{vk}^{(c)}\Big|_0, \\ \overline{T}_a \boldsymbol{\phi}_{fk}^{(a)}\Big|_{L_a} &- \overline{T}_b \boldsymbol{\phi}_{fk}^{(b)}\Big|_0 - \overline{T}_c \boldsymbol{\phi}_{fk}^{(c)}\Big|_0 = \mathbf{0}, \end{aligned} \tag{3.11}$$

where the modes have been split as $\boldsymbol{\phi}_1 = \left(\boldsymbol{\phi}_v^\top, \boldsymbol{\phi}_\omega^\top\right)^\top$, $\boldsymbol{\phi}_2 = \left(\boldsymbol{\phi}_f^\top, \boldsymbol{\phi}_m^\top\right)^\top$. This implies that for *rigid* joints, where rotating degrees of freedom are constrained, the resulting mode shapes will always satisfy the joint constraints. However, when considering joints that do not constrain some of the rotational degrees of freedom (e.g., hinges, ball joints), the constraints will not be satisfied by the modes when the relative angle between the participating beams in the joint changes with time. This is due to the use of velocities and forces being expressed in local coordinates. However, the error of the approximated solution employing these modes will remain small for small angular perturbations around the frozen configuration under which the linearisation has been performed.

3.1.3 Concentrated Masses

Many non-structural components in aircraft-like configurations are modelled as lumped or concentrated masses, and particularly so when the airframe is described using a network of beams. These bodies, usually attached rigidly to the airframe, do not contribute to the overall stiffness of the structure but exert extra forces or moments due to their non-negligible inertia properties. Particular examples are engines, trimming ballasts or localised payloads, which can be modelled as bodies with concentrated mass and inertia properties. Similarly as before, we describe how a generic rigid body, with a concentrated mass and non-negligible mass distribution, can be accounted for in the modes computation.

In the following, capital letters are used to denote vector quantities expressed in the global, inertial frame of reference. We start by writing the force and moment balance for a given rigid body l about its centre of mass in an inertial frame of reference, with point mass m_l and tensor of inertia J_l, under external forces and moments $\boldsymbol{F}_l$ and $\boldsymbol{M}_l$, which only include the forces that the rest of the structure produce on it (note that modes are

[1]The expression *frozen* is used here to refer to the constant rotation matrices arising from the linearisation. Note that angular degrees of freedom are still allowed to be nonzero for joints allowing rotations (e.g., hinges, ball constraints)

computed in unforced conditions, therefore directly applied external forces on the lumped mass are assumed to be zero):

$$\begin{aligned} \boldsymbol{F}_l &= m_l \dot{\boldsymbol{V}}_l, \\ \boldsymbol{M}_l &= \dot{J}_l \boldsymbol{\Omega}_l + J_l \dot{\boldsymbol{\Omega}}_l. \end{aligned} \tag{3.12}$$

The translational $\boldsymbol{V}_l$ and angular $\boldsymbol{\Omega}_l$ velocities about the centre of mass of the lumped body, expressed in an inertial frame of reference, are related to the local velocities at the attachment with the structure $\boldsymbol{v}_l$ and $\boldsymbol{\omega}_l$ (in the case that there is more than one beam participating in the joint, one is chosen to define the local frame). Considering a rigid connection between the beam and the lumped body, the kinematic relationship is

$$\begin{aligned} \boldsymbol{V}_l &= T_l \left(\boldsymbol{v}_l + \widetilde{\boldsymbol{\omega}_l} \boldsymbol{r}_l \right), \\ \boldsymbol{\Omega}_l &= T_l \boldsymbol{\omega}_l, \end{aligned} \tag{3.13}$$

where T_l is the transformation matrix (2.38) and $\boldsymbol{r}_l$ is the distance of the lumped body with respect to the point of the structure where it is attached. Then, it follows that

$$\begin{aligned} \dot{\boldsymbol{V}}_l &= \dot{T}_l \left(\boldsymbol{v}_l + \widetilde{\boldsymbol{\omega}_l} \boldsymbol{r}_l \right) + T_l \left(\dot{\boldsymbol{v}}_l - \widetilde{\boldsymbol{r}_l} \dot{\boldsymbol{\omega}}_l \right), \\ \dot{\boldsymbol{\Omega}}_l &= \dot{T}_l \boldsymbol{\omega}_l + T_l \dot{\boldsymbol{\omega}}_l. \end{aligned} \tag{3.14}$$

As can be easily checked, the transformation matrix satisfies the following time evolution equation

$$\dot{T}_l = T_l \widetilde{\boldsymbol{\omega}_l}. \tag{3.15}$$

Since the lumped mass is rigidly attached to the structure, the equivalent external forces at the union with the structure, written in local coordinates (which we denote by $\boldsymbol{f}_l$ and $\boldsymbol{m}_l$) are obtained from $\boldsymbol{F}_l$ and $\boldsymbol{M}_l$. Combining (3.12), (3.13) and (3.15)

$$\begin{aligned} \boldsymbol{f}_l &= T_l^\top \boldsymbol{F}_l = m_l \left(\dot{\boldsymbol{v}}_l - \widetilde{\boldsymbol{r}_l} \dot{\boldsymbol{\omega}}_l + \widetilde{\boldsymbol{\omega}_l} \boldsymbol{v}_l + \widetilde{\boldsymbol{\omega}_l}^2 \boldsymbol{r}_l \right), \\ \boldsymbol{m}_l &= T_l^\top \boldsymbol{M}_l + \widetilde{\boldsymbol{r}_l} \boldsymbol{f}_l = \widetilde{\boldsymbol{\omega}_l} \hat{J}_l \boldsymbol{\omega}_l + \hat{J}_l \dot{\boldsymbol{\omega}}_l + \widetilde{\boldsymbol{r}_l} \boldsymbol{f}_l, \end{aligned} \tag{3.16}$$

where $\hat{J}_l = T_l^\top J_l T_l$ is the inertia tensor of the lumped body with respect the local (beam) frame of reference. Since the orientation of the body is constant with respect the local basis, it is the case that $\dot{\hat{J}}_l = 0$. After some algebraic manipulation, the previous results can be expressed as

$$M_l \begin{pmatrix} \dot{\boldsymbol{v}}_l \\ \dot{\boldsymbol{\omega}}_l \end{pmatrix} + \mathcal{L}_1 \left(\begin{pmatrix} \boldsymbol{v}_l \\ \boldsymbol{\omega}_l \end{pmatrix} \right) M_l \begin{pmatrix} \boldsymbol{v}_l \\ \boldsymbol{\omega}_l \end{pmatrix} = \begin{pmatrix} \boldsymbol{f}_l \\ \boldsymbol{m}_l \end{pmatrix}, \tag{3.17}$$

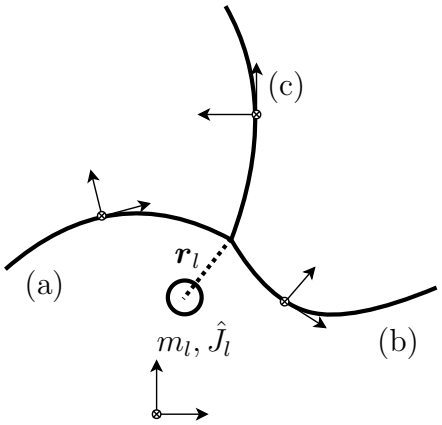


Figure 3.2: Example of a three beam rigid joint with a lumped mass at a distance $\boldsymbol{r}_l$. Dashed line represents an infinitely rigid link.

where

$$M_l = \begin{pmatrix} m_l I_3 & -m_l \widetilde{\boldsymbol{r}}_l \\ m_l \widetilde{\boldsymbol{r}}_l & \hat{J}_l - m_l \widetilde{\boldsymbol{r}}_l{}^2 \end{pmatrix} \tag{3.18}$$

is the inertia matrix of the lumped body with respect to the local frame of reference at the attachment point s_l. Equation (3.17), with a structure strongly resembling that of (2.1), is essentially the degeneracy of the intrinsic equations (2.1) to the infinitely rigid case. To obtain the corresponding modes, the extra eigenvalue problem obtained from linearisation of equation (3.17) has to be added to the rest of eigenvalue problems (3.6):

$$\boldsymbol{\phi}_{2k}^{(l)} = \omega_k M_l \boldsymbol{\phi}_{1k}^{(l)}, \tag{3.19}$$

where, following the same notation, $\boldsymbol{\phi}_{1k}^{(l)}$ and $\boldsymbol{\phi}_{2k}^{(l)}$ define the velocity and force/moment mode vectors of the lumped body. Similarly to the beam network case, the constraints enforcing the rigid link between the structure and the lumped body must be accounted for. Following the previous example of three networked beams, we consider now a rigid joint between them and a lumped body attached to the joint through a rigid link as shown in Fig. 3.2. Then the constraint relationships are as follows:

$$\begin{pmatrix} \overline{T}_a & 0 \\ 0 & \overline{T}_a \end{pmatrix} \boldsymbol{\phi}_{1k}^{(a)} \Big|_{L_a} = \begin{pmatrix} \overline{T}_b & 0 \\ 0 & \overline{T}_b \end{pmatrix} \boldsymbol{\phi}_{1k}^{(b)} \Big|_0 = \begin{pmatrix} \overline{T}_c & 0 \\ 0 & \overline{T}_c \end{pmatrix} \boldsymbol{\phi}_{1k}^{(c)} \Big|_0 = \begin{pmatrix} \overline{T}_a & 0 \\ 0 & \overline{T}_a \end{pmatrix} \Big|_{L_a} \boldsymbol{\phi}_{1k}^{(l)}, \tag{3.20}$$

$$\begin{pmatrix} \overline{T}_a & 0 \\ 0 & \overline{T}_a \end{pmatrix} \boldsymbol{\phi}_{2k}^{(a)} \Big|_{L_a} - \begin{pmatrix} \overline{T}_b & 0 \\ 0 & \overline{T}_b \end{pmatrix} \boldsymbol{\phi}_{2k}^{(b)} \Big|_0 - \begin{pmatrix} \overline{T}_c & 0 \\ 0 & \overline{T}_c \end{pmatrix} \boldsymbol{\phi}_{2k}^{(c)} \Big|_0 + \begin{pmatrix} \overline{T}_a & 0 \\ 0 & \overline{T}_a \end{pmatrix} \Big|_0 \boldsymbol{\phi}_{2k}^{(l)} = \mathbf{0}, \tag{3.21}$$

where, for instance, the local frame of reference of the beam a has been chosen to express the inertial properties of the lumped body and hence the use of $\overline{T}_a$ in the corresponding terms of the conditions above.

3.1.4 Modes Computation

The general eigenvalue problem, accounting for a configuration with n_b beams (b_1, b_2, ..., b_{n_b}) and n_l lumped components (l_1, l_2, ..., l_{n_l}), reads

$$\omega_k \text{blkdiag}\left(\begin{pmatrix} M_{b_1} & 0 \\ 0 & -C_{b_1} \end{pmatrix}, \cdots, \begin{pmatrix} M_{b_{n_b}} & 0 \\ 0 & -C_{b_{n_b}} \end{pmatrix}, \begin{pmatrix} M_{l_1} & 0 \end{pmatrix}, \cdots \begin{pmatrix} M_{l_{n_l}} & 0 \end{pmatrix}\right) \boldsymbol{\Phi}_{all} = \text{blkdiag}\left(\begin{pmatrix} 0 & E_{b_1}+\frac{\partial}{\partial s} \\ -E_{b_1}^\top+\frac{\partial}{\partial s} & 0 \end{pmatrix}, \cdots, \begin{pmatrix} 0 & E_{b_{n_b}}+\frac{\partial}{\partial s} \\ -E_{b_{n_b}}^\top+\frac{\partial}{\partial s} & 0 \end{pmatrix}, \begin{pmatrix} 0 & I_6 \end{pmatrix}, \cdots, \begin{pmatrix} 0 & I_6 \end{pmatrix}\right) \boldsymbol{\Phi}_{all}, \tag{3.22}$$

where

$$\boldsymbol{\Phi}_{all} = \left(\begin{pmatrix} \boldsymbol{\phi}_{1k}^{(b_1)} \\ \boldsymbol{\phi}_{2k}^{(b_1)} \end{pmatrix}^\top, \cdots, \begin{pmatrix} \boldsymbol{\phi}_{1k}^{(b_{n_b})} \\ \boldsymbol{\phi}_{2k}^{(b_{n_b})} \end{pmatrix}^\top, \begin{pmatrix} \boldsymbol{\phi}_{1k}^{(l_1)} \\ \boldsymbol{\phi}_{2k}^{(l_1)} \end{pmatrix}^\top, \cdots, \begin{pmatrix} \boldsymbol{\phi}_{1k}^{(l_{n_l})} \\ \boldsymbol{\phi}_{2k}^{(l_{n_l})} \end{pmatrix}^\top \right)^\top \tag{3.23}$$

gathers the eigenfunctions of all beam sub-components and eigenvectors of all lumped bodies and is subject to

$$G_c \, \boldsymbol{\Phi}_{all}|_{\{s_\partial\}}, \tag{3.24}$$

where G_c gathers all possible constraints — i.e., natural boundary conditions for the ends that do not participate in any joint (3.7), constraints between jointed beams (3.11) or constraints involving lumped bodies and different beams (3.21) — and $\boldsymbol{\Phi}_{all}|_{\{s_\partial\}}$ denotes the vector formed by evaluating the eigenfunctions of each beam at its boundaries (analogously to the single beam case in (3.8)) plus the mode vectors associated to the lumped bodies.

Mode shapes can be analytically computed from (3.6) only for very simple geometries [112]. In practice, however, they can be computed from a finite-element 3D model of the structure [155], however requiring an extra effort to obtain the corresponding force/moment modes, since finite-element models are usually obtained from displacement-based formulations. Here, we present a spectral method to obtain the mode shapes (both $\boldsymbol{\phi}_1$ and $\boldsymbol{\phi}_2$) directly from the intrinsic equations turning to spectral discretisation of the spatial coordinate (note that this is required due to the presence of the spatial derivative $\frac{\partial}{\partial s}$ in (3.6)). This method has been found to be robust against spurious modes, in contrast to other spatial discretisation methods such as finite differences or finite elements. The use of shape-prescribed basis functions avoids the appearance of spurious, non-physical modes that typically arise from conventional discretisation methods, characterised by high-frequency spatial oscillations. Besides, these spurious modes often display *physical* frequencies (i.e., associated eigenvalues), which hinders their identification (in order to remove them from the set of modes that will be used to construct approximate solutions),

requiring of careful post-processing and inspection of the obtained eigenvectors.

For this purpose, a spectral collocation method, based on the use of Chebyshev polynomials of the first kind as function basis (Fig. 3.3), is employed. These are defined as

$$T_n(x) = \cos\left(n\cos^{-1}(x)\right), \quad x \in [-1, 1]. \tag{3.25}$$

The next step is to expand each of the unknown space-dependent variables in (3.22) (i.e., each of the ith beam eigenfunctions) using N Chebyshev polynomials

$$\begin{pmatrix} \boldsymbol{\phi}_1^{(b_i)}(s) \\ \boldsymbol{\phi}_2^{(b_i)}(s) \end{pmatrix} = \sum_{n=0}^{N-1} \boldsymbol{a}_n^{(b_i)} T_n(x), \tag{3.26}$$

where the change of variable $x = -1 + \frac{2}{L}s$ has been introduced. Then, a system of linear equations in terms of the new expansion coefficients $\boldsymbol{a}_n$ is constructed by evaluating the differential equation (3.22) at the Chebyshev *collocation* points defined by

$$x_j = -\cos\left(\frac{j\pi}{N}\right), \quad j = 0, \cdots, N-1. \tag{3.27}$$

Note that evaluation of the spatial derivatives can be computed analytically, since an analytical expression for $\frac{d}{dx}T_n(x)$ is easily obtained. A consequence of the use of such spectral method is that the problem (3.22) loses the sparsity within each beam subproblem, due to the coupling between the different Chebyshev polynomials. This is shown in Fig. 3.4 for an example structure consisting of 8 different beam components and a lumped mass. Substitution of (3.26) into the constraint equations (3.24) similarly involves all the expansion coefficients, since the spatial evaluation is transferred onto each of the Chebyshev polynomials. A detailed description of collocation and spectral methods using Chebyshev polynomials to solve partial differential equations, as well as an insight on their properties as function basis, can be found in [25].

As a result, a finite dimensional, constrained eigenvalue problem is obtained

$$\begin{aligned} A_{cheb}\boldsymbol{A} &= \omega B_{cheb}\boldsymbol{A}, \\ G_{cheb}\boldsymbol{A} &= \boldsymbol{0}, \end{aligned} \tag{3.28}$$

where $\boldsymbol{A} = \left(\boldsymbol{a}_0^{(b_1)\top}, \cdots, \boldsymbol{a}_{N-1}^{(b_1)\top}, \cdots, \boldsymbol{a}_0^{(b_{n_b})\top}, \cdots, \boldsymbol{a}_{N-1}^{(b_{n_b})\top}, \boldsymbol{\phi}_{1k}^{(l_1)\top}, \boldsymbol{\phi}_{2k}^{(l_1)\top}, \cdots, \boldsymbol{\phi}_{1k}^{(l_{n_l})\top}, \boldsymbol{\phi}_{2k}^{(l_{n_l})\top}\right)^\top$ contains all the Chebyshev expansion coefficients for each of the beams and also the velocity and force modes of the lumped bodies. Matrices A_{cheb} and B_{cheb} still possess a block diagonal structure, where each full (i.e., not sparse) block corresponds to each of

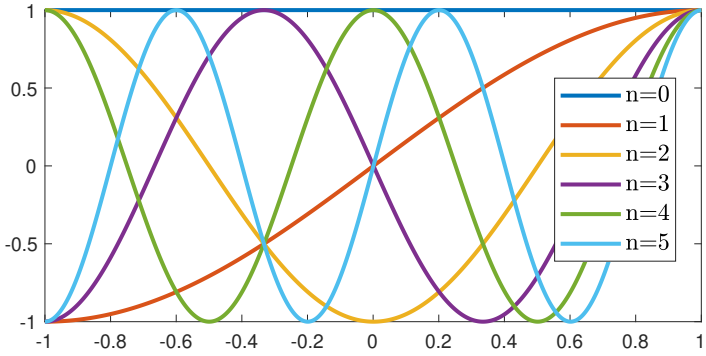


Figure 3.3: First six Chebyshev polynomials.

the different beams comprising the structure (Fig. 3.4), since the couplings between the diverse components that form up the structure are only present in the constraint matrix G_{cheb}.

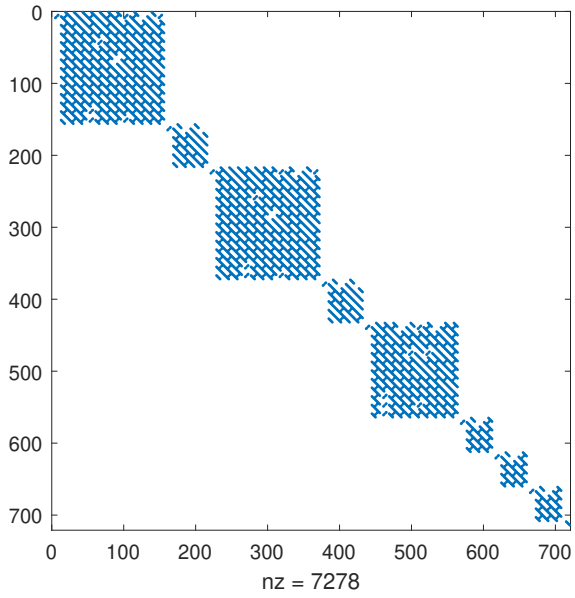


Figure 3.4: Sparsity of an example A_{cheb} matrix from an 8 beam and one lumped mass assembly.

The constrained eigenvalue problem (3.28) can be solved by projection onto the null space of the constraint matrix G_{cheb}, using a transformation matrix Z, so that $\boldsymbol{A} = Z\boldsymbol{A}_z$ and $G_{cheb}Z = 0$ [61, §6]. Then, the resulting unconstrained eigenproblem is solved, using the projected vector $\boldsymbol{A}_z \in \text{null}(G_{cheb})$

$$\omega \left(Z^\top T_{cheb}^{-1} B_{cheb} Z\right) \boldsymbol{A}_z = \left(Z^\top T_{cheb}^{-1} A_{cheb} Z\right) \boldsymbol{A}_z. \tag{3.29}$$

The null-space matrix Z can be obtained by

$$Z = P \begin{pmatrix} -G_{cheb,fr}^{-1} \tilde{G}_{chev} \\ I \end{pmatrix}, \tag{3.30}$$

where $G_{cheb,fr}$ is a full-rank block of G_{cheb}, usually revealed after some simple permutation (described by the matrix P above) or other rank-revealing procedures, $\tilde{G}_{chev}$ are the resulting leftover columns of G_{chev} and with the identity matrix in (3.30) with appropriate dimensions (number of columns minus number of rows in G_{chev}).

Note also that before the problem is pre-multiplied by $Z^\top$ in (3.29), the left side is projected into the Chebyshev space by means of the transformation matrix T_{cheb}. This is a matrix with the same block-diagonal structure of A_{cheb} and B_{cheb}, where each of the square blocks (corresponding to a different beam in the network) has 12×12 block-entries $I_{12} T_j(x_i)$. The entries of T_{cheb} corresponding to the eigenvalue sub-problems associated to the lumped bodies are just the identity, since no transformation into the Chebyshev space is performed there.

3.2 Modal Aeroelastic Description

Once the mode shapes $\boldsymbol{\phi}_1$ and $\boldsymbol{\phi}_2$ are readily available, they are employed to enable model reduction not only of the structural intrinsic equations but also of the vortex lattice description of the unsteady aerodynamics. As will be described next, the modes are used to obtain, directly, a low-order nonlinear representation of the intrinsic beam equations. Moreover, a strategy to obtain a concise, finite-dimensional approximation to the finite-rotations is sought next to account for gravity forces (or other orientation-dependent forces). Regarding the unsteady aerodynamics model, the structural modes are used to reduce the dimensions of the inputs and outputs of the system, since they are naturally tied to the geometry and kinematics of the structure. With this first input/output truncation, a subsequent efficient state-order reduction of the linearised UVLM model is then performed.

3.2.1 Nonlinear Intrinsic Equations in Modal Coordinates

The order reduction of the structural model commences by considering a truncated approximation to the state variables using N_m eigenfunctions, that is,

$$\boldsymbol{x}_1(s,t) = \sum_{j=1}^{N_m} \boldsymbol{\phi}_{1j}(s) q_{1j}(t), \qquad \boldsymbol{x}_2(s,t) = \sum_{j=1}^{N_m} \boldsymbol{\phi}_{2j}(s) q_{2j}(t), \tag{3.31}$$

where $q_{1j}(t),\ q_{2j}(t) : \mathbb{R}_+ \to \mathbb{R}$ are the temporal coefficients of the expansion. The next step is to substitute the expansions (3.31) into the intrinsic equations and perform a Galerkin projection to obtain a set of nonlinear ordinary differential equations in terms of the expansion coefficients $q_{1j}(t),\ q_{2j}(t)$. This is done by pre-multiplying the set of PDEs by the corresponding mode shapes (i.e., the momentum balance equation (2.22) by the linear/angular velocities modes $\boldsymbol{\phi}_{1i}$ and the compatibility equation (2.23) by the force/moment sectional resultant modes $\boldsymbol{\phi}_{2i}$) and then integrating over the entire spatial domain defined by the network of beams in the assembly.

To obtain the structural low-order model, the intrinsic equations with linearised damping terms (2.22) and (2.23) are employed, avoiding thus the extra complexity of accounting for the full nonlinear damping terms in (2.13) and (2.14). While the effect of retaining the full damping terms has been thoroughly studied in the infinite-dimensional scenario and in a highly-resolved finite element implementation, its role in the modal space is out of the scope of the present work, however it poses a compelling future line of investigation. In practice, the tested numerical cases employ moderate to low damping coefficients and all show sensible and physical dissipation properties.

We continue to consider the general network configuration with n_b beams (b_1, b_2, ..., b_{n_b}) and n_l lumped components (l_1, l_2, ..., l_{n_l}). Then, the modes obtained from (3.22)–(3.24) are conveniently normalised so that

$$\begin{aligned} \sum_{m=1}^{n_b} \int_0^{L_{b_m}} \boldsymbol{\phi}_{1i}^{(b_m)\top} M_{b_m} \boldsymbol{\phi}_{1j}^{(b_m)} ds + \sum_{n=1}^{n_l} \boldsymbol{\phi}_{1i}^{(l_n)\top} M_{l_n} \boldsymbol{\phi}_{1j}^{(l_n)} = \delta_{ij}, \\ \sum_{m=1}^{n_b} \int_0^{L_{b_m}} \boldsymbol{\phi}_{2i}^{(b_m)\top} C_{b_m} \boldsymbol{\phi}_{2j}^{(b_m)} ds = \delta_{ij}, \end{aligned} \tag{3.32}$$

where δ_{ij} is the Kronecker delta, since the modes computed around the origin are orthogonal to each other [112]. The resulting finite-dimensional model from the modal Galerkin

projection, using implicit summation over the index l, reads

$$\dot{\boldsymbol{q}}_1 = \Omega \boldsymbol{q}_2 + \Sigma \boldsymbol{q}_1 - q_{1l}\Gamma_1^l \boldsymbol{q}_1 - q_{2l}\Gamma_2^l \boldsymbol{q}_2 + \boldsymbol{\eta}_e, \tag{3.33a}$$

$$\dot{\boldsymbol{q}}_2 = -\Omega \boldsymbol{q}_1 + q_{2l}(\Gamma_2^l)^\top \boldsymbol{q}_1, \tag{3.33b}$$

where the matrix of coefficients of the linear subsystem Ω is a diagonal matrix containing all the eigenvalues of the N_m modes used in the solution approximation,

$$[\Omega]_{ij} = \sum_{m=1}^{n_b} \int_0^{L_{b_m}} \boldsymbol{\phi}_{1i}^{(b_m)\top} \left(E_{b_m} + \frac{\partial}{\partial s} \right) \boldsymbol{\phi}_{2j}^{(b_m)} ds + \sum_{n=1}^{n_l} \boldsymbol{\phi}_{1i}^{(l_n)\top} \boldsymbol{\phi}_{2j}^{(l_n)}, \tag{3.34}$$

and

$$[\Sigma]_{ij} = \sum_{m=1}^{n_b} \int_0^{L_{b_m}} \boldsymbol{\phi}_{1i}^{(b_m)\top} \left(D_{0_{b_m}} + D_{1_{b_m}} \frac{\partial}{\partial s} + D_{2_{b_m}} \frac{\partial^2}{\partial s^2} \right) \boldsymbol{\phi}_{1j}^{(b_m)} ds \tag{3.35}$$

are the entries of the damping matrix in modal coordinates. The vector $\boldsymbol{\eta}_e$ contains the projection onto the modal space of all the external (distributed) forces acting along each of the beams $\boldsymbol{f}_e^{(b_m)}$ as well as (point) forces acting on the lumped components $\boldsymbol{f}_e^{(l_n)}$

$$[\boldsymbol{\eta}_e]_i = \sum_{m=1}^{n_b} \int_0^{L_{b_m}} \boldsymbol{\phi}_{1i}^{(b_m)\top} \boldsymbol{f}_e^{(b_m)} ds + \sum_{n=1}^{n_l} \boldsymbol{\phi}_{1i}^{(l_n)\top} \boldsymbol{f}_e^{(l_n)}. \tag{3.36}$$

Any external applied point force or moment (including boundary excitation) would be evaluated using the previous expression by replacing the continuous $\boldsymbol{f}_e^{(b_m)}$ (if the point force is applied on a beam location) by a delta function times the magnitude of the applied force.

The quadratic nonlinear terms are expressed by means of N_m matrices ($l = 1, \ldots, N_m$), whose coefficients are given by

$$\left[\Gamma_1^l\right]_{ij} = \sum_{m=1}^{n_b} \int_0^{L_{b_m}} \boldsymbol{\phi}_{1i}^{(b_m)\top} \mathcal{L}_1 \left(\boldsymbol{\phi}_{1j}^{(b_m)} \right) M_{b_m} \boldsymbol{\phi}_{1l}^{(b_m)} ds + \sum_{n=1}^{n_l} \boldsymbol{\phi}_{1i}^{(l_n)\top} \mathcal{L}_1 \left(\boldsymbol{\phi}_{1j}^{(l_n)} \right) M_{l_n} \boldsymbol{\phi}_{1l}^{(l_n)}, \tag{3.37}$$

$$\left[\Gamma_2^l\right]_{ij} = \sum_{m=1}^{n_b} \int_0^{L_{b_m}} \boldsymbol{\phi}_{1i}^{(b_m)\top} \mathcal{L}_2 \left(\boldsymbol{\phi}_{2j}^{(b_m)} \right) C_{b_m} \boldsymbol{\phi}_{2l}^{(b_m)} ds. \tag{3.38}$$

We note that system (3.33) has inherited the quadratic skew-symmetric structure of the nonlinear terms in (2.22)–(2.23), which implies energy conservation. As a matter of fact, the energy written in modal space ϵ_q (i.e., the expression resulting from substituting the approximated solution (3.31) into (2.9)) is

$$\epsilon_q(t) = \frac{1}{2}\boldsymbol{q}_1^\top \boldsymbol{q}_1 + \frac{1}{2}\boldsymbol{q}_2^\top \boldsymbol{q}_2. \tag{3.39}$$

It is easy to show that the modal energy rate is

$$\dot{\epsilon}_q(t) = \boldsymbol{q}_1^\top \left(\Sigma \boldsymbol{q}_1 + \boldsymbol{\eta}\right), \tag{3.40}$$

which follows from differentiating (3.39) with respect to time, substituting in equations (3.33) and noting that the higher order terms vanish due to the skew-symmetry of the quadratic terms. We see that in the modal space, as in the infinite-dimensional scenario (2.10), under no external forcing and without damping, the energy is a conserved quantity.

3.2.2 Displacements and Finite Rotations

As already mentioned, if the local orientation of the structure is required, the evolution equation for the quaternions (2.36) needs to be added to equations (2.22) and (2.23), since rotations are not part of the primary variables. This is the case of gravity forces, which are fixed with respect to an inertial frame of reference, but require of the local orientation of the beam to compute its contribution on the intrinsic beam dynamics (2.41).

The temporal evolution equation (2.36) describes the dynamics of finite-rotations parameterised by an infinite-dimensional quaternion field. The purpose of this section is to provide two alternative approaches to obtain a low order finite-dimensional representation of rotations suited to the modal intrinsic description (3.33) alongside the corresponding gravitational contribution $\boldsymbol{\eta}_g$ in (3.33). Following the previously introduced nomenclature, we define the reduced finite-dimensional quaternion state as $\boldsymbol{q}_\xi$, and we seek its time evolution equation, expected to have the quadratic form (as is clear from (2.36))

$$\dot{\boldsymbol{q}}_\xi = q_{1l}\Gamma^l_\xi \boldsymbol{q}_\xi. \tag{3.41}$$

Attending to the structure of the transformation matrix (2.38), needed to evaluate (2.41), the gravity force contribution will have quadratic structure too

$$\boldsymbol{\eta}_g = q_{\xi l}\Gamma^l_g \boldsymbol{q}_\xi. \tag{3.42}$$

The two proposed finite-dimensional approximations are an interpolation-based scheme and a modal Galerkin projection of the time-evolution equation (2.36), similar to the one employed for the intrinsic equations. A consequence of using quaternions to parametrise rotations is that $\|\boldsymbol{\xi}\| = 1$ is necessary for T to be orthogonal [72, ch. 6]. Hence, it is desirable that the employed approximations are unit-norm preserving. Both approaches and their unit-norm preservation properties are now described.

Spline Interpolation

With this first approach, the time-evolution of quaternions is tracked at chosen, fixed points along the spatial coordinate s and a Catmull-Rom interpolation scheme is constructed between these points [15]

$$\boldsymbol{\xi}(s,t) = S(s)\boldsymbol{q}_\xi(t), \tag{3.43}$$

where $\boldsymbol{q}_\xi(t) = (\boldsymbol{\xi}_0^\top, \cdots, \boldsymbol{\xi}_{N_\xi}^\top)^\top : \mathbb{R}_+ \to \mathbb{R}^{4(N_\xi+1)}$ gathers the set of quaternions at the chosen spatial coordinates $s_{k+1} = s_k + \frac{L}{N_\xi}$, $k = 0, \cdots, N_\xi$ of a uniform grid with N_ξ intervals. The matrix $S(s) \in \mathbb{R}^{4\times 4(N_\xi+1)}$ contains cubic piece-wise polynomials ensuring smooth matching ($C^1([0, L])$) of all the tracked quaternions.

With this approach, we obtain the corresponding matrices to construct (3.41) and (3.42):

$$\Gamma_\xi^l = \text{blkdiag}\left(\mathcal{U}(\phi_{\omega l}(s_0)), \mathcal{U}(\phi_{\omega l}(s_1)), \cdots, \mathcal{U}(\phi_{\omega l}(s_{N_\xi}))\right) \tag{3.44}$$

and

$$\left[\Gamma_g^l\right]_{ij} = \sum_{m=1}^{n_b} \int_0^{L_{b_m}} \boldsymbol{\phi}_{1i}^{(b_m)\top} M_{v_{b_m}} T_{jl}(S_j, S_l)^\top \boldsymbol{g} ds + \sum_{n=1}^{n_l} \boldsymbol{\phi}_{1i}^{(l_n)\top} M_{v_{l_n}} \left. T_{jl}(S_j, S_l)^\top \right|_{s_{l_n}} \boldsymbol{g}, \tag{3.45}$$

where S_j is the jth column of $S(s)$ and

$$T_{jl}(\boldsymbol{\xi}^{(j)}, \boldsymbol{\xi}^{(l)}) = \left(\xi_0^{(j)}\xi_0^{(l)} - \boldsymbol{\xi}_v^{(j)\top}\boldsymbol{\xi}_v^{(l)}\right) I_3 + 2\boldsymbol{\xi}_v^{(j)}\boldsymbol{\xi}_v^{(l)\top} + 2\xi_0^{(j)}\widetilde{\boldsymbol{\xi}_v^{(l)}}. \tag{3.46}$$

The accuracy of the spline approach depends on the refinement of the spatial grid used, with an absolute error of the order $\mathcal{O}(h_\xi^3)$ [88], where $h_\xi = L/N_\xi$ is the length of the grid intervals. Errors are kept within (time) integration accuracy at grid points. The Nyquist criterion, based on the highest spatial frequency of the angular velocity modes, provides a lower bound on the number of grid points to choose for the error estimate $\mathcal{O}(h_\xi^3)$ to hold valid.

Modal-Based Expansion

An alternative approximation, analogous to the construction of (3.33), involves a modal expansion of the quaternions:

$$\boldsymbol{\xi}(s,t) = \bar{\boldsymbol{\xi}}(s) + \sum_{j=1}^{N_m} \boldsymbol{\phi}_{\xi j}(s) q_{\xi j}(t), \tag{3.47}$$

for chosen quaternion mode shapes $\phi_{\xi j} : [0, L] \to \mathbb{R}^4$, with coefficients $q_{\xi j} : \mathbb{R}_+ \to \mathbb{R}$, and where $\bar{\boldsymbol{\xi}}(s)$ defines the undeformed rotation field, that is, $\bar{\boldsymbol{\xi}}' = \mathcal{U}(\boldsymbol{\kappa}_0)\bar{\boldsymbol{\xi}}$.

We now define mode shapes $\boldsymbol{\phi}_{\xi j}$ to be the eigenfunctions of the linearised time evolution equation (2.36) around the unloaded and undeformed configuration,

$$\frac{\partial}{\partial t}\delta\boldsymbol{\xi} = \mathcal{U}_t \delta\boldsymbol{\omega}, \tag{3.48}$$

where

$$\mathcal{U}_t(\bar{\boldsymbol{\xi}}) = \frac{\partial}{\partial \boldsymbol{x}} \left(\mathcal{U}(\boldsymbol{x})\bar{\boldsymbol{\xi}}\right) = \frac{1}{2} \begin{pmatrix} -\bar{\boldsymbol{\xi}}_v^\top \\ \bar{\boldsymbol{\xi}}_0 I_3 + \widetilde{\bar{\boldsymbol{\xi}}}_v \end{pmatrix} \tag{3.49}$$

is the equivalent inverse tangent operator for quaternions with $\mathcal{U}_t(\bar{\boldsymbol{\xi}})^\top \mathcal{U}_t(\bar{\boldsymbol{\xi}}) = \frac{1}{4} I_3$. Finally, mode shapes for the quaternions are obtained from (3.48) using the angular components of the velocity modes $\boldsymbol{\phi}_{1j}$

$$\boldsymbol{\phi}_{\xi j} = \mathcal{U}_t(\bar{\boldsymbol{\xi}})\boldsymbol{\phi}_{\omega j}. \tag{3.50}$$

However, a more favourable approximation, concerning unit-norm preservation, is obtained if an *augmented* modal expansion is used, that is, one in which $\bar{\boldsymbol{\xi}}$ is removed from (3.47) and employed as a *shifting equilibrium* mode $\boldsymbol{\phi}_{\xi 0} = \bar{\boldsymbol{\xi}}$:

$$\boldsymbol{\xi}(s,t) = \sum_{j=0}^{N_m} \boldsymbol{\phi}_{\xi j}(s) q_{\xi j}(t). \tag{3.51}$$

We construct a time evolution system for $\boldsymbol{q}_\xi$ applying a Galerkin projection to the time evolution equation (2.36) using mode shapes (3.50) and $\boldsymbol{\phi}_{\xi 0} = \bar{\boldsymbol{\xi}}$:

$$A_\xi \dot{\boldsymbol{q}}_\xi = U_\xi(\boldsymbol{\omega})\boldsymbol{q}_\xi, \tag{3.52}$$

where A_ξ and $U_\xi(t)$ are matrices independent of the spatial coordinate s

$$[A_\xi]_{ij} = \sum_{m=1}^{n_b} \int_0^{L_{b_m}} \boldsymbol{\phi}_{\xi i}^{(b_m)\top} \boldsymbol{\phi}_{\xi j}^{(b_m)} ds \tag{3.53}$$

$$[U_\xi(\boldsymbol{\omega})]_{ij} = \sum_{m=1}^{n_b} \int_0^{L_{b_m}} \boldsymbol{\phi}_{\xi i}^{(b_m)\top} \mathcal{U}(\boldsymbol{\omega}(s,t)) \boldsymbol{\phi}_{\xi j}^{(b_m)} ds. \tag{3.54}$$

Note that $U_\xi = -U_\xi^\top$ for all t, since the skew-symmetry of $\mathcal{U}$ is inherited, and $A_\xi = A_\xi^\top$. Now, suppose that $\boldsymbol{q}_\xi$ is a solution to the time evolution equation (3.52) and satisfies the initial conditions $\|\boldsymbol{\xi}(s,0)\|_2^2 = 1$ for all s, then $\sum_{m=1}^{n_b} \int_0^{L_{b_m}} \|\boldsymbol{\xi}(s,t)\|_2^2 \, ds / L_{b_m} = 1$, $t \geq 0$. That is, the space-averaged unit norm is preserved. The proof is as follows.

First, we use expansion (3.51) to compute

$$\frac{1}{2}\frac{d}{dt} \|\boldsymbol{\xi}(s,t)\|_2^2 = \boldsymbol{q}_\xi(t)^\top \Phi_\xi(s)^\top \Phi_\xi(s) \dot{\boldsymbol{q}}_\xi(t), \tag{3.55}$$

where $\Phi_\xi(s)$ is a matrix formed by the horizontal concatenation of all modes shapes $\boldsymbol{\phi}_{\xi j}$.

Next, using (3.52)

$$\frac{1}{2}\frac{d}{dt} \|\boldsymbol{\xi}(s,t)\|_2^2 = \boldsymbol{q}_\xi^\top \Phi_\xi^\top \Phi_\xi A_\xi^{-1} U_\xi(\boldsymbol{\omega}) \boldsymbol{q}_\xi. \tag{3.56}$$

Integrating (3.56) along space we get

$$\begin{aligned} \sum_{m=1}^{n_b} \frac{1}{L_{b_m}} \int_0^{L_{b_m}} \frac{d}{dt} \|\boldsymbol{\xi}(s,t)\|_2^2 \, ds &= \sum_{m=1}^{n_b} \frac{1}{L_{b_m}} \int_0^{L_{b_m}} 2\boldsymbol{q}_\xi^\top \Phi_\xi^\top \Phi_\xi A_\xi^{-1} U_\xi(\boldsymbol{\omega}) \boldsymbol{q}_\xi ds \\ &= \frac{2}{L} \boldsymbol{q}_\xi^\top A_\xi A_\xi^{-1} U_\xi(\boldsymbol{\omega}) \boldsymbol{q}_\xi = 0, \end{aligned}$$

which concludes the proof and where the definition (3.53) and the skew-symmetry property of U_ξ have been used.

With this approach, the forcing term (3.42) is constructed now in terms of the quaternion mode shapes with the matrix

$$\left[\Gamma_g^l\right]_{ij} = \sum_{m=1}^{n_b} \int_0^{L_{b_m}} \boldsymbol{\phi}_{1i}^{(b_m)\top} M_{v_{b_m}} T_{jl}(\boldsymbol{\phi}_j, \boldsymbol{\phi}_l)^\top \boldsymbol{g} ds + \sum_{n=1}^{n_l} \boldsymbol{\phi}_{1i}^{(l_n)\top} M_{v_{l_n}} \, T_{jl}(\boldsymbol{\phi}_j, \boldsymbol{\phi}_l)^\top \big|_{s_{l_n}} \boldsymbol{g}, \tag{3.57}$$

and the evolution equation for the quaternion approximation is expressed, using results (3.53) and (3.54), via the matrices

$$\Gamma_\xi^l = A_\xi^{-1} U_\xi(\boldsymbol{\phi}_{\omega l}). \tag{3.58}$$

Note that a system where expansion (3.47) is used can always be recovered by imposing $q_{\xi 0}(t) = 1$, achieved by zeroing the first rows of the above matrices Γ_{ξ}^{l}. This however breaks the skew-symmetry and the average unit-norm preservation property is hence lost.

Displacements

Since displacements are typically not required to time-march the resulting structural low-order model, no reduction technique to decrease the computational cost to evaluate them is sought. Hence, at a given spatial coordinate s, they can be obtained by mere post-processing of the modal solution via the temporal evolution equation

$$\dot{\boldsymbol{r}}(s,t) = T(\boldsymbol{\xi}(s)) \sum_{j=1}^{N_m} \boldsymbol{\phi}_{vj}(s) q_{1j}(t), \tag{3.59}$$

where the rotation field $\boldsymbol{\xi} = \boldsymbol{\xi}(\boldsymbol{q}_{\xi})$ can be recovered by any of the two introduced approximations (3.43) or (3.51).

3.2.3 Modal Aerodynamic Description

As previously introduced, the objective here is to use the mode shapes to reduce the inputs and outputs of a linearised UVLM description. Due to the convergence requirements of typical UVLM implementations, fine discretisations of the grids used to model the lifting surfaces and wakes are the norm, resulting in high-dimensional input and output vectors [43]. As described by (2.46), the inputs ($\boldsymbol{\zeta}_b$, $\dot{\boldsymbol{\zeta}}_b$) and outputs ($\boldsymbol{y}_A$) to the system are, respectively, the coordinates and velocities of the UVLM bound lattice grid and the forces and moments at those same points. Under the assumption that the sections rotate rigidly, the inputs can be mapped onto the displacements and velocities, $\boldsymbol{r}, \dot{\boldsymbol{r}}$, (and the finite-rotation counterparts, parameterised by quaternions $\boldsymbol{\xi}$, $\dot{\boldsymbol{\xi}}$) of the wing or lifting surface beam centreline and the output to the external (aerodynamic) forcing $\boldsymbol{f}_a$ applied on the same centreline by

$$\boldsymbol{\zeta}_b = \mathcal{K}_{\zeta}(s, \boldsymbol{r}, \boldsymbol{\xi}), \tag{3.60}$$

$$\dot{\boldsymbol{\zeta}}_b = \mathcal{K}_{\dot{\zeta}}(s, \dot{\boldsymbol{r}}, \dot{\boldsymbol{\xi}}), \tag{3.61}$$

$$\boldsymbol{f}_a = \mathcal{K}_f(s, \boldsymbol{y}_A). \tag{3.62}$$

The mappings $\mathcal{K}_{\zeta}$, $\mathcal{K}_{\dot{\zeta}}$ and $\mathcal{K}_f$ are nonlinear and dependent on the instantaneous geometry and kinematics of the beam. However, their linearised versions, to which we refer without

the curly notation (K_ζ, $K_{\dot\zeta}$ and K_f), are constant. Hence, as described in detail in [63] (where finite-rotations are parametrised using Cartesian rotation vectors) displacement and rotation vector linear perturbations from an undeformed reference state (and the time-derivative counterparts) are directly linked by constant coefficient matrices to the linear UVLM inputs ($\delta\boldsymbol{\zeta}_b$, $\delta\dot{\boldsymbol{\zeta}}_b$).

We now show how the UVLM input perturbations are related to the modal intrinsic variables. We use again the notation introduced in Chapter 2 to define perturbations $\delta(\bullet)$ to the reference linearisation point $(\bar{\bullet})$.

Perturbation in the velocities $\left(\delta\dot{\boldsymbol{r}}^\top,\, \delta\dot{\boldsymbol{\xi}}^\top\right)^\top$ are easily related to the velocity modes $\boldsymbol{q}_1$, as will be shown next. The velocities at the undeformed, linearisation point are zero $\bar{\boldsymbol{v}} = \bar{\boldsymbol{\omega}} = \boldsymbol{0}$, also giving $\dot{\bar{\boldsymbol{r}}} = \boldsymbol{0}$, $\dot{\bar{\boldsymbol{\xi}}} = \boldsymbol{0}$ (by equations (2.40) and (2.36)). The rotation field at linearisation $\bar{\boldsymbol{\xi}}$ is solution to $\bar{\boldsymbol{\xi}}' = \mathcal{U}(\boldsymbol{\kappa}_0)\bar{\boldsymbol{\xi}}$, and hence $\bar{T} = T(\bar{\boldsymbol{\xi}})$. Then, linearisation of equations (2.40) and (2.36) yield

$$\delta\dot{\boldsymbol{r}} = \bar{T}\delta\boldsymbol{v}, \tag{3.63}$$

$$\delta\dot{\boldsymbol{\xi}} = \mathcal{U}_t(\bar{\boldsymbol{\xi}})\delta\boldsymbol{\omega}. \tag{3.64}$$

Then the perturbations $\left(\delta\dot{\boldsymbol{r}}^\top,\, \delta\dot{\boldsymbol{\xi}}^\top\right)^\top$ can be expressed in terms of the velocity modes $\boldsymbol{q}_1$ as follows

$$\begin{pmatrix} \delta\dot{\boldsymbol{r}} \\ \delta\dot{\boldsymbol{\xi}} \end{pmatrix} = \begin{pmatrix} \bar{T} & 0 \\ 0 & \mathcal{U}_t(\bar{\boldsymbol{\xi}}) \end{pmatrix} \sum_{j=1}^{N_m} \boldsymbol{\phi}_{1j}(s) q_{1j}(t). \tag{3.65}$$

Regarding the perturbations in displacements and rotations $\left(\delta\boldsymbol{r}^\top, \delta\boldsymbol{\xi}^\top\right)^\top$, they will be expressed by means of a new modal set of *displacement coordinates*, defined as $\boldsymbol{q}_0$. They can be defined from either the velocity or force/moment modal expansion coefficients ($\boldsymbol{q}_1$ or $\boldsymbol{q}_2$, respectively), since they can be recovered by time integration of translational and angular velocities (by (2.40) and (2.36)) or by space integration of strains and curvatures (by (2.39) and (2.35)).

The proposed expansion for the displacements and finite rotations is inspired by (3.65) and uses the same mode shapes as the velocities $\boldsymbol{\phi}_{0j} = \boldsymbol{\phi}_{1j}$, with expansion coefficients q_{0j}:

$$\begin{pmatrix} \delta\boldsymbol{r} \\ \delta\boldsymbol{\xi} \end{pmatrix} = \begin{pmatrix} \bar{T} & 0 \\ 0 & \mathcal{U}_t(\bar{\boldsymbol{\xi}}) \end{pmatrix} \sum_{j=1}^{N_m} \boldsymbol{\phi}_{0j}(s) q_{0j}(t). \tag{3.66}$$

With this, the inputs and outputs of the linearised UVLM implementation (2.45) can be

linked to the modal displacement and velocity coordinates $\boldsymbol{q}_0$ and $\boldsymbol{q}_1$

$$\delta \boldsymbol{u}_A = \begin{pmatrix} K_{\zeta q_0} & 0 \\ 0 & K_{\dot{\zeta} q_1} \end{pmatrix} \begin{pmatrix} \boldsymbol{q}_0 \\ \boldsymbol{q}_1 \end{pmatrix}, \tag{3.67}$$

where the linear mappings $K_{\zeta q_0}$ and $K_{\dot{\zeta} q_1}$ account for the linearisation of the nonlinear mappings (3.60) and (3.61) (blocks K_ζ and $K_{\dot{\zeta}}$ in Fig 3.5) and the defined expansions for the perturbations (3.66) and (3.65) (ϕ blocks in Fig 3.5). This allows a notable reduction in the input vector size from typical $\mathcal{O}(10^3 - 10^4)$ inputs to $\mathcal{O}(10)$ modes. Analogously, the output can be expressed in modal space by

$$\boldsymbol{\eta}_a = K_{\eta y} \delta \boldsymbol{y}_a, \tag{3.68}$$

where $K_{\eta y}$ includes the linearised mapping (3.62) and subsequent projection onto the modal space (blocks K_y and $\phi^\top$ in Fig. 3.5, respectively).

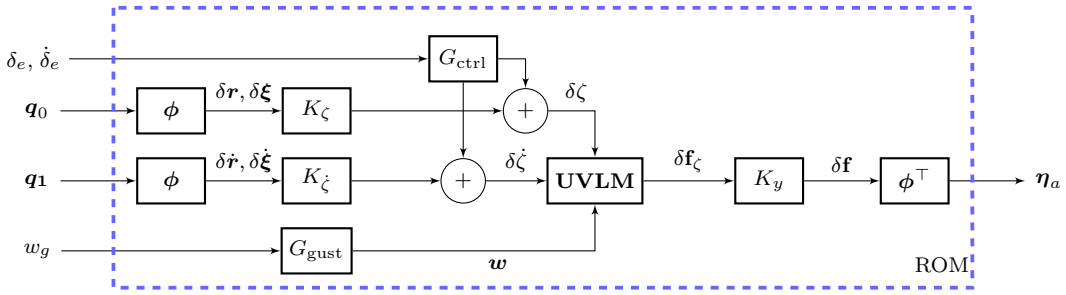


Figure 3.5: Block diagram description of the aerodynamic system with modal inputs and outputs projected onto modal coordinates. (Adapted and reproduced here with the permission of N. Goizueta)

With this first reduction on the input/output dimensionality of the system, as shown in Fig. 3.5 (where additional inputs such as control surface deflection and deflection rates and a vertical gust disturbance are displayed), efficient model order reduction can be sought. A particular suitable strategy is a Krylov-subspace based strategy, which is a moment-matching method that takes advantage of the reduction in the number of input-output transfer functions (due to the described truncation after projection onto modal space). At its core, the method aims to match the n first derivatives (i.e., the moments) of the transfer functions of the system at chosen points in the complex plane (i.e., the interpolation points). It is highly efficient for large systems, since it relies on matrix-vector multiplications to build the Krylov subspaces. The details of the procedure alongside its implementation in linearised UVLM models is given in [63]. Balancing methods have also been tailored to the structure of the linearised UVLM formulation, yielding efficient frequency-limited balanced methods that effectively remove high order

modes introduced by the fine-discretisation requirements of the UVLM descriptions but that have no significant relevance in the input/output behaviour. The particularities of such implementation can be found in [101, 102].

Ultimately, both methods result in (left) W and (right) V projection matrices which allow reduction of the linearised aerodynamic state $\delta\boldsymbol{x}_A$, as defined in (2.46), into a new low-order vector state which, using the same nomenclature as before, is defined as

$$\boldsymbol{q}_\Gamma = W^\top \delta\boldsymbol{x}_A. \tag{3.69}$$

The reduced linearised UVLM with modal input and outputs reads

$$\begin{aligned} \dot{\boldsymbol{q}}_\Gamma &= A_q \boldsymbol{q}_\Gamma + B_q \left(\boldsymbol{q}_0^\top, \boldsymbol{q}_1^\top\right)^\top, \\ \boldsymbol{\eta}_a &= C_q \boldsymbol{q}_\Gamma + D_q \left(\boldsymbol{q}_0^\top, \boldsymbol{q}_1^\top\right)^\top, \end{aligned} \tag{3.70}$$

with reduced state space matrices $(\bullet)_q$

$$\begin{aligned} A_q &= \mathcal{T}_{d\to c}\left(W^\top A V\right), \\ B_q &= \mathcal{T}_{d\to c}\left(W^\top B\right), \\ C_q &= \mathcal{T}_{d\to c}\left(CV\right), \\ D_q &= \mathcal{T}_{d\to c}\left(D\right), \end{aligned} \tag{3.71}$$

where (A, B, C, D) is the linear discrete-time time-invariant system in (2.45) and $\mathcal{T}_{d\to c}(\bullet)$ denotes a discrete- to continuous-time transformation, such as a bilinear transformation [62], of the resulting reduced state-space matrices.

Scaling of the variables involved in the UVLM formulation is useful to obtain a state-space representation of the linear aerodynamics $(\breve{A}, \breve{B}, \breve{C}, \breve{D})$ valid for all incompressible flight velocities. If this is the case, a reference length dimension b (half the wing chord), flight velocity U_∞ and flow density ρ are used to scale all UVLM inputs and outputs. Therefore, when assembling the reduced order-model (3.70) of the state space resulting from the scaled UVLM equations $(\breve{A}, \breve{B}, \breve{C}, \breve{D})$, this is rewritten with the following scaling terms

$$\begin{aligned} t_\infty \dot{\boldsymbol{q}}_\Gamma &= \breve{A}_q \boldsymbol{q}_\Gamma + \breve{B}_q \left(\boldsymbol{q}_0^\top, t_\infty \boldsymbol{q}_1^\top\right)^\top \\ \boldsymbol{\eta}_a &= q_\infty \left(\breve{C}_q \boldsymbol{q}_\Gamma + \breve{D}_q \left(\boldsymbol{q}_0^\top, t_\infty \boldsymbol{q}_1^\top\right)^\top\right), \end{aligned} \tag{3.72}$$

where $t_\infty = bU_\infty^{-1}$ is the reference time scale of the flow and $q_\infty = \frac{1}{2}\rho U_\infty^2$ is the dynamic pressure.

Computation of Modal Displacements

The remaining aspect which requires further discussion is the link between the newly introduced displacement modal coefficients $\boldsymbol{q}_0$ and the intrinsic modal coordinates $\boldsymbol{q}_1$ and $\boldsymbol{q}_2$. The two alternative methods to obtain $\boldsymbol{q}_0$ are discussed next.

From substitution of the displacement/quaternion expansion (3.66) into (3.65) it is obvious that the coefficients $\boldsymbol{q}_0$ can be obtained directly from temporal integration of the velocity modal coefficients $\boldsymbol{q}_1$:

$$\dot{\boldsymbol{q}}_0 = \boldsymbol{q}_1. \tag{3.73}$$

Alternatively, we consider now the spatial evolution equations to compute the displacements (2.39) and quaternion field (2.35). Their linearisation yields

$$\delta \boldsymbol{r}' = \delta T \boldsymbol{e}_1 + \bar{T}\delta\boldsymbol{\gamma}, \tag{3.74}$$

$$\delta \boldsymbol{\xi}' = \mathcal{U}(\boldsymbol{\kappa}_0)\delta\boldsymbol{\xi} + \mathcal{U}_t(\bar{\boldsymbol{\xi}})\delta\boldsymbol{\kappa}. \tag{3.75}$$

Pre-multiplying (3.74) by $\bar{T}^\top$ and (3.75) by $\mathcal{U}_t^\top$ and after considerable manipulation, equations (3.74)–(3.75) can be rewritten as

$$\left(I_6\frac{\partial}{\partial s} + \begin{pmatrix} \widetilde{\boldsymbol{\kappa}}_0 & \widetilde{\boldsymbol{e}}_1 \\ 0 & \widetilde{\boldsymbol{\kappa}}_0 \end{pmatrix}\right)\begin{pmatrix} \bar{T}^\top\delta\boldsymbol{r} \\ 4\mathcal{U}_t^\top\delta\boldsymbol{\xi} \end{pmatrix} = \begin{pmatrix} \delta\boldsymbol{\gamma} \\ \delta\boldsymbol{\kappa} \end{pmatrix} = \sum_{j=1}^{N_m} C\boldsymbol{\phi}_{2j}(s)q_{2j}(t). \tag{3.76}$$

Upon substitution of the proposed expansion for the displacement and quaternion perturbations (3.66) into the previous result, it leads to

$$\left(\frac{\partial}{\partial s} - E^\top\right)\sum_{j=1}^{N_m}\boldsymbol{\phi}_{0j}(s)q_{0j}(t) = \sum_{j=1}^{N_m} C\boldsymbol{\phi}_{2j}(s)q_{2j}(t), \tag{3.77}$$

where the definition of the E matrix (2.7) and the property $\mathcal{U}_t^\top\mathcal{U}_t = \frac{1}{4}I_3$ have been used. As expected, the expression above has the same structure as the linear part of the compatibility equation (2.23). Therefore, and due to our choice for the displacement/rotation modes $\boldsymbol{\phi}_{0j} = \boldsymbol{\phi}_{1j}$, after a Galerkin projection procedure to solve for (3.77), the same linear relationship between $\dot{\boldsymbol{q}}_2$ and $\boldsymbol{q}_1$ in the second equation of (3.33) is obtained for $\boldsymbol{q}_2$ and $\boldsymbol{q}_0$. Hence, the modal displacements/rotations can be obtained from

$$\boldsymbol{q}_0 = -\Omega^{-1}\boldsymbol{q}_2. \tag{3.78}$$

The latter method to compute modal displacements is the one preferred for unconstrained

flexible structural systems exhibiting rigid body motions, such as aircraft-like structures. In these cases, computing the modal displacements from direct time-integration of velocities as in (3.73) would lead to highly unstable systems. To understand this, consider the equation for the velocity and the force/moment states of the reduced model in modal coordinates (3.33). The set of steady rigid-body solutions in modal space are characterised by $\dot{\boldsymbol{q}}_1 = \dot{\boldsymbol{q}}_2 = \mathbf{0}$ and with $\boldsymbol{q}_1 \neq \mathbf{0}$. In the flexible case, we have additionally that $\boldsymbol{q}_2 \neq \mathbf{0}$. This implies that rigid-body velocity solutions have to satisfy $\boldsymbol{q}_1 \in \ker\left(-\Omega + q_{2l}(\Gamma_2^l)^\top\right)$, by the second equation in (3.33). For a deformed configuration where $\boldsymbol{q}_2 \neq \mathbf{0}$, we have that $\ker(-\Omega) \subset \ker\left(-\Omega + q_{2l}(\Gamma_2^l)^\top\right)$, and hence rigid-body velocities $\boldsymbol{q}_1$ might have nonzero elastic modal components (i.e., the set of possible $\boldsymbol{q}_1$ solutions giving $\dot{\boldsymbol{q}}_2 = \mathbf{0}$ is larger). In other words, in a deformed configuration, since the velocities in the intrinsic formulation are expressed in a local frame of reference, the decomposition of rigid-body velocities might need of nonzero higher-order modal components.

The UVLM formulation is built from the modes around the undeformed configuration, and, by construction, it is insensitive to inputs corresponding to displacements obtained from the rigid body modes. That is, the transfer functions corresponding to modal displacements $\dot{\boldsymbol{q}}_0 = \boldsymbol{q}_1$, $\boldsymbol{q}_1 \in \ker(-\Omega)$ are zero. As explained above, when the structure undergoes deformation, rigid-body solutions result in $\boldsymbol{q}_1$ states with nonzero constant entries where the UVLM transfer functions of the associated $\boldsymbol{q}_0$ are nonzero (causing a windup in the corresponding $\boldsymbol{q}_0$ obtained by time-integration of $\boldsymbol{q}_1$). Consequently, as long as the structure is deformed, nonzero velocity components associated to elastic modes are part of the (steady state) rigid-body solutions. This causes an apparent incompatibility between steady states of the structural model and the aerodynamic model, which has been observed to lead to highly unstable coupled systems. As pointed out earlier, this undesired phenomenon is effectively suppressed if modal displacements are retrieved from the modal forces as in (3.78).

3.2.4 Coupled Aeroservoelastic System

As mentioned in Chapter 2, the UVLM description (2.45) (and the obtained low-order model (3.70)) allows us to account for the effect of external velocities such as gusts and of control surface deflections on the unsteady aerodynamics. Therefore, a complete aeroelastic system with aerodynamic and gravity forcing, and with gust intensities as disturbances to the system $\boldsymbol{w}$ (with predefined gust spatial profiles) and control surface deflections (and

rate deflections) gathered in the input vector $\boldsymbol{u}$ (as shown in Fig. 3.5), has the form

$$\begin{aligned}
\dot{\boldsymbol{q}}_1 &= \Omega\boldsymbol{q}_2 + \Sigma\boldsymbol{q}_1 - q_{1l}\Gamma_1^l\boldsymbol{q}_1 - q_{2l}\Gamma_2^l\boldsymbol{q}_2 + \underbrace{q_{\xi l}\Gamma_g^l\boldsymbol{q}_\xi}_{\text{gravity}} + \underbrace{\bar{\boldsymbol{\eta}}_a + C_q\boldsymbol{q}_\Gamma + D_q\left(\boldsymbol{q}_0^\top, \boldsymbol{q}_1^\top, \boldsymbol{u}^\top, \boldsymbol{w}^\top\right)^\top}_{\text{aerodynamic forcing}},\\
\dot{\boldsymbol{q}}_2 &= -\Omega\boldsymbol{q}_1 + q_{2l}(\Gamma_2^l)^\top\boldsymbol{q}_1,\\
\dot{\boldsymbol{q}}_\xi &= q_{1l}\Gamma_\xi^l\boldsymbol{q}_\xi,\\
\dot{\boldsymbol{q}}_\Gamma &= A_q\boldsymbol{q}_\Gamma + B_q\left(\boldsymbol{q}_0^\top, \boldsymbol{q}_1^\top, \boldsymbol{u}^\top, \boldsymbol{w}^\top\right)^\top,
\end{aligned} \tag{3.79}$$

where $\bar{\boldsymbol{\eta}}_a$ accounts for the possible nonzero aerodynamic forces at the UVLM linearisation point and where the closure relationship for $\boldsymbol{q}_0$ has to be chosen between (3.73) or (3.78). If the first relationship is selected, the state vector has to be augmented to include $\boldsymbol{q}_0$.

In the next section we describe how data-driven methodologies can be used to enhance the low-order, nonlinear aeroservoelastic model obtained from first-principles and analytical manipulation described by (3.79). The improvement effort is twofold. First, a data-driven model of gravitational forces is sought (also applicable to other orientation-dependent forces or terms), which allows us to link the gravity modal forcing directly to the intrinsic variables (namely $\boldsymbol{q}_2$) and remove the need for explicit computation of finite-rotations (Eq. 3.41), which leads to a substantial reduction in the size of the final system. Note that, if the modal approximation for the quaternions is chosen, $\boldsymbol{q}_\xi$ has the same dimensions as $\boldsymbol{q}_1$ and $\boldsymbol{q}_2$, while the spline method typically yields larger models. Second, a more accurate model of the unsteady aerodynamics is searched for by appealing to data-driven modelling, since the analytical methods described above are limited to first-order approximations. However, as it will be discussed next, physical insights provided by these first order approximations can be exploited to pre-process and condition the training data for a more successful and sensible model fitting exercise.

3.3 Data-Driven Model Fitting

In the quest for further reduction and enhancement of the modal aeroservoelastic description for control (3.79) we explore data-driven methods. These are regarded as accessory improvements to the main nonlinear low-order modelling effort provided by the intrinsic equations in modal coordinates (3.33). Extensive numerical evidence has shown that low-order models of the intrinsic equations in modal coordinates provide very accurate results with very concise descriptions [15, 16] when compared to higher-order models. Besides, this physics-based model-order reduction inherits desirable physical properties from the full PDEs such as energy-preservation and first order time derivatives with only quadratic

nonlinearities. Without significant room for improvement in the structural low-order modelling, these data-based strategies are focused on improving the models of gravitational and aerodynamic forcing and on expressing them in terms of the intrinsic, modal variables $\boldsymbol{q}_1$ and $\boldsymbol{q}_2$.

As it was seen in § 3.2.2, accounting for gravity forces in the intrinsic formulation requires simulation of finite rotations alongside the structural intrinsic equations. The addition of the quaternion time-evolution equations adds additional and undesirable model complexity and hence by turning to data-driven strategies we aim to express the gravity forcing, in modal coordinates, by means of the least possible number of variables avoiding the computation of the (approximated) entire rotation field. As will be discussed next, this is possible by seeking (data-driven) approximations to the gravity forcing as a function of only one quaternion and the force/moment sectional resultants modal coefficients $\boldsymbol{q}_2$.

Regarding the low-order models for the unsteady aerodynamics introduced in § 3.2.3, which are limited to first-order approximations of unsteady vortex lattice methods (3.70), they have been found to be remarkably accurate in aeroelastic simulations of clamped structures [13]. However, these linear reduced-order models fail to capture second-order effects such as variations of the induced drag or of the dynamic pressure, which makes these models insufficient for the simulation of free-flying aircraft-like structures undergoing large rigid-body motions. Therefore, by fitting a higher-order model to the nonlinear unsteady vortex lattice data, we seek to capture those effects and hence obtain suitable and more accurate descriptions.

To obtain the necessary data to train the models we will rely on the full nonlinear aeroelastic simulations of SHARPy (Simulation of High Aspect Ratio aeroplanes and wind turbines in Python), Imperial College nonlinear aeroelasticity open source toolbox [41]. SHARPy couples a finite element implementation of displacement-based geometrically-exact beams [58, 140] with an unsteady vortex lattice model [42, 43, 86, 108]. The process by which the data sets, used for the model fittings, are obtained from SHARPy and translated into the modal space will be shown in § 3.3.3.

Amongst the diverse available machine-learning methods, a sparsity-promoting (with L1-norm regularisation on the fitting model coefficients) regression algorithm is chosen [148]. This is justified by the simplicity of the resulting models, which can be chosen to be polynomials in the chosen model variables. Such approach not only allows analytical manipulation of the resulting models (beneficial to obtain the sensitivities of the system, as will be discussed in § 4.3.3) but also reduces computational complexity. This is in contrast to artificial neural-network based strategies, where the use of more complex functions

(usually sigmoids) hinders computational efficiency. Moreover, the input-output maps required to model gravitational forces and the unsteady aerodynamic forces are typically smooth. Then it is expected that polynomial expressions are sufficient to reproduce such mappings accurately. In particular, quadratic expressions will be sought, hence matching the computational complexity of the geometrically nonlinear terms in (3.79) and justified by the second-order effects of the unsteady aerodynamics absent from the former model.

Given a nonlinear mapping $y = f(\boldsymbol{x})$, with $\boldsymbol{x} \in \mathbb{R}^{n_x}$ and $y \in \mathbb{R}$, and n_d data pairs of inputs $X = (\boldsymbol{x}^1, \cdots, \boldsymbol{x}^{n_d}) \in \mathbb{R}^{n_x \times n_d}$ and outputs $Y = (y^1, \cdots, y^{n_d}) \in \mathbb{R}^{1 \times n_d}$, the L1-regularised (Lasso) regression aims to find the coefficients $\boldsymbol{\beta}$ of a model $y = \boldsymbol{\beta}^\top \Theta(\boldsymbol{x})$ by solving the minimisation problem

$$\min_{\boldsymbol{\beta}} \|Y - \boldsymbol{\beta}^\top \Theta(X)\|_2^2 + \lambda \|\boldsymbol{\beta}\|_1, \tag{3.80}$$

where λ is the Lasso penalty factor and $\Theta(\boldsymbol{x})$ is a library of analytical functions of $\boldsymbol{x}$, which in our case would consist of the identity, linear and quadratic combinations of the entries in $\boldsymbol{x}$

$$\Theta(X) = \begin{pmatrix} 1 & & 1 \\ x_1^1 & & x_1^{n_d} \\ \vdots & & \vdots \\ x_{n_x}^1 & & x_{n_x}^{n_d} \\ (x_1^1)^2 & \cdots & (x_1^{n_d})^2 \\ x_1^1 x_2^1 & & x_1^{n_d} x_2^{n_d} \\ \vdots & & \vdots \\ (x_{n_x}^1)^2 & & (x_{n_x}^{n_d})^2 \end{pmatrix}. \tag{3.81}$$

A common practice in optimisation-based model-fitting algorithms is to normalise both inputs and outputs to better condition the optimisation problem. Then, (3.80) has to be slightly modified to account for the mentioned scaling. The normalisation is performed so that each input or output of the data ensembles lie within the interval $[-1, 1]$, which for a particular snapshot x_i of a given data ensemble $\{x_i\}_{i=1}^{n_d}$, this is performed as

$$\breve{x}_i = -1 + 2 \frac{x_i - \min\limits_i \{x_i\}_{i=1}^{n_d}}{\max\limits_i \{x_i\}_{i=1}^{n_d} - \min\limits_i \{x_i\}_{i=1}^{n_d}}, \tag{3.82}$$

where $\breve{(\bullet)}$ represents, here, the normalised values. The minimisation problem that should be solved, instead of (3.80), is

$$\min_{\breve{\boldsymbol{\beta}}} \|\breve{Y} - \breve{\boldsymbol{\beta}}^\top \Theta(\breve{X})\|_2^2 + \lambda \|\breve{\boldsymbol{\beta}}\|_1. \tag{3.83}$$

The relationship between the normalised and non-normalised model coefficients can be represented by a linear transformation

$$\boldsymbol{\beta} = A_\beta \breve{\boldsymbol{\beta}} + \boldsymbol{b}_\beta, \tag{3.84}$$

where the coefficients of $\boldsymbol{\beta}$ associated to the unit input (i.e., the source or bias term of the quadratic expression) receive contributions from all normalised coefficients $\breve{\boldsymbol{\beta}}$, the linear coefficients of $\boldsymbol{\beta}$ receive contributions from the normalised linear and quadratic coefficients and the quadratic ones differ from the normalised counterparts only by a scaling factor (i.e., the matrix A_β is upper-triangular).

Next, we describe the choice of variables that will populate the general models $y = \boldsymbol{\beta}^\top \Theta(\boldsymbol{x})$, which will substitute the corresponding gravity and aerodynamic blocks of our aeroelastic system (3.79).

3.3.1 Gravity Forcing

Here we seek to obtain a model for gravity forcing bypassing the computation of finite-rotations. This will allow us to eliminate the third equation in (3.79), which typically results in additional systems of equations comparable in size to the ODEs for $\dot{\boldsymbol{q}}_1$ or $\dot{\boldsymbol{q}}_2$.

Motivated by the fact that finite rotations can be computed at any given time instance by spatial integration of the local curvatures (2.35), and that the gravity forcing only depends on the local orientation of the structure (2.41), the projection of gravity forces onto modal coordinates can be expressed as a function of the modal force/moment sectional resultants $\boldsymbol{q}_2$ and one quaternion at a given spatial coordinate s_0, that is, $\boldsymbol{\eta}_g = \boldsymbol{\eta}_g\left(\boldsymbol{q}_2, \boldsymbol{\xi}_{s_0}\right)$. Note that to integrate (2.35) in space, the temporal evolution of the rotations in at least one point in the structure, needs to be tracked. Therefore, if a quadratic expression is chosen as a model to fit, gravity forcing can be accounted by substituting (3.41) and (3.42) by

$$\dot{\boldsymbol{\xi}}_{s_0} = \mathcal{U}\left(\sum_{j=1}^{N_m} \boldsymbol{\phi}_{\omega j}(s_0) q_{1j}\right) \boldsymbol{\xi}_{s_0}, \tag{3.85}$$

$$[\boldsymbol{\eta}_g]_i = \boldsymbol{\beta}_{g_i}^\top \Theta\left(\left(\boldsymbol{q}_2^\top, \boldsymbol{\xi}_{s_0}^\top\right)^\top\right). \tag{3.86}$$

Provided that data ensembles of the form $\{(\boldsymbol{\eta}_g)_i, (\boldsymbol{q}_2)_i, (\boldsymbol{\xi}_{s_0})_i\}_{i=1}^{n_d}$ are created, then the coefficients $\boldsymbol{\beta}_g$ from (3.86) can be identified by solving the regularised minimisation problem (3.83).

3.3.2 Aerodynamic Forcing

Regarding the aerodynamic forcing, the fitting exercise is twofold. On the one hand, a model for the dynamic evolution of a choice of reduced aerodynamic states has to be found. On the other hand, the static map defining the output equation (with which aerodynamic forces are obtained from the instantaneous aerodynamic states, kinematics and geometry of the lifting surfaces) needs to be fitted too.

As already hinted by the first-order approximation to the UVLM dynamics given by the ROM (3.70), the inputs to both the aerodynamic states time-evolution and output equations can be described by the modal displacements/rotations vector $\boldsymbol{q}_0$ and the modal velocities vector $\boldsymbol{q}_1$, together with other predefined inputs such as control surface deflections $\boldsymbol{u}$ or gust intensities $\boldsymbol{w}$. Hence, we seek more accurate order-reduced UVLM descriptions, expressed in modal coordinates, by considering quadratic expressions for both the aerodynamic states time-evolution (which will replace the terms involving the A_q and B_q matrices in (3.79), i.e., the last equation) and the output equation (which will substitute the terms involving the C_q and D_q matrices in (3.79)):

$$\begin{aligned}[\dot{\boldsymbol{q}}_\Gamma]_i &= \boldsymbol{\beta}_{\Gamma_i}^\top \Theta\left(\left(\boldsymbol{q}_0^\top, \boldsymbol{q}_1^\top, \boldsymbol{q}_\Gamma^\top, \boldsymbol{u}^\top, \boldsymbol{w}^\top\right)^\top\right), \\ [\boldsymbol{\eta}_a]_i &= \boldsymbol{\beta}_{a_i}^\top \Theta\left(\left(\boldsymbol{q}_0^\top, \boldsymbol{q}_1^\top, \boldsymbol{q}_\Gamma^\top, \boldsymbol{u}^\top, \boldsymbol{w}^\top\right)^\top\right).\end{aligned} \tag{3.87}$$

In this case, two sets of data ensembles of the forms $\{(\dot{\boldsymbol{q}}_\Gamma)_i, (\boldsymbol{q}_0)_i, (\boldsymbol{q}_1)_i, (\boldsymbol{q}_\Gamma)_i, (\boldsymbol{u})_i, (\boldsymbol{w})_i\}_{i=1}^{n_d}$ and $\{(\boldsymbol{\eta}_a)_i, (\boldsymbol{q}_0)_i, (\boldsymbol{q}_1)_i, (\boldsymbol{q}_\Gamma)_i, (\boldsymbol{u})_i, (\boldsymbol{w})_i\}_{i=1}^{n_d}$ have to be created to obtain the identified coefficients $\boldsymbol{\beta}_\Gamma$ and $\boldsymbol{\beta}_a$ by solving two minimisation problems (3.83). Note that $\boldsymbol{q}_0$ can be replaced by $\boldsymbol{q}_2$, following the linear approximation (3.78), seeking a direct link between the aerodynamic model and the intrinsic variables $(\boldsymbol{q}_1, \boldsymbol{q}_2)$.

3.3.3 Training Data Acquisition

The nonlinear aeroelasticity toolbox SHARPy is used to obtain the necessary training data. As stated above, it solves for a geometrically-exact beam formulation based on displacements and finite rotations, which are parametrised using Cartesian rotation vectors. The elastic displacements $\boldsymbol{R}_A$ and rotations $\boldsymbol{\Psi}_A$ of each of the nodes, resulting from a finite element discretisation, are with respect to a body-attached frame of reference A, located at the spatial coordinate s_A. The description of the dynamics is completed by the addition of the linear and angular velocities of such frame, $\boldsymbol{v}_A, \boldsymbol{\omega}_A$, and its orienta-

tion with respect an inertial frame of reference, parametrised with a quaternion $\boldsymbol{\xi}_A$. The relationship between this set of variables and the intrinsic local velocities $(\boldsymbol{v}, \boldsymbol{\omega})$ is given by

$$\begin{aligned}\boldsymbol{v}(s,t) &= T(\boldsymbol{\Psi}_A(s,t))\dot{\boldsymbol{R}}_A(s,t) + T(\boldsymbol{\Psi}_A(s,t))\left(\boldsymbol{v}_A(t) + \widetilde{\boldsymbol{\omega}}_A(t)\boldsymbol{R}_A(s,t)\right),\\ \boldsymbol{\omega}(s,t) &= T_t(\boldsymbol{\Psi}_A(s,t))\dot{\boldsymbol{\Psi}}_A(s,t) + T_t(\boldsymbol{\Psi}_A(s,t))\boldsymbol{\omega}_A(t),\end{aligned} \tag{3.88}$$

while the local strains and curvatures $(\boldsymbol{\gamma}, \boldsymbol{\kappa})$ are obtained from the following relationships

$$\begin{aligned}\boldsymbol{\gamma}(s,t) &= T(\boldsymbol{\Psi}_A(s,t))\boldsymbol{R}'_A(s,t) - T(\boldsymbol{\Psi}_A(s,0))\boldsymbol{R}'_A(s,0),\\ \boldsymbol{\kappa}(s,t) &= T_t(\boldsymbol{\Psi}_A(s,t))\boldsymbol{\Psi}'_A(s,t) - T_t(\boldsymbol{\Psi}_A(s,0))\boldsymbol{\Psi}'_A(s,0),\end{aligned} \tag{3.89}$$

where $T(\boldsymbol{\Psi}_A(s,t))$ is the transformation matrix between the local frame of reference and the body-attached frame A [58] and $T_t(\boldsymbol{\Psi}_A(s,t))$ is the tangential rotation operator [137].

The data acquisition process from SHARPy is schematised in Fig. 3.6. It starts by obtaining the equilibrium, trim conditions with SHARPy. This, gives us both the (discrete, nodal) aerodynamic and gravitational forces at the trim configuration $\bar{\boldsymbol{f}}_a, \bar{\boldsymbol{f}}_g$, respectively. Using the discrete version of (3.36), where the space-integration is replaced by the use of the discrete modes (evaluated at the same nodes as the finite element implementation in SHARPy), the trim aerodynamic and gravitational forces in modal coordinates are obtained $\bar{\boldsymbol{\eta}}_a, \bar{\boldsymbol{\eta}}_g$.

With these, the intrinsic modal trim solution is obtained $\bar{\boldsymbol{q}}_1, \bar{\boldsymbol{q}}_2$ by finding the steady solution to (3.33). Now, time-histories of modal inputs $\boldsymbol{q}_1(t), \boldsymbol{q}_2(t)$ are obtained by adding perturbations to the trim solution. These are related to the intrinsic variables $\boldsymbol{v}, \boldsymbol{\omega}, \boldsymbol{\gamma}, \boldsymbol{\kappa}$ by the modal expansions (3.31). Therefore, the displacement and Cartesian rotation fields $\boldsymbol{R}_A$ and $\boldsymbol{\Psi}_A$ are obtained through spatial integration of equations (3.89). Note these equations are analogous to (2.39) and (2.35) for an inertial frame coinciding with the body-attached frame A. Then, the time-derivative counterparts $\dot{\boldsymbol{R}}_A$ and $\dot{\boldsymbol{\Psi}}_A$ are easily obtained from (3.88), once the rigid-body velocities of the frame A are computed from

$$\begin{pmatrix} \boldsymbol{v}_A \\ \boldsymbol{\omega}_A \end{pmatrix} = \sum_{j=1}^{N_m} \boldsymbol{\phi}_{1j}(s_A) q_{1j}. \tag{3.90}$$

Adding control surface deflection inputs to the obtained $\boldsymbol{R}_A$, $\boldsymbol{\Psi}_A$ and $\dot{\boldsymbol{R}}_A$, $\dot{\boldsymbol{\Psi}}_A$, $\boldsymbol{v}_A$, $\boldsymbol{\omega}_A$, all the necessary data for a fully prescribed UVLM simulation is ready, where only the UVLM module is run in SHARPy for the obtained structural time-histories. However, a small correction to account for the error introduced by expansions (3.31) (which is also

a source of discrepancy between the modal and SHARPy trim solutions) is added to the displacement and rotation time-histories before they are fed as an input to the simulations in SHARPy, as shown in Fig. 3.6. These correction terms, namely $\bar{\boldsymbol{R}}_A - \boldsymbol{R}_A(0)$, $\bar{\boldsymbol{\Psi}} - \boldsymbol{\Psi}_A(0)$, $-\dot{\boldsymbol{R}}_A(0)$, $-\dot{\boldsymbol{\Psi}}_A(0)$ and those for the velocities of the frame A, $\bar{\boldsymbol{v}}_A - \boldsymbol{v}_A(0)$ and $-\boldsymbol{\omega}_A(0)$, ensure that simulations start from SHARPy original trim conditions, effectively removing any accumulated errors after the described manipulation.

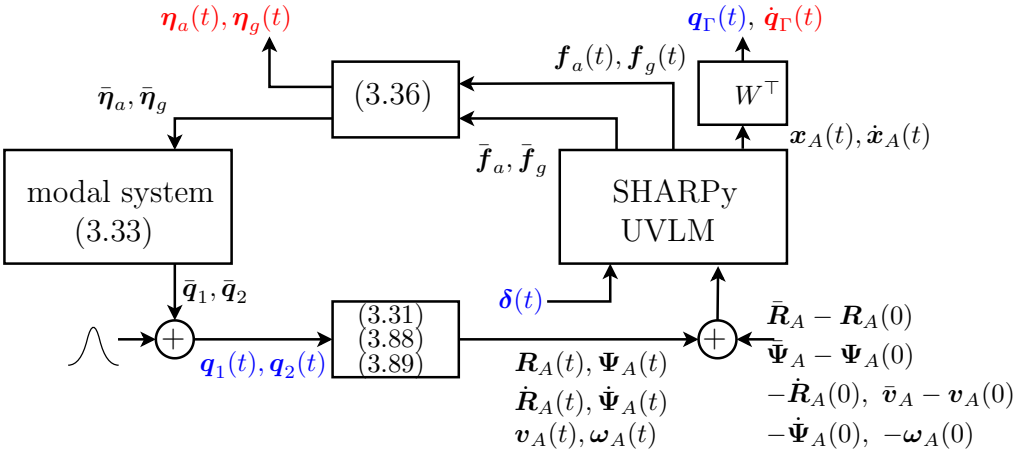


Figure 3.6: Training data acquisition scheme.

The outcome of SHARPy unsteady vortex lattice simulations are the time histories of aerodynamic forces $\boldsymbol{f}_a(t)$, expressed on the local frame of reference, which upon projection using (3.36), result in modal aerodynamic forcing $\boldsymbol{\eta}_a(t)$. Gravitational forces $\boldsymbol{f}_g(t)$ can be easily obtained from SHARPy's nonlinear gravity force distribution at trim, expressed in the body-attached frame A, $\bar{\boldsymbol{f}}_g^A$, because of the prescribed structural solution. Since the temporal evolution of the rotation field $\boldsymbol{\Psi}_A(t)$ and of the rotation of the frame A, $\boldsymbol{\xi}_A(t)$, are known, the time history of gravitational forces $\boldsymbol{f}_g(t)$ is simply obtained, for each node i, by

$$(\boldsymbol{f}_g)_i(t) = \begin{pmatrix} T((\boldsymbol{\Psi}_A)_i(t))T^\top(\boldsymbol{\xi}_A(t))T(\bar{\boldsymbol{\xi}}_A) & 0 \\ 0 & T((\boldsymbol{\Psi}_A)_i(t))T^\top(\boldsymbol{\xi}_A(t))T(\bar{\boldsymbol{\xi}}_A) \end{pmatrix} \left(\bar{\boldsymbol{f}}_g^A\right)_i, \tag{3.91}$$

where T is used here to denote indistinctly the associated rotation matrix from the body attached frame A to the local frame of reference (parameterised in SHARPy using Cartesian rotation vectors) and the rotation matrix from the body attached frame A to the inertial frame of reference (parameterised in SHARPy using a quaternion). Then, by projection, modal gravity forcing is obtained $\boldsymbol{\eta}_g(t)$.

The full aerodynamic states and its time derivatives $\boldsymbol{x}_A(t)$ and $\dot{\boldsymbol{x}}_A(t)$ (see UVLM state-space representation in (2.45)–(2.46)) are also obtained from SHARPy's UVLM solution. These will be reduced, from typical dimensions $\mathcal{O}(10^4 - 10^5)$, using a projection matrix $W^\top$. This projector can be derived under linear assumptions as described in § 3.2.3,

with the expectation that a reduced state, with physically relevant components, can be obtained, easing the model-fitting task. Alternatively, more data-driven strategies, such as principal component analysis of the data ensembles, can be employed to obtain a projector tailored to the particular data used for training.

Therefore, all the necessary elements to seek for models in the form of (3.86) and (3.87) are obtained through the proposed data acquisition scheme: the data inputs to train the models, highlighted in blue in Fig. 3.6, are snapshots of the prescribed histories of modal coefficients $\boldsymbol{q}_1(t)$ and $\boldsymbol{q}_2(t)$, together with reduced aerodynamic states $\boldsymbol{q}_\Gamma(t)$ and additional inputs such as control surface deflections $\boldsymbol{\delta}(t)$. The output data pairs will be formed by snapshots of the time-history responses of modal gravity and aerodynamic forces $\boldsymbol{\eta}_a(t), \boldsymbol{\eta}_g(t)$, as well as the time-derivatives of the reduced aerodynamic states $\dot{\boldsymbol{q}}_\Gamma(t)$, shown in red in Fig. 3.6. The objective is to obtain rich and representative enough data sets by means of multiple simulations, where the modal excitation to produce the time histories of modal inputs $\boldsymbol{q}_1(t), \boldsymbol{q}_2(t)$ is deemed crucial and should be performed sensibly. The choice of projection matrix $W^\top$ is regarded to be equally decisive in the success of the model-fitting procedure. Details regarding these two latter choices are further discussed in the results chapter in § 6.3.

Chapter 4

Control and Estimation Framework

The chosen control and estimation strategies for the presented framework are a nonlinear model predictive controller and a moving horizon estimator. These employ the modal-based reduced-order model described in Chapter 3, which aims to characterise the controlled systems using as compact descriptions as possible, since both methods rely on repeatedly solving open-loop, nonlinear optimal control problems in real time alongside the controlled system time evolution. Once the solution (control inputs) based on the internal model underpinning the controller is obtained at a particular time instance, the control signals are applied to the system, hence closing the feedback loop until a subsequent optimal problem is solved in a future time instant. The optimal control problems are typically defined for quadratic cost functions in terms of the decision variables and the system states. Hence, the nonlinearity emanates from the system nonlinear dynamics, to which the problems are constrained. Input and state constraints are also easily accounted for by these approaches, which is advantageous in many flexible structure application problems (e.g., maximum allowable stresses to alleviate fatigue, maximum allowable displacements to prevent collision of flexible components, etc.). Thus, this chapter presents the control framework placing emphasis on the particularities that allow us to obtain efficient schemes, leveraging the structure of the underpinning finite-dimensional models, which open the door to real-time implementation.

4.1 Model Predictive Control

We follow the conventional discrete-time MPC formulation of [123] for (state and input) constrained nonlinear systems, where full state feedback and no disturbances are assumed.

Specifically, we solve the following nonlinear optimal control problem over a time horizon τ_c at each sampling point $t_i = t_{i-1} + \tau_s$, where the (control) prediction horizon is split into N_c intervals,

$$\min_{\boldsymbol{q}_{ae}^k, \boldsymbol{u}^k} \quad \frac{1}{2}\sum_{k=0}^{N_c-1}\left(\hat{\boldsymbol{q}}_{ae}^{k\top} Q_c \hat{\boldsymbol{q}}_{ae}^k + \hat{\boldsymbol{u}}^{k\top} R_c \hat{\boldsymbol{u}}^k\right) + \frac{1}{2}\hat{\boldsymbol{q}}_{ae}^{N_c\top} P_c \hat{\boldsymbol{q}}_{ae}^{N_c} \tag{4.1a}$$

$$\text{s.t.} \quad \boldsymbol{q}_{ae}^0 = \boldsymbol{q}_{ae}^c, \tag{4.1b}$$

$$\boldsymbol{q}_{ae}^{k+1} = \boldsymbol{f}(\boldsymbol{q}_{ae}^k, \boldsymbol{u}^k, \boldsymbol{w}^k), \qquad k = 0, \cdots, N_c - 1, \tag{4.1c}$$

$$\boldsymbol{u}_l \leq \boldsymbol{u}^k \leq \boldsymbol{u}_u, \qquad k = 0, \cdots, N_c - 1, \tag{4.1d}$$

$$\boldsymbol{q}_{ae,l} \leq \boldsymbol{q}_{ae}^k \leq \boldsymbol{q}_{ae,u}, \qquad k = 1, \cdots, N_c, \tag{4.1e}$$

$$\frac{1}{2}\hat{\boldsymbol{q}}_{ae}^{N_c\top} P_c \hat{\boldsymbol{q}}_{ae}^{N_c} \leq a. \tag{4.1f}$$

The vector $\boldsymbol{q}_{ae} = \left(\boldsymbol{q}_1^\top, \boldsymbol{q}_2^\top, \boldsymbol{q}_\xi^\top, \boldsymbol{q}_\Gamma^\top\right)^\top$ is the modal aeroelastic states vector and $\boldsymbol{u}$ and $\boldsymbol{w}$ are the system control inputs and external disturbances as defined in the fully-coupled aeroelastic system (3.79).

Positive semidefinite matrices $Q_c, P_c \succcurlyeq 0$ and $R_c \succcurlyeq 0$ are considered. The errors $\hat{\boldsymbol{q}}_{ae} = \boldsymbol{q}_{ae} - \bar{\boldsymbol{q}}_{ae}$ and $\hat{\boldsymbol{u}} = \boldsymbol{u} - \bar{\boldsymbol{u}}$ are defined with respect to a reference, equilibrium state $\bar{\boldsymbol{q}}_{ae}$ with control $\bar{\boldsymbol{u}}$ and disturbance $\bar{\boldsymbol{w}}$ (typically the trim solution, with $\bar{\boldsymbol{w}} = \boldsymbol{0}$). As seen in the set of constraints of (4.1), the optimal control problem is subject to initial conditions (4.1b), with $\boldsymbol{q}_{ae}^c$ defining the sample of the (internal) system state at the beginning of the MPC horizon. This initial condition might be retrieved directly from the controlled system, assuming full (low-order) state feedback. However, this is typically not the case in practice, since measurements and sensors are usually limited. As described later in § 4.2, this limitation can be overcome by posing a further optimal problem whose solution will produce an estimate of the current state of the system. The optimal control problem is subjected to nonlinear, discrete-time evolution equation (4.1c), where $\boldsymbol{f}$ is obtained by time integration of the continuous-time system (3.79) along each MPC sub-interval of length $\frac{\tau_c}{N_c}$. Box constraints on the control input (4.1d) and possibly on some of the states (4.1e) are also considered. Terminal state constraints might also be imposed (4.1f), to ensure stability and convergence of the closed-loop MPC dynamics [123].

Two important challenges arise from the application of NMPC to nonlinear systems describing very flexible structures, such as (3.79). On the one hand, the smallest system that typically results from describing the motion of a very flexible structure in three dimensions is of the order of $\mathcal{O}(50)$. To avoid solving nonlinear programs (NLPs) of impractical size, due to the fact that the numerical integration time step of (3.79) may be required

to be very small, since it is linked to the highest frequency of the retained modes and of the linear aerodynamics, the discrete-time system (4.1c) is constructed using several (typically ranging from tens to hundreds) time steps of a chosen integration scheme (we consider 4th order Runge-Kutta, RK4, and mixed implicit-explicit integration schemes) to maintain the number of MPC sub-intervals to computationally tractable $N \sim \mathcal{O}(10)$. This is in contrast to typical MPC setups on simpler systems, where one (or very few) time steps of a chosen time-integrator [151] are employed to construct (4.1c).

The second challenge concerns the addition of rotations as states of our system, which are required to evaluate orientation-dependent forcing terms such as gravity. This introduces a set of linearly unstabilisable states, creating a control challenge and necessitates alternative NMPC stability results to standard approaches [123] if one seeks to establish theoretical convergence and stability guarantees. These conventional results on MPC [123] rely on appropriate construction of state and control stage costs (defined by positive definite matrices $Q_c \succ 0$ and $R_c \succ 0$) and state terminal cost ($P_c \succ 0$), which define the optimisation cost function (4.1a) used to prove stability using Lyapunov-based arguments. Determination of a set (defined by a in (4.1f)) into which the state needs to be driven by the controller at the end of the MPC horizon is often required, which ensures that once the state reaches this terminal region (where the nonlinear terms are no longer dominant) a stabilising linear controller can be found which would eventually stabilise the system. Therefore, stabilisability of the underlying linearised system is a key requirement, which our low-order system (3.79) does not satisfy.

In particular, linearisation of (3.79) around an equilibrium point, where $\boldsymbol{q}_1 = \mathbf{0}$, transforms the linearised equation for the quaternion approximation (3.41) into pure integration of the angular velocities, expressed by means of $\boldsymbol{q}_1$, causing rank deficiency of the linearised state matrix.

Since this is a recurrent problem encountered every time rotations are included as part of the state-space of the internal control model, we formulate a specific NMPC design strategy with associated convergence results in the following section. We will start by introducing the theoretical control system that one expects to obtain from the proposed modal-based reduced-order model (3.79), when it includes any approximation to the quaternions, and we show it possesses a linear subsystem with a particular structure (4.3)–(4.4). Then, the rest of the section is devoted to present a suitable NMPC framework that leverages the particular form of our system with which theoretical convergence and stability guarantees can be established. To improve readability, the proofs of the theoretical statements that follow throughout the discussion are given in Appendix A.

NMPC Convergence for Partially Unstabilisable Systems Arising from Geometrically Nonlinear Beam Dynamics

We start by rewriting the discrete-time dynamics of the MPC formulation (4.1c), which is constructed by time-integrating the continuous-time internal model (3.79) over each MPC sub-interval, in terms of the error $\hat{\boldsymbol{q}}_{ae}$ around the reference $\bar{\boldsymbol{q}}_{ae}$. This reads

$$\hat{\boldsymbol{q}}_{ae}^{k+1} = \boldsymbol{\mathcal{F}}(\hat{\boldsymbol{q}}_{ae}^{k}, \hat{\boldsymbol{u}}^{k}) = \mathcal{A}\hat{\boldsymbol{q}}_{ae}^{k} + \mathcal{B}\hat{\boldsymbol{u}}^{k} + \hat{\boldsymbol{\mathcal{F}}}(\ \hat{\boldsymbol{q}}_{ae}^{k}, \hat{\boldsymbol{u}}^{k}). \tag{4.2}$$

The linear matrices $(\mathcal{A}, \mathcal{B})$ can be obtained by time-integration of the sensitivity equations, as defined later in § 4.3.3 by Eqs. (4.17)–(4.18). The functional $\hat{\boldsymbol{\mathcal{F}}}$ defines the higher-order terms that would be obtained by subtracting from (4.1c) the linear contribution $(\mathcal{A}, \mathcal{B})$. Standard MPC results [123] require the pair $(\mathcal{A}, \mathcal{B})$ to be stabilisable.

Consequently, we perform two state transformations to reveal the underlying stabilisable properties of our particular linear subsystem $(\mathcal{A}, \mathcal{B})$. The first transformation (T_1) is a staircase decomposition, which splits the state vector $\hat{\boldsymbol{q}}_{ae}$ into controllable and uncontrollable modes. A subsequent Schur decomposition (T_2), allows us to identify stable modes amongst the ones revealed to be uncontrollable, due for instance to structural damping. After these two consecutive transformations, Eq. (4.2) is rewritten in terms of the new state vector $\boldsymbol{x} = T_2 T_1 \hat{\boldsymbol{q}}_{ae}$

$$\boldsymbol{x}^{k+1} = \boldsymbol{f}(\boldsymbol{x}^{k}, \boldsymbol{u}^{k}) = A\boldsymbol{x}^{k} + B\boldsymbol{u}^{k} + \hat{\boldsymbol{f}}(\boldsymbol{x}^{k}, \boldsymbol{u}^{k}), \tag{4.3}$$

where $\boldsymbol{x}^k \in \mathbb{R}^n$ and $\boldsymbol{u}^k \in \mathbb{R}^m$, and the hat superscript in the state and input variables is dropped to alleviate notation. The linear part of this new system is governed by matrices $T_1^\top T_2^\top \mathcal{A} T_2 T_1 = A \in \mathbb{R}^{n\times n}$ and $T_1^\top T_2^\top \mathcal{B} = B \in \mathbb{R}^{n\times m}$ and the function $\hat{\boldsymbol{f}} : \mathbb{R}^n \times \mathbb{R}^m \to \mathbb{R}^n$ defines the quadratic and higher-order terms of the nonlinear dynamics. Therefore, the particular structure of system (4.3) is revealed, which has the form

$$A = \begin{pmatrix} A_w & A_d \\ 0 & I_{n_2} \end{pmatrix}, \quad B = \begin{pmatrix} B_w \\ 0 \end{pmatrix}, \tag{4.4}$$

corresponding to a decomposition of state $\boldsymbol{x} = \begin{pmatrix} \boldsymbol{w}^\top & \boldsymbol{d}^\top \end{pmatrix}^\top$ into stabilisable $\boldsymbol{w}$ and unstabilisable $\boldsymbol{d}$ modes. In particular $A_w \in \mathbb{R}^{n_1\times n_1}$ and $B_w \in \mathbb{R}^{n_1\times m}$ form a stabilisable pair and $\boldsymbol{w} \in \mathbb{R}^{n_1}$, while $A_d \in \mathbb{R}^{n_1\times n_2}$ and $\boldsymbol{d} \in \mathbb{R}^{n_2}$. As stated before, a system with the form (4.3)–(4.4) defines a general theoretical form of a control system that arises after applying a staircase and a Schur decomposition to the linearised discrete-time sys-

tem (4.1c), where the unstabilisable modes $\boldsymbol{d}$ appear due to (have components in) the quaternion states $\boldsymbol{q}_\xi$.

To implement a model predictive control algorithm to exploit the particular structure of (4.3), let $P_w \in \mathcal{S}^{n_1}_{++}, P_d \in \mathcal{S}^{n_2}_{++}, R \in \mathcal{S}^m_{++}$ and $\beta > 0$. We replace the cost function in (4.1a) (with stage costs defined by matrices Q_c and R_c and terminal cost by P_c) using new stage $\ell : \mathbb{R}^n \times \mathbb{R}^m \to \mathbb{R}_+$ and terminal $V_f : \mathbb{R}^n \to \mathbb{R}_+$ costs, defined by

$$\ell(\boldsymbol{x}, \boldsymbol{u}) := \frac{\beta}{4}\|\boldsymbol{w}\|^2_{P_w} + \|\boldsymbol{u}\|^2_R, \quad V_f(\boldsymbol{x}) := \|\boldsymbol{w}\|^2_{P_w}, \quad x = \left(\begin{smallmatrix}\boldsymbol{w}\\ \boldsymbol{d}\end{smallmatrix}\right). \tag{4.5}$$

The new MPC cost function that we employ can now be defined.

Definition 1. *Let $N \in \mathbb{N}$ and $U \subseteq \mathbb{R}^m$ be the set of admissible control inputs. Then the MPC cost function $V_N : \mathbb{R}^n \times U^N \to \mathbb{R}$ is given by*

$$V_N(\boldsymbol{x}, \boldsymbol{u}) := \sum_{k=0}^{N-1} \ell(\boldsymbol{x}^k, \boldsymbol{u}^k) + V_f(\boldsymbol{x}^N),$$

where $\boldsymbol{x}^0 = \boldsymbol{x}$ and $\boldsymbol{x}^k = \boldsymbol{\phi}(k; \boldsymbol{x}, \boldsymbol{u})$. Here, $\boldsymbol{\phi}(k; \boldsymbol{x}, \boldsymbol{u})$ denotes the state of the system after k steps under the dynamics $\boldsymbol{x}^{k+1} = \boldsymbol{f}(\boldsymbol{x}^k, \boldsymbol{u}^k)$ (Eq.(4.3)).

We will optimise the MPC cost function over input sequences that drive the state, in N steps, to compact subsets of the form

$$\chi(\omega, \delta) := \left\{\boldsymbol{x} = \left(\begin{smallmatrix}\boldsymbol{w}\\ \boldsymbol{d}\end{smallmatrix}\right) \in \mathbb{R}^n : \|\boldsymbol{w}\|^2_{P_w} \le \omega,\ \|\boldsymbol{d}\|^2_{P_d} \le \delta\right\},$$

where $\omega, \delta > 0$ will be chosen later. These subsets give an idea of the relative sizes of the controllable and unstabilisable modes of our system. Hence, small values of δ are desirable since they imply that the effect of unstabilisable modes in the performance of the controller is kept at a minimum.

To this end, denoting $\boldsymbol{\phi}_{N,\boldsymbol{x}}(\boldsymbol{u}) = \phi(N; \boldsymbol{x}, \boldsymbol{u}) : U^N \to \mathbb{R}^n$, we define for each $\boldsymbol{x} \in \mathbb{R}^n$ the set (possibly empty) of control sequences that can drive the system to $\chi(\omega, \delta)$ by

$$\mathcal{U}_{N,\omega,\delta}(\boldsymbol{x}) = \phi^{-1}_{N,\boldsymbol{x}}(\chi(\omega, \delta)), \qquad \boldsymbol{x} \in \mathbb{R}^n,$$

and the set of states that can reach $\chi(\omega, \delta)$ in N steps by $X_{N,\omega,\delta} = \{\boldsymbol{x} \in \mathbb{R}^n : \mathcal{U}_{N,\omega,\delta}(\boldsymbol{x}) \neq \emptyset\}$.

The following technical assumptions are required.

Assumption 2. *For any $N \in \mathbb{N}$, there exists $\omega_0, \delta_0 > 0$ such that:*

(i) (Invariance) For any $0 < \omega < \omega_0$ and $0 < \delta < \delta_0$, the sets $\chi(\omega, \delta)$ are control invariant.

(ii) (Regularity) For any $\epsilon > 0$, there exists $\eta > 0$ such that for any $\omega < \omega_0, \delta < \delta_0$ and $\boldsymbol{x} \in X_{N,\omega,\delta}$,

$$d_H\left(\mathcal{U}_{N,\omega,\delta}(\boldsymbol{x}), \mathcal{U}_{N,\omega,\delta+\eta}(\boldsymbol{x})\right) \leq \epsilon.$$

Here, $d_H(\cdot,\cdot)$ is the Hausdorff distance between compact subsets.

Condition (i) states that for any $\boldsymbol{x} \in \chi(\omega,\delta)$, there exists $\boldsymbol{u} \in U$ such that $\boldsymbol{f}(\boldsymbol{x},\boldsymbol{u}) \in \chi(\omega,\delta)$. Consequently, $\mathcal{U}_{N,\omega,\delta}(\boldsymbol{x}) \neq \emptyset$ for any $\boldsymbol{x} \in \chi(\omega,\delta)$ with $\omega < \omega_0, \delta < \delta_0$ and $X_{N,\omega,\delta} \neq \emptyset$. Hence, there exist initial states from which $\chi(\omega,\delta)$ can be reached in N steps. Condition (ii) is a mild regularity condition stating that a small relaxation in the terminal constraint corresponds to a small increase in the set of admissible control inputs.

Finally, we define the optimal cost functions

$$V^*_{N,\omega,\delta}(\boldsymbol{x}) := \min_{\boldsymbol{u} \in \mathcal{U}_{N,\omega,\delta}(\boldsymbol{x})} V_N(\boldsymbol{x},\boldsymbol{u}), \qquad \boldsymbol{x} \in X_{N,\omega,\delta},$$

and denote the first value of an optimising input trajectory $\boldsymbol{\kappa}_{N,\omega,\delta}(\boldsymbol{x})$, meaning that the closed-loop MPC system evolves according to $\boldsymbol{x}^+ = \boldsymbol{f}(\boldsymbol{x}, \boldsymbol{\kappa}_{N,\omega,\delta}(\boldsymbol{x}))$.

Design of Weighting Matrices

Design of the stage cost ℓ, terminal cost V_f, and terminal constraint set $\chi(\omega,\delta)$ relies on appropriate construction, namely conditions (4.6), (4.7), of the matrices P_w, P_d and R. The following Lemma implies that appropriate choices always exist and can be constructed by solving linear matrix inequalities (LMIs).

Lemma 3. *Let A_w, A_d and B_w be the system matrices from (4.4). Then there exist $P_w \in \mathcal{S}^{n_1}_{++}, P_d \in \mathcal{S}^{n_2}_{++}, R \in \mathcal{S}^m_{++}$, a constant $0 < \beta < 1$ and control gain matrices $K_w \in \mathbb{R}^{m \times n_1}, K_d \in \mathbb{R}^{m \times n_2}$ such that*

$$X = \begin{pmatrix} \begin{pmatrix} (1-\beta)P_w^{-1} & 0 \\ 0 & P_d^{-1} \end{pmatrix} & \begin{pmatrix} P_w^{-1}(A_w + B_w K_w)^\top & 0 \\ P_d^{-1}(A_d + B_w K_d)^\top & 0 \end{pmatrix} \\ (*) & \begin{pmatrix} P_w^{-1} & 0 \\ 0 & P_d^{-1} \end{pmatrix} \end{pmatrix} \succeq 0, \tag{4.6}$$

and

$$Y = \begin{pmatrix} \begin{pmatrix} \frac{\beta}{4}P_w^{-1} & 0 \\ 0 & \frac{1}{2}P_d^{-1} \end{pmatrix} & \begin{pmatrix} P_w^{-1}K_w^\top \\ P_d^{-1}K_d^\top \end{pmatrix} \\ (*) & R^{-1} \end{pmatrix} \succeq 0. \tag{4.7}$$

Proof. See Appendix A. □

Note that (4.6) and (4.7) can be imposed as LMI conditions for fixed $0 < \beta < 1$. The importance of these conditions is that they guarantee existence of a linear controller, namely $\boldsymbol{u} = K_w\boldsymbol{w} + K_d\boldsymbol{d}$, under which the terminal cost $V_f(\boldsymbol{x}) = \|\boldsymbol{w}\|_{P_w}^2$ can be appropriately controlled. This is now explained by introducing several intermediate lemmas.

First, bounds on the size of controllable modes $\boldsymbol{w}$ and the stage cost associated to one step of the linear (system (4.3) with $\hat{\boldsymbol{f}} = \boldsymbol{0}$) closed-loop dynamics under control $\boldsymbol{u} = K_w\boldsymbol{w} + K_d\boldsymbol{d}$ can be established, for matrices obtained from Lemma 3.

Lemma 4. *Suppose that* (4.6) *and* (4.7) *hold. Let* $\hat{A}_w$ *and* $\hat{A}_d$ *be as above and let* $K = \begin{pmatrix} K_w & K_d \end{pmatrix}$. *Then for any* $\boldsymbol{x} = \left(\begin{smallmatrix} \boldsymbol{w} \\ \boldsymbol{d} \end{smallmatrix}\right) \in \mathbb{R}^n$

$$\|\hat{A}_w\boldsymbol{w} + \hat{A}_d\boldsymbol{d}\|_{P_w}^2 - \|\boldsymbol{w}\|_{P_w}^2 \leq -\beta\|\boldsymbol{w}\|_{P_w}^2 + \|\boldsymbol{d}\|_{P_d}^2. \tag{4.8}$$

and

$$\ell(\boldsymbol{x}, K\boldsymbol{x}) \leq \frac{\beta}{2}\|\boldsymbol{w}\|_{P_w}^2 + \frac{1}{2}\|\boldsymbol{d}\|_{P_d}^2. \tag{4.9}$$

Proof. Follows from a Schur complement argument. □

Using these bounds, we show that, now, one step of the full nonlinear dynamics (system (4.3)) with linear control $\boldsymbol{u} = K_w\boldsymbol{w} + K_d\boldsymbol{d}$ and for states within the subset $\chi(\omega, \delta)$, produces a decay of the controllable modes $\boldsymbol{w}$ and a maximum possible growth of the unstabilisable modes $\boldsymbol{d}$ that can be quantified.

Lemma 5. *Suppose* (4.6) *and* (4.7) *hold. Let* $\eta > 0$. *There exists* $\omega > 0$ *such that for any* $0 < \delta < \frac{\omega\beta}{3}$ *the following is true: for any* $\boldsymbol{x} \in \chi(\omega, \delta)$, *if* $\boldsymbol{x}^+ = (A+BK)\boldsymbol{x} + \hat{\boldsymbol{f}}(\boldsymbol{x}, K\boldsymbol{x})$ *is one step of the nonlinear dynamics* (4.3) *under the linear control* $\boldsymbol{u} = K\boldsymbol{x}$, *with* K *as above, then*

$$V_f(\boldsymbol{x}^+) - V_f(\boldsymbol{x}) + \ell(\boldsymbol{x}, K\boldsymbol{x}) \leq 2\|\boldsymbol{d}\|_{P_d}^2 \tag{4.10}$$

and $\boldsymbol{x}^+ \in \chi(\omega, \delta + \eta)$.

Proof. See Appendix A. □

Finally, Lemma 6 shows that one step of the closed-loop MPC scheme is able to decrease the cost function in Definition 1.

Lemma 6. *Suppose that Assumption 2 holds and* (4.6), (4.7) *are satisfied. For any* $\epsilon > 0$*, there exist* $0 < \omega < \omega_0$ *and* $0 < \delta < \delta_0$ *such that for any* $\boldsymbol{x} \in X_{N,\omega,\delta}$*, we have* $\boldsymbol{x}^+ = f(\boldsymbol{x}, \boldsymbol{\kappa}_{N,\omega,\delta}(\boldsymbol{x})) \in X_{N,\omega,\delta}$ *and*

$$V^*_{N,\omega,\delta}(\boldsymbol{x}^+) \leq V^*_{N,\omega,\delta}(\boldsymbol{x}) - \frac{\beta}{4}\|\boldsymbol{w}\|^2_{P_w} + 2\delta + \epsilon.$$

Proof. See Appendix A. □

Application to MPC Algorithm

We are now in position to present the main result, which shows that the MPC trajectory converges to a known compact subset of state space.

Theorem 7. *Suppose that Assumption 2 holds and* (4.6), (4.7) *are satisfied. Let* $(\boldsymbol{x}^k)_{k\geq 0}$ *denote the closed-loop MPC trajectory* $\boldsymbol{x}^{k+1} = f(\boldsymbol{x}^k, \boldsymbol{\kappa}_{N,\omega,\delta}(\boldsymbol{x}))$ *and let* $\epsilon > 0$*. Then there exists* $\omega > 0, \delta > 0$ *such that whenever* $\boldsymbol{x}^0 \in X_{N,\omega,\delta}$*, it follows that*

$$\boldsymbol{x}^{k_0} \in \chi(\omega^*, \delta),$$

for some $k_0 \in \mathbb{N}$*, where* $\omega^* := 4\beta^{-1}(2\delta + \epsilon)$*. Furthermore, if* $\omega^* \leq \omega$*,*

$$\limsup_{k\to\infty} \|\boldsymbol{w}^k\|^2_{P_w} \leq \frac{4}{\beta}(2\delta + \epsilon) + \frac{4}{\beta}\max\left\{V^*_{N,\omega,\delta}(\boldsymbol{x}) : \boldsymbol{x} \in \chi(\omega^*, \delta)\right\}$$

Proof. See Appendix A. □

The practical implication of Theorem 7 is that the LMI conditions (4.6), (4.7) can be used to impose as large as possible value of β, in order to improve the final bound. That is, in practice, it is desirable that the corresponding value of δ is very small (compared to β), while maintaining feasibility of the nonlinear optimal control problem for a relatively large value of ω. This corresponds to widening the set of states from which the NMPC scheme will converge asymptotically. We note finally, that the bound on the eventual state tends to zero as $\epsilon, \delta \to 0$. That is, if a control exists which can drive the linearly uncontrollable states close to the origin, then the controllable states can also be made arbitrarily small.

4.2 Moving Horizon Estimation

As seen in the MPC problem statement, the initial condition of the optimal control problem (4.1) is a sample of the actual system state. However, this sample $\boldsymbol{q}_{ae}^{c}$ can be obtained by solving the dual nonlinear problem of MPC, relying on the, available and usually limited, measurements of the controlled system: a nonlinear moving horizon estimation (NMHE) problem, cast in a similar form to (4.1):

$$\min_{\boldsymbol{q}_{ae}^{e},\boldsymbol{w}^{k}} \quad \frac{1}{2}\hat{\boldsymbol{q}}_{ae}^{e\top} P_e \hat{\boldsymbol{q}}_{ae}^{e} + \frac{1}{2}\hat{\boldsymbol{w}}^{-N_e\top} R_e \hat{\boldsymbol{w}}^{-N_e} + \sum_{k=-N_e}^{0} \frac{1}{2}\hat{\boldsymbol{y}}_{ae}^{k\top} Q_e \hat{\boldsymbol{y}}_{ae}^{k} \tag{4.11a}$$

$$\text{s.t.} \quad \boldsymbol{q}_{ae}^{-N_e} = \boldsymbol{q}_{ae}^{e}, \tag{4.11b}$$

$$\boldsymbol{q}_{ae}^{k+1} = \boldsymbol{f}(\boldsymbol{q}_{ae}^{k}, \boldsymbol{u}^{k}, \boldsymbol{w}^{k}), \qquad k = -N_e, \cdots, -1, \tag{4.11c}$$

$$\boldsymbol{w}_l \leq \boldsymbol{w}^{k} \leq \boldsymbol{w}_u, \qquad k = -N_e, \cdots, -1, \tag{4.11d}$$

$$\boldsymbol{q}_{ae,l} \leq \boldsymbol{q}_{ae}^{k} \leq \boldsymbol{q}_{ae,u}, \qquad k = -N_e + 1, \cdots, 0. \tag{4.11e}$$

Here, the unknown parameters found upon solution of the above nonlinear problem are the external disturbance $\boldsymbol{w}^{k}$ together with the initial state of the system $\boldsymbol{q}_{ae}^{e}$ at the beginning of the estimation horizon τ_e (i.e., the initial condition). The functional $\boldsymbol{f}$ in (4.11c) is the same system as in (4.1), and terminal constraints on some of the states might be also considered (e.g., control surface deflections, part of the state space, are known at the sampling time). Now, the functional subject to minimisation aims to penalise the error $\hat{\boldsymbol{y}}_{\boldsymbol{ae}} = \boldsymbol{y} - \boldsymbol{y}_{\boldsymbol{e}}$ between a measured output $\boldsymbol{y}$ from the actual system and the estimated output produced by the internal model, which is chosen to be a linear function of the vector state, $\boldsymbol{y}_{\boldsymbol{e}} = \mathcal{L}(\boldsymbol{q}_{ae})$. Similarly, a quadratic cost function is built with a weighting matrix $Q_e \succcurlyeq 0$. The cost function is also enhanced by the two first terms in (4.11a), where the errors $\hat{\boldsymbol{q}}_{ae}^{e} = \boldsymbol{q}_{ae}^{e} - \boldsymbol{q}_{ae,r}^{e}$ and $\hat{\boldsymbol{w}}^{-N_e} = \boldsymbol{w}^{-N_e} - \boldsymbol{w}_r$ are penalised, with $P_e \succcurlyeq 0$ and $R_e \succcurlyeq 0$. The quantities $\boldsymbol{q}_{ae,r}$ and $\boldsymbol{w}_r$ are reference state and disturbance which are initialised with the reference values $\bar{\boldsymbol{q}}_{ae}$ and $\bar{\boldsymbol{w}}$ but are updated at every sampling point by the state and disturbances at the start of the second sub-interval of the previous MHE solution. This is done to improve initial convergence of the estimation problem, since it provides extra information of the reference configuration around which the estimation begins, and also of the subsequent ones, since the information of the previous estimations can be exploited.

Once the NLP (4.11) is solved, the final state of the estimation window, $\boldsymbol{q}_{ae}$ at $k = 0$, corresponds to the estimated initial condition $\boldsymbol{q}_{ae}^{c}$ of the MPC problem (4.11). Both

control inputs $\boldsymbol{u}$ and external disturbances $\boldsymbol{w}$ are considered to be constant along each of the sub-intervals within the MHE/MPC problem definitions. It is also assumed that the estimator has knowledge of all the past control inputs history while several assumptions can be taken regarding how to extrapolate the disturbance into the control predictive horizon. These will be discussed in each of the application examples.

4.3 Optimal Problem Solution

The nonlinear problems arising from the estimation and control strategies are very similar and can be solved in almost identical procedures. Written as in (4.1) and (4.11), the nonlinear optimal problems are already parametrised following a multiple shooting approach [23], dividing the prediction/estimation horizons according to the splittings dictated by the MHE and MPC interval setups. In the following, the control problem is taken as the example for which the implementation details are described. However, they are analogous to the estimation problem counterpart.

4.3.1 Sequential Quadratic Programming

The solution to the problem (4.1) is sought iteratively using a Sequential Quadratic Programming (SQP) [110, ch. 18] strategy, where the steps $\Delta\boldsymbol{p}$ in the iteration $\boldsymbol{p}_{i+1} = \boldsymbol{p}_i + \Delta\boldsymbol{p}$ are obtained solving the following quadratic program:

$$\min_{\Delta\boldsymbol{p}} \quad \Delta\boldsymbol{p}^\top \boldsymbol{g}_i + \frac{1}{2}\Delta\boldsymbol{p}^\top H_i \Delta\boldsymbol{p} \tag{4.12a}$$

$$\text{s.t.} \quad \left(\boldsymbol{q}_{ae}^0\right)_i + \Delta\boldsymbol{q}_{ae}^0 = \boldsymbol{q}_{ae}^c, \tag{4.12b}$$

$$\begin{aligned}\left(\boldsymbol{q}_{ae}^{k+1}\right)_i + \Delta\boldsymbol{q}_{ae}^{k+1} &= \boldsymbol{f}(\boldsymbol{q}_{ae}^k, \boldsymbol{u}^k, \boldsymbol{w}^k)_i \\ &\quad + \frac{d\boldsymbol{f}(\boldsymbol{q}_{ae}^k, \boldsymbol{u}^k, \boldsymbol{w}^k)}{d\boldsymbol{p}^k}\Delta\boldsymbol{p}, \qquad k = 0, \cdots, N_c - 1,\end{aligned} \tag{4.12c}$$

$$\boldsymbol{u}_l \leq (\boldsymbol{u}^k)_i + \Delta\boldsymbol{u}^k \leq \boldsymbol{u}_u, \qquad k = 0, \cdots, N_c - 1, \tag{4.12d}$$

$$\boldsymbol{q}_{ae,l} \leq \left(\boldsymbol{q}_{ae}^k\right)_i + \Delta\boldsymbol{q}_{ae}^k \leq \boldsymbol{q}_{ae,u}, \qquad k = 1, \cdots, N_c, \tag{4.12e}$$

$$\left| \left(\frac{1}{2}\hat{\boldsymbol{q}}_{ae}^{N\top} P \hat{\boldsymbol{q}}_{ae}^N \right)_i + \left(\hat{\boldsymbol{q}}_{ae}^N\right)_i^\top P \Delta\boldsymbol{q}_{ae}^N \right| \leq a, \tag{4.12f}$$

where $\boldsymbol{p} = \left(\ldots, \boldsymbol{q}_{ae}^{k\top}, \ldots, \boldsymbol{u}^{k\top}, \ldots\right)^\top$ is the set of all optimisation parameters (namely state initial conditions and control inputs of each MPC sub-interval) and the subscript

i denotes the current optimisation iteration. This quadratic program is constructed using the gradient $\boldsymbol{g}_i$ and the Hessian, H_i, of the Laplacian of the constrained minimisation problem, $\mathcal{L} = \mathcal{F} + \boldsymbol{\lambda}^\top \boldsymbol{\mathcal{C}}$, where $\mathcal{F}$ is the cost function (4.1a) and $\boldsymbol{\mathcal{C}}(\boldsymbol{q}_{ae}^k, \boldsymbol{u}^k) \leq 0$ is the set of constraints (4.1b)-(4.1f), with $\boldsymbol{\lambda}$ its corresponding multipliers. Note that linearisation of a positive quadratic constraint such as (4.1f) requires the use of absolute value in (4.12f) for consistency. Also, linearisation of (4.1c) might lead to discontinuous, unfeasible intermediate iterates. The Hessian is approximated by the Broyden–Fletcher–Goldfarb–Shanno update formula [110, ch. 6].

The use of multiple shooting allows speed up of the implementation, since the computational bottleneck of the methodology (time-integration of (4.1c) and the evaluation of its sensitivities to construct its linearised version (4.12c) as required by the SQP approach) can be parallelised. Furthermore, multiple shooting has been shown to improve convergence of NLPs [23].

In the following sections we show how the time integration of the system and its sensitivity equations is performed and the associated computational cost is analysed. As will be shown, integration of the analytically derived sensitivity equations from the continuous-time system (3.79), required to construct the linearisations in (4.12c), offers a computational advantage over black-box solutions based on automatic differentiation.

4.3.2 Internal Model Time Integration

As already mentioned, the discrete-time dynamics denoted by $\boldsymbol{f}$ in (4.1c) are obtained by steps of a chosen numerical time-integration scheme. When the problem is purely structural, the chosen time-integration is a convenient explicit RK4 integration scheme. However, an important particularity of an aeroelastic description such as (3.79) is that it can result in a system with a very stiff linear subsystem. In particular, the eigenvalues of the linear part are dominated by the structural eigenvalues, $\mathrm{diag}(\Omega)$, and the aerodynamic eigenvalues $\sigma(A_q)$. For many application examples this leads to a large gap between structural and aerodynamic eigenvalues. The latter become excessively large and make the use of efficient explicit integration schemes, such as RK4, impractical: explicit integration schemes require a time step which is tied to the inverse of the maximum eigenvalue of the linear subsystem, assuming the nonlinear counterpart does not display stiff behaviour. This problem is observed to worsen as one strives to reduce the linear aerodynamic state-space model, where the absolute value of the eigenvalues of the resulting reduced order model can substantially increase.

To overcome the imposition of impractical small time steps for integration, we rewrite system (3.79) splitting the linear $L(\boldsymbol{q}_{ae})$ and nonlinear $N(\boldsymbol{q}_{ae}, \boldsymbol{u}, \boldsymbol{w})$ contributions, where the latter one also includes non-autonomous terms (control inputs, disturbances, etc.)

$$\dot{\boldsymbol{q}}_{ae} = L(\boldsymbol{q}_{ae}) + N(\boldsymbol{q}_{ae}, \boldsymbol{u}, \boldsymbol{w}), \tag{4.13}$$

with

$$L(\boldsymbol{q}_{ae}) = \begin{pmatrix} \Sigma + D_{q1} & \Omega - D_{q0}\Omega^{-1} & 0 & C_q \\ -\Omega & 0 & 0 & 0 \\ 0 & 0 & 0 & 0 \\ B_{q1} & -B_{q0}\Omega^{-1} & 0 & A_q \end{pmatrix} \boldsymbol{q}_{ae}, \tag{4.14}$$

$$N(\boldsymbol{q}_{ae}, \boldsymbol{u}, \boldsymbol{w}) = \begin{pmatrix} -q_{1l}\Gamma_1^l & -q_{2l}\Gamma_2^l & q_{\xi l}\Gamma_g^l & 0 \\ q_{2l}(\Gamma_2^l)^\top & 0 & 0 & 0 \\ q_{\xi l}\Gamma_\xi^l & 0 & 0 & 0 \\ 0 & 0 & 0 & 0 \end{pmatrix} \boldsymbol{q}_{ae} + \begin{pmatrix} D_{q\dot{\delta}} \\ 0 \\ 0 \\ B_{q\dot{\delta}} \end{pmatrix} \boldsymbol{u} + \begin{pmatrix} D_{qw} \\ 0 \\ 0 \\ B_{qw} \end{pmatrix} \boldsymbol{w} + \begin{pmatrix} \boldsymbol{\eta} \\ 0 \\ 0 \\ 0 \end{pmatrix}, \tag{4.15}$$

where the modal displacements have been chosen to be computed from the force/moment modal coefficients (3.78), the modal external forcing $\boldsymbol{\eta}$ includes the possible nonzero aerodynamic forcing at the UVLM linearisation point $\bar{\boldsymbol{\eta}}_a$ and other external forces such as thrust, and the aerodynamic input matrices have been split into the distinct contributions of modal displacements ($\boldsymbol{q}_0$), velocities ($\boldsymbol{q}_1$), control surface deflections and deflection rates ($\boldsymbol{\delta}$, $\dot{\boldsymbol{\delta}}$) and external disturbance velocities $\boldsymbol{w}$ such that $B_q = \big(B_{q0}, B_{q1}, B_{q\delta}, B_{q\dot{\delta}}, B_{qw}\big)$ and $D_q = \big(D_{q0}, D_{q1}, D_{q\delta}, D_{q\dot{\delta}}, D_{qw}\big)$. Note that the control surface deflections have been excluded from the set of control inputs, since these are pure integration of the rates. Hence, if no actuator model is considered, the deflection rates are chosen as inputs and the system (3.79) can still be described generally with state $\boldsymbol{q}_{ae}$ and inputs $\boldsymbol{u}$ if, for instance, control surface deflections are included as part of the aerodynamic states $\boldsymbol{q}_\Gamma$ and the A_q and C_q matrices are augmented with the corresponding input matrices $B_{q\delta}$ and $D_{q\delta}$, respectively, and the relationship between deflection and deflection rates is accounted for in $B_{q\dot{\delta}}$

The nonlinear terms in (4.15) are generally not stiff, hence an IMEX (Implicit-Explicit) integration scheme, where the linear subsystem is integrated using an implicit method and the nonlinear using an explicit scheme, results a very suitable alternative. We employ a RK-based IMEX time-integration scheme consisting of a 2-stage DIRK (diagonally implicit Runge-Kutta) for the linear subsystem and a 3-stage ERK (Explicit Runge-Kutta) for the nonlinear one. Hence, one time step $t^{n+1} = t^n + \Delta t$ of the chosen multi-stage IMEX

integration consists of the following steps

$$\boldsymbol{k}_1^N = N(t^n, \boldsymbol{q}_{ae}^n)\Delta t, \tag{4.16a}$$
$$\boldsymbol{k}_1^L = L(t^n + \gamma\Delta t, \boldsymbol{q}_{ae}^n + \gamma\boldsymbol{k}_1^L + \gamma\boldsymbol{k}_1^N)\Delta t, \tag{4.16b}$$
$$\boldsymbol{k}_2^N = N(t^n + \gamma\Delta t, \boldsymbol{q}_{ae}^n + \gamma\boldsymbol{k}_1^L + \gamma\boldsymbol{k}_1^N)\Delta t, \tag{4.16c}$$
$$\boldsymbol{k}_2^L = L(t^n + \Delta t, \boldsymbol{q}_{ae}^n + (1-\gamma)\boldsymbol{k}_1^L + \gamma\boldsymbol{k}_2^L + \delta\boldsymbol{k}_1^N + (1-\delta)\boldsymbol{k}_2^N)\Delta t, \tag{4.16d}$$
$$\boldsymbol{k}_3^N = N(t^n + \Delta t, \boldsymbol{q}_{ae}^n + (1-\gamma)\boldsymbol{k}_1^L + \gamma\boldsymbol{k}_2^L + \delta\boldsymbol{k}_1^N + (1-\delta)\boldsymbol{k}_2^N)\Delta t, \tag{4.16e}$$
$$\boldsymbol{q}_{ae}^{n+1} = \boldsymbol{q}_{ae}^n + (1-\gamma)(\boldsymbol{k}_1^L + \boldsymbol{k}_2^N) + \gamma(\boldsymbol{k}_2^L + \boldsymbol{k}_3^N), \tag{4.16f}$$

where $\gamma = (2-\sqrt{2})/2$ and $\delta = -2\sqrt{2}/3$ give an overall second-order accurate scheme [17]. This integration method solves the impracticality of having to use very small time steps and does not add extra online computational effort, since the matrix inverse required to solve equations (4.16b) and (4.16d) can be performed upfront and stored in memory for a fixed time step.

4.3.3 Sensitivity Analysis

The chosen numerical integration scheme (i.e., either a RK4 or the proposed mixed integrator described in the previous section) is used not only to simulate (3.79) along each MHE/MPC interval, but also the system sensitivity equations, necessary for our particular implementation of the MHE and MPC strategies. The sensitivity equations are used to evaluate the first-order derivatives of the state $\boldsymbol{q}_{ae}$ with respect to initial conditions $\boldsymbol{q}_{ae,0}$ at a time $t = t_0$ and control inputs $\boldsymbol{u}$ (for the control problem) or external disturbances $\boldsymbol{w}$ (for the estimation problem). They can be derived analytically, and hence integrated along with the forward simulation of (3.79). We similarly use the control problem as an example in the following, however, the arguments are directly transferable to the estimation case. Hence, assuming constant input $\boldsymbol{u}$ throughout the integration window, the sensitivity equations read

$$\frac{d}{dt}\left(\frac{d\boldsymbol{q}_{ae}}{d\left(\boldsymbol{q}_{ae,0}, \boldsymbol{u}\right)}\right) = \frac{\partial \boldsymbol{h}}{\partial \boldsymbol{q}_{ae}}\left(\frac{d\boldsymbol{q}_{ae}}{d\left(\boldsymbol{q}_{ae,0}, \boldsymbol{u}\right)}\right) + \left(0,\ \frac{\partial \boldsymbol{h}}{\partial \boldsymbol{u}}\right), \tag{4.17}$$

with initial conditions

$$\left(\frac{d\boldsymbol{q}_{ae}}{d\left(\boldsymbol{q}_{ae,0}, \boldsymbol{u}\right)}\right)(t_0) = (I,\ 0)\,. \tag{4.18}$$

The functional $\boldsymbol{h}$ above is used to denote system (3.79) compactly, written in implicit form. Solving for (4.17)–(4.18) shows better scalability relative to the system size than

AD-based differentiation techniques, in which knowledge of the structure of the system of equations is not leveraged. Here, the Jacobian $\frac{\partial \boldsymbol{h}}{\partial \boldsymbol{q}_{ae}}$ is

$$\frac{\partial \boldsymbol{h}}{\partial \boldsymbol{q}_{ae}} = \begin{pmatrix} \Sigma - \frac{\partial}{\partial \boldsymbol{q}_1}\left(q_{1l}\Gamma^l_1 \boldsymbol{q}_1\right) + D_{q1} & \Omega - D_{q0}\Omega^{-1} - \frac{\partial}{\partial \boldsymbol{q}_2}\left(q_{2l}\Gamma^l_2 \boldsymbol{q}_2\right) & \frac{\partial}{\partial \boldsymbol{q}_\xi}\left(q_{\xi l}\Gamma^l_g \boldsymbol{q}_\xi\right) & C_q \\ -\Omega + \frac{\partial}{\partial \boldsymbol{q}_1}\left(q_{2l}\left(\Gamma^l_2\right)^\top \boldsymbol{q}_1\right) & \frac{\partial}{\partial \boldsymbol{q}_2}\left(q_{2l}\left(\Gamma^l_2\right)^\top \boldsymbol{q}_1\right) & 0 & 0 \\ \frac{\partial}{\partial \boldsymbol{q}_1}\left(q_{\xi l}\Gamma^l_\xi \boldsymbol{q}_1\right) & 0 & \frac{\partial}{\partial \boldsymbol{q}_\xi}\left(q_{\xi l}\Gamma^l_\xi \boldsymbol{q}_1\right) & 0 \\ B_{q1} & -B_{q0}\Omega^{-1} & 0 & A_q \end{pmatrix}. \tag{4.19}$$

The derivatives of the quadratic terms, $q_{al}\Gamma^l_{(\bullet)}\boldsymbol{q}_b$, present in the expression above are computed as follows. While the derivative with respect the second term is straightforward to compute

$$\frac{\partial}{\partial \boldsymbol{q}_b}\left(q_{al}\Gamma^l_{(\bullet)}\boldsymbol{q}_b\right) = q_{al}\Gamma^l_{(\bullet)}, \tag{4.20}$$

the derivative with respect the first term is the horizontal concatenation of the matrix-vector products

$$\frac{\partial}{\partial \boldsymbol{q}_a}\left(q_{al}\Gamma^l_{(\bullet)}\boldsymbol{q}_b\right) = \left(\Gamma^1_{(\bullet)}\boldsymbol{q}_b, \cdots, \Gamma^{N_m}_{(\bullet)}\boldsymbol{q}_b\right). \tag{4.21}$$

The term $\frac{\partial \boldsymbol{h}}{\partial \boldsymbol{u}}$ is typically direct to compute too (note that, for instance, control surface or thrust inputs are linear in (3.79)).

The associated cost of computing all the necessary derivatives to construct (4.12), which requires the evaluation of the derivatives of all final states with respect to initial states and control inputs, is roughly constant for the nonlinear equations (i.e., the sensitivity analysis cost remains proportional to the cost of one forward simulation, independently of the problem size). Observing the structure of (3.79), we identify that the computational bottleneck lays with the evaluation of the nonlinear terms defined by matrices $\Gamma^l_{(\bullet)}$. These computations have a complexity, based on the total number of product operations, of the order $\mathcal{O}(N_m^3)$, which predominate over the rest of matrix-vector multiplications which scale with $\mathcal{O}(N_m^2)$. We see that solving the sensitivity analysis (4.17)–(4.18) involves the matrix multiplication $\frac{\partial \boldsymbol{h}}{\partial \boldsymbol{q}_{ae}}\frac{d\boldsymbol{q}_{ae}}{d\left(\boldsymbol{q}_{ae,0},\boldsymbol{u}\right)}$ in (4.17), with a cost of the order $\mathcal{O}(N_m^3)$ (note that usually $\dim(\boldsymbol{u}^k) \ll N_m$). The evaluation of coefficients in (4.19) has also a complexity $\mathcal{O}(N_m^3)$. Therefore, we can conclude that the cost of solving the adjoint equations and computing the sensitivity analysis is proportional to solving one forward simulation, regardless of the dimension of the problem.

Most of the current available optimal control packages use automatic differentiation, which offers machine precision sensitivities, with forward-mode being very efficient in problems where $m > n$ and backward-mode more suitable for problems $n > m$ (for a function

$f : \mathbb{R}^n \to \mathbb{R}^m$, where n derivatives of m variables are needed). However, a sweep in either of the modes has a complexity proportional to solving f once [66]. In our particular case, due to the nonlinear terms present in (3.79), even the cost of the backward mode, where $\dim(\boldsymbol{q}_{ae})$ sweeps are necessary, would scale with $\mathcal{O}(N_m^4)$. This reveals the competitive advantage of analytical sensitivity/adjoint methods over AD based implementations for this kind of nonlinear system, as it is numerically investigated in § 5.2.3. Besides, the sensitivity equations can be derived analytically in a straightforward manner as it has been demonstrated.

Chapter 5

Numerical Examples I: Proofs of Concept

In this chapter we provide illustrative examples covering all the methodologies described so far. These are numerical examples on fundamental configurations presented as proofs of concept for the conceived framework, and are outlined next.

The first numerical application case, in § 5.1, is devoted to validate the novel extension of Kelvin-Voigt damping to the nonlinear intrinsic beam equations and to analyse its effect on the three-dimensional dynamics of very flexible structures.

The subsequent numerical examples focus on the application of the derived low-order aeroservoelastic models to control problems. In § 5.2, we start with a validation study of the presented control framework on an optimal control problem involving a very flexible swinging pendulum. Using our proposed control model, a dramatic reduction in the computational effort involved in the solution of nonlinear optimal control problems is observed, when compared to conventional models of very flexible structures. Favourable convergence rates of our modal-based nonlinear structural model and algorithmic implementations aimed at speeding up the solution of optimal problems (namely multiple shooting and analytical sensitivities) are two key aspects of our framework. These play a crucial role in the reduction of overall computational cost and hence are discussed using this numerical example with detail.

In § 5.3, the control framework is utilised to underpin the model predictive control strategy. This example showcases its application on a purely structural problem, where the proposed MPC setup that has been derived to prove theoretical stability and convergence properties

of the MPC scheme applied to our low-order geometrically-exact beam models, is put to the test.

5.1 Analysis of Damped Intrinsic Beam Equations

In this first numerical example we aim to validate the proposed generalisation of the Kelvin-Voigt damping model to the intrinsic nonlinear beams setting. To the best of our knowledge, studies of the dynamics of damped very flexible structures in three dimensions, modelled by means of geometrically-exact models, are absent from the literature. Hence, a study of a two-dimensional damped nonlinear (with von-Kármán nonlinear strain-displacement relationships) Euler-Bernoulli beam is chosen as means of validation test case. Subsequently, the three-dimensional response of a damped very flexible structure is analysed and is used to verify the theoretical findings on energy decay and new equilibrium solutions shown in § 2.1.3 and § 2.1.4.

5.1.1 Damping Model Verification

In order to validate the damping model and study its influence on the dynamics of very flexible structures a test case involving a two-dimensional (Kelvin-Voigt) damped nonlinear Euler-Bernoulli beam, investigated in [141], is chosen. Appendix B shows the relationship of the intrinsic beam equations with standard beam formulations, such as the Euler-Bernoulli model, providing the necessary insights for this validation test case. This will study the dynamic response of the beam under the excitation of a moving transverse harmonic point-force $P(t) = P_0 \sin(\omega t)$. The beam is set up as seen in Fig. 5.1, with one of the ends pinned and the other simply supported, free to move axially, where an axial compression load Q is applied. The pre-stressed state induced by the axial load triggers nonlinear phenomena which makes the setup a rich test case, in which the relevance of both nonlinear terms arising from elastic deformations and from viscoelastic behaviour is revealed.

A straight uniform beam with the properties gathered in Table 5.1 is considered in the reference paper [141]. There, the responses of a linear and nonlinear version of the beam are gathered for diverse excitation frequencies. Their damping is modelled as Kelvin-Voigt damping, however damping nonlinear terms are neglected ([141, eq. (8)]). Therefore, their results are comparable to our linearised damping terms model (2.22)–(2.24).

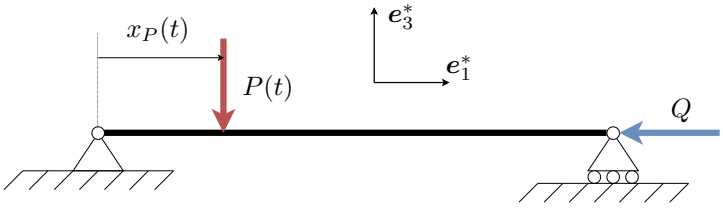


Figure 5.1: Setup of the beam subjected to pre-stress caused by an axial compressive force Q and excited with a moving harmonic force $P(t)$.

Table 5.1: Beam structural properties of the test case [141]

Length	L	30 m
Mass per unit length	μ	1500 kg/m
Cross sectional area	A	0.36 m^2
Cross sectional moment of inertia	I_2	0.0234 m^4
Young modulus	E	35 GPa
Buckling critical load	Q_{cr}	9, 330 kN
First bending mode frequency	ω_b	7.83 rad/s
Damping coefficient[1]	η	0.01, 0.001, 0.0001 s

Simulations corresponding to three different models are presented. The nomenclature employed is the following: (*i*) *L. Dyn. – L. Damp.* refers to a linearised version of the nonlinear intrinsic beam equations with (already) linearised damping (2.22)–(2.24) about the axial stressed initial configuration $\bar{f}_1 = -Q$, and a linearised displacement evolution equation (2.40). This set of results is then comparable to those labelled as *linear* in [141]. (*ii*) *NL. Dyn. – L. Damp.* refers to the model (2.22)–(2.24) itself, where geometrical nonlinear effects are retained but higher order terms arising from damping are neglected. Its results are comparable to those labelled as *nonlinear* in the reference paper, as long as von-Kármán's assumptions of large transverse displacements, moderate rotations and small strains hold. Finally, (*iii*) *NL. Dyn. – NL. Damp.* refers to the full nonlinear model (2.13)–(2.15). For this last model no comparison is available, however, as it will be shown, it is also considered to emphasise the relevant role of the nonlinear damping terms. Full expressions to retrieve displacements and rotations, (2.40) and (2.36) are used for the two *NL. Dyn.* models. Results shown in Fig. 5.2 correspond to the particular case [141, Fig. 9c] where an initial pre-stress compression due to an axial force of $Q = 0.1Q_{cr}$, where $Q_{cr} = \frac{\pi^2 E I_2}{L^2}$ is the Euler-Bernoulli buckling critical load, is applied. Three different

[1]Only results corresponding to the intermediate damping coefficient of $\mu = 0.001$ s are provided in [141]. However, higher and lower damping coefficients are considered here to get a deeper insight on the role of nonlinear damping terms.

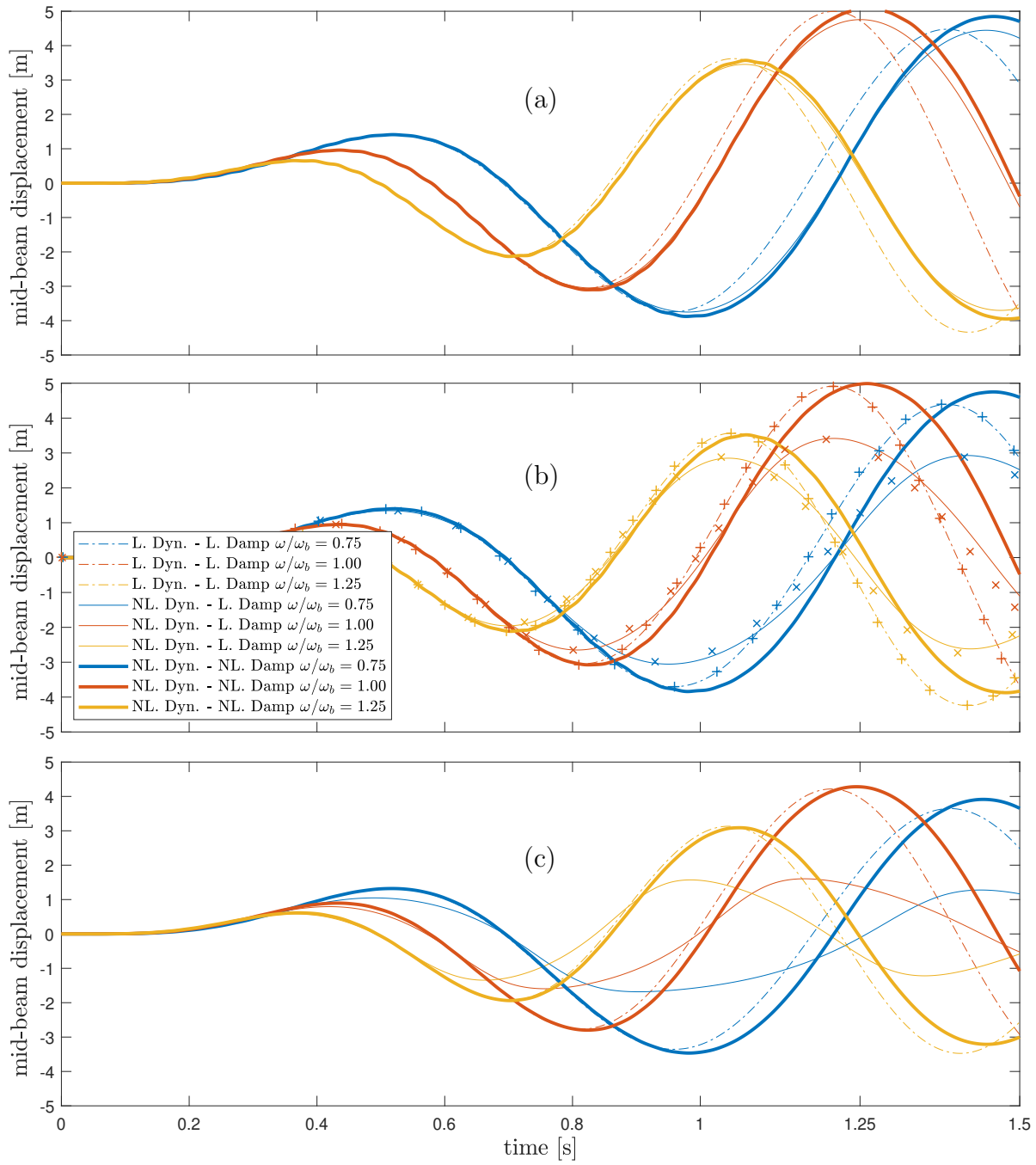


Figure 5.2: Mid-beam displacement for damping coefficients of (a) $\eta = 0.0001\,\mathrm{s}$, (b) $\eta = 0.001\,\mathrm{s}$ and (c) $\eta = 0.01\,\mathrm{s}$. Markers (+) and (×) in (b) refer to linear and nonlinear reference results of [141], respectively.

excitation frequencies for the harmonic load $P(t)$, corresponding to 0.75, 1.0 and 1.25 times the first bending mode frequency, ω_b, are considered and the amplitude of the harmonic force is $P_0 = 2,000\,\mathrm{kN}$. This applied external point-force moves with a constant velocity of $v = 20\,\mathrm{m/s}$, $x_P(t) = 20t$, and the mid-beam deflection, positive downwards, is the studied variable.

In order to simulate an Euler-Bernoulli beam within the intrinsic formulation as indicated by (B.1) the mass matrix is set to $M = \text{diag}(\mu,\, \cdot,\, \mu,\, \cdot,\, 10^{-5}\mu I_2/A,\, \cdot)$ while the compliance matrix $C^{-1} = \text{diag}(EA,\, \cdot,\, 10^5 EA,\, \cdot,\, EI_2,\, \cdot)$, where the dots $(\cdot)$ denote that the entries are irrelevant due to the uncoupled (2D) nature of the problem. The 10^5 factors in M and C are used to replicate Euler-Bernoulli hypotheses of negligible rotary inertia and infinite shear rigidity. To match the structural damping, the damping matrix is $C_\tau = \text{diag}(\eta,\, 0,\, 0,\, 0,\, \eta,\, 0)$, where equal damping coefficients are chosen for the axial and bending degrees of freedom. Results shown correspond to a finite element discretisation of the structural intrinsic equations using quadratic shape functions, with 40 elements, and an implicit mid-point rule integration scheme with a time step $\Delta t = 0.00015\,\text{s}$, for which results are deemed converged. Details on the finite element implementations of the damped intrinsic equations are given in appendix C.

Gathered in Fig. 5.2, are the mid-beam vertical displacements for three different damping coefficients. Only results for the intermediate damping value $\eta = 0.001\,\text{s}$ are given in the reference [141], and the comparison is shown in Fig. 5.2b. We observe an excellent agreement between the reference linear results (+ markers) and those obtained with our *L.Dyn. – L. Damp.* model, across the range of tested excitation frequencies. Regarding the nonlinear case, very satisfactory agreement is also achieved between our *NL.Dyn. – L. Damp.* model results and the reference ($\times$ markers), albeit a slight discrepancy can be noticed towards the end of the simulation. This suggests that von-Kármán's strain-displacement relationships do not deviate significantly from those given by the geometrically-exact theory for moderate displacements and the comparison remains appropriate. Results simulating the nonlinear terms arising from damping (neglected in the reference paper) are also included, *NL.Dyn. – NL. Damp.*. The notable discrepancy between them and those where the effect of damping is linearised but geometrically nonlinear effects are still retained, *NL.Dyn. – L. Damp.*, suggests that the role of damping nonlinear terms is, indeed, considerably relevant to the overall dynamics. This could be initially inferred from the difference between equilibrium solutions presented in § 2.1.3 and § 2.1.4 (respectively (2.20) and (2.34)), which suggests that linearised damping is more dissipative.

Two other scenarios have been simulated, where lower $\eta = 0.0001\,\text{s}$ (Fig. 5.2a) and higher $\eta = 0.01\,\text{s}$ (Fig. 5.2c) damping coefficient have been tested. The suggestion that linearised damping produces more dissipative results, already observed in Fig. 5.2b, is confirmed in Fig. 5.2c, where a higher damping coefficient leads to an increase in the difference between the responses of the *NL.Dyn. – NL. Damp.* and the *NL.Dyn. – L. Damp.* set of results. However, when the damping coefficient is decreased (Fig. 5.2a) we observe how both nonlinear responses start to coalesce, distinguishing themselves from the linear response,

characterised by its faster dynamics.

5.1.2 Response of a Damped Highly Flexible Hinged Beam

To investigate more in depth the three-dimensional dynamics of beams with the proposed damping model, we simulate the response of a very flexible beam with a ball-joint hinge on one end (3D rotations are allowed) and free on the other end, as seen in Fig. 5.3, where gravity effects are not simulated to isolate the impact of damping in the dynamics. We use models *NL. Dyn. – L. Damp.* and *NL. Dyn. – NL. Damp.* of the previous section (i.e., both geometrically nonlinear models with linearised and full damping terms, respectively), for which thin line and thick line are used throughout all the figures shown next, following the same thickness line style as the one used in the previous section.

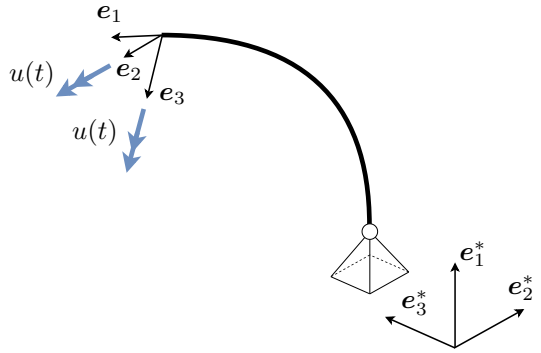


Figure 5.3: Setup of the three-dimensional highly-elastic hinged beam subject to two following point torque inputs $u(t)$ applied at the free end.

The structure is a straight uniform beam with mass and compliance matrices $M = \text{diag}(1,\ 1,\ 1,\ 4{\cdot}10^{-4},\ 2{\cdot}10^{-4},\ 2{\cdot}10^{-4})$ and $C = \text{diag}(10^5,\ 5{\cdot}10^3,\ 5{\cdot}10^3,\ 1,\ 1,\ 2)$, all with appropriate units. This choice of structural parameters and boundary conditions provides us with a very flexible structural test case displaying large elastic and rigid-body displacements and rotations. The beam is excited with an input signal

$$u(t) = \frac{1}{2}\sin(\omega t)\left(\mathcal{H}_0(t) - \mathcal{H}_{0.5}(t)\right),$$

where $\mathcal{H}_{t_0}(t)$ is the Heaviside step function at $t = t_0$, with $\omega = 4\pi = 0.82\omega_b$, where ω_b is the frequency of the structural first bending mode (that is, forcing is only active during the first period of the sinusoidal signal, $t \in [0, 0.5]\,\text{s}$). This input is applied at the free end and with equal magnitude in the $\boldsymbol{e}_2$ and $\boldsymbol{e}_3$ components:

$$m_2(L,t) + \eta E I_2 \omega_2'(L,t) = m_3(L,t) + \eta E I_3 \omega_3'(L,t) = u(t), \tag{5.1}$$

$$m_2(L,t) + \eta \dot{m}_2(L,t) = m_3(L,t) + \eta \dot{m}_3(L,t) = u(t), \tag{5.2}$$

for models *NL. Dyn. – L. Damp.* and *NL. Dyn. – NL. Damp.* respectively. Details on the implementation of these boundary conditions on the two distinct FE damped models are given in Appendix C.

The asymmetry in bending stiffness and the excitation in both transverse directions serve to trigger geometrically nonlinear effects in which torsion and transverse bending motions are coupled. Uniform damping across all degrees of freedom is chosen $C_\tau = \mathrm{diag}(\eta, \eta, \eta, \eta, \eta, \eta)$, and three different values of $\eta = 0.01, 0.001, 0.0001\,\mathrm{s}$ are studied. The presented results have been similarly obtained by a FE discretisation of the intrinsic equations, using 40 elements and a time step of $\Delta t = 0.001\,\mathrm{s}$ for a total simulation time of 50 s, for which numerical convergence of the results is achieved.

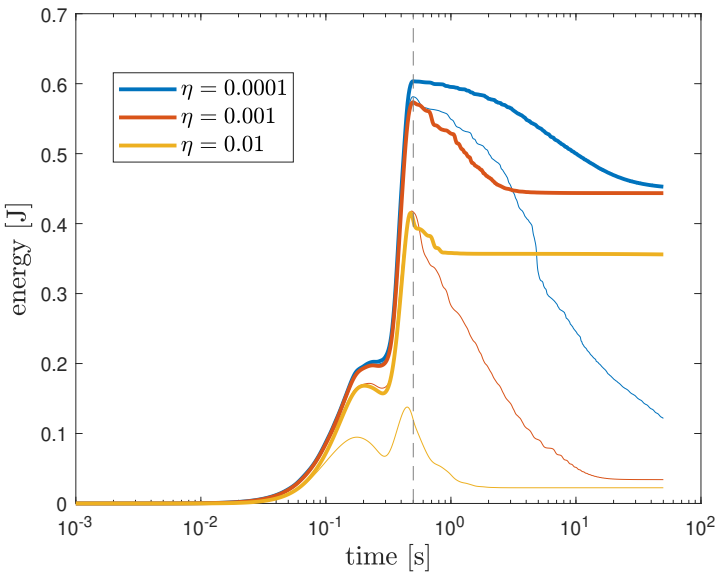


Figure 5.4: Total energy (kinetic + potential) of the beam as a function of time for the three different damping coefficients considered. Thick line corresponds to full nonlinear damping, thin line to linearised damping.

We first look at the total energy of the beam and the corresponding decay rates for the three studied values of damping. Fig. 5.4 shows the evolution of the total energy of the beam for the entire simulation window of 50 s, where a logarithmic scale for the abscissa coordinate is used to ease visualisation of the first 0.5 s (with $t = 0.5\,\mathrm{s}$ marked with a vertical dashed line), where the external forcing is active. A first observation is that for every damping coefficient, the model with linearised damping (thin lines) is consistently more dissipative than the full damping terms counterpart, and leads to lower energy states at the end of the simulation. It is also seen that in the case with lower damping coefficient

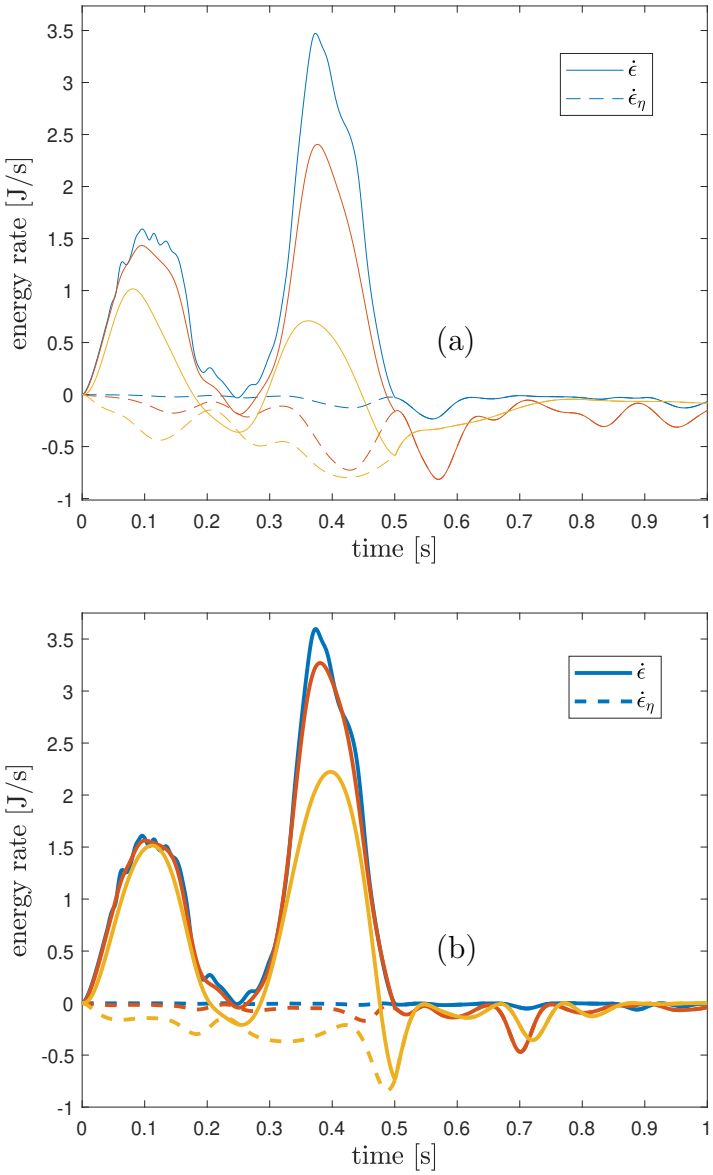


Figure 5.5: Total energy rate $\dot{\epsilon}$ and damping dissipation rate $\dot{\epsilon}_\eta$ for the three different damping coefficients (colour code follows Fig.5.4) for the linearised (top) and the full nonlinear damping cases (bottom).

equilibrium conditions are not reached with any of the two models within the simulated window, contrary to the rest of responses, where the energy curves are clearly seen to flatten and eventually reach a constant level.

The higher dissipation produced by the linearised damping model is better visualised in Fig. 5.5a, where the energy decay rates $\dot{\epsilon}(t) = \langle \boldsymbol{x}_1, M\dot{\boldsymbol{x}}_1 \rangle + \langle \boldsymbol{x}_2, C\dot{\boldsymbol{x}}_2 \rangle$ against time are shown for the *NL. Dyn. – L. Damp.* model. When compared to the full-damping counterpart (Fig. 5.5b), all the curves are lower. That is, when the energy rate is positive during

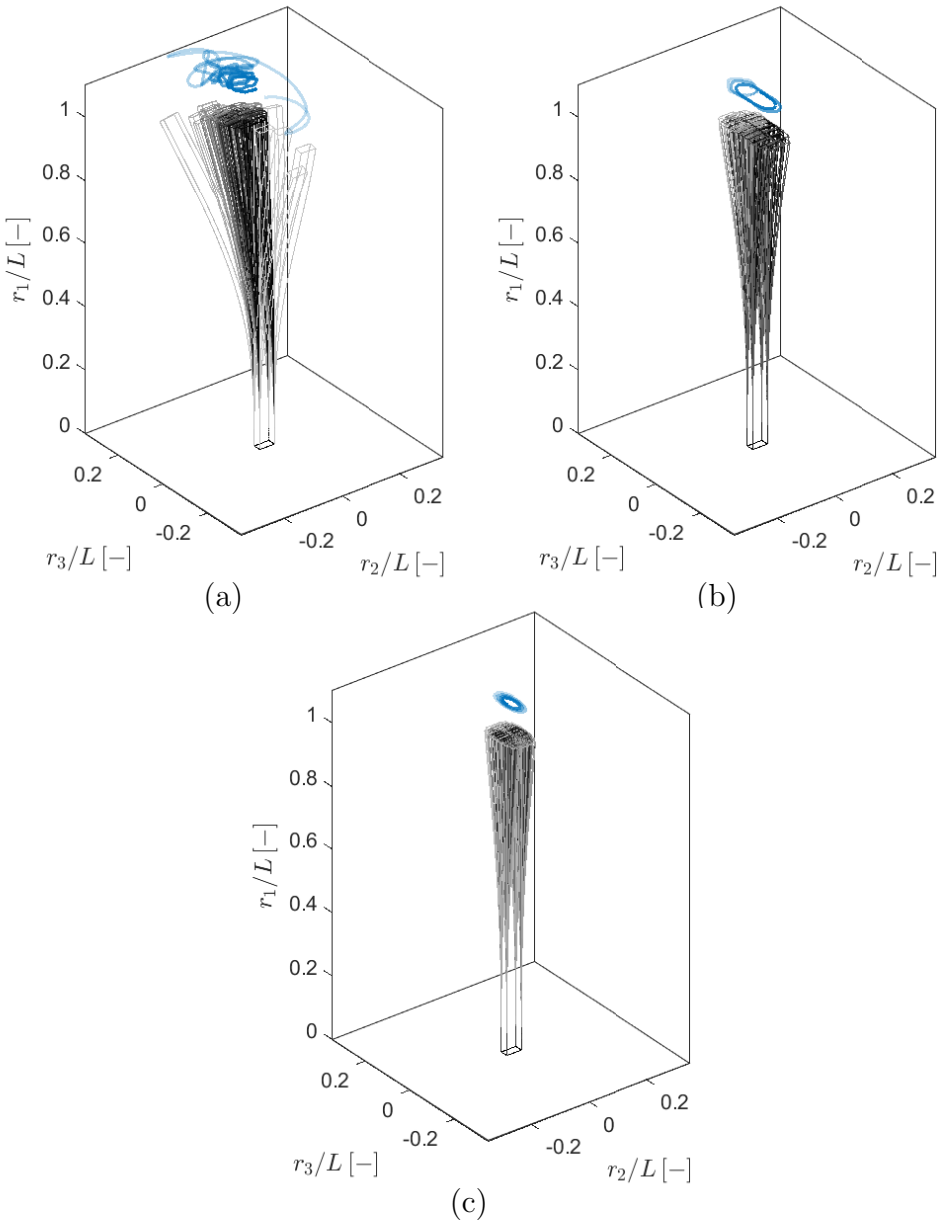


Figure 5.6: Snapshots of the beam every 0.1 s for the linearised damping case and $\eta = 0.001$ s, including the projection on a horizontal plane of the tip displacement trace. Shade darkens with time and (a) $t \in [0, 5]$ s, (b) $t \in [5, 10]$ s, (c) $t \in [10, 15]$ s.

the excitation phase, a lower influx of energy is transmitted to the system, and when it is negative higher dissipation is experienced. Both Fig. 5.5a and Fig. 5.5b show the total energy rate of the system in solid line, computed by evaluating the previous general energy rate expression ($\dot{\epsilon}(t) = \langle \boldsymbol{x}_1, M\dot{\boldsymbol{x}}_1 \rangle + \langle \boldsymbol{x}_2, C\dot{\boldsymbol{x}}_2 \rangle$) numerically. The dissipation produced by damping $\dot{\epsilon}_\eta$ is also shown in dashed lines and is computed by numerically evaluating the expressions (2.19), (2.32). The total energy rate includes the excitation power influx, and we notice that from $t \geq 0.5$ both dashed and solid lines merge (agreement down to machine precision error), since the external forcing vanishes, which validates the analytically

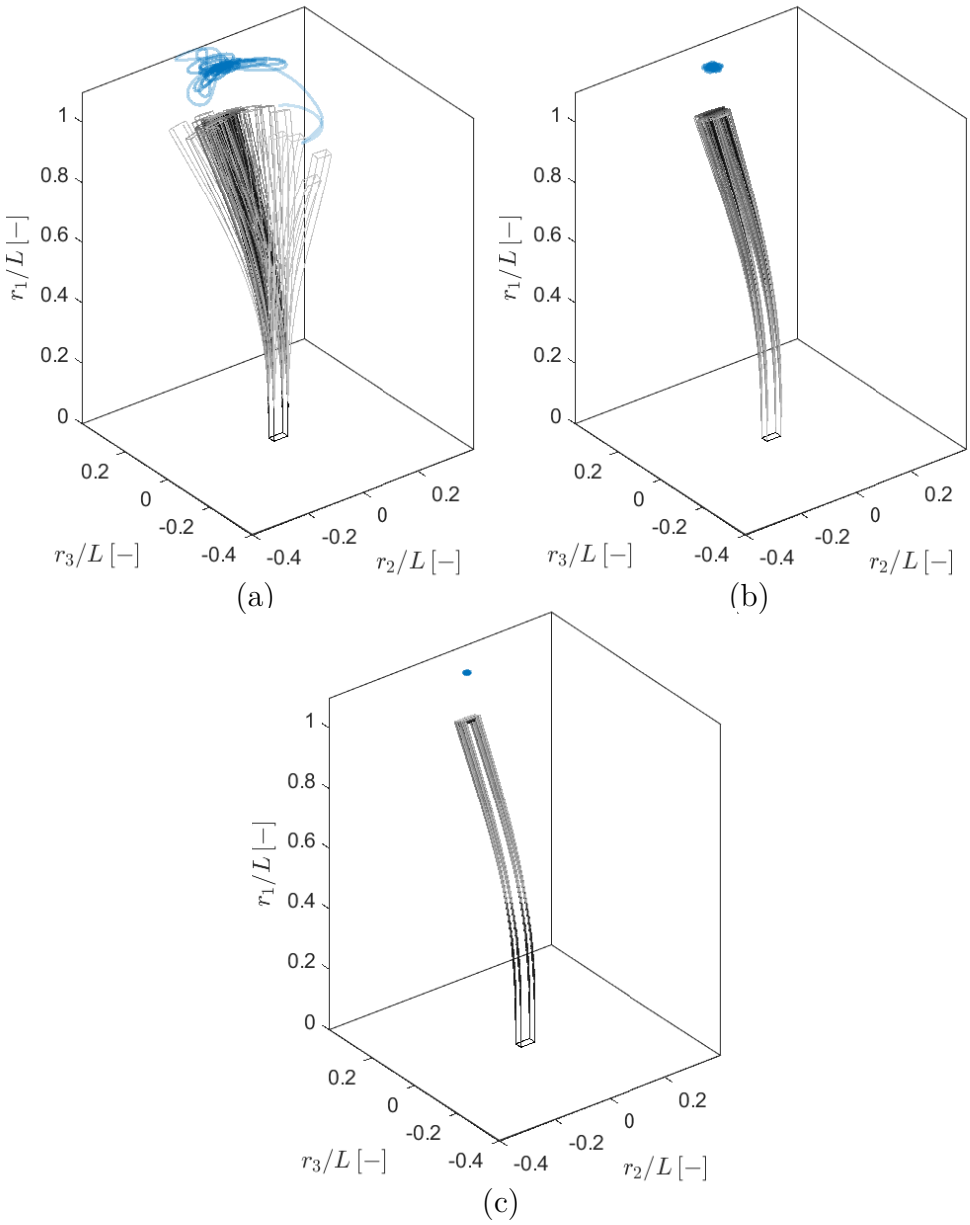


Figure 5.7: Snapshots of the beam every 0.1 s for the full nonlinear damping case and $\eta = 0.001$ s, including the projection on a horizontal plane of the tip displacement trace. Shade darkens with time and (a) $t \in [0, 5]$ s, (b) $t \in [5, 10]$ s, (c) $t \in [10, 15]$ s.

derived energy rates (2.19)–(2.32).

Finally, we analyse now the equilibrium solutions imposed by damping in a more qualitative manner. We focus the attention on the intermediate damping case $\eta = 0.001$ s, for which we observe in Fig. 5.4 that equilibrium is virtually reached for both models. The solution corresponding to the *NL. Dyn. – L. Damp.* model at the end of the simulation consists of an almost pure rotation around the longitudinal axis with negligible remaining stress. Indeed, the only non-negligible angular velocity component at $t = 50$ s

is $\omega_1 = 12.963\,\text{rad/s}$, which gives a kinetic energy of $\epsilon_K = \frac{1}{2} i_1 L \omega_1^2 = 0.0336\,\text{J}$ matching almost exactly the remaining energy shown in Fig. 5.4 of $\epsilon = 0.0341\,\text{J}$. This is in line with (2.34), which states that the equilibrium solution set consists of rigid-body type of motions which do not generate gyroscopic effects (i.e., pure translations or rotation about longitudinal axis for straight beams). Since the beam is pinned at one end, longitudinal rotation, which is the by-product of the bending-torsion coupling given by the structural properties, is the only admissible equilibrium solution. Snapshots of the beam displacements, relative to a body-attached frame of reference at the base (to ease visualisation), are given in Fig. 5.6, where the beam converges to the initial unstressed straight configuration (whilst rotating around $\boldsymbol{e}_1$).

The equilibrium solution for the *NL. Dyn. – NL. Damp.* is more complex, as already suggested by (2.20). As seen in Fig. 5.7, the displacements relative to the rotating frame of reference of the beam base show a bent configuration about the less stiff axis. This stressed configuration is in equilibrium with the gyroscopic forces induced by a small but non-negligible rigid-body rotation of the beam about the hinged joint.

It is therefore apparent that nonlinear terms arising from damping in geometrically nonlinear beams are not negligible, especially where rigid-body motions are present. Not considering them leads to an overestimation of damping, where physical equilibrium solutions, such as those given by (2.20) and shown in Fig. 5.7c, are inevitably ignored.

5.2 Swinging Pendulum Optimal Control Problem

After this first example on the effect of damping on the full intrinsic equations, we now place the focus on the proposed model for control (3.33) (where it will remain for the rest of the application examples). This developed control framework is employed in this first example to solve an optimal control problem, originally described by Wang *et al.* [157] and later studied in [100]. This consists of finding a control law so that the leftward horizontal velocity of a planar, very flexible pendulum of length L, $-V_1(L, t_f)$, in the fixed frame of reference is maximised at the end of a time window of t_f seconds. The flexible pendulum is subject to external gravity forces too. With this purpose, a nonlinear optimal control problem similar to (4.1) is posed with its objective function (5.3) replaced by

$$F_{opt} = \kappa_1 V_1(L, t_f) + \kappa_2 P\left(u(t)\right) \tag{5.3}$$

for some constants κ_1 and κ_2. The control signal $u(t)$ is a moment applied at the root of the hinged pendulum, with positive direction as defined in Fig. 5.8, remaining bounded by some saturation limits $-M_{max} \leq u(t) \leq M_{max}$ and being subject to initial and final constraints $u(0) = u(t_f) = 0$. The term $P\left(u(t)\right)$ in (5.3) penalises actuation energy

$$P\left(u(t)\right) = \frac{1}{2}\int_0^{t_f} \left(\pi_1 u(t)^2 + \pi_2 \dot{u}(t)^2\right) dt, \tag{5.4}$$

where π_1 and π_2 are further tuning constants.

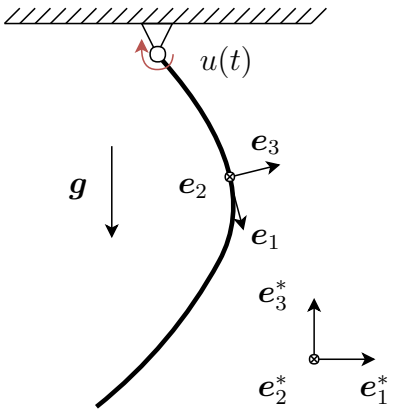


Figure 5.8: Sketch of the the swinging pendulum optimal problem. The pendulum is vertical and straight in its equilibrium position.

5.2.1 Model Convergence Studies

The model of the described flexible pendulum for our control framework is the modal-based structural ROM (3.33) with gravity terms computed using the more accurate spline method (Eqs. (3.43) and (3.45)). The idea here is to reproduce benchmark results using our modelling framework, hence model accuracy and fidelity is prioritised over system size reduction.

A consequence of using the modal-based formulation, whose solution basis is global in space, to locally evaluate the time evolution equations for rotations (2.36) and displacements (2.40), is that errors are introduced which accumulate over the time-integration and result in the individually evaluated points in the structure drifting apart, known phenomenon that was previously observed in [156]. Periodic *regularisations* in the rotation and displacement fields are performed to keep these errors within a tolerable margin, updating them by integrating equations (2.35) and (2.39) in space [156].

The structural parameters of the pendulum are selected to match the properties used in [153]: $M = \text{diag}(\mu, \mu, \mu, 0, 0, 0)$, with $\mu = 1\,\text{kgm}^{-1}$, $C = \text{diag}(EA, \cdot, GA_3, \cdot, EI_2, \cdot)^{-1}$, with $EA = 10^4\,\text{N}$, $GA_3 = 10^6\,\text{N}$ and $EI_2 = 1\,\text{Nm}^2$ and damping matrices $D_0 = D_1 = 0$ and $D_2 = \text{diag}(0, 0, 0, 0, d_b, 0)$, with $d_b = 0.01\,\text{Nms}^2$. The pendulum is a straight structure in its equilibrium, with length $L = 1\,\text{m}$ and no centre of mass offset.

The main convergence exercise involves the choice of the modal basis size N_m, which should include the physically relevant modes in the dynamics of the problem. An analysis of the reduction error is shown in Fig. 5.9, where each basis has been constructed using an equal number of axial and bending modes. The test case for this convergence study is the dynamic response of the pendulum, starting from the hanging vertical straight configuration, under the external, open-loop excitation of a torque moment shown in Fig. 5.10 and gravitational forces.

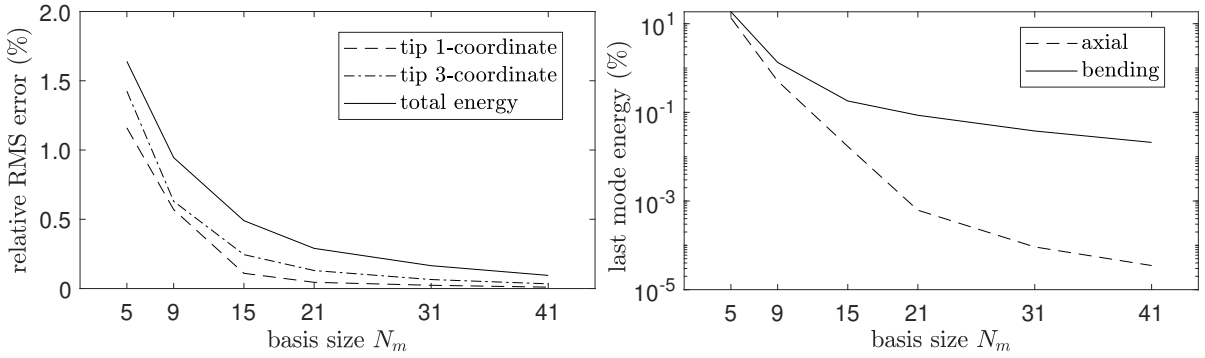


Figure 5.9: RMS error (a) and last mode energy contribution (b) vs N_m.

In Fig. 5.9a the RMS errors[2] of the tip coordinates and the total energy of the system are displayed for modal expansions with varying base size. The error is computed with respect to a reference solution with $N_m = 81$, for which the results are considered fully converged. All simulations have been performed employing the same time step and regularisation rate to isolate the effect of system size in the convergence. Fig. 5.9b displays another convergence metric: the maximum instantaneous energy over the simulation window of the highest-frequency axial and bending modes (i.e., those defining the truncation threshold). The energies are normalised using the total (maximum) elastic energy (potential plus kinematic, excluding the rigid-body mode). This metric provides us with an idea of how well the expansion resolves the physics, with low values of energy indicating negligible contribution of the last modes in the problem.

It has been considered that a basis with $N_m = 21$ provides a reasonable computational

[2]Given a reference $x_r(t)$, the relative error is $\sqrt{\int_0^{t_f}(x - x_r)^2 dt / \int_0^{t_f} x_r^2 dt}$

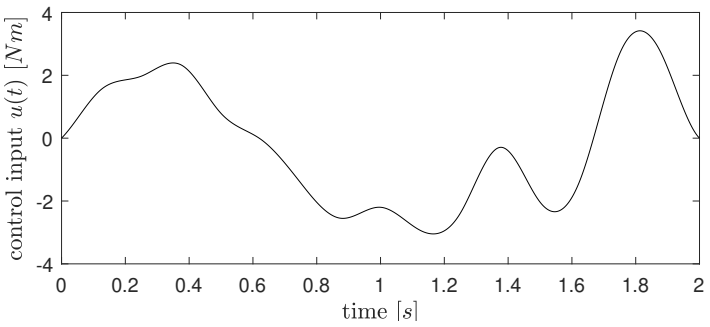


Figure 5.10: Control signal used for the open loop convergence studies.

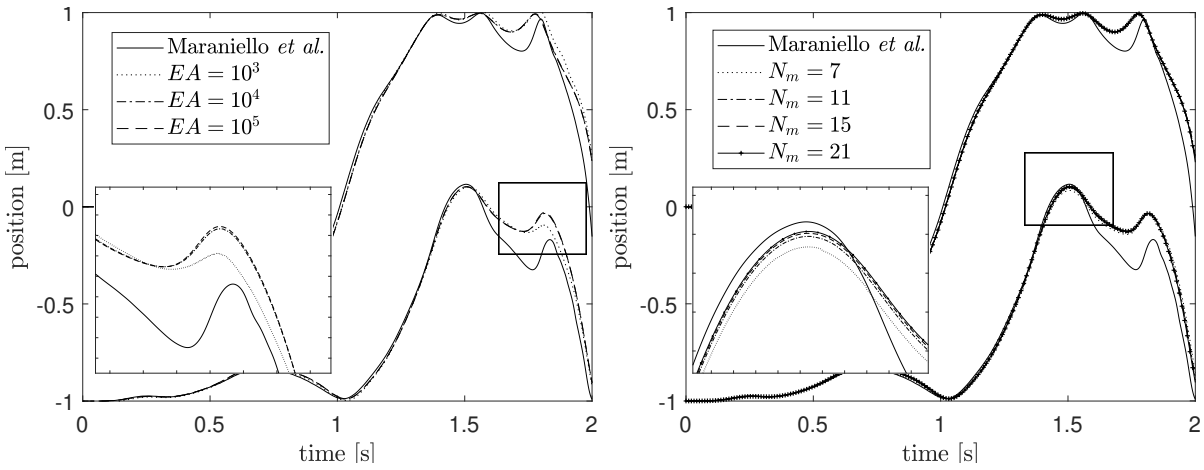
cost while accurately reproducing the dynamics of the problem. With this basis, the last bending and axial modes represent a 0.086% and a 0.00062% of the maximum elastic energy, in contrast to the clearly unresolved case with $N_m = 5$, for example, where these ratios are 18.59% and 13.57%, respectively. The response of the pendulum tip to the excitation (Fig. 5.10) is shown in Fig. 5.11b for a solution obtained for varying number of modes, validating the choice of $N_m = 21$ modes, which are found to reproduce the dynamics accurately.

Wang's *et al.* [153] nonlinear optimal problem statement assumes a structure with infinite axial and transverse stiffness. An important advantage of the intrinsic formulation is that the change of primary variables linearises the equations of motion for this problem, since nonlinear effects come from the coupling between axial and bending modes. Setting infinite axial stiffness EA automatically forces all axial modes to vanish, meaning that nonlinear phenomena are lost in the two-dimensional context [112]. Therefore, convergence as $EA \to \infty$ with finite axial force is studied in Fig. 5.11a.

It is observed that the initially selected large value of $EA = 10^4$ already provides converged results (see Fig. 5.11a). Further increasing the axial stiffness would considerably increase the computational cost of the simulations, since the integration time step is linked to the highest frequency of the modes retained in the approximation. Although not necessary to trigger nonlinear effects, similar convergence behaviour is observed when varying the shear stiffness GA_3.

Maraniello's *et al.* [100] results have also been included as a reference. Good agreement is obtained, albeit with some deviation towards the end of the simulation, which is attributed to the fact that [100] does not account for structural damping but uses a Newmark-β integration scheme which adds numerical dissipation, while the modal-based approach has been shown to have better energy-preservation properties [164].

We focus now on the choice of discretisation for the approximation to the quaternion



(a) (b)

Figure 5.11: Axial stiffness EA (a) and number of modes N_m convergence studies (b). Above, the pendulum tip x-coordinate, below, its z-coordinate.

field. From the Nyquist criterion, and inspecting equation (2.35), one can conclude that the spacing between the tracked quaternions should be, at most, half the period of the highest (spatial) frequency mode, in order to be able to recover its spatial distribution. The highest frequency mode has a spatial period of around $0.2L$ in the bending moment component, which justifies the choice of a grid with 10 intervals. Indeed, very satisfactory results are observed, even when the highest space-frequency modes are excited towards the end of the simulation, as shown in Fig. 5.12a. It is also seen that the interpolation scheme has good unit-norm preservation properties (Fig. 5.12b). Finally, in Fig. 5.12c and Fig. 5.12d the spatial distribution reconstruction produced by the Catmull-Rom spline is shown, accurately reproducing the true quaternion spatial distribution resulting from the integration of curvatures (2.35).

5.2.2 Solution to Optimal Problem Parameterised by Multiple Shooting

Following the presented convergence studies, the subsequent (closed-loop) optimal problem results have been obtained using a model constructed with $N_m = 21$ modes, selected in ascending frequency order, including 10 axial and 10 bending elastic modes and the only rigid-body mode of the pendulum. A uniform spatial grid with $N_\xi = 10$ intervals has been constructed to keep track of the quaternions. Finally, a fourth-order Runge-Kutta explicit scheme is the choice for time integration. A time step equal to 0.1 times the period of the highest frequency mode has been found to suffice convergence criteria, with rotation regularisations every 50 time steps. These are performed by integrating equation

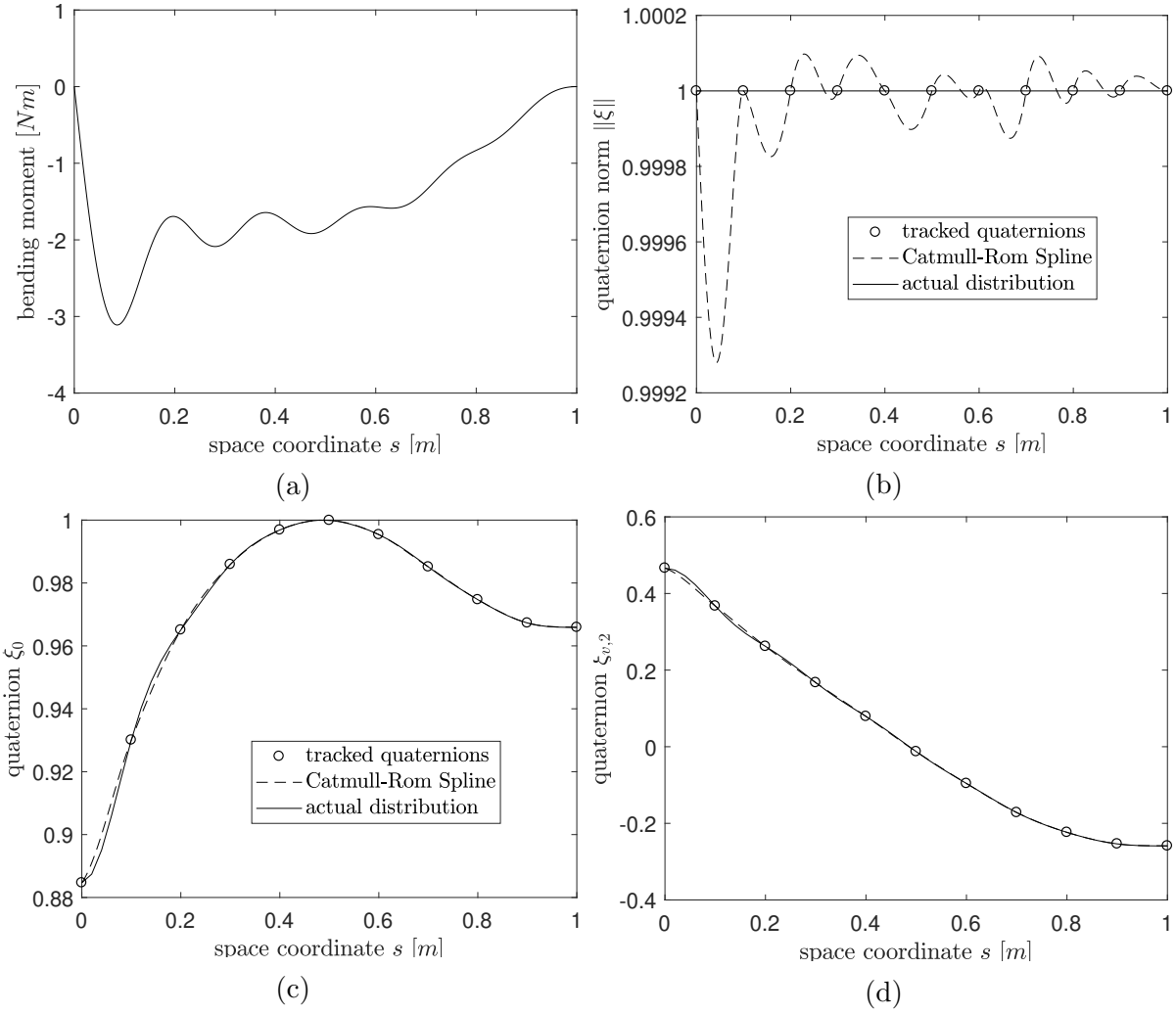


Figure 5.12: Bending moment (a), quaternion norm (b), quaternion scalar component ξ_0 (c) and quaternion second vector component $\xi_{v,2}$ (d) spatial distributions. Results at $t = 1.83\ s$.

(2.35) using a RK4 scheme with a spatial resolution of $0.02L$. The tracked quaternions, time-integrated up to that instant (3.44), are then substituted by those resulting from the spatial integration.

The optimal problem defined for constants $t_f = 2\ s$, $M_{max} = 3.5\ Nm$, $\kappa_1 = 1$, $\kappa_2 = 1$, $\pi_1 = 1$, $\pi_2 = 0.01$, with appropriate dimensional units, has been solved using a discrete sine series with $N_c = 16$ and frequencies $f_l = 0.5l/t_f$ as a control parametrisation $u(t) = \sum_{l=1}^{N_c} u_l \sin 2\pi f_l t$ (which automatically satisfies initial and final conditions $u(0) = u(t_f) = 0$) and for a number of multiple shooting time intervals ranging from 4 to 95.

Results are obtained with a Matlab script running on an Intel(R) Xeon(R) CPU E5-2630 v3 @ 2.40GHz processor, using Matlab default parallel pool with 12 workers and with an optimisation stop tolerance of 10^{-5} on $\nabla_{\boldsymbol{p}}\mathcal{L}$ (4.12). To contextualise the computational

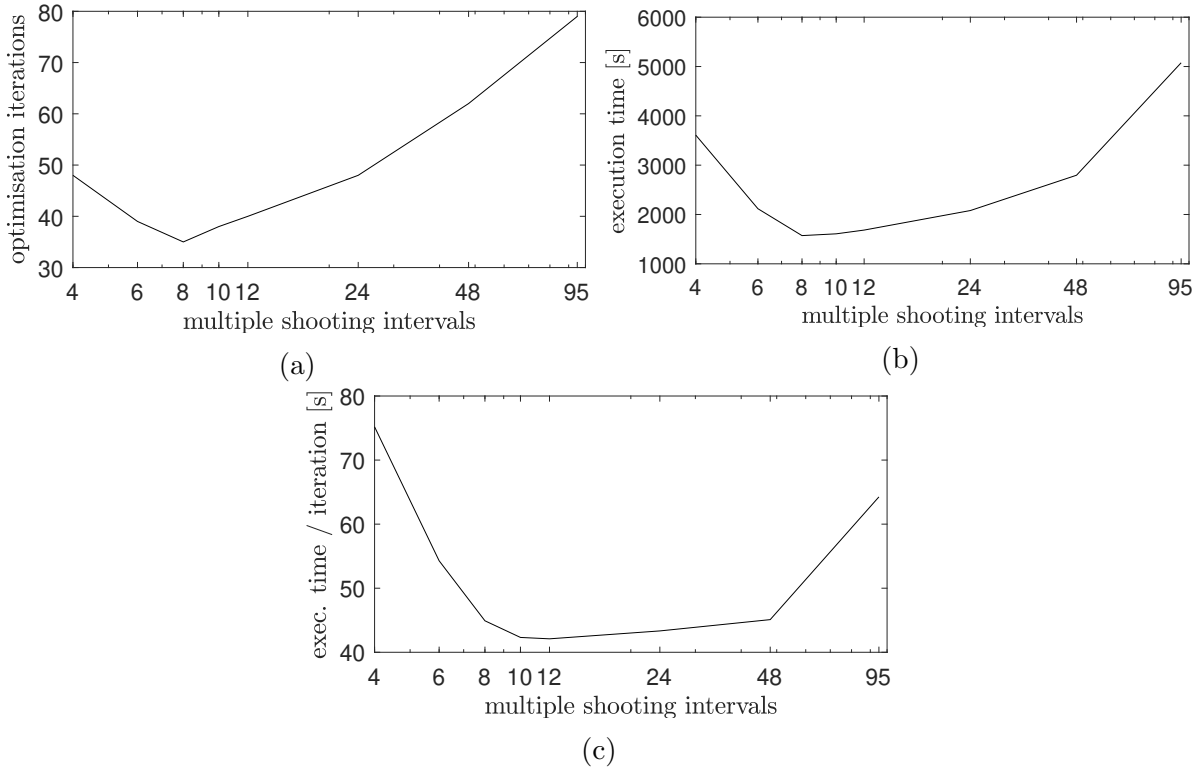


Figure 5.13: Number of optimisation iterations (a), execution time (b) and execution time per iteration (c) vs multiple shooting intervals.

achievement of our proposed control framework, the single shooting approach of [100], which modelled the structure using a displacement-based geometrically-exact beam formulation which required solving the optimal problems using finite differences, needed the use of the UK National Supercomputing resource, ARCHER.

As seen in Fig. 5.13a, the multiple shooting parametrisation improves convergence of the nonlinear problem by reducing the number of optimisation (SQP) iterations until 8 intervals, where there is a minimum. Further increasing this number, however, increases the dimension of the optimal problem and convergence is slowed. The total execution time (Fig. 5.13b), also displays a minimum at 8 intervals, which results from the combined effect of the mentioned multiple shooting influence on the convergence (Fig. 5.13a) and the parallelisation acceleration (Fig. 5.13c). This last plot clearly displays how the execution time per optimisation iteration decreases until 12 intervals (note that 12 processors are used), it remains roughly constant for the range $12 - 48$ after which it increases again, since the QP solution (4.12) takes over the forward and sensitivity time-integrations, in terms of computational cost.

A number of intervals below 4 makes the proposed scheme unstable and the single shooting case (i.e., the case in which the problem time horizon t_f is taken as a whole and no time

intervals are constructed) fails unless initial sub-relaxation is applied (that is, diminishing by some factor the step size resulting from the solution of the quadratic problem (4.12) within the SQP iteration). Applying a sub-relaxation factor between 0.1 and 0.5 within the first 30 iterations, the single shooting eventually converges towards the same solution but with an execution time that is an order of magnitude higher ($13,454$ s and 47 iterations). Hence, the multiple shooting implementation not only accelerates the simulation but also becomes necessary to ensure convergence for highly nonlinear problems (at least with the proposed optimisation algorithm).

All multiple-shooting cases have converged to the same minimum, with the solution $u(t)$ of the optimal control problems shown in Fig. 5.14a, while the snapshots of the pendulum motion are presented in Figs. 5.14b–5.14d. The solution has a minimum in the cost function $F = -6.64$, with an end-of-simulation leftward horizontal velocity of 12.06 m/s. These values differ slightly from Maraniello's [100], where a minimum of $F = -9.63$ and a velocity of 13.11 m/s are obtained. Discrepancies might be due, again, to differences in the nature of the employed numerical integration and optimisation schemes and mathematical models describing the structure, which as already mentioned, reference [100] does not account for structural damping.

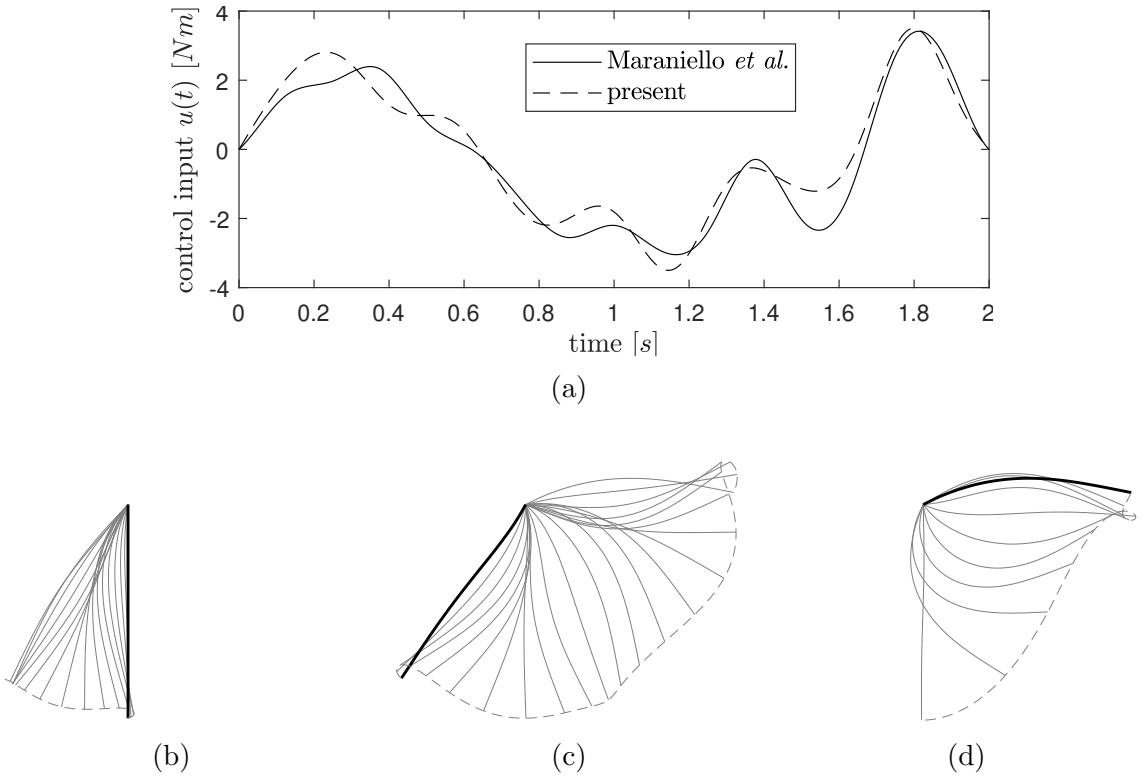


Figure 5.14: Optimal control input (a). Snapshots (grey) of the pendulum trajectory at a rate of 25 fps for $t \in [0, 0.72]$ (b), $t \in [0.72, 1.60]$ (c) and for $t \in [1.60, 2]$ (d). The black line represents the initial configuration of the shown interval and the grey, dashed, one the tip path.

5.2.3 Computational Cost of Sensitivity Analysis

Here, the computationally favourable scaling of the sensitivity equations of § 4.3.3 relative to the forward simulation is numerically assessed. This is another distinct feature of our control framework, tailored to the intrinsic modal formulation. For this comparison, the previous model of pendulum is employed adding extra modes for the transverse direction. The execution time of integrating system (3.33) with gravity terms using the modal approach (3.58)–(3.57) along a simulation time of 2s is divided by the total number of time steps taken. The time integration is performed using a RK4 scheme with a time step of 0.25 times the smallest period of the modes included in the expansion, which suffices convergence criteria. Thus, an approximation of the execution time of a single time-integration step is obtained, smoothing possible fluctuations in the performance. This is repeated for a modal basis with a varying size ranging from 20 to 80 modes. The same procedure is applied when solving the complete sensitivity equations (4.18)-(4.17), necessary to linearise the continuity constraints (4.1c) in a multiple-shooting optimal control

problem parameterisation. Execution times correspond to a Matlab script running on an Intel(R) Xeon(R) CPU E5-2630 v3 @ 2.40GHz processor.

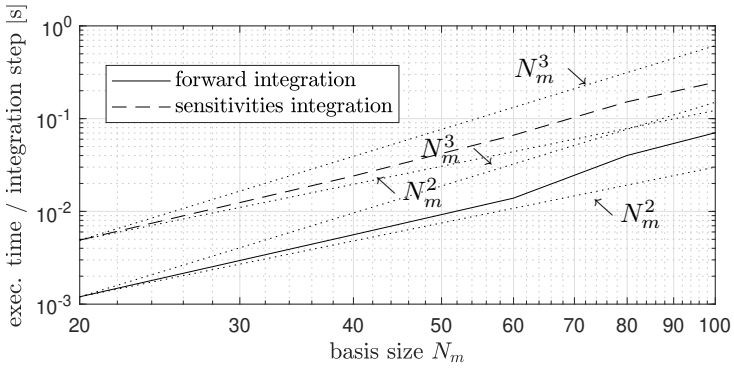


Figure 5.15: Execution time per time step of the forward (solid line) and sensitivity (dashed line) problems, with dotted lines showing the +2 and +3 slopes.

As observed in Fig. 5.15, the execution times per RK4 iteration of the forward simulation and the sensitivity system scale with the number of modes to a power which lays within 2 and 3. As previously discussed in § 4.3.3, the theoretical complexity of both systems scales with N_m^3. Execution time and computational complexity are closely related, though not fully equivalent. The former is highly dependent on the internal architecture and algorithmic functioning of the in-built functions, while the later is assumed to be roughly the number of product operations. Nonetheless, and most importantly, we note that the costs of the sensitivity problem and of the forward simulation remain proportional, regardless of the size of the system which proves our size-independence claim. Evaluation of the sensitivities is, at worst, five times more expensive than the forward one (which might be explained by the fact that five extra nonlinear terms, corresponding to Γ_1, Γ_2, $\Gamma_2^\top$, Γ_g and Γ_ξ have to be evaluated in (4.19)).

5.3 Nonlinear Control of a Very Flexible Inverted Pendulum

In this numerical example the control framework introduced in the previous case is employed to underpin a model predictive controller to stabilise a very flexible inverted pendulum. Three different cases are considered. We start with a two-dimensional reference-tracking problem without gravity effects. This is followed by a more complex three-dimensional reference-tracking problem without gravity forcing, where nonlinear couplings between torsion and bending are expected to pose a more challenging control problem. Fi-

nally, the last case is a disturbance rejection/regulation problem where a three-dimensional pendulum is to be stabilised under the action of gravity.

For the first two described cases we will use results from standard NMPC [123], since the system is linearly stabilisable around the desired equilibrium. However, since the last case includes simulation of gravity forces (for which rotations have to be accounted for in the internal model) it allows us to put in practice the theoretical results that followed from the discussion on the proposed novel MPC strategy of § 4.1, which enables us to establish convergence and stability guarantees using our particular low-order descriptions of geometrically nonlinear beams.

Regarding the controller setup, three different implementations are tested, aiming to highlight the superiority of the nonlinear controller. All of the implementations are based on the modal, finite-dimensional structural ROM (3.33) with an approximated rotation field (given by Eqs.(3.41) and (3.42)) where gravity forces are considered. The implementations are labelled as follows: (i) A linear implementation, *LMPC*, which uses a linearisation of (3.33) around a reference $\bar{\boldsymbol{q}}$ equilibrium solution, constructing and solving a QP (linear dynamics plus quadratic cost function) at each sampling time, (ii) the converged nonlinear controller, *NMPC*, and a (iii) real-time iteration, *RTI-NMPC*, where one SQP iteration (4.12) is solved at each sampling time, without shifting of the optimisation variables.

For the controlled plant we test two scenarios, both with full nonlinear terms. We either use the same (modal) system as the internal model of the MPC (referred to as the *nominal* case), so we can make use of standard MPC convergence guarantees and of the results obtained in §4.1. However, we also demonstrate that excellent performance is achieved when the control scheme is applied to the *ground truth* system, implemented using a high-order finite-element discretisation of the intrinsic beam equations (2.22)–(2.23), whose details are gathered in appendix C, and a spline interpolation scheme where rotation information is required, since both discretisations have errors that are known to be bounded by the grid size.

The three introduced cases are presented below, all assuming slight damping with $D_0 = D_1 = 0$ and $D_2 = 10^{-4}\text{diag}(1, 0, 0, 1, 1, 1)$.

5.3.1 2D Clamped Case

For the first two-dimensional case (contained in the $1-3$ plane), a clamped, straight uniform beam of $L = 1$ is considered, with mass matrix $M = \text{diag}(1, 1, 1, 0, 8.33 \cdot 10^{-5}, 0)$

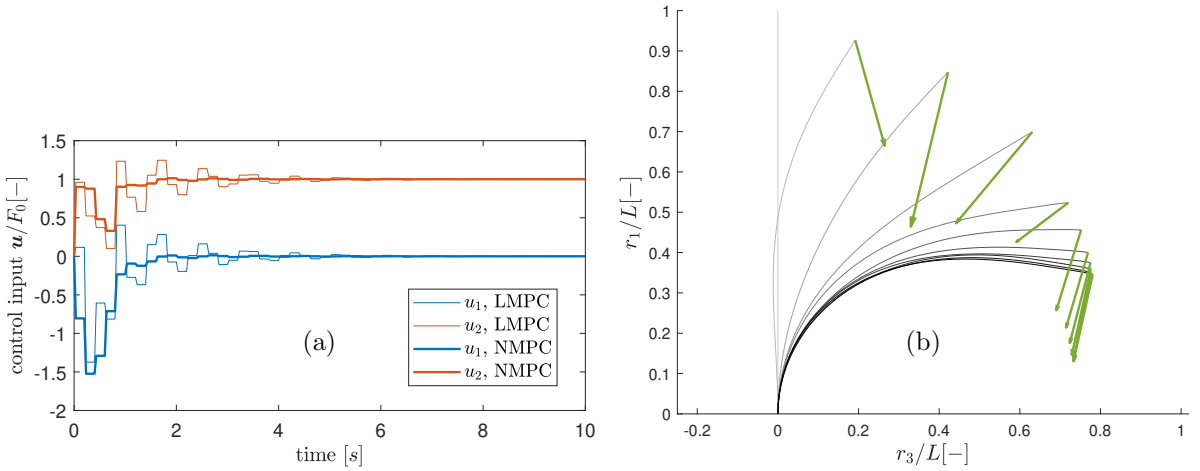


Figure 5.16: (a) Control input comparison for the *nominal* case of all the linear and converged MPC controllers and (b) snapshots every 0.2 s of the control action of the *NMPC* controller (with resultant applied force in green).

and compliance matrix $C = \text{diag}(100, \cdot, 10^5, \cdot, 0.5, \cdot)^{-1}$, all with appropriate units.

The beam is initially in a straight equilibrium position (light grey line in Fig. 5.16b) and the controller is required to bring the structure to a deformed position (black line in Fig. 5.16b), described by a reference state $\bar{\boldsymbol{q}}$ in (4.1a). This deformed configuration is the steady solution to a follower transverse force, of magnitude $F_0 = 2$ N, applied at the tip. The controller, however, is set up to act via two degrees of freedom $\boldsymbol{u} = (f_1, f_3)^\top$, where f_3 and f_1 are transverse and axial follower point forces:

$$\boldsymbol{x}_2(L,t) = (f_1(t), 0, f_3(t), 0, 0, 0)^\top . \tag{5.5}$$

The controller internal models are constructed with a basis with $N_m = 4$, including the first two axial and bending modes. The sampling time is $\tau_s = 0.2$ s and the prediction horizon is $\tau_c = 2$ s (0.079 and 0.79 times the period of the first bending mode, respectively), giving $N_c = 10$ subintervals. Finally, control saturation (4.1d) is set as $u_u = -u_l = 2.5F_0$ and the cost function (4.1a) is constructed with $Q = \text{blkdiag}(I_{N_m}, I_{N_m})$ and control penalty $R = 0.01I_2$.

Regarding the *nominal* case, a terminal penalty weight P has been found and a terminal region (4.1f) with $a = 1.98$ has been estimated following [123] MPC design for constrained nonlinear systems (since the system is linearly stabilisable around $\bar{\boldsymbol{q}}$). Attending to the obtained results, both linear and nonlinear implementations exhibit fairly similar behaviour, as seen in Fig. 5.16a, albeit with *LMPC* producing a notably higher oscillatory response and settling time.

It is interesting to note that both controllers exploit nonlinear buckling, to bring the structure closer to the reference condition in a shorter time (which effectively decreases the cost function (4.1a)): the controller applies a compression axial force, depicted by negative values of the blue lines in Fig. 5.16a which effectively causes the beam to buckle, as the increase in curvature of the lower section of the beam in Fig. 5.16b suggests. Despite the *LMPC* controller not accounting for nonlinear dynamic simulations it is able to capture some intrinsic nonlinear phenomena due to the linearisation of the system around the deformed, reference configuration and to the repetitive sampling and updating of the optimal solution.

It is also compelling to look at the case where the controller is applied to the *true* system, shown in Fig. 5.17. At first glance, results provided by the *LMPC* and *NMPC* appear very similar to the previous case, especially for the *NMPC*. However, for the *LMPC* implementation the oscillations already present in the previous case are further amplified, due to the addition of uncertainty corresponding to the lack of knowledge of the nonlinear effects. From this numerical exploration, it is implied that, firstly, the *NMPC* implementation appears robust to plant uncertainty, and secondly, that just a few modes (2 modes per motion) suffice to control the actual system. We also note that the *RTI-NMPC* implementation opts for a smoother and somewhat slower response which consists of applying a transverse force progressively, maintaining the control axial input close to zero.

5.3.2 3D Clamped Case

In the three-dimensional case, a similar problem has been tested. Again, a clamped, straight uniform beam of the same length with mass matrix $M = \text{diag}(1, 1, 1, 1.67 \cdot 10^{-4}, 8.33 \cdot 10^{-5}, 8.33 \cdot 10^{-5})$ and compliance matrix $C = \text{diag}(100, 10^5, 10^5, GJ, 0.5, 1)^{-1}$ are

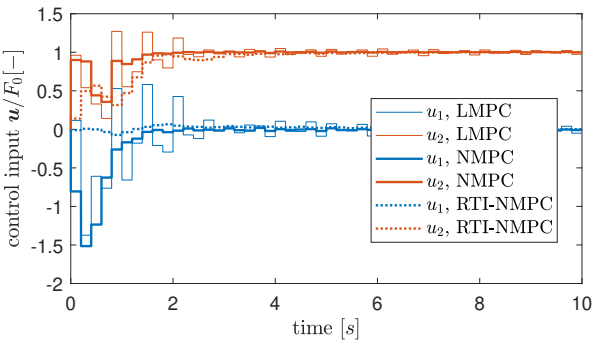


Figure 5.17: Control input comparison of all the three controllers acting on the *true* system.

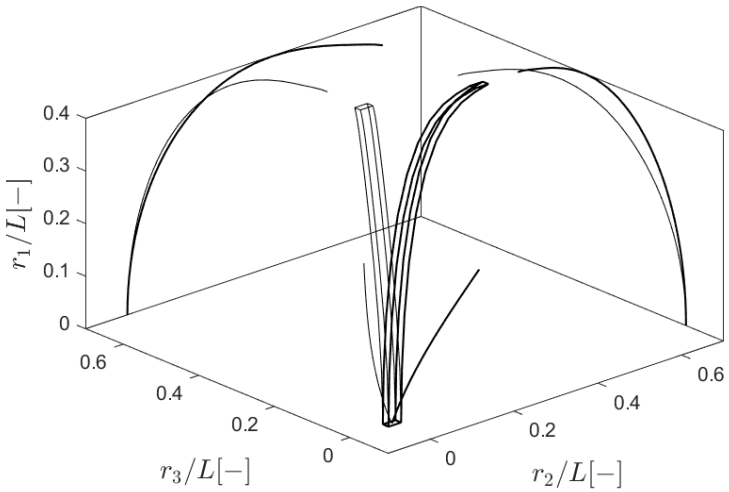


Figure 5.18: Target position for the less flexible (thin stroke) and more flexible (thicker stroke) beams, where projections onto each plane have been included and where the width of the beam specifies the direction of higher stiffness.

considered, where we will use two different values for $GJ = 0.33EI$ and $0.67EI$, where $EI = (EI_2 + EI_3)$. The deformed target configuration is the steady solution to two transverse follower forces of magnitude $F_0 = 2$ N each applied at the tip. The non-symmetric equilibrium position (due to $EI_2 \neq EI_3$), shown in Fig. 5.18, will entail geometrical couplings between the bending modes in the two transverse directions and torsion. By using different values of GJ, the influence of the nonlinearities on the performance of the different controllers will be revealed. Note how in the more flexible case (thick line) in Fig. 5.18, the target solution shows an increase in twist, laying further away from the symmetric solution that $EI_2 = EI_3$ would produce.

The controller inputs are, here, three follower forces applied at the tip $\boldsymbol{u} = (f_1, f_2, f_3)^\top$:

$$\boldsymbol{x}_2(L,t) = (f_1(t), f_2(t), f_3(t), 0, 0, 0)^\top . \tag{5.6}$$

The controller parameters (prediction horizon and intervals) are the same as in the 2D case except for the number of modes, which is now $N_m = 8$: two torsion modes and two bending modes corresponding to the other transverse direction are added. Similarly to the previous 2D case, the system is fully stabilisable around $\bar{\boldsymbol{q}}$, and a much smaller terminal region of $a = 0.03$ is estimated to satisfy the necessary conditions for convergence and stability of the closed-loop MPC [123].

It is in this 3D case that the nonlinear effects become more relevant when compared to the 2D one, since the follower forces at the tip are very sensitive to the overall twist of the

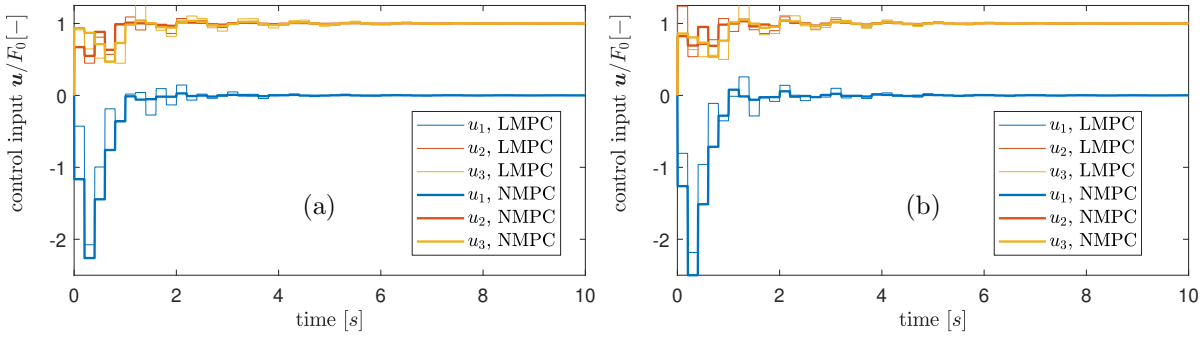


Figure 5.19: Control input comparison of *LMPC* and *NMPC* for the *nominal* case for a torsion stiffness of (a) $GJ = 0.67EI$ and of (b) $GJ = 0.33EI$.

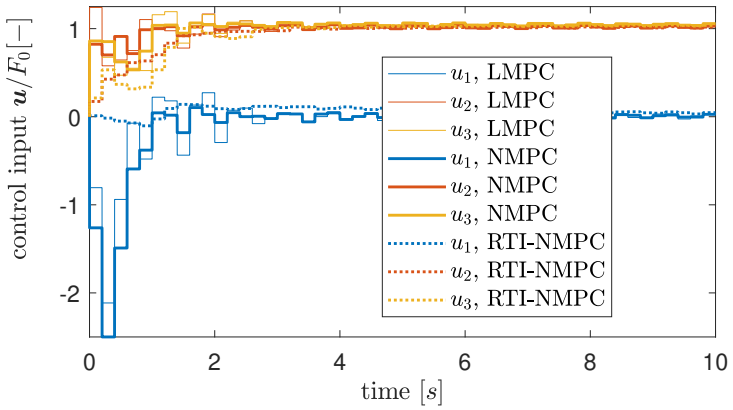


Figure 5.20: Control input comparison of the three controllers on the *true* system for the more flexible beam case.

beam. This is observed in Fig. 5.19, which shows how the *LMPC* controller becomes more oscillatory and starts to diverge from the *NMPC* response, particularly the transverse force inputs, as the beam becomes more flexible in torsion (Fig. 5.19b), eventually leading to failure for values of $GJ \lessapprox 0.167EI$, where the *NMPC* still shows convergence. The *NMPC* shows more effective control, even reaching saturation on the control input u_1 for the more flexible beam case.

Similarly, we include simulations of the more flexible case ($GJ = 0.33EI$) where the three different MPC implementations are set to control the *true* system. The corresponding obtained control inputs are gathered in Fig. 5.20. The difference between the results on the *nominal* system and on the *true* system is larger in the 3D scenario, where even the more robust *NMPC* shows higher oscillations throughout most of the simulation, however it successfully stabilises the system. The *RTI-NMPC* implementation follows the same tendency as in the 2D case and achieves stabilisation, producing a smooth solution by increasing gradually the control input until the target configuration is reached.

5.3.3 3D Case on a Moving Base with Gravity Effects

Finally, a case including gravity is presented, and hence, the rotation field needs to be simulated. It is in this case where the bespoke MPC setup described in § 4.1 can be used to ensure the convergence of the closed-loop dynamics. The problem is now a disturbance rejection one, where an inverted pendulum is to be stabilised via control of the moving base using follower force inputs in every direction $\boldsymbol{u} = (f_1, f_2, f_3)^\top$

$$\boldsymbol{x}_2(0,t) = -\left(f_1(t), f_2(t), f_3(t), 0, 0, 0\right)^\top, \tag{5.7}$$

where the minus sign here arises from the distinct sign convention between internal ($\boldsymbol{x}_2$ variable) and external forces (input) for $s = 0$. The system is perturbed with an initial rigid-body angular velocity of $\sqrt{2}\,\mathrm{rad/s}$ with equal components in both transverse directions, with the similar aim as in the previous 3D case to trigger nonlinear behaviour.

The pendulum is a straight beam with $L = 1$, with free boundary conditions on both ends except that the structure is prevented from spinning around its longitudinal axis only at the base (twisting deformations are still allowed). The beam has a mass matrix $M = \mathrm{diag}(1, 1, 1, 9 \cdot 10^{-5}, 6 \cdot 10^{-5}, 3 \cdot 10^{-5})$ and compliance matrix $C = \mathrm{diag}(5000, 5 \cdot 10^4, 5 \cdot 10^4, 0.05, 2, 1)^{-1}$, with appropriate units.

To set up the MPC controller we use a sampling period of $\tau_s = 0.2$ s and a prediction time horizon of $\tau_c = 4$ s (1.01 and 20.1 times the period of the first bending mode in the 3-direction), which results in $N_c = 20$ intervals. The controller model uses 13 mode shapes which include two axial, four bending (two for each direction), two torsion and the five rigid-body modes corresponding to the described configuration.

For a first test case, we use the spline approach to parametrise rotations described by matrices (3.43) and (3.45), using a grid with two intervals within the internal model. This results in a state space with 36 states: 13 q_1-states, 8 q_2-states, 12 q_ξ quaternion components and 3 extra states which correspond to the displacement of the base in the global reference

$$\dot{\boldsymbol{r}}_b = T(\boldsymbol{\xi}_0)\Phi_{1v}(0)\boldsymbol{q}_1, \tag{5.8}$$

where Φ_{1v} is a matrix constructed by horizontally concatenating the three first components (translational velocity) of the velocity mode shapes $\boldsymbol{\phi}_1$. As discussed previously, linearisation of (3.33) coupled to an approximation of the rotation field gives unstabilisable modes (in this case 10), which have components in both the quaternion field, the four bending and two torsion q_2-states.

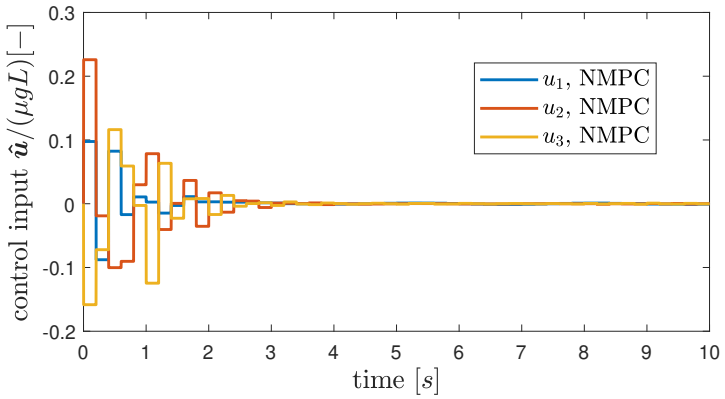


Figure 5.21: Control input in the *nominal* case using the present *NMPC* design for $\delta = 0.0001$.

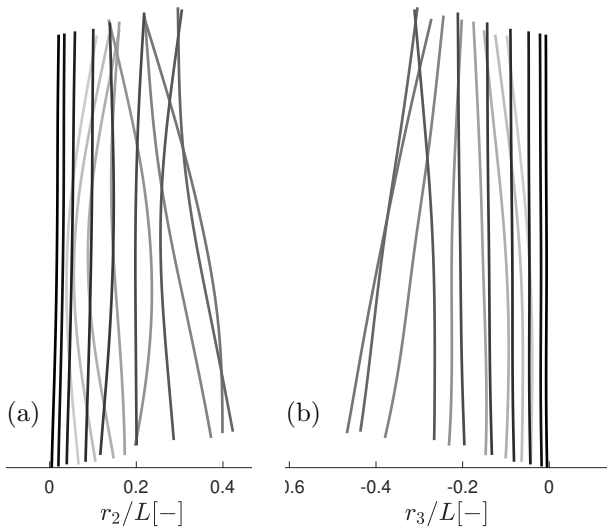


Figure 5.22: Fifteen snapshots for $t \in [0.1, 6]$ s, with logarithmic spacing in time, of the controlled pendulum in the (a) 1-2 and the (b) 1-3 planes, with shade darkening for increasing time.

This means that the structure can be brought to a state where velocities are zero (i.e., equilibrium) but with remaining deformed configurations due to the presence of gravitational forces (from the internal model point of view). However, we want to shrink the set of all these possible undesired equilibrium points, that is, the control objective is to stabilise the system to a point where velocities are zero, and the remaining stress configuration is minimum. To achieve this, we make use of the bespoke NMPC machinery described in § 4.1.

Initially, we have to solve the LMI system (4.6) and (4.7) for a fixed β. We are interested in the highest value of β possible, since it is linked with desirable decay rates, and we obtain for this particular system, a value of $\beta = 0.0092$, together with weight matrices P_w and

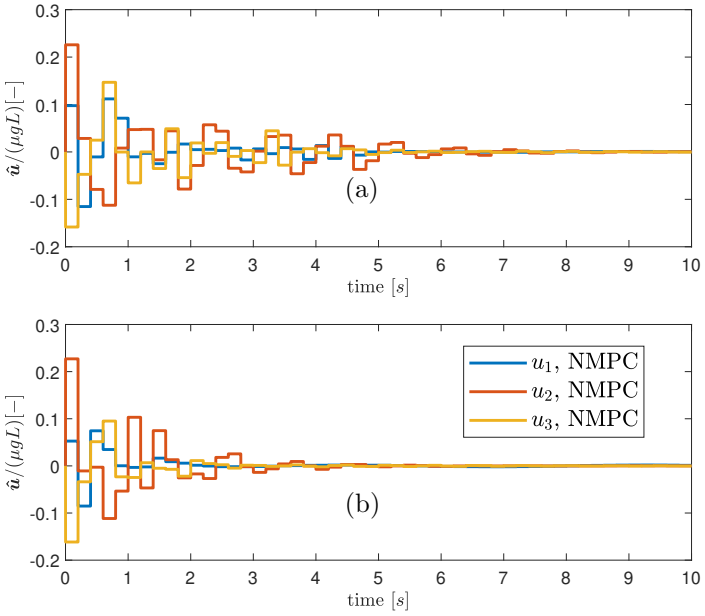


Figure 5.23: Control input for both the (a) spline and the (b) modal finite-dimensional approximations for the quaternions applied to the *true* system.

P_d with $1.05 \leq \sigma(P_w) \leq 66.12$, $1.25 \leq \sigma(P_d) \leq 22.06$, and $R = 10^{-4}\text{diag}(1.35, 1.05, 1.23)$.

Next, by Lemma 5, the existence of (possibly very small) constants δ and ω which lead to decay of the MPC cost function is assured. We estimate values of δ and ω for which the condition (A.3) of Lemma 5 is satisfied, at least for a large cloud of points within the corresponding balls that δ and ω define. We are interested in attaining the lowest possible values for δ and the highest possible for ω (i.e., to minimise the effect of unstabilisable modes and widen the set of stable modes from where convergence is assured), achieving very reasonable values of $\delta = 0.0001$ and $\omega = 0.178$. These terminal constraints are imposed as in (4.1f), however splitting the constraint into one for the stabilisable modes and a second for the unstabilisable ones, using the two state-transformation matrices described in § 4.1.

Very good performance is obtained in the *nominal* case, as suggested by the resulting control input trajectories shown in Fig. 5.21, with stabilisation achieved efficiently and inputs close to zero for $t \geq 4$. Snapshots showing how the control achieves stabilisation of the structure are provided in Fig. 5.22.

We now show how even when applied to the *true* system (i.e., the resolved numerical simulation of the PDEs), stabilisation is achieved using both the modal and the spline approximations to the quaternion field. The system constructed with the modal approximation to the quaternion field has exactly the same structure, represented generically

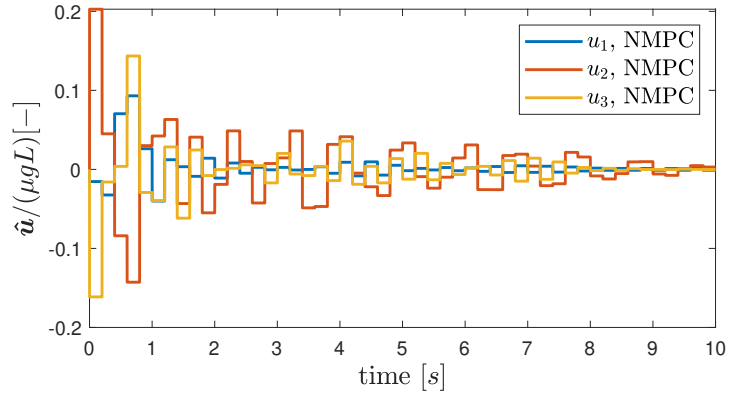


Figure 5.24: Control input on the *true* system using the present *NMPC* design for $\delta = 0.0001$ and constraint on vertical base displacement.

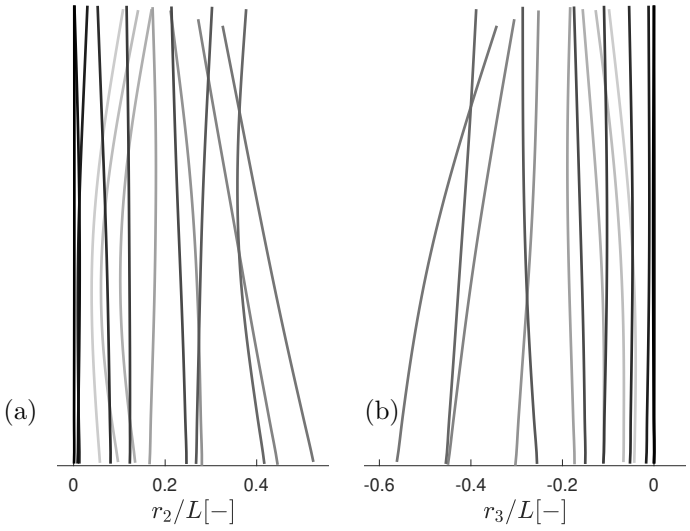


Figure 5.25: Fifteen snapshots for $t \in [0.1, 10]$ s, with logarithmic spacing in time, of the controlled pendulum in the (a) 1-2 and the (b) 1-3 planes, with shade darkening with time for the vertical displacement constrained case.

by expressions (3.41) and (3.42), resulting in the same number of stabilisable modes as the spline approximation model. Although the same $\beta = 0.0092$ is obtained for this new system, different parameters result from the MPC design: $\delta = 0.0001$ has been found to be the same, however we need a smaller $\omega = 0.068$ and weight matrices P_w and P_d have $1.06 \leq \sigma(P_w) \leq 139.87$, $1.25 \leq \sigma(P_d) \leq 69.00$, and $R = 10^{-4}\text{diag}(2.74, 1.72, 2.17)$. Indeed, both internal models achieve stabilisation showing only a slight increase in oscillatory response due to the uncertainty arising from the plant/model mismatch. This gives evidence that the modal approximation for the quaternions performs as efficiently as the spline method for moderate rotations also when applied to the *true* system.

We go even further to exploit the potential of MPC to place constraints on the states

to simulate a case where we constrain the vertical displacement of the base to be zero, emulating the scenario where the pendulum has to be controlled maintaining the base in a horizontal 2D plane. Employing the internal model equipped with the spline approximation and using the previously obtained MPC parameters applied to the *true* system, the obtained results are again very satisfactory. Despite a slower stabilisation of the pendulum as observed in Fig. 5.24 due to the extra constraints that the control inputs must satisfy, we see that the vertical displacement of the base in Fig. 5.25 is effectively suppressed.

Chapter 6

Numerical Examples II: Realistic Configurations

In this chapter, the control framework that has been validated and tested in the previous chapter solving fundamental examples is now used to explore fully coupled aeroelastic systems, where the control framework is further used to implement the dual problem of MPC: a moving horizon estimator. We consider clamped wing examples in § 6.1 and a free-flying vehicle in § 6.2, aeroelastically representative of HALE aircraft concepts, which highlight the need for nonlinear control to exploit unconventional stabilising mechanisms. Finally, the last example in § 6.3, focuses on the improvements obtained by means of data-driven modelling and its implications in control performance.

6.1 Aeroelastic Control of Very Flexible Clamped Wings

In this section, the control framework which has been, so far, used to solve purely structural control problems is employed for the first time in an aeroelastic setting. Before attempting to solve any control problem, the internal model for control constructed as in (3.79) is tested on open-loop test cases to study the validity of the linear aerodynamic model. In the aeroelastic setting, the control framework is augmented with the dual of the MPC problem: a moving horizon estimator (MHE). This is motivated by the fact that in typical aeroelastic applications sensors are limited, and the new aerodynamic states introduced by the the UVLM formulation are not trivially measured. This is in contrast

to purely structural applications, where the first few modes of the structure can be easily recovered from strategically located sensors, making full-state feedback (of the low-order internal model for control) essentially possible.

Two clamped wing models are studied here, after verification of our low-order aeroelastic framework fitted with a linear UVLM ROM (3.79), against a well known aeroelastic benchmark, namely the flutter analysis of the Goland wing [12]. The first one introduces a very flexible, high aspect ratio wing used in a gust alleviation control problem. This model will be the one we will use to assess the impact of the linearised aerodynamic model on the overall dynamics, comparing several open-loop test cases against solutions obtained with SHARPy [41]. This is Imperial College's nonlinear aeroelasticity toolbox, which, as previously described in 3.3.3, employs a (nonlinear) unsteady vortex lattice method coupled with a geometrically-exact, displacement-based beam model. The second case will put the control framework to the test with a flutter suppression problem of a very flexible wing with faster dynamics.

6.1.1 Gust Load Alleviation of a High Aspect Ratio Very Flexible Wing

A very flexible, high aspect ratio clamped wing in a variable speed flow is presented as test bed for the proposed aeroelastic control framework. The objective is to introduce a gust-load alleviation controller. The wing under test is a modified Goland wing (essentially a longer version, to increase the flexibility of the resulting wing) with geometrical and structural properties outlined in Table 6.1 and an aileron spanning the outboard 20% of the wing and 50% of the chord for control. An aerodynamic plane of symmetry is imposed on the y-z plane (the wing root) to simulate wall conditions that result in the lack of three dimensional effects at the wing root. The global frame of reference is located at the wing root and any angles specified will be defined at this point; local, body-attached frames are shown in Fig. 6.1 about which structural properties are defined. Note that aerodynamic sections are assumed to rotate rigidly about the elastic axis (i.e., there is no chordwise deformation in the aerodynamic surface).

The aerodynamic model employed in the MHE/MPC framework will be based on the system obtained linearising the SHARPy nonlinear UVLM reference with a prescribed wake model about the undeformed wing with 5 degrees angle of attack. The aerodynamic inputs and outputs are projected onto the structural coordinates, as schematically shown in Fig. 3.5, with the addition of three inputs: the aileron deflection, aileron deflection

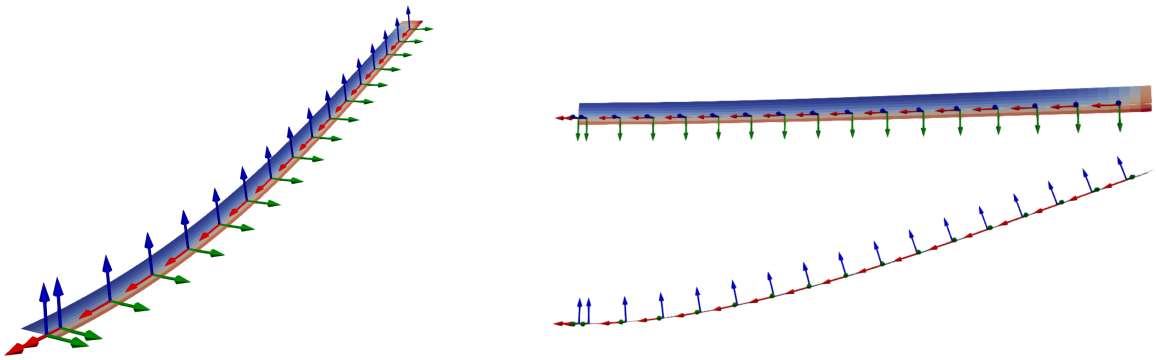


Figure 6.1: 3D, top and front views of the nonlinear aeroelastic equilibrium deformation. Displayed the local frames of reference x-red, y-green and z-blue. (By N. Goizueta)

Table 6.1: High aspect ratio, flexible wing properties

Span	L	45.72 m
Chord	$2b$	1.8288 m
Mass per unit length	μ	20.71 kg/m
Mass moments of inertia per unit length	I_{xx}	8.64 kg m
	I_{yy}	0.86 kg m
	I_{zz}	7.77 kg m
Out-of-plane bending stiffness	EI_{yy}	9.77 MN m^2
In-plane bending stiffness	EI_{zz}	977 MN m^2
Torsional stiffness	GJ	98.7 MN m^2
Axial stiffness	EA	1 MN
Shear stiffness	GA	10 MN
Centre of mass offset (in body-attached FOR)	$\boldsymbol{r}_{cm}$	$(0, -0.1829, 0)^\top$ m
Elastic axis from leading edge (in body-attached FOR)	$\boldsymbol{r}_{ea}$	$(0, -0.6035, 0)^\top$ m

rate and external flow vertical velocity at the leading edge. The resulting state-space is similar to that depicted in Fig. 3.5, where G_{gust} represents a gust system that convects the single gust input defined at the leading edge downstream to the rest of the wing and propagates it uniformly across the span.

A suitable discretisation for the aerodynamic grid and structural elements has been found by measuring the wing tip deflection and total aerodynamic forces from the SHARPy trimmed wing model until measurements converged, which resulted in a model discretised with 8 panels in chord, 64 panels in span (resulting in 32 structural beam elements) and an 80-panel wake (i.e., a 10-chord wake length). This equates to a linear system with 13321 states, including the gust system states. It is clear how this system is not suitable for control applications due to its large size, so a Krylov-subspace model order reduction is performed on the UVLM module to reduce it to a manageable size for control purposes, as discussed in § 3.2.3.

The Krylov-subspace ROM is obtained interpolating at the DC gain (steady-state) and only interpolating once to reduce the number of factorisations required. Contrary to the Goland wing verification case [12], where only the two first modes of the wing were retained in the flutter analysis, the input-output dimensionality of the current case is much larger, with 27 inputs and 12 outputs (the first twelve structural modes are used to construct the modal-based system), so even when the Krylov subspace order is reduced, the resulting ROM is of considerable size. However, to exploit the fact that the number of outputs is considerably smaller than the number of inputs, we can construct a single Krylov subspace on the observability side to obtain a single projector matrix W [63]. Since this matrix is orthogonal, we can take $V = W^\top$ and build the ROM as in (3.71). The result of building this ROM with a 3rd-order ($r_c = 3$) Krylov-subspace is a stable realisation with 36 states[1].

Prior to analysing the control problem, it is worth evaluating the impact, both structural and aerodynamic, that nonlinearities have on a wing capable of deforming significantly, and whether it is appropriate to use linear models as part of the MHE/MPC framework for these type of problems. Therefore, using SHARPy, the full nonlinear problem (nonlinear aerodynamics and structure) is compared against three modal-based low-order models (3.79) constructed with the first 12 natural modes of the beam, with varying degree of nonlinearity, all coupled with the same reduced aerodynamic model linearised around an undeformed initial condition. The three structural models and the associated labels used in results and figures consist of: i) a fully linearised model (3.79) around the undeformed configuration and linearised displacements equation (3.59) (*L struct*), ii) a linearised model (3.79) around the undeformed configuration retaining the kinematic nonlinear couplings, i.e., the rotation/displacement equations (3.41) (using a modal approximation to the quaternions (3.58), (3.57)) and (3.59) (herein referred to as semi-linear, *SL struct*) and iii) the original modal-based nonlinear model (3.79) and rotation/displacement equations (3.41) and (3.59) (*NL struct*). These are subject to three dynamic tests to evaluate the validity of the linear aerodynamics: a release from the undeformed initial condition at a 5 deg angle of attack at different air speeds (without gravitational forces), an external vertical velocity input and an aileron input (both with gravity effects). The last two simulations start from the nonlinear equilibrium condition in a 30 m/s wind with the clamped root section at 5 deg angle of attack — the deformed equilibrium state. All test cases that employ reduced linear aerodynamics use the same system that is linearised about the undeformed condition and defined in non-dimensional time. Consequently, the only parameters that vary are the scaling terms that depend on

[1]The construction of the ROM from SHARPy is the work of N. Goizueta.

the dynamic pressure and velocity in (3.72).

Dynamic Response of the Wing Released at Different Free Stream Velocities Without Gravity Effects

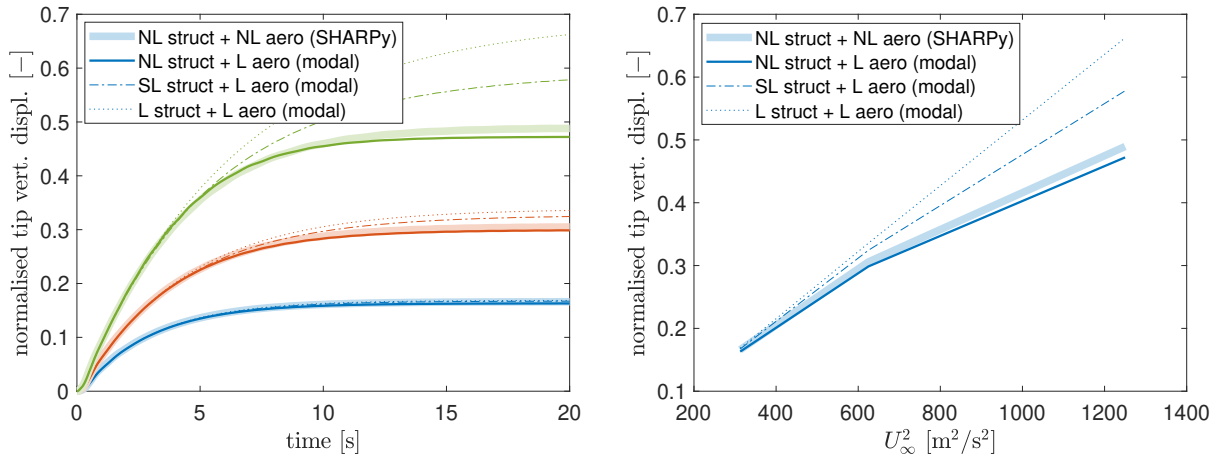


Figure 6.2: Dynamic response (left) of the wing release at three different free stream velocities. Steady state values against velocity squared shown on the right. (SHARPy results by N. Goizueta)

Fig. 6.2 shows the vertical wing tip displacement over time when the wing is released from the undeformed condition at 5 deg angle of attack and three different free stream velocities: 17.67 m/s, 25.00 m/s and 35.35 m/s (blue, red and green in Fig. 6.2). This corresponds to a doubling in dynamic pressure (with constant density $\rho = 1.02\,\mathrm{kg/m^3}$) at each step to visualise the effects of nonlinearity with greater ease. At the lowest velocity, all models show a steady-state wing tip displacement approaching a vertical displacement of 17% span, matching well with the nonlinear reference response predicted by SHARPy. However, as velocity is increased to double and quadruple the initial dynamic pressure, the discrepancy is most apparent in the linear structural models. Fig. 6.2 also shows the static equilibrium wing tip position from where it is clear how the nonlinear structural models differ from the linear trend established by the fully linearised model as dynamic pressure is increased.

Since all models but SHARPy's employ the same linear aerodynamics, it is clear that the greatest source of error emanates from the use of a linear structural model, unable to capture important physics such as the follower force effects as the wing deforms. On the other hand, the case with the nonlinear structural model shows very good agreement compared to the SHARPy reference. Only a small underestimation of the deflection is observed at the highest speed where the wing deforms to a considerable 48% of span

(the deformed wing in these conditions was shown in Fig. 6.1) despite the use of linear aerodynamics. Since this case employs a nonlinear structural model, the discrepancies between it and SHARPy can be attributed mainly to the differences between linear and nonlinear aerodynamics. This is supported by structural-only comparisons between the nonlinear modal-based structural model and SHARPy structural model that have shown excellent comparisons as seen, for instance, in the first numerical example of the chapter.

The linear aerodynamic model differs with its nonlinear counterpart in the assumption of small perturbations to the grid coordinates such that the aerodynamic influence coefficients (AICs) become constant and the wake frozen in shape. In the nonlinear case in which AICs change as the wing deforms, the influence that bound panels have on each other changes. Under significant nonlinear deformation, the greatest variations in geometry are most obvious in a global sense, where, for instance, the distance between root and tip panels is reduced. However, since the influence between panels is governed by the Biot-Savart law, inversely proportional to their relative distance squared, the differences become negligible [67]. On the contrary, the linearised formulation would impose a heavier penalty on systems with large local deformations (e.g., the free flapping wingtip concept of [161]), unlike the present case (Fig. 6.1). Therefore, it is unlikely that the linearisation of the AICs in the UVLM formulation is directly responsible for the mismatch.

The small differences observed at 35 m/s in Fig. 6.2 are due to the negative twist deformation (washout) that the wing experiences and its effect (a reduction in lift) being more notable in the linear case. The reason behind this resides in the use of linear projectors to map the position and rotation of the structural nodes onto the aerodynamic grid coordinates. The linear transformation K_ζ in Fig. 3.5 causes an effective change of chord length at a particular section when the beam is twisted. In other words, the linear rotation of a section results in a projection of the chord, increasing its effective length and therefore generating more lift, effect that would scale linearly with the twist angle. Nonetheless, this error that results from the linearised aerodynamic model at significant deformations is below 4% of the span, which justifies its use as a controller model.

Input-Output Dynamic Tests with Gravity Effects

The remaining two tests explore how well the aeroelastic response is captured by the reduced linear aerodynamic system in comparison to the SHARPy reference when the system is excited by an external vertical gust or an aileron input. Fig. 6.3 shows the wing tip vertical displacement over time for the two cases, both starting from the equilibrium (trim) condition when the root section is clamped at 5 deg in a 30 m/s uniform wind. The

vertical gust profile consists of a 2 s ramp to -3 m/s and constant thereafter. Similarly, the aileron input is a 2 s ramp to a -5 deg deflection (positive downwards) that is then held constant. Again, the comparison between the two models which differ particularly in the aerodynamics shows a very similar deflection, with the reduced model capturing well both the transient and steady-state response. This is of particular importance in maintaining the assumption that reduced linear aerodynamics can be used as representative model for control, since the effect of both external disturbances and aileron inputs are very well matched when compared to the nonlinear, full-order UVLM even when the wing experiences significant deflection. Finally, the smoothness and damping of the response are worth commenting upon. Both with linear and nonlinear aerodynamics, the introduction of external inputs do not excite any higher-order structural modes and the bending response is significantly over-damped. These slow dynamics are likely attributed to the large inertia of the wing requiring a significant disturbance to excite higher-order modes and beneficial for the control problem, since a larger sampling time may be sufficient to capture the relevant dynamics.

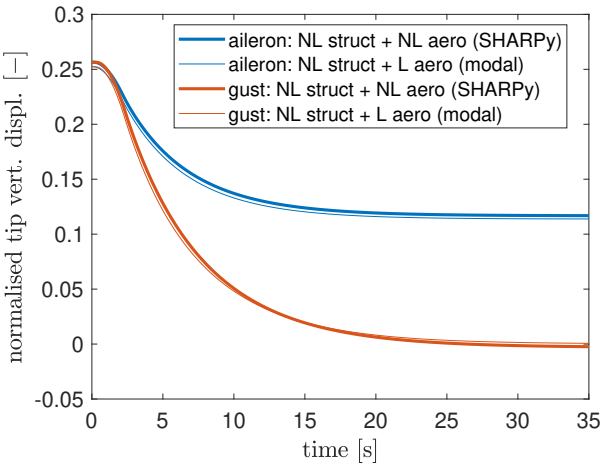


Figure 6.3: Comparison of the dynamic response of the wing to external gust and aileron inputs with SHARPy nonlinear reference. (SHARPy results by N. Goizueta)

From these tests it is clear that using a reduced, linear aerodynamic model is not detrimental when attempting to capture the dynamic aeroelastic response of a very flexible wing, provided that the structural model is capable of capturing the geometric nonlinearities present. Removing them from the structural description produces significant mismatch with respect to the full nonlinear model, whereas the choice of a linear aerodynamic model introduces only small errors even when deflections are significant when compared to the linearisation state. Hence, our assumption that the linear aerodynamic model coupled with the modal-based nonlinear structural model can be used as part of a model predictive control framework to control clamped structures with considerable deformations is

justified and will be demonstrated in the following section.

Estimation and Control in a Gust Alleviation Problem

The previously described wing, with structural properties gathered in Table 6.1, is now used in a gust-load alleviation (GLA) problem set-up, where the nonlinear estimation and control strategies described in Chapter 4 are employed. The wing, with a root angle of attack of 5 deg, is initially at equilibrium in a flow with airspeed $U_\infty = 25$ m/s in the positive y-axis of the global frame of reference (see Fig. 6.1) and density $\rho = 1.02$ kg/m^3. The external forces are gravity, which acts along the negative z-axis of the global frame of reference, and a $1 - \cos$ shaped gust

$$w_g(t) = \frac{W}{2}\left(1 - \cos\left(\frac{\pi U_\infty (t - t_g)}{H_g}\right)\right)\left(\mathcal{H}\left(t_g\right) - \mathcal{H}\left(t_g + \frac{2H_g}{U_\infty}\right)\right), \tag{6.1}$$

which reaches the wing root leading edge at $t_g = 0.1$ s, with intensity $W = 2$ m/s, span $H_g = 90$ m and $\mathcal{H}(t)$ denoting the Heaviside step function at time t.

Both the estimator and controller employ the nonlinear low-order model (3.79), equipped with the first 12 modes (ordered in ascending natural frequency) of the structure. Modal displacements $\boldsymbol{q}_0$ are computed by direct time integration of modal velocities (3.73). The aerodynamic model corresponds to the reduced order model of the linearised UVLM at a 5 deg angle of attack configuration, as described in the previous section. On the other hand, we use a finite element discretisation of the nonlinear intrinsic equations (2.22)–(2.23), as described in the appendix C, to model the controlled system structural dynamics plus linearisation of a UVLM, which uses the FE solution as nodal inputs and has undergone a mild model reduction process. This is done to ease and speed up the simulation of the controlled system, since the resulting UVLM has a size of the order $\mathcal{O}(10^4)$. This model already provides us with sufficient plant-model mismatch to assess the performance and robustness of both the estimation and control strategies.

Here, the continuous-time version of the open-loop nonlinear optimal control problems (4.1) and (4.11) (where the cost function involves integration over time of the quadratic penalties) are solved until the Karush–Kuhn–Tucker (KKT) conditions are satisfied with a tolerance of 10^{-4} and 10^{-5} (for the MHE and MPC problems, respectively). Three different control scenarios have been considered, to showcase diverse optimisation parameters. The first case uses a sampling period of $\tau_s = 0.25$ s with $N_e = 12$ and $N_c = 24$ with input constraints (deflection rate) $\dot{\delta}_{\max} = -\dot{\delta}_{\min} = 10$ deg/s and state constraints (deflection angle) $\delta_{\max} = -\delta_{\min} = 5$ deg. To assess the effect on performance of control saturation,

the second case is set up with the exact same parameters as the first one except for no constraints on the deflection rate or angle. The chosen sampling period is of the order of a fifth of the period associated to the third and fourth natural modes of the structure (with frequencies of 1.14 and 1.20 Hz). This rather small sampling time should increase robustness of the controller/estimator against model mismatch errors. The estimator horizon is of the order of half the period of the first mode (bending), with a frequency of 0.18 Hz, while the control horizon is of the same order of this low frequency mode. These are deemed to be sufficient for successful estimation and control performance, as suggested by the numerical findings. Finally, a third case, with no control saturation and where the sampling time has been doubled is considered to show the control performance sensitivity with respect to the latter parameter.

In all cases the MHE receives measurements of the translational velocities at four different stations of the wing, $0.25L$, $0.5L$, $0.75L$ and L, with weighting matrix Q_e equal to the identity, while the MPC penalises the perturbed energy of the system with respect to the static deformed configuration by setting $Q_c = \text{blkdiag}(0_{N_m}, I_{N_m}, I_{N_m}, 0_{N_m+1}, 0_{N_\Gamma}, 0)$ and $\bar{\boldsymbol{q}}_{ae}$ the equilibrium point of (3.79) at $U_\infty = 25\,\text{m/s}$. The gust intensity is estimated by the MHE as the external disturbance to the sytem.

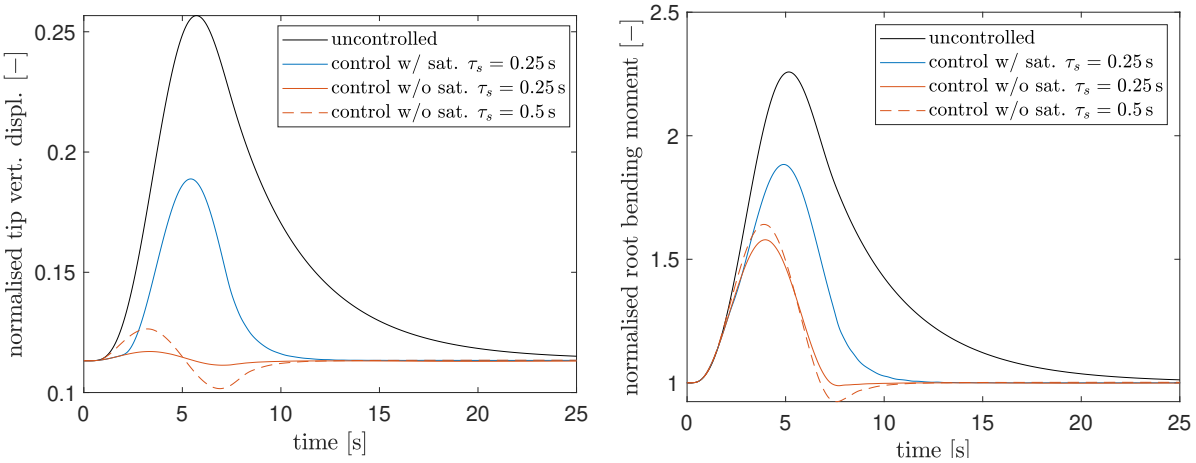


Figure 6.4: Normalised wing tip vertical displacement (left) and root bending moment (right).

Fig. 6.4 shows the vertical displacement as a fraction of the wing span and the wing root bending moment normalised with the value at static initial equilibrium ($-99.79\,\text{kNm}$) for the three different controlled scenarios and the uncontrolled case. As observed, in the uncontrolled case the gust causes the wing tip to experience a deflection 2.27 times that of the static equilibrium. All control cases achieve successful reduction in the deflection, with the faster, no-saturation, case virtually suppressing it. It is also revealed that

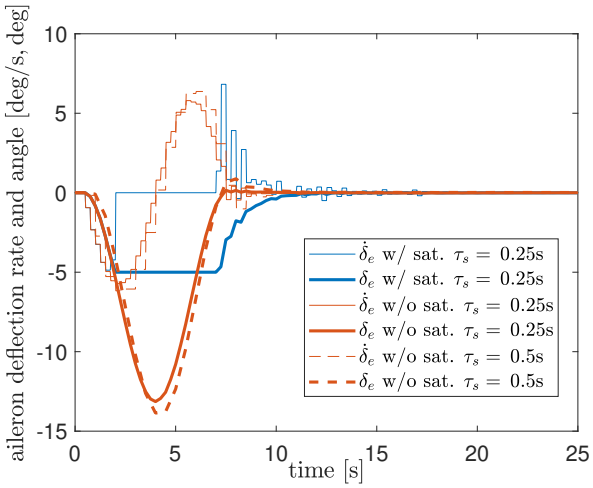


Figure 6.5: Aileron deflection rate (control input) and deflection angle.

increasing the sampling time reduces the suppression performance. Regarding the root bending moment, a key metric in gust load alleviation, the gust produces a maximum moment of 2.26 times that of the static equilibrium. Again, both the saturation and unconstrained control scenarios reduce notably the load at the root, 16.61% and 30.35% peak load reduction, respectively (slightly lower 27.40% for the slower controller), but most importantly they decrease the time the wing is being overloaded.

The corresponding control inputs are gathered in Fig. 6.5, where the blue lines belong to the case with saturation, where the aileron deflection angle reaches its minimum allowed deflection, and the red to the unconstrained ones (dashed lines corresponding to the slower control case). These commands would be very unlikely to be achieved by conventional control strategies such as, for example, a PID controller. For a PID controller, the response is a reaction to some chosen measurement and highly sensitive to the local placement of the sensor. For instance, in the unconstrained case, we see that our method, using knowledge of the system physics and penalising globally the perturbed energy of the system, is able to virtually suppress the wing tip-displacement, as shown in Fig. 6.4. If a PID controller was employed, measuring the wing-tip vertical velocity, such a reduction would not be possible since measurements would be nearly zero and no control would be applied. If strains were to be used to feed the PID instead, the controller would need very fine tuning to not overreact (since strains are rather high even when the wing displacements are negligible). Another important advantage is that MHE and MPC parameters are less case-dependent, and similar outcomes using the same set-up should be expected for gusts of varying intensities and spans. Moreover, constraints in the control inputs are seamlessly embedded in the optimal control problems, while their addition to other control techniques may result in less elegant and rather cumbersome approaches.

6.1.2 Flutter Suppression of a Pazy Wing Model

The Pazy wing [19] shown in Fig. 6.6 is a very flexible wing model designed as an aeroelastic benchmark case that inspires the demonstrator for the proposed control framework. The original wing, conceived to be tested in a wind tunnel, is 55 cm in span and 10 cm in chord and consists of a rectangular aluminium spar with evenly spaced Nylon ribs with a NACA0018 airfoil profile. An Oralight skin covering the ribs gives the wing its aerodynamic shape. Finally, a Nylon wing tip rod is fitted to modify the wing dynamics and reduce the first torsional mode frequency. The control problem at hand employs an approximated wing model, with constant spanwise stiffness and inertia properties, that are listed in Tables 6.2, 6.3 and 6.4. The frame of reference in which these properties are expressed corresponds to the local frame of reference, x being along the beam reference line positive outboard, z pointing upward and y completing the set. A simulated aileron located on the outboard 20% of span and 50% chord that will be used as the control input. Later iterations of the Pazy wing model have been explored by Goizueta *et al.* in [64].

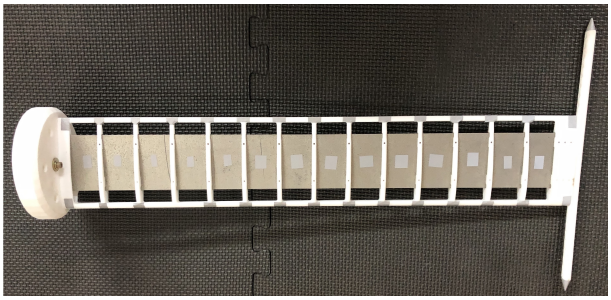


Figure 6.6: Pazy wing experimental model.

Table 6.2: Beam model stiffness matrix.

Axial stiffness	EA	7.16 MN
Out-of-plane shear stiffness	GA_y	1 MN
In-plane shear stiffness	GA_z	3.31 MN
Torsional stiffness	GJ	7.2 N m^2
Out-of-plane bending stiffness	EI_{yy}	4.67 N m^2
In-plane bending stiffness	EI_{zz}	3.31 kN m^2

The stability analysis[2] of this constant-properties version of the wing shows that the dynamic stability is dependent on the wing deflection, which in open-loop conditions is a unique function of the root angle of attack and the dynamic pressure. The results in Fig. 6.7, obtained using the Pazy wing model in SHARPy, show that the flutter speed decreases with angle of attack because of the increased wing deflection. In the frequency

[2]Stability analysis by N. Goizueta work.

Table 6.3: Beam model mass and geometrical properties.

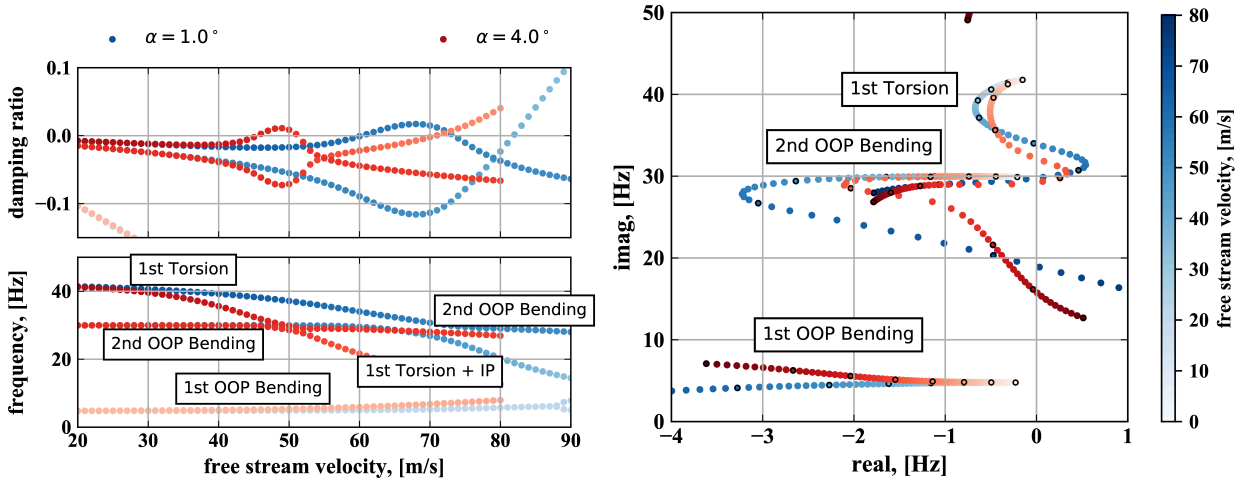
Span	L	$0.55\,\mathrm{m}$
Chord	$2b$	$0.1\,\mathrm{m}$
Elastic axis reference line	$y_{\mathrm{ea}}/(2b)$	0.0
Leading edge line	$y_{\mathrm{le}}/(2b)$	0.4475
Centre of gravity line	$y_{\mathrm{cg}}/(2b)$	-3.5×10^{-3}
Mass per unit length		$0.55\,\mathrm{kg/m}$
Inertia per unit length	I_{xx}	$3.030 \times 10^{-4}\,\mathrm{kg\,m}$
	I_{yy}	$1.515 \times 10^{-4}\,\mathrm{kg\,m}$
	I_{zz}	$3.636 \times 10^{-3}\,\mathrm{kg\,m}$

Table 6.4: Wing tip rod mass and inertia properties.

Position	$\boldsymbol{r}_{\mathrm{b}}$	$(0.555, -0.005, 0)^{\top}\,\mathrm{m}$
Mass	m_{rod}	$19.95\,\mathrm{g}$
Inertia	I_{xx}	$1.2815 \times 10^{-4}\,\mathrm{kg\,m^2}$
	I_{yy}	$2.87 \times 10^{-7}\,\mathrm{kg\,m^2}$
	I_{zz}	$1.17 \times 10^{-4}\,\mathrm{kg\,m^2}$

plot in Fig. 6.7a it is illustrated how flutter occurs at the coalescence of the first torsion and second out-of-plane bending modes, an event that is brought forward by larger deformations which are driven by an increase in angle of attack. However, the first flutter mode can be stabilised by further increasing the deflection. In open-loop, for a given angle of attack, this can be achieved by increasing the free stream velocity, which leads to the *hump* in positive damping ratio seen in the V-g plot. To further explore the relation between stability and deflection, Fig. 6.8 shows the stability boundaries for different deflections and velocities. The region of instability of the first flutter mode is clearly seen and also how that mode becomes stable after a certain deflection. The instability seen at larger deformations corresponds to the first torsion and first bending flutter mode, that has a much higher onset of instability speed. This dependency of flutter on the wing deformation can be used as leverage by the controller as, in closed-loop, the aileron can be used to change the deflection of the wing to alter the stability properties, which on Fig. 6.8 would correspond to moving in a roughly horizontal line (for a constant velocity).

As indicated by the stability analysis results, this wing makes for a compelling flutter-suppression problem, where both the nonlinear estimation and control strategies described in Chapter 4 are put to the test. The wing is released from the undeformed configuration with a root angle of attack of $4\,\mathrm{deg}$ in a uniform flow with airspeed $U_\infty = 50$ m/s and density $\rho = 1.225$ kg/m^3. Besides the aerodynamic forcing, the other actuating external force is gravity. As shown in Fig. 6.7 and Fig. 6.8, such an airspeed places the wing within the first unstable regime, and soon after its release (from around $t > 0.5\,\mathrm{s}$) flutter starts



(a) (b)

Figure 6.7: Stability analysis of the wing with (a) stability plot at two non-zero angles of attack and (b) root locus diagram. (Figures by N. Goizueta)

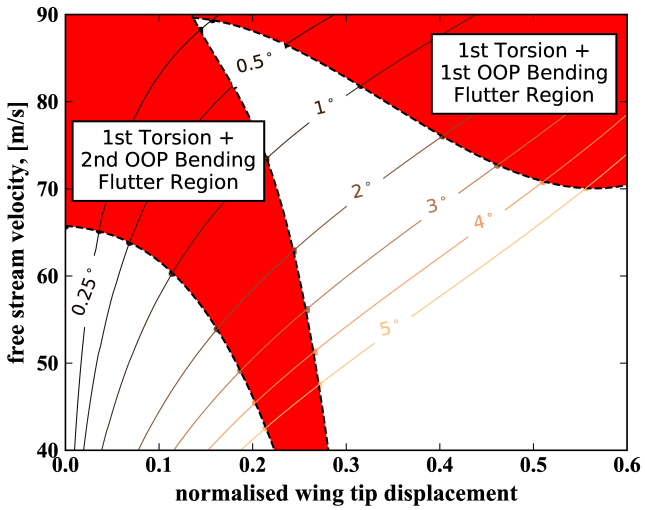


Figure 6.8: Wing flutter instability regions. (Figure by N. Goizueta)

to develop. It is then that the control framework (nonlinear MHE and MPC) is switched on.

The model used within the estimation and control strategies is the modal-based system (3.79), constructed with 9 modes: the first three out-of-plane bending, the first three torsion, the first two in-plane bending and the first axial modes of the structure. The aerodynamic model corresponds to the reduced order model of the linearised UVLM at a rigid 4 deg root angle of attack configuration[3], following a Krylov-based model-order reduction process [13]. The original UVLM employs a spanwise discretisation using 128

[3]The ROM model is obtained by N. Goizueta.

nodes, a chordwise discretisation which divides the chord into 8 intervals and a wake extending 8 chord lengths, resulting in a system with 11,273 states: this is unmanageable for NMPC/NMHE. Similarly to the control cases with the previous wing model, we set up the closed-loop control problem using a finite element discretisation of the nonlinear intrinsic equations (2.22)–(2.23) to model the controlled system structural dynamics coupled to a full-order linearisation of the UVLM.

As shown in the following two subsections, by slightly modifying the control parameters the controller aims to suppress oscillations induced by flutter via two completely distinct actuation mechanisms: while the first one opts for the more obvious response where the aileron is deflected in an oscillatory manner to directly counteract flutter, the second one consists of a less evident response where the aileron aim is to increase the wing deformation to take it outside of the unstable region, where the controller knowledge of the wing stability around nonlinear equilibria is exploited. In both set of results, the open-loop nonlinear optimal control problems (4.1) and (4.11) are solved until the KKT conditions are satisfied with a tolerance of 10^{-4} for both the MHE and MPC problems.

Flutter Suppression Via Direct Actuation

In this case, both the estimation and control problems are set up with a rather small sampling time of $\tau_s = 0.0025\,\text{s}$ (≈ 0.075 times the flutter oscillation period, τ_f), with equal estimation and control horizons of $\tau_e = \tau_c = 0.06\,\text{s}$ ($\approx 1.8\tau_f$). Similarly to the previous GLA problem, involving the high-aspect ratio wing, the MHE measures the translational velocities at four different stations of the wing: $0.25L$, $0.5L$, $0.75L$ and L, with weighting matrix $Q_e = 0.1I$. Here, the cost function of the MHE optimisation problem (4.11) is enhanced by adding the weighing term $P_e = \text{blkdiag}(I_{N_m}, 0_{N_m}, I_{N_m}, I_{N_m+1}, I_{N_\Gamma}, 1)$, which penalises deviations on all the states except for the velocities, which due to flutter, are subject to large variations. To suppress flutter oscillations, the MPC cost function only places a penalty on velocity, with $Q_c = \text{blkdiag}(0_{N_m}, I_{N_m}, 0_{N_m}, 0_{N_m+1}, 0_{N_\Gamma}, 0)$ and two different control constraints on aileron deflection have been explored: a stricter constraint of $\delta_{\max} = -\delta_{\min} = 5\,\text{deg}$ and a more permissive one of $\delta_{\max} = -\delta_{\min} = 15\,\text{deg}$.

With this choice of parameters, the controller actuation is an oscillatory one as seen in Fig. 6.9, where the flap is deflected synchronously to the flutter vibrations in order to directly counteract its effect. In both cases, the controller reaches the aileron deflection saturation limits, capping the actuation in the more tightly constrained case a more prolonged time, as clearly seen in the bottom plot of Fig. 6.9. The outcome of both control inputs is a wing which experiences a transition from the free flutter oscillations

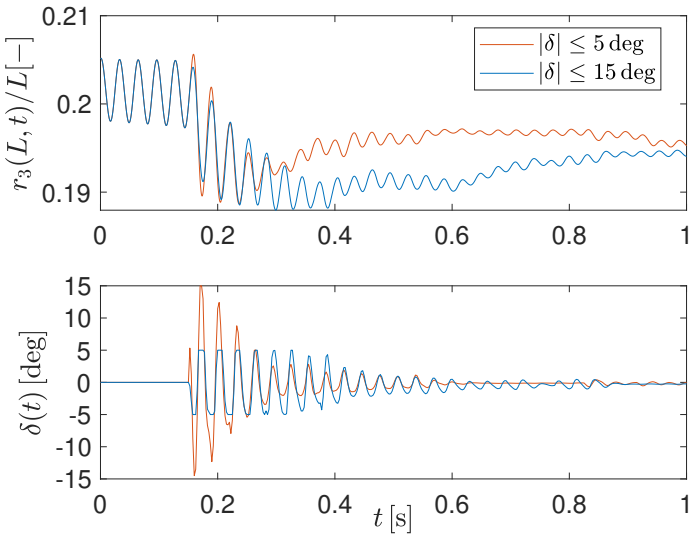


Figure 6.9: Normalised wing tip displacement and aileron deflection vs time for the flutter suppression direct actuation mechanism.

to a forced response driven by the flap actuation, where oscillations are intensified during the few instants following the activation of the controller at $t = 0.15\,\mathrm{s}$ in Fig. 6.9, and with a final substantial reduction in the flutter oscillations: a decrease of over an 80% in the amplitude of the wing-tip vertical deflection, in both saturation cases, is obtained. Where stricter saturation limits are applied, the transition oscillations are milder but are extended over a longer period of time. Due to the plant-model mismatch, the controller is observed to react occasionally after the main suppression is achieved (e.g., at around $t = 0.85\,\mathrm{s}$) in both cases, however showing a robust behaviour throughout the simulated time window.

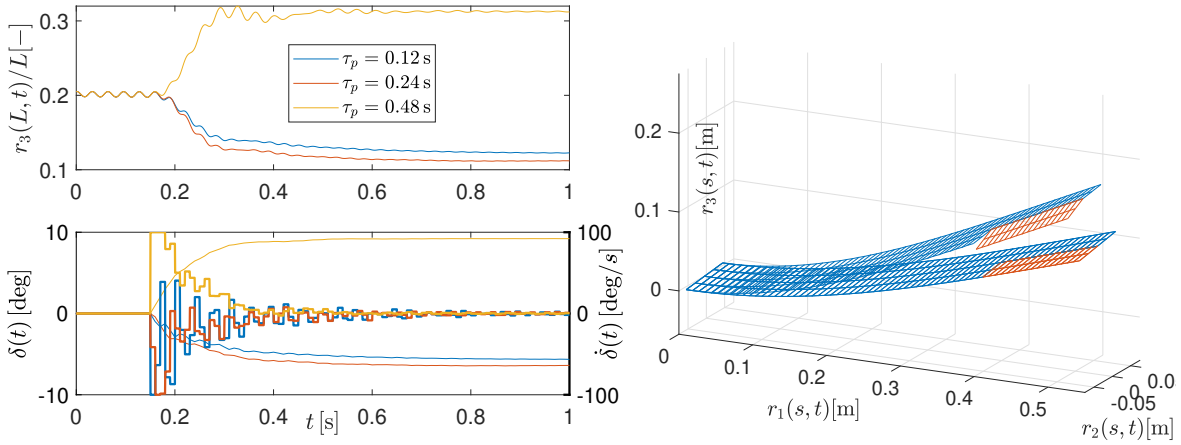
Flutter Suppression Via Deformation Control

For this second flutter suppression case, the estimation/control framework uses a longer sampling time of $\tau_s = 0.01\,\mathrm{s}$ (≈ 0.33 times the flutter oscillation period, τ_f), with an estimation horizon of $\tau_e = 0.12\,\mathrm{s}$ ($\approx 3.6\tau_f$). Three different values for the prediction horizon have been explored, ranging from $\tau_e = 0.12\,\mathrm{s}$ ($\approx 3.6\tau_f$) to $\tau_e = 0.48\,\mathrm{s}$ ($\approx 14.4\tau_f$). The MHE measures the same variables as in the previous case with identical additional penalty term $\|\boldsymbol{q}_{ae} - \boldsymbol{q}^e_{ae,r}\|_{P_e}$. Here, the MPC also penalises the velocity states only, with $Q_c = \mathrm{blkdiag}(0_{N_m}, I_{N_m}, 0_{N_m}, 0_{N_m+1}, 0_{N_\Gamma}, 0)$, but an additional terminal penalty with $P_c = 5Q_c$ is added. Control constraints on aileron deflection and deflection rate of $\delta_{\max} = -\delta_{\min} = 15\,\mathrm{deg}$ and $\dot{\delta}_{\max} = -\dot{\delta}_{\min} = 100\,\mathrm{deg/s}$ are placed with mild actuation penalty $R_c = 0.01$.

With this set of parameters, characterised by a longer prediction horizon than the previous test case, a higher penalty on the velocity states at the end of the prediction horizon and a light actuation penalty, the controller opts for an alternative minimum. This consists of a change in the deformation state of the wing to configurations where the initial flutter instability is no longer present and aerodynamics are more dissipative, which favours the control purpose of dampening out the residual oscillations.

As seen in Fig. 6.10a, for the longest prediction horizon case, the flap is deflected in a rather smooth way from an initial 0 angle to a constant final angle of 9.2 deg. This leads to the wing increasing its deformation gradually until it stabilises at a normalised wing tip deflection of 31% (see Fig. 6.10b) while experiencing some oscillations during the transient period (from $t = 0.2$ to $t = 0.4$ s in Fig. 6.10a) which die out fairly rapidly thanks to the increased aerodynamic damping acting on such deformed regime. As the prediction horizon is decreased, a change in the target local minimum of the MPC is observed, as shown by the red and blue lines of Fig. 6.10a, where the closed-loop response is now a wing moving towards a less deformed state, achieved by a negative aileron deflection, which effectively brings the structure outside the instability region too (note how for $U_\infty = 50$ m/s escaping the unstable region can be achieved by either moving horizontally to the left or to the right). The rationale behind this change in the response is not trivial, and to avoid this bistable closed-loop response a further penalty on larger/smaller deformations might be considered. It is observed, however, that when the prediction horizon is long enough less actuation is required, as suggested by a less oscillatory flap deflection rate in Fig. 6.10a, possibly since aerodynamic damping is given more time to damp out the remaining oscillations. For shorter predictive horizons, this damping has less effect and a more oscillatory response of the controller is required to attenuate vibrations throughout the transient response.

This set of results is indeed very remarkable, since the ability of the controller to predict the different stability regions arising from varying levels of deformation, leveraging the full-nonlinear simulations that underpin the framework, is highlighted. Even control approaches, based on successive linearisations around instantaneous configurations, which are usually labelled as nonlinear control strategies too, would not be able to recreate such a response. This case demonstrates, again, that despite the use of linear aerodynamics, the main nonlinear phenomena that is present in the dynamics of aeroelastic systems is successfully captured by the modal-based system and hence it provides a very suitable model to underpin nonlinear MHE and MPC strategies.



(a) (b)

Figure 6.10: (a) Normalised wing tip displacement, aileron deflection and rate for the deformation-control-based mechanism and (b) 3D view of the initial and final wing configurations.

Control using a Realistic Plant Model

The example above is an exercise on MPC design, enabled by using less computationally demanding simulation models (yet higher-resolved versions of the internal control models), that was carried out to determine the diverse flutter suppression control mechanisms on such wing model.

An interface to communicate the simulation platform SHARPy with the control framework[4] by means of a user datagram protocol (UDP) is implemented to test the control framework in the more realistic scenario offered by fully nonlinear aeroelastic simulations of SHARPy. Based on the knowledge gained with the previous exercise, the control framework is built similarly using the first nine structural modes of vibration: the first three out-of-plane bending, the first three torsion, the first two in-plane bending and the first axial modes of the structure. The aerodynamic model is a reduced order model of the linearised UVLM at a 4 deg angle of attack configuration with 42 states. Now, the modal forces vector $\boldsymbol{q}_2$ is used to compute the modal displacements $\boldsymbol{q}_0$, as in (3.78).

As it was found, smaller sampling times with shorter estimation and control horizons lead to a *direct actuation* flutter-suppression mechanism, where the flap deflection counteracted the flutter vibrations with an oscillatory response. However, when longer sampling times with also longer control prediction horizons were chosen, the controller was seen to switch to a nonlinear-exploiting mechanism, acting via deformation control, where the wing was

[4]The implementation of the UDP interface in SHARPy is the work of N. Goizueta

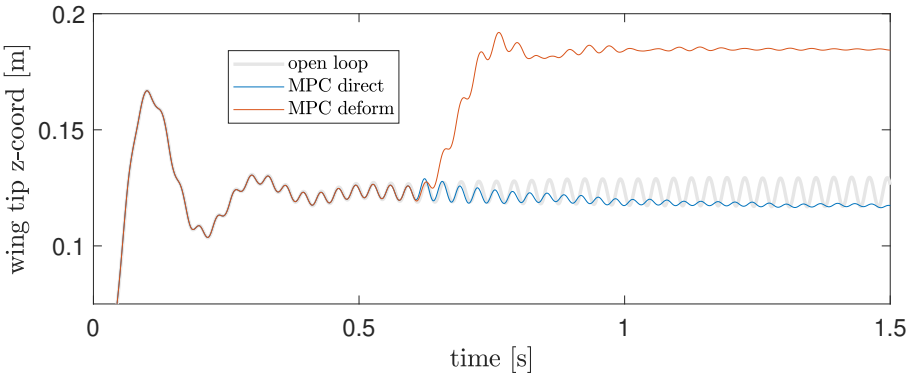


Figure 6.11: Time history of the vertical displacement of the Pazy wing for the open-loop and control cases.

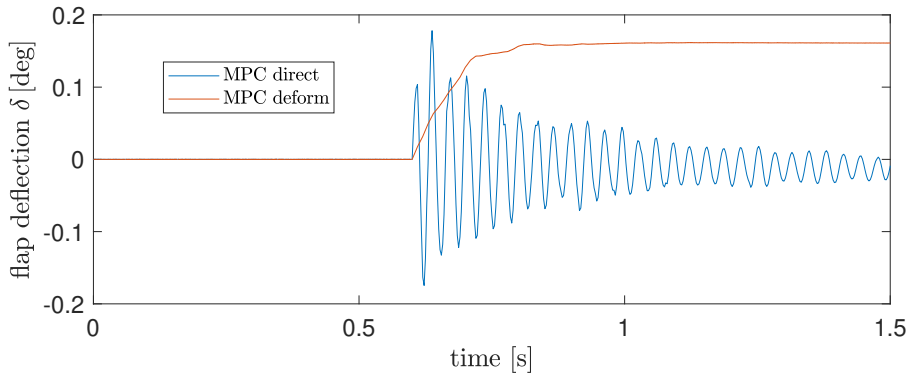
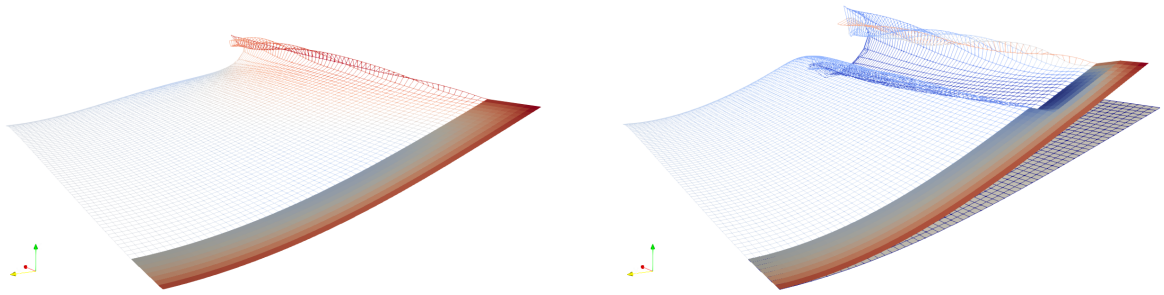


Figure 6.12: Time history of the flap deflection for the two considered control cases.

brought to a more deformed stable configuration. Based on this prior knowledge we construct two similar MPC setups to the ones described in the previous example aiming to reproduce, now using SHARPy as a host to simulate the controlled system[5], the same observed control mechanisms. For this purpose, for the *direct actuation* setup, a sampling time of $\tau_s = 0.0025\,\text{s}$ is chosen (≈ 0.075 times the flutter oscillation period, τ_f), with equal estimation and control horizons of $\tau_e = \tau_c = 0.06\,\text{s}$ ($\approx 1.8\tau_f$). The MPC cost function only places a penalty on velocity states, with $Q_c = \text{blkdiag}(I_{N_m}, 0)$ and a control constraint on flap deflection $|\delta| \leq 15\,\text{deg}$. For the *deformation control* case, a longer sampling time of $\tau_s = 0.01\,\text{s}$ (≈ 0.33 times the flutter oscillation period, τ_f) is selected, with an estimation horizon of $\tau_e = 0.12\,\text{s}$ ($\approx 3.6\tau_f$) and a prediction horizon of $\tau_e = 0.48\,\text{s}$ ($\approx 14.4\tau_f$). The MPC also penalises the velocity states only, with $Q_c = \text{blkdiag}(I_{N_m}, 0)$, but an additional terminal penalty with $P_c = 5Q_c$ is considered. Control constraints on aileron deflection and deflection rate of $|\delta| \leq 15\,\text{deg}$ and $|\dot{\delta}| \leq 100\,\text{deg/s}$ are placed with mild actuation penalty $R_c = 0.01$. In both cases, except for the distinct horizons, the

[5]SHARPy model for the closed-loop simulations was set up by N. Goizueta

MHE is configured analogously: the translational velocities at four different locations of the wing ($0.25L$, $0.5L$, $0.75L$ and L) are measured, with weighting matrix $Q_e = 0.1I$. An enhancing penalty weight $P_e = \text{blkdiag}(0_{N_m}, I)$ is considered aimed at providing some knowledge about the static deformation about which flutter develops.



(a) (b)

Figure 6.13: Pazy wing (a) at 0.5s in flutter prior to control actuation and (b) at 1.5s once the controller increases the wing deflection to suppress flutter, with the open loop counterpart shown in dark shade. (Figures by N. Goizueta)

Showing exceptional robustness and consistency, very similar results are now obtained when the low-order control framework is employed to stabilise the model of the Pazy wing in SHARPy. The main difference from previous results resides in the fact that the controller is now applied to an aeroelastic model based on a full nonlinear aerodynamic description. The successful outcome in this more realistic scenario further justifies our choice of an internal linearised aerodynamic model, reinforcing the idea that the effect of nonlinear AICs in the resulting aerodynamic forces is negligible when compared to the follower force effect, which is captured with our model. Gathered in Fig. 6.11 are the wing tip vertical displacement histories for both control cases superimposed to the open-loop simulation. We observe that after release of the wing, the onset of flutter occurs around $t = 0.4\,\text{s}$ while the controller is switched on at $t = 0.6\,\text{s}$. The behaviour of the nonlinear controller in this more realistic scenario confirms the performance predicted in the previous design synthesis exercise. In the *direct* actuation setup, an oscillatory deflection of the aileron is produced, which counteracts in a direct manner the flutter-induced vibrations, as shown in Fig. 6.12. The *deformation* control setup, opts for a rather smooth deflection of the aileron to bring the structure to a higher deformation level, hence exploiting the nonlinear knowledge that this new configuration is a stable region. This actuation mechanism would correspond to an increase in deformation (abscissa axis) for constant velocity $U_\infty = 50$ of a point that originally sits in the unstable region depicted in Fig. 6.8 (corresponding to $U_\infty = 50\,\text{m/s}$ and $\alpha = 4\,\text{deg}$), where the increase in deformation

is achieved, now, via aileron deflection instead of via root angle of attack.

While both actuation mechanisms achieve effective flutter suppression, as seen by the reduction in tip oscillation amplitudes in Fig. 6.11, the *deformation* control strategy achieves virtual complete suppression, since the oscillations will eventually die out due to the stabilising aerodynamic damping present in such configuration. The higher-deformation configuration to which the wing is brought as a result of the MPC feedback is compared to the initial unstable configuration in the two snapshots of the simulation in Fig. 6.13, corresponding approximately to the time instants $t = \{0.5, 1.5\}\,\mathrm{s}$. In this figure, the nonlinear aerodynamic formulation in SHARPy is shown quite visually in the form of the wake roll-up at the wing tip, caused by the influence of wake vortices on one another and their ability to rotate freely in space.

6.2 Aeroelastic Control of a Very Flexible HALE Concept Aircraft

To demonstrate the capabilities of the MPC-MHE framework on a very flexible aircraft we make use of a High-Altitude Long-Endurance concept, employed by del Carre *et al.*, who provide a detailed description of the model in [44]. The HALE aircraft, shown schematically in Fig. 6.14, has a traditional configuration with a high aspect ratio (32) main wing and a T-tail mounted tailplane, where the control surfaces — a rudder and an all-moving elevator — are located. The weight of the aircraft is 78.25 kg including a 50 kg payload at the wing-fuselage intersection, point at which the propeller is also located. This central heavy payload causes the aircraft wings to deflect significantly in trimmed flight, forming a characteristic U-shape. The cruise speed for this aircraft is in the range of $10 - 15\,\mathrm{m/s}$. No propulsion or control surface actuator systems are modelled, thus the control inputs to the aircraft will be thrust applied directly at the propeller location and the deflection and rate of the control surfaces.

6.2.1 Rigid and Flexible Trim Solutions

Since the aim of our control internal model (3.79) is to provide an accurate proxy for the *ground truth* system modelled in SHARPy, we start by comparing the static solutions for the HALE aircraft, which are essential to set up the control and estimation problems with the reference values $\bar{\boldsymbol{q}}_{ae}$ and $\bar{\boldsymbol{u}}$. The internal aeroelastic system for control (3.79)

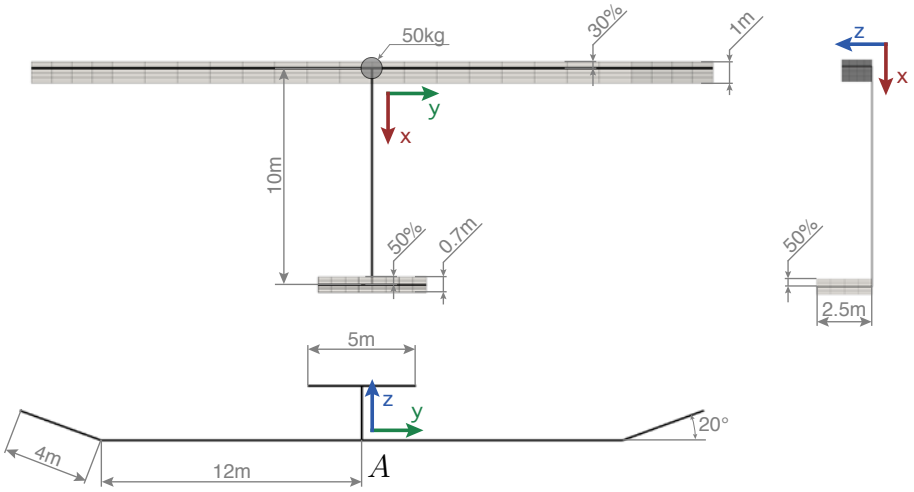


Figure 6.14: 3-view schematic of HALE aircraft [44], displaying the body-attached frame of reference A.

is constructed using the first 17 normal modes of the aircraft, ordered by increasing natural frequency, from which 6 correspond to the different rigid body motions of the aircraft (3 translations plus 3 rotations about the aircraft principal axis of inertia). From the remaining 11 elastic modes, 6 are symmetric modes (longitudinal dynamics) while the rest are antisymmetric (lateral dynamics). These have been computed for the total payload of 50 kg. Here, velocity modes are regarded as perturbations from the steady horizontal flight velocity, since the intrinsic equations (2.22)–(2.23) are invariant with respect to rigid-body motions. Therefore the actual velocity of the aircraft is recovered by adding up the initial horizontal flight velocity and the additional velocities from the modal solution $\boldsymbol{q}_1$.

Next, we compare both the trim solutions for the rigid case, where the structure is assumed infinitely rigid, and for the flexible case. To compute the trim solutions with our modal system (3.79) we consider dynamic simulations where a point in the structure is *clamped*, to maintain the aircraft in the desired horizontal flight trajectory, until convergence to a steady state is reached. We choose to clamp the wing-fuselage intersection, and we define there a body-attached frame A (Fig. 6.14), whose velocity, using our modal approximation, is $\left(\boldsymbol{v}_A^\top, \boldsymbol{\omega}_A^\top\right)^\top = \Phi_1(s_A)\boldsymbol{q}_1$, where $\Phi_1(s_A) = (\phi_{11}(s_A), \ldots, \phi_{1N_m}(s_A)) \in \mathbb{R}^{6\times N_m}$ is the horizontal concatenation of the velocity modes at that given location. We follow by computing the following matrices: $Z_{v_A} \in \mathbb{R}^{6\times N_m}$, which span $\ker(\Phi_1(s_A))$, and its orthogonal subspace $R_{v_A} = \Phi_1^\top(s_A) \in \mathbb{R}^{N_m\times 6}$, i.e., the row space of $\Phi_1(s_A)$. Consider now,

the projection matrices

$$P_z = Z_{v_A}(Z_{v_A}^\top Z_{v_A})^{-1} Z_{v_A}^\top, \tag{6.2a}$$

$$P_r = R_{v_A}(R_{v_A}^\top R_{v_A})^{-1} R_{v_A}^\top, \tag{6.2b}$$

which project $\boldsymbol{q}_1$ into the null and row spaces, respectively. Hence, given thrust, angle of attack and elevator deflection, the dynamic solution of (3.79) with the equation for $\dot{\boldsymbol{q}}_1$ projected using P_z ensures that the frame A remains fixed throughout the simulation eventually reaching a (deformed) steady state due to aerodynamic damping. Projecting now the nonzero $\dot{\boldsymbol{q}}_1$ remaining at the end of the simulation using P_r gives us the *clamping* forces necessary to maintain the aircraft at those conditions $\left(\boldsymbol{f}_A^\top, \boldsymbol{m}_A^\top\right)^\top = P_r \dot{\boldsymbol{q}}_1$. Hence, the trim problem consists of finding the zeros of $\left(\boldsymbol{f}_A^\top, \boldsymbol{m}_A^\top\right)^\top$, which, in the longitudinal case, has only three possible nonzero components. This is solved iteratively using a Newton-Raphson algorithm, where the Jacobian can be explicitly obtained thanks to the sensitivity equations (4.17)–(4.18) described in the previous chapter, and will eventually yield the trim angle of attack, thrust input and elevator deflection. The described trim process is summarised in Algorithm 1.

Algorithm 1 Trim algorithm

Set U_∞ and take a linearised UVLM ROM around $\bar{\alpha}$
Set steady state and clamping forces tolerances ϵ_1, ϵ_2
Compute P_z and P_r (6.2)
Initial guess : α, δ_e, T
Update $\boldsymbol{\phi}_{\xi j}$ according to new rigid rotation α and set state $\delta\theta = \alpha - \bar{\alpha}$
converge = FALSE
while NOT converge **do**
  repeat
    Integration of (3.79) and (4.17)–(4.18) with $\dot{\boldsymbol{q}}_1 \leftarrow P_z \dot{\boldsymbol{q}}_1$
  until $\|P_z \dot{\boldsymbol{q}}_1\| < \epsilon_1$
  if $\|P_r \dot{\boldsymbol{q}}_1\| < \epsilon_2$ **then**
    converge = TRUE
  else
    Perform step of Newton-Raphson algorithm
    $(\alpha, \delta_e, T) \leftarrow (\alpha, \delta_e, T) - J^{-1} P_r \dot{\boldsymbol{q}}_1$
    Update $\boldsymbol{\phi}_{\xi j}$ according to new rigid rotation α and set state $\delta\theta = \alpha - \bar{\alpha}$
  end if
end while

Shown in Fig. 6.15 are the trim parameters α, δ_e, T — i.e., angle of attack, elevator deflection and thrust setting — for both a rigid HALE configuration and the original, flexible one corresponding to the static solutions of our system (3.79) for a forward flight velocity of $U_\infty = 10\,\text{m/s}$. The obtained trim parameters have been normalised using SHARPy nonlinear solutions, which are (α, δ_e, T) = (3.89 deg, -0.649 deg, 4.698 N) for the rigid case and (α, δ_e, T) = (4.151 deg, -1.124 deg, 4.7940 N) for the flexible one. For a better visualisation, since thrust values are the ones experiencing greater variations, they are displayed using a different axis scale (right axis) in Fig. 6.15. The different displayed trim solutions have been obtained using six different aerodynamic ROMs[6] of the scaled UVLM equations, differing only in the reference linearisation (rigid) angles of attack. Then, the trim angle of attack differs from the latter in that it defines the actual angle of attack of the aircraft, whose effect in the system is through an additional input in the ROM (3.70) of Euler angles perturbation $\delta\boldsymbol{\chi}$ (the angle of attack contribution could also have been obtained through perturbations in rigid body velocities, see [63]).

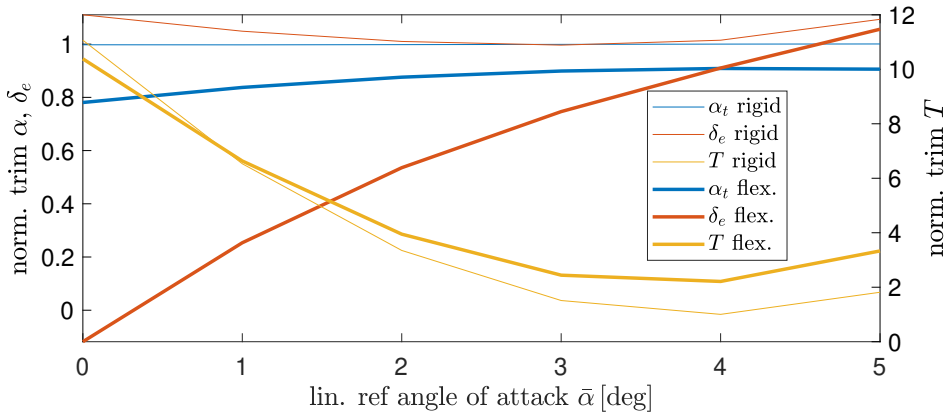


Figure 6.15: Normalised trim parameters as a function of the linearisation angle of attack.

Despite not being used in the simulations that will follow, the rigid case (solid thin lines in Fig. 6.15) is considered here as a means of internal model validation and to show that, when no elastic deformations are present, the discrepancies between SHARPy nonlinear solutions and the ones obtained with our modal framework reside solely in the linearisation of angles used in the aerodynamic ROM model. As a matter of fact, all lines are observed to coalesce around 1 (note the normalised quantities) when the angle of attack at which the UVLM is linearised approaches SHARPy trim value of 3.893 deg.

Focusing now on the solution to the flexible problem, a first observation is that all the obtained trim angles of attack are consistently lower than the nonlinear solution of SHARPy, with a value of $\alpha = 3.77\,\text{deg}$ for the one using the linearised UVLM around 4 deg. Re-

[6]The construction of the ROMs is the work of N. Goizueta

garding the thrust setting, there appears to be a non-vanishing offset for which we obtain twice as much thrust than was required in the full nonlinear scenario for the closest solution. Analysis of the discrepancies in this case is far more intricate, since there are many possible sources of error in the proposed approximations. On the one hand, linearisation of the deformation and rotation displacement inputs can contribute to a larger generation of lift, which translates into lower required trim angles of attack, and variation in induced drag is not captured since it is a second order effect. On the other hand, the trim solution is very sensitive to the correct centre of mass prediction, which is a known challenge using the modal-based approximated system [154, ch. 6]. All in all, results for the system based on the linearisation of the aerodynamics about 4 deg result in a trim solution of $(\alpha,\, \delta_e,\, T) = (3.772\,\text{deg},\, -1.023\,\text{deg},\, 10.604\,\text{N})$, which is arguably a good approximation to SHARPy reference nonlinear solution. This is further justified, when this nonlinear solution is used as guess parameters and the necessary *clamping forces*, as described in Algorithm 1, are found to be $(\boldsymbol{f}_A^\top, \boldsymbol{m}_A^\top) = (-2.36,\, 0,\, -71.86,\, 0,\, 40.00\,\text{m},\, 0)\,\text{N}$: the error in the vertical force component represents less than the 10% of the overall weight of the aircraft, which is considered to be a rather satisfactory result, given all the errors than can arise from the interplay between the different approximations taken and the extreme loading case that it is being simulated, involving very large deformations.

Since the MPC problem is expressed by means of control input perturbations from the reference, trim values (of the internal model), the incremental solutions can be fed back directly to SHARPy. However, the offset between SHARPy trim values and the internal model will have to be taken into account when placing constraints on control inputs, since we want them to be respected in the realistic scenario of SHARPy.

6.2.2 Stabilisation After Payload Drop

For this control test case, the HALE aircraft model is set up to be flying at a forward flight velocity of $U_\infty = 10\,\text{m/s}$ at the trim configuration. After a short time lapse, half of the HALE payload (which represents the 31.95% of the aircraft total weight) is released, which is a sudden, intense perturbation after which the aircraft undergoes a large drop in the angle of attack while it quickly gains altitude in a response resembling that of a slingshot. Another consequence of the mass release is that the mass distribution of the resulting aircraft is severely modified, as observed in Fig.6.16, and the centre of gravity is dangerously pushed towards the tail, posing a challenging control problem. The affected dynamics of the aircraft, as well as the new stability properties, must be managed properly by the control framework for successful stabilisation.

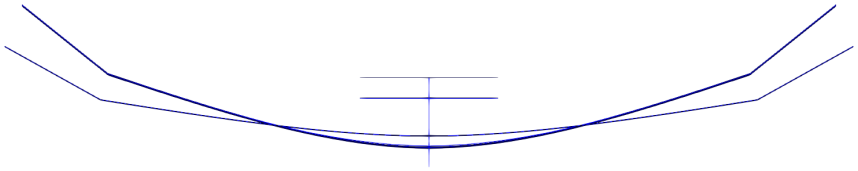


Figure 6.16: Wing loading and deformation changes before and after the mass drop in open loop. (Figure by N. Goizueta)

Before presenting the MPC closed-loop results it is compelling to assess the performance of the internal controller model and compare it to SHARPy full nonlinear simulations. For this purpose, the aeroelastic system in modal coordinates (3.79), constructed with a Krylov-based UVLM ROM aerodynamic model as described above, is slightly modified to include the effect of the mass ejection on the dynamics. This has been internally modelled considering the force that the lumped mass exerts on the structure using (3.17). It is considered a single point mass (i.e., with negligible distributed inertia properties) with $m_l = -25\mathcal{H}_{t_0}(t)$, where $\mathcal{H}_{t_0}$ is the Heaviside function defined at $t_0 = 0.125\,\text{s}$. Then, its contribution in the modal mass matrix and in the nonlinear kinematic gyroscopic Γ^l_{1,m_l} and gravity Γ^l_{g,m_l} terms of the internal modal dynamics equation (3.33a) can be computed from the lumped contributions in (3.32), (3.37) and (3.57), resulting in

$$\left(I+m_l\Phi_{1v}^\top(s_A)\Phi_{1v}(s_A)\right)\dot{\boldsymbol{q}}_1 = \Omega\boldsymbol{q}_2 - q_{1l}\Gamma^l_1\boldsymbol{q}_1 - q_{2l}\Gamma^l_2\boldsymbol{q}_2 + q_{\xi l}\Gamma^l_g\boldsymbol{q}_\xi + m_l\left(-q_{1l}\Gamma^l_{1,m_l}\boldsymbol{q}_1 + q_{\xi l}\Gamma^l_{g,m_l}\boldsymbol{q}_\xi\right), \tag{6.3}$$

where s_A is the location of the lumped mass, which coincides with that of the body-attached frame A and $\Phi_{1v} = (I\ 0)\left(\phi_{11}(s_A),\ldots,\phi_{1N_m}(s_A)\right) \in \mathbb{R}^{3\times N_m}$ is the horizontal concatenation of the three first components of the velocity modes at that given location. Using Woodbury's matrix inversion lemma [162], we avoid the $N_m \times N_m$ matrix inversion required to write (3.79) in the form of $\boldsymbol{h}$ (see section 4.3.3), and instead we obtain

$$\begin{aligned}\dot{\boldsymbol{q}}_1 = \left(I - m_l\Phi^\top\left(I + m_l\Phi\Phi^\top\right)^{-1}\Phi\right)\left(\Omega\boldsymbol{q}_2 - q_{1l}\Gamma^l_1\boldsymbol{q}_1 - q_{2l}\Gamma^l_2\boldsymbol{q}_2 + q_{\xi l}\Gamma^l_g\boldsymbol{q}_\xi\right.\\ \left. + m_l\left(-q_{1l}\Gamma^l_{1,m_l}\boldsymbol{q}_1 + q_{\xi l}\Gamma^l_{g,m_l}\boldsymbol{q}_\xi\right)\right),\end{aligned} \tag{6.4}$$

where subscripts in Φ have been dropped to alleviate notation and now the inversion is performed on the more manageable 3×3 matrix $\left(I + m_l\Phi\Phi^\top\right)$.

The open loop results are gathered in Fig. 6.17, where three very relevant variables in the aircraft flight dynamics response are compared to SHARPy full nonlinear simulations, namely the instantaneous airspeed of the aircraft U (measured as the velocity magnitude

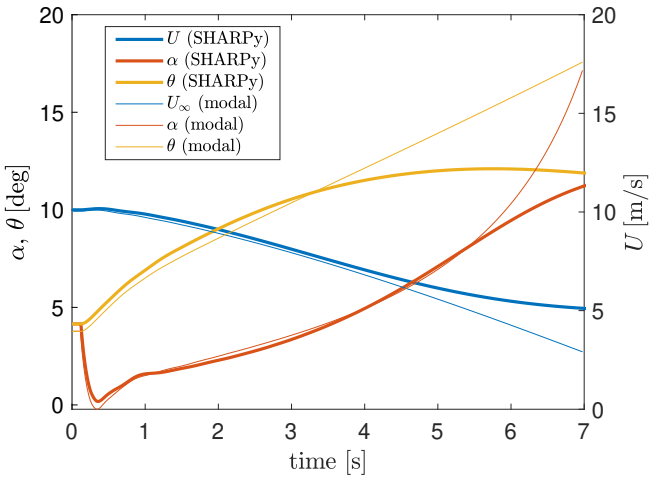


Figure 6.17: Payload drop open-loop results. (SHARPy results by N. Goizueta)

of the body attached frame of reference A), the angle of attack of the aircraft (measured as the angle between the velocity of the frame A and the horizontal axis of the same frame) and the pitch of the aircraft (measured as the angle between the x-axis of the frame A and the inertial horizontal direction). As briefly mentioned above, the sudden release of the payload causes an abrupt drop in the aircraft angle of attack (due to the upwards velocity of the airframe as a reaction to the drop), and maintains a positive growth for the portrayed simulation window. The drastic change in the aircraft centre of mass also leads to a progressive increase in the aircraft pitch, which ends up stabilising after the first five seconds of simulation. Finally, the velocity undergoes a substantial continuous decrease due to the climbing trajectory following the mass drop.

Results obtained using our nonlinear aeroelastic low-order model (thin lines in Fig. 6.17) show very good agreement with the highly-resolved full nonlinear simulations for up to 5 seconds, which is deemed very remarkable given the challenging test case, and more importantly, it is sufficient for control. After such a period of time, and in contrast to the comparisons performed on clamped wings in the previous examples, the results start to diverge, which is thought to be caused mainly due to the decrease in velocity U (note that no updating of the scaling terms in Eq. (3.72) is performed in the modal simulation) and of the linearisation approximations introduced by the aerodynamic model which fail to capture induced drag accurately (both second order effects). Note also that both simulations start from slightly differing values of α and θ due to the mentioned difference in trim solutions. On the grounds that the modal-based approximate model offers a fair description of the nonlinear behaviour for a large enough time window in such a challenging case, it is considered sufficient to underpin both NMHE and NMPC strategies, where the internal model only needs to provide simulations over finite-time

horizons. Moreover, these horizons are typically chosen not to be very large (of the order of the period of the lowest-frequency structural mode) since we are mainly interested in the transient behaviour. Note that for longer horizon objectives an outer loop reference governor can always be designed to address lower-frequency, long-term behaviour of the aircraft.

Importantly, the internal simulations required for the control framework are performed at a fraction of the computational cost of higher fidelity models. As a comparison, 1 second of physical simulation, using the model discretisation given in Tab. 6.5, takes SHARPy around 2,200 s of CPU time (taking an average of 2 iterations per time step) to run on an Intel(R) Xeon(R) Silver 4114 CPU @2.20GHz, while the same time lapse is simulated in roughly 2.5 seconds (1,000 times faster) with our nonlinear reduced-order model (3.79) in a Matlab R2018b script run on an Intel(R) Xeon(R) CPU E5-2630 v3 @ 2.40GHz machine. This implies that, with parallelisation, each MPC/MHE iteration will run well below real time even using this non-dedicated software.

Table 6.5: SHARPy model of HALE aircraft numerical discretisation

3-noded FE elements	Wing	16
	Fuselage	8
	Vertical Tailplane	8
	Horizontal Tailplane	8
UVLM	Chordwise Panels	16
	Wake Length	10 chords
	Total Bound Panels	1792
	Total Wake Panels	17920
Time step		6.25 ms

We now describe the control problem. The HALE aircraft model is initially trimmed in SHARPy for a level flight at $U_\infty = 10\,\mathrm{m/s}$ and 50% of the payload located at the intersection between the wings and the fuselage is released shortly after the start of the simulation[7]. The objective of the MHE/MPC framework is to stabilise the aircraft after the sudden perturbation, of which it does not have any information other than the estimator guess of the lost payload, whose formulation is described next. This problem is representative of more general scenarios, such as a sudden relocation of the aircraft centre of mass due to payload loosening or unnoticed loss of an airframe component. As previously described, the estimator is responsible for providing an estimate of the state at the current sampling point together with an estimate of the external disturbances to the system, which here, the only one considered is the lost mass. Then the disturbance effect of the system is modelled as described before, replacing m_l for the unknown w

[7]Simulation in SHARPy was set up by N. Goizueta

(found upon solution of the MHE problems) in expression (6.4). The internal model is constructed using the same number of modes as already described above, and a sampling time of $\tau_s = 0.2\,\text{s}$ is chosen. For the estimator, a horizon of $N_e = 6$ is chosen (1.2 s), which is 0.59 times the first (bending) elastic mode period. The local translation velocities at five different locations along the main wing are the measurements $\boldsymbol{y}$ fed to the MHE. These are the intersection between the wings and the fuselage, the joint between the two semi-wings (2 for each side) and the wing tip (2 for each side). The matrix Q_e is taken equal to the identity, penalising errors in estimation equally for each of the sensors, and $P_e = I$ $R_e = 1$. For the control counterpart, a slightly longer horizon with $N_c = 12$ (2.4 s) is chosen, which represents a window slightly longer than the period of the first bending mode. Control is slightly penalised with $R_c = 0.05I$ while $Q_c = \text{blkdiag}(I_6, 0)$, meaning that we mainly choose to penalise rigid body velocity perturbations with the aim to maintain a levelled flight avoiding the drastic drop in velocity that is observed in the open-loop response in Fig. 6.17 and the dangerous increase in angle of attack which could potentially lead to stall. Thrust is constrained to be in a range of $[0, 15]\,\text{N}$ while elevator deflection and deflection rates are constrained to $\pm 15\,\text{deg}$ and $\pm 100\,\text{deg/s}$, respectively. As mentioned, for the thrust and aileron deflection a bias is introduced in the constraints to take into account the mismatch in the trim values, since we want this constraints to be satisfied in the realistic model.

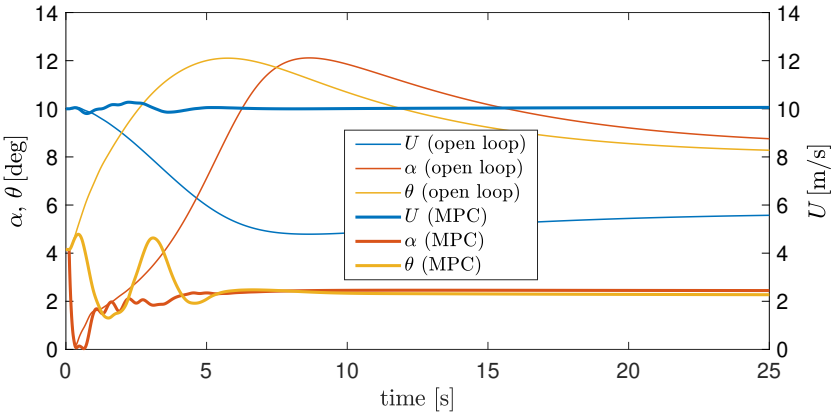


Figure 6.18: Open-loop vs. MPC closed-loop response comparison. (Open-loop simulation by N. Goizueta)

The closed-loop response can be seen in Fig. 6.18, in which it is compared to the open-loop response for reference. First, very successful control of the flight velocity is achieved, only slightly deviating from the initial 10 m/s during the subsequent 3-4 seconds to the payload drop. The angle of attack experiences a similar sudden drop at the beginning, due to the impossibility to counteract the initial upwards velocity induced by the release, followed by some low-amplitude mild oscillations. However, its drastic increase has been

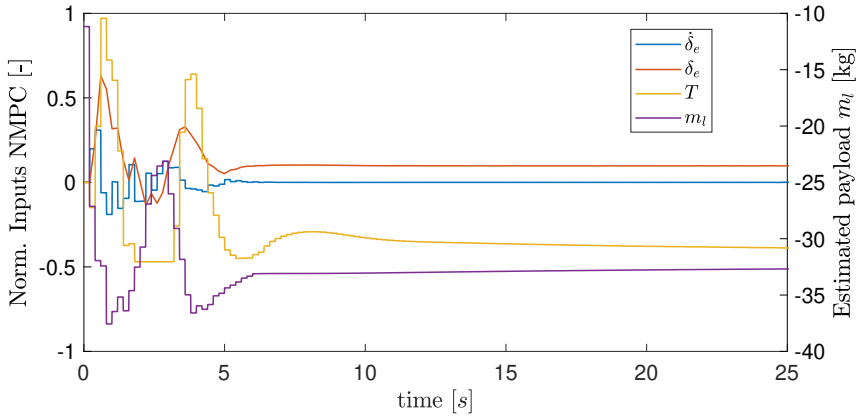


Figure 6.19: Normalised control inputs and estimated mass.

effectively suppressed. Regarding the pitch of the aircraft, it experiences some oscillations with higher amplitude but it is also seen to be controlled with high efficacy. This is, perhaps, the most visual effect of the controller, since the notorious nose-up configuration adopted by aircraft in the open-loop trajectory as seen in Fig. 6.20 is suppressed. The overall closed-loop performed as expected, and the aircraft is virtually stabilised after 4-5 seconds of the payload release.

Gathered in Fig. 6.19 are the inputs produced by the NMPC and the estimation of the lost payload provided by the NMHE. The shown MPC inputs are the increments with respect trim values and have been normalised with the maximum allowed increment. Both the aileron and thrust signals are seen to be oscillatory, responding to the corrections needed to maintain the flight velocity. The aileron input and thrust setting are seen to stabilise around different steady state values to account for the new trim conditions corresponding to the lighter configuration of the aircraft after the mass loss. Note that the aircraft is left with a residual vertical velocity (the pitch and angle of attack do not end up coinciding exactly), which is explained by the plant-model mismatch and the different steady solutions that are obtained with both models as already seen in the trim solutions comparison. This mismatch is also believed to explain the offset and the fluctuations of the estimated payload. Note that the leftover difference is within a tolerable 7 kg, in line with the observed discrepancies in the *clamping* forces necessary to match trim values with SHARPy, which is a representative measure of the mismatch error. Nevertheless, this does not hinder the closed-loop performance, as suggested by the results.

It is worth mentioning that these results suggest that the control framework is able to exploit the nonlinear knowledge of the system. As seen in Fig. 6.16, the release of 50% of the aircraft payload severely affects the wing loading, which adopts a much less deformed configuration. Hence, the controller has to be able to drive the system to a different

nonlinear steady solution while the estimator needs to fit the changing internal dynamics (due to a significant variation of m_l, which modifies the internal model as described in (6.4)) with the observed measurements.

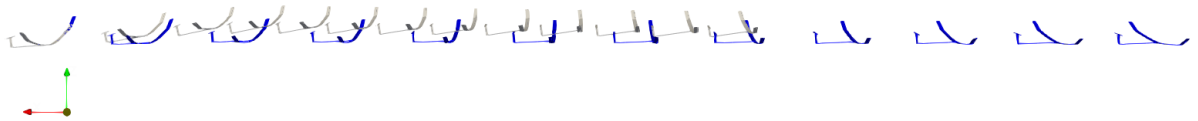


Figure 6.20: Trajectory of the controlled HALE aircraft in blue over 30s, shown at 2.5s intervals, alongside the open-loop trajectory in grey. (Figure by N. Goizueta)

6.3 Data-Driven Enhanced Aeroelastic Model for Control

The previous results have been found sufficient for successful aeroelastic control, as suggested by the cases portrayed in the sections above. However, the short/medium-term dynamics of our internal model, in the free-flying scenario above, are seen to diverge, as can be observed in Fig. 6.17. The discrepancies in Fig. 6.17, between full nonlinear aeroelastic simulations in SHARPy and the internal aeroelastic model constructed with a linearised UVLM result from responses of the latter model characterised by a drastic deceleration of the vehicle. Analysis of our results suggests that this can be caused by the linear UVLM ROM being transparent to variations in flight velocity (and hence dynamic pressure) and the use of linear approximations to rotations in the computation of aerodynamic forces, which are then subject to the follower force effect as they are coupled with the intrinsic equations; the variation in drag force is believed to be overestimated due to an excessive horizontal projection of the lift, during rigid body rotations, and the fact that the observed decrease in velocity after the mass drop does not translate in reduction of the aerodynamic forces (through dynamic pressure). This combined effect leads to undesirable unstable models of free-flying highly flexible aircraft, especially so in the context of seeking internal models for MPC/MHE.

Therefore, data-driven modelling is explored here to search for more accurate internal descriptions of the previously described HALE aircraft model (Fig. 6.14). To overcome this observed limitation of the UVLM linearisation, and as discussed in § 3.3, second-order models, where these effects are expected to be appropriately captured, will be sought from data ensembles obtained from full nonlinear unsteady vortex lattice simulations. Besides, a model of gravity forces as a function of the intrinsic modal variables, as introduced in

§ 3.3, which will avoid the necessity of explicitly computing the rotation field, will also be sought.

6.3.1 Training Data and Model Regression

To obtain the n_d data ensembles necessary to train our models, we must obtain first a series of structural data time-histories which will then be fed to the nonlinear UVLM simulations in SHARPy, as depicted in Fig. 3.6. We have employed 94 simulations of 10 s each, for which the inputs have been obtained as follows. First, for a more physical intuition of the prescribed structural motions we define a range for the angle of attack, flight velocity and pitch: $\pm 10\,\text{deg}$, $\pm 6\,\text{m/s}$ and $\pm 20\,\text{deg}$, respectively, about the nonlinear trim values $(\bar{\alpha}, \bar{U}, \bar{\theta}) = (4.1566\,\text{deg}, 10\,\text{m/s}, 4.1566\,\text{deg})$ and time-histories $\alpha(t)$, $U(t)$, $\theta(t)$ are generated, in this proof of concept, using *1-cos* perturbations to the trim values. Each of the amplitudes for the *1-cos* perturbations are randomly chosen, using a constant probability function within the defined intervals. For the frequencies, random values using the same probability function are chosen from the interval $[0.067,\ 0.2]\,\text{Hz}$. This is in line with the observed slower flight dynamics of the vehicle. The angle of attack, flight velocity and pitch amplitudes and frequencies are chosen for each variable independently. The resulting time histories can be related to the velocity of the body-attached frame of reference A, which can then be used to define a time history for the first six (rigid-body) modes $\boldsymbol{q}_1^{rb}$ of the $\boldsymbol{q}_1$ vector.

$$\boldsymbol{q}_1^{rb}(t) = \boldsymbol{\Phi}_{1v}^{-1}(s_A) \begin{pmatrix} -U(t)\cos(\alpha(t)) \\ 0 \\ -U(t)\sin(\alpha(t)) \\ 0 \\ \dot{\theta}(t) \\ 0 \end{pmatrix}. \tag{6.5}$$

The rest of modal inputs (i.e., symmetric/longitudinal elastic modal velocities and elastic forces/moments) are also prescribed using perturbations with amplitudes $\pm(5, 3, 3, 3, 2, 1)^\top$ and $\pm(20, 8, 3, 2, 2, 1)^\top$, respectively, with *1-cos* signals of slightly faster random frequencies in the range $[0.13,\ 0.4]\,\text{Hz}$ to the modal trim solutions $\bar{\boldsymbol{q}}_1$ and $\bar{\boldsymbol{q}}_2$. Similarly to the construction of the flight mechanics (rigid-body modes) perturbations, all elastic amplitudes and frequencies are (randomly) chosen for each mode independently, therefore for each excitation time-history all amplitudes and frequencies are distinct and uncorrelated between modes. The amplitudes for these perturbations can be selected to cover the range

of observed typical responses in representative application problems where the model is to be employed. Here, since the internal models will be tested against gust perturbations, a range of open-loop simulations with gusts of different intensities and spans have been post-processed (i.e., the obtained structural data has been projected onto modal coordinates, after transformation to the intrinsic variables using Eqs. (3.88),(3.89)) to quantify the expected excitation ranges. Perturbations on elevator input are also defined with random amplitudes between $\pm 7.5\,\text{deg}$ around the trim value and frequencies in the range $[0.13,\ 0.4]\,\text{Hz}$ for the *1-cos* temporal signals.

The time-histories of modal inputs, $\boldsymbol{q}_1(t)$, $\boldsymbol{q}_2(t)$, which excite all modes simultaneously, are then transformed to nodal displacements, $\boldsymbol{R}_A$, and finite-rotations, $\boldsymbol{\Psi}_A$, as shown in Fig. 3.6, and are used to solve for the fully nonlinear UVLM equations with prescribed structural motions in SHARPy. Each of the simulations provides us with the aerodynamic solution, consisting of the state space $\left(\boldsymbol{\Gamma}_b^\top, \boldsymbol{\Gamma}_w^\top, \dot{\boldsymbol{\Gamma}}_b^\top, \boldsymbol{\zeta}_w^\top\right)^\top$ as given by (2.43). Besides the full aerodynamic state, these structural prescribed simulations in SHARPy also yield the distribution of aerodynamic and gravitational forces (the latter obtained as described in § 3.3.3), which after projection onto modal coordinates will be used to obtain a data-driven approximation for the modal aerodynamic and gravitational forces.

As already introduced in § 3.3.3, several choices can be made now regarding the projection matrix used to reduce the highly-dimensional aerodynamic state space on to smaller subspaces, in order to obtain concise UVLM descriptions via data-driven model regression. One option, based on first-principles intuition, would be to use the projection matrices obtained from a model-order reduction (either Krylov-based or frequency-limited balanced methods) of the linearised UVLM equations. Then, construction of the state perturbations (2.46) can be computed from the data ensembles $\left\{(\boldsymbol{\Gamma}_b)_i, (\boldsymbol{\Gamma}_w)_i, (\dot{\boldsymbol{\Gamma}}_b)_i, (\boldsymbol{\zeta}_w)_i\right\}_{i=1}^{n_d}$ and reduced states $\{(\boldsymbol{q}_\Gamma)_i\}_{i=1}^{n_d}$ can be obtained after projection using $W^\top$. This method has been however disregarded since the perturbations from the linearisation point of the data ensembles are very large and hence this projection can be far from optimal. Moreover, circulation derivatives are found to be very noisy in the computed nonlinear simulations, introducing an undesirable level of distortion to the training data. Instead, a more traditional data-driven approach has been considered. Taking inspiration from the full nonlinear state-space representation of the UVLM equations (2.43), where the derivatives of the bound circulations are used to augment the state only because the forces (output) depend on them (they are not needed for the time-marching of the pure UVLM equations), we perform a singular value decomposition of the UVLM state ensembles excluding

the circulation time-derivatives

$$U^\top SV = \left\{ \begin{pmatrix} \boldsymbol{\Gamma}_b \\ \boldsymbol{\Gamma}_w \\ \boldsymbol{\zeta}_w \end{pmatrix}_i - \begin{pmatrix} \bar{\boldsymbol{\Gamma}}_b \\ \bar{\boldsymbol{\Gamma}}_w \\ \bar{\boldsymbol{\zeta}}_w \end{pmatrix} \right\}_{i=1}^{n_d}, \tag{6.6}$$

and where the trim solution has been subtracted. The first few singular values are shown to contain most of the energy in the data, with the first 10 containing already $\sum_{i=1}^{10}\sigma_i^2/\sum_{i=1}^{n_d}\sigma_i^2 > 99.5\%$. Therefore, the first few columns of $U^\top$, also known as the POD (Proper Orthogonal Decomposition) modes of the data ensembles, are used to project the highly-dimensional UVLM states (for the particular discretisation of the HALE model given in § 6.2, the state has a dimension of $78,015$) onto a subset several orders of magnitude smaller. Then, selecting the first 10 modes, the projection matrix of Fig. 3.6 is $\left[W^\top\right]_{ij} = [U]_{i=\{1,\dots,10\},j}$.

After such data post-processing, the data ensembles necessary to seek for low-order data-driven time evolution equations for the reduced aerodynamic states and its corresponding output functions, which give the aerodynamic forces, are obtained: $\{(\dot{\boldsymbol{q}}_\Gamma)_i, (\boldsymbol{q}_1)_i, (\boldsymbol{q}_2)_i, (\boldsymbol{q}_\Gamma)_i, (\delta_e)_i, (\dot{\delta}_e)_i\}_{i=1}^{n_d}$ and $\{(\boldsymbol{\eta}_\Gamma)_i, (\boldsymbol{q}_1)_i, (\boldsymbol{q}_2)_i, (\boldsymbol{q}_\Gamma)_i, (\delta_e)_i, (\dot{\delta}_e)_i\}_{i=1}^{n_d}$.

Similarly, the data ensembles for the proposed model of gravitational forcing are $\{(\boldsymbol{\eta}_g)_i, (\boldsymbol{q}_2)_i, (\boldsymbol{\xi}_{s_A})_i\}_{i=1}^{n_d}$, where the location of the body-attached frame A is the chosen point to track the only quaternion needed for the model. The time-histories of the rotation quaternion $\boldsymbol{\xi}_{s_A}(t)$ are direct to obtain using (3.85), since the angular velocity of the frame A, $\boldsymbol{\omega}_A$, is also a prescribed magnitude derived from the modal velocity excitation $\boldsymbol{q}_1$ (as given by (3.90)).

We employ the normalised regression problem (3.83), which for the particular application of obtaining the time-evolution equation for the aerodynamic states, will be slightly modified to account for physical constraints on the model coefficients. The constraints that we want to impose are linear on the non-normalised coefficients $\boldsymbol{\beta}$, since they refer to physical properties that are desirable for the obtained data-driven model to inherit. They are gathered in the matrix-vector relationship

$$C_\beta \boldsymbol{\beta} = \boldsymbol{d}_\beta. \tag{6.7}$$

Instead of solving the constrained minimisation problem formed by Eqs. (3.83) and (6.7), we solve, instead, the normalised regularisation problem (3.83) within the null space of the constraint matrix C_β using MATLAB's inbuilt function `fitrlinear` (which solves the regression problem using the `sparsa` algorithm of [163]). In order to do so, we split

the solution $\breve{\boldsymbol{\beta}} = Z\breve{\boldsymbol{\beta}}_z + \breve{\boldsymbol{\beta}}_p$, where Z spans the null space of the matrix $C_\beta A_\beta$ and $\breve{\boldsymbol{\beta}}_p$ is a particular solution of (6.7) after the normalisation relationship (3.84) is substituted. The null space matrix Z can be obtained similarly to (3.30). Substituting $\breve{\boldsymbol{\beta}} = Z\breve{\boldsymbol{\beta}}_z + \breve{\boldsymbol{\beta}}_p$ in the normalised regression problem (3.83) we see that the inputs and outputs to feed into MATLAB's `fitrlinear` function have to be modified to $Z^\top \Theta(\breve{X})$ and $\breve{Y} - \breve{\boldsymbol{\beta}}_p^\top \Theta(\breve{X})$, respectively. Therefore, the obtained (normalised) coefficients automatically satisfy the constraints imposed by (6.7). Note that for constraints affecting the coefficients associated to different outputs (e.g., energy-preserving quadratic terms), the regression problem has to be solved for all the equations at once. This is performed by concatenating the ensembles of all output values in an augmented output vector $\breve{Y}$ and by constructing a block-diagonal matrix for the inputs, where each block is a copy of the input library $\Theta(\breve{X})$.

The constraints that we will impose are aimed at improving the stability of the reduced UVLM model, namely the time evolution equation for the reduced aerodynamic states (that is, the first equation in (3.87)). First, we constrain the trim inputs to remain a fixed point of our data-driven model, which can be expressed as a linear combination of the model coefficients $\boldsymbol{\beta}$. Second, we constrain the quadratic terms associated to the reduced aerodynamic states to be energy-preserving [131, Eq. 2.4], taking as the energy the product $\frac{1}{2}\boldsymbol{q}_\Gamma^\top \boldsymbol{q}_\Gamma$, and we force all the nonlinear couplings between $\boldsymbol{q}_\Gamma$ and the rest of the inputs to be zero. This allows us to check for global boundedness of the obtained data-driven models following the indications of [131]. There, sufficient conditions to prove global boundedness of ordinary differential equations with quadratic nonlinear terms are given. These conditions, gathered in Theorem 1 of [131], require negative definiteness of the linear terms of a shifted system (which involves linear and quadratic terms of the original system), which can be easily checked *a posteriori* solving an LMI constructed with the matrices obtained from the data-driven coefficients $\boldsymbol{\beta}$. If these condition are satisfied, it follows that the system exhibits a trapping region to which all solutions are globally attracted, ensuring global stability of the underlying system.

While it is unclear whether our low-order models of the UVLM equations should necessarily satisfy the imposed particular structure (energy-preserving nonlinear terms and uncoupled quadratic terms involving $\boldsymbol{q}_\Gamma$ and the other non-autonomous inputs), this allows us to guarantee that the data-driven models are stable for fixed inputs $(\boldsymbol{q}_1, \boldsymbol{q}_2, \delta_e, \dot{\delta}_e)$, which is critical for MPC/MHE internal simulations, without excessive penalisation on the model fitting error. Nevertheless, this stability definition is not very restrictive (it encompasses systems with globally stable limit cycles or fixed points, for instance) and following physical intuition it enables us to guarantee some sort of stability of the data-

driven reduced-order models; the full-nonlinear UVLM equations appear to be globally stable, in the sense that for a prescribed arbitrary structural configuration (i.e., for fixed inputs to the UVLM) the solution always shows convergence (i.e., circulation intensities converge to steady values and the wake panels stabilise in a particular, fixed layout) and it is then reasonable to expect that the reduced-order models should inherit similar stability characteristics.

The results of the fitting optimisation have been gathered in the tables below, where the maximum values shown are over the different output equations and all magnitudes refer to the normalised regression problem and coefficients, except for the second-to-last row, which shows the actual mean squared error. This is computed as the squared error averaged over the ensemble size $\frac{1}{n_d}\|Y - \boldsymbol{\beta}^\top \Theta(X)\|_2^2$.

Table 6.6: Gravity modal forcing

$[\boldsymbol{\eta}_g]_i = \boldsymbol{\beta}_{g_i}^\top \Theta\left(\left(\boldsymbol{q}_2^\top, \boldsymbol{\xi}_{s_0}^\top\right)^\top\right)$	
Lasso penalty λ	10^{-6}
Max. sparsity	3.51%
Coefficients tolerance	10^{-8}
Gradient tolerance	10^{-8}
Number of coefficients	57
Number of constraints	0
Max. norm. error	$3.6 \cdot 10^{-5}$
Max. error	$4.49 \cdot 10^{-3}$
Max no. iterations	85

Table 6.7: Low-order aerodynamic states dynamics

$[\dot{\boldsymbol{q}}_\Gamma]_i = \boldsymbol{\beta}_{\Gamma_i}^\top \Theta\left(\left(\boldsymbol{q}_1^\top, \boldsymbol{q}_2^\top, \boldsymbol{q}_\Gamma^\top, \delta_e, \dot{\delta}_e\right)^\top\right)$	
Lasso penalty λ	10^{-6}
Total sparsity	2.96%
Coefficients tolerance	10^{-12}
Gradient tolerance	10^{-12}
Number of coefficients	7570 (10 outputs $\times$757 inputs)
Number of constraints	5440 (trim, energy-preserving, sym. quad. terms)
Max. norm. error	$7.03 \cdot 10^{-3}$
Max. error	518.00
Total no. iterations	$7,495$

The regression problems show, in general, very low normalised errors, which is an indication that the quadratic polynomial expressions offer an arguably good data-driven approximation to the input-output mappings that we are seeking. As said before, constraining the regression problem for the dynamics of the low-order aerodynamic states

Table 6.8: Aerodynamic forces output equation

$$[\boldsymbol{\eta}_a]_i = \boldsymbol{\beta}_{a_i}^\top \Theta\left(\left(\boldsymbol{q}_1^\top, \boldsymbol{q}_2^\top, \boldsymbol{q}_\Gamma^\top, \delta_e, \dot{\delta}_e\right)^\top\right)$$

Lasso penalty λ	10^{-6}
Max. sparsity	45.81%
Coefficients tolerance	10^{-9}
Gradient tolerance	10^{-9}
Number of coefficients	406
Number of constraints	0
Max. norm. error	$1.19 \cdot 10^{-4}$
Max. error	4.07
Max no. iterations	50,000 (reached iteration limit)

(Table 6.7) does not hinder significantly the quality of the fit; the maximum normalised error of the unconstrained regressions is already $4.3 \cdot 10^{-3}$, that is, 39% lower that of the constrained one, however both are of the same order of magnitude. An interesting observation is that in the aerodynamic force output equation (Table 6.8), the achieved sparsity in the model coefficients is much higher than in the rest of the regressions, possibly highlighting the identification of patterns in the data such as aerodynamic stiffness and damping, which directly link the forces to the modal coefficients $\boldsymbol{q}_2$ and $\boldsymbol{q}_1$, respectively. Finally, the unsteady aerodynamics time-evolution model (Table 6.7) has been shown to exhibit a trapping region by virtue of the conditions in [131], which ensure global stability of the system for fixed inputs $(\boldsymbol{q}_1, \boldsymbol{q}_2, \delta, \dot{\delta})$.

6.3.2 Open-Loop Improvements

The obtained data-driven models for the gravity forcing and for the low-order nonlinear UVLM are fitted in our aeroelastic internal model (3.79). The equation for the quaternion field approximation $\dot{\boldsymbol{q}}_\xi = q_\xi^l \Gamma_\xi^l \boldsymbol{q}_1$ is substituted by the evolution equation of a single quaternion (first equation in (3.86)), for which we have chosen the quaternion associated to the rotation of the body-attached frame A, and the modal gravity forcing term $q_\xi^l \Gamma_g^l \boldsymbol{q}_\xi$ is replaced by the second equation in (3.86). Regarding the UVLM model, the linear matrices (A_q, B_q, C_q, D_q) in (3.79) are substituted by the data-driven expressions (3.87).

Next, we compare the response of the fully-coupled internal aeroelastic system employing the described data-driven sub-components to *ground truth* fully nonlinear aeroelastic simulations obtained with SHARPy and also to our original internal model based on linearised UVLM low-order models (3.79) (this is the same used in the previous section example). The data-driven model for gravity introduces no perceptible changes in the overall dy-

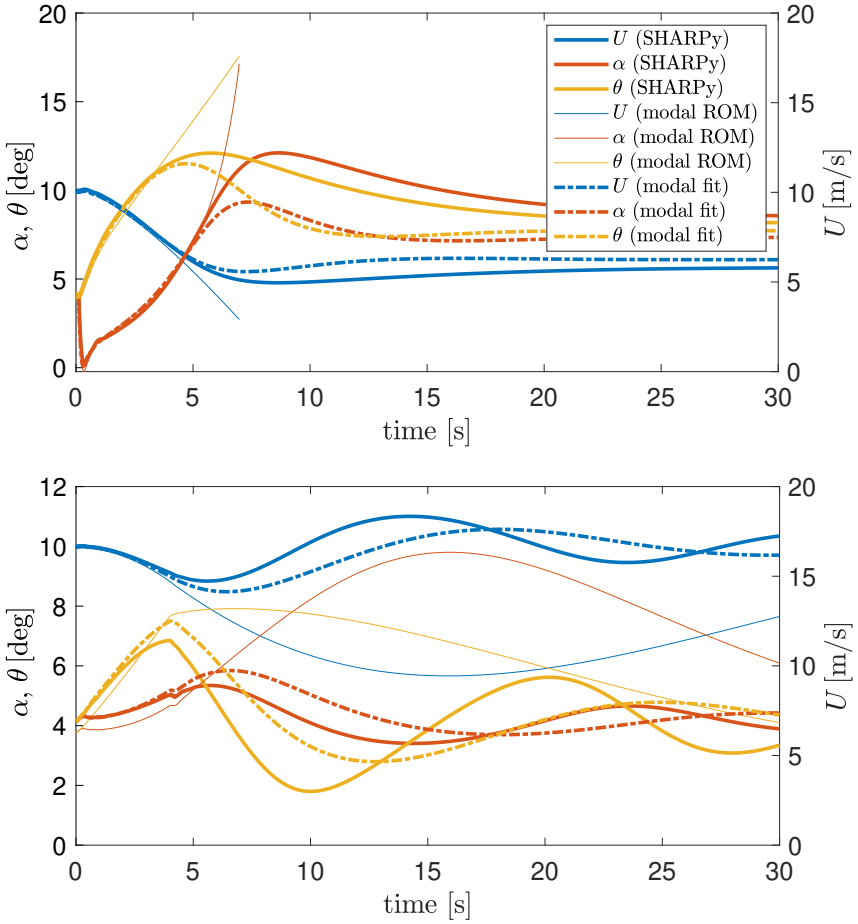


Figure 6.21: Open loop response comparisons. Payload drop case (top) and elevator input case (bottom).

namics when compared to the modal-based quaternion and gravity approximations used in the example above (which make use of Eqs. (3.58)–(3.57)). Its main contribution, hence, is the simplification of the model of gravity within the modal intrinsic formulation. Therefore, the comparison below aims to highlight, qualitatively, the potential of the data-driven model of the unsteady aerodynamics to improve model accuracy.

For this comparison exercise, two test cases are considered, with large rigid-body motions which should reveal the limitations of the original, linear-aerodynamics-based internal models and the improvements of the data-driven additions. The first is the payload drop case of the previous example, which has already highlighted the model shortcomings. The second, is the response to an increment of elevator deflection of -1 deg for 4 s from trim conditions, which leads the aircraft to a notable nose-up pitch, reducing its flight velocity and increasing the angle of attack, which is known to cause divergent results using our original internal models.

The comparisons are gathered in Fig. 6.21. As seen before, the original internal model, based on a linear UVLM ROM (thin solid line in Fig. 6.21), diverges dramatically in the payload drop case (top figure), with eventual blowup of the solution after the first few seconds of simulation. We see, that for this case, the model fitted with the data-driven gravity and aerodynamic terms (dashed lines) substantially improves the initial response and most importantly, the solution remains bounded showing very reasonable agreement with the full nonlinear simulations. Regarding the elevator input case (bottom figure), the original model again shows similar behaviour, however this time producing a bounded solution. This is characterised by a response with an apparent overestimation of drag, where the flight velocity and the angle of attack experience an exaggerated response; the former is reduced to values of around 6 m/s and the latter almost doubles the maximum observed angle of attack of the ground truth simulation. We see that the data-driven enhanced model substantially improves the amplitudes of the predicted response, however showing a slight phase delay with respect SHARPy simulations. It is believed that the main remaining source of discrepancy between the data-driven-enhanced modal-based internal models and the ground truth simulations is the truncation error due to the use of a limited number of modes (17 in this case, from which only 9 are active in these longitudinal cases), to which simulations of unconstrained structures are known to shown increased sensitivity [154, ch. 6].

6.3.3 Effect on MPC/MHE Performance

In this subsection the effect of the data-driven improvements to our original internal model (3.79) on the MPC closed-loop performance is analysed. For this purpose, two different problem setups are considered. The first is a disturbance rejection problem under gust perturbations, where different gust spans are considered, all with a considerable intensity of 20% the horizontal flight velocity. The second is the payload drop case from the previous example, where increasing values of the dropped payload are considered to reveal the robustness of the controller in providing new stable configurations after the sudden change of the inertia distribution of the aircraft.

The setup of both problems is very similar to that of the previous section, with the main difference being that the external disturbance which must be estimated is a vector of external modal forces $\boldsymbol{\eta}$, added to the equation of motion in (3.79), which gathers the effect of either the payload drop or the gust encounter on the system dynamics. A difference in the MPC/MHE implementation between the two cases is that in the gust-rejection setup, the disturbance estimated by the MHE is extrapolated in the MPC horizon

by a linear decay over the first $N_c/2$ intervals and then is set to zero over the remaining intervals, while in the payload drop case the disturbance is held constant throughout the entire MPC window. The internal models are constructed using the first 17 modes of vibration, including the 6 rigid-body modes, and a sampling time of $\tau_s = 0.2\,\mathrm{s}$ is chosen. The estimator employs a horizon with $N_e = 6$ (1.2 s, 0.59 times the period of the first — bending — elastic mode) and the local translation velocities at five different locations along the main wing are the measurements $\boldsymbol{y}$ fed to the MHE. The matrix Q_e is taken equal to the identity, penalising errors in estimation equally for each of the sensors, and $P_e = I$ $R_e = 1$. A small stage penalty on the disturbance at each interval is also introduced, with weighing matrix $R = 10^{-4}$. A constraint on the unit-norm of the quaternion associated to the frame A has been added to the initial state of the first interval of the MHE window (the quaternion states at subsequent intervals automatically satisfy this constraint due to the dynamics (4.11c) constraint), so that it provides physically sensible rotation estimates. For the MPC, $N_c = 12$ intervals are used (2.4 s). Control action is slightly penalised with $R_c = 0.001I$ and setting to 0.001 the entry of Q_c corresponding to the aileron deflection (control surface deflections are part of the augmented state). The stage and terminal costs are chosen to penalise deviations in the trim velocity of the body attached frame A by setting $P_c = Q_c = \mathrm{blkdiag}(\Phi(s_A)^\top \Phi(s_A), 0)$. Thrust input is constrained to be in a range of $[0, 15]\,\mathrm{N}$ while elevator deflection and deflection rates are constrained to lie in the range $[-7.82,\ 5.43]\,\mathrm{deg}$ and $\pm 7.48\,\mathrm{deg/s}$, to keep the control inputs within the upper and lower limits of the training data ensembles.

The two tested internal models differ only in that one is built using the data-driven model for the unsteady aerodynamics, as described in the section above, while the other one employs a reduced-order model (A_q, B_q, C_q, D_q) of the unscaled linearised UVLM at a rigid-body angle of attack of 4 deg, obtained using the Krylov-based method of SHARPy. The latter results in a stable realisation with 68 aerodynamic states. Both employ the data-driven model for the gravitational forcing. The reference trim solution of both internal models have been forced to be for the same angle of attack, thrust setting and aileron deflection as the nonlinear solution provided by SHARPy to ease the comparison, as opposed to what was done before. This leads to the introduction of a corrective *clamping* force ($P_r \dot{\boldsymbol{q}}_1$ in Algorithm 1) to ensure that the vehicle maintains the required horizontal flight velocity, which gives an idea of the mismatch between the internal models and the nonlinear SHARPy trim solution, and also leads to different trim modal solutions. These corrective forces, normalised by the total weight of the aircraft ($W = 78.25g\,\mathrm{N}$, including the entire payload), have been found to be $(\boldsymbol{f}_A^\top, \boldsymbol{m}_A^\top)/W = (-0.001,\ 0,\ -0.066,\ 0,\ -0.004\,\mathrm{m},\ 0)$ and $(\boldsymbol{f}_A^\top, \boldsymbol{m}_A^\top)/W = (0.011,\ 0,\ -0.214,\ 0,\ 0.094\,\mathrm{m},\ 0)$ for the internal model using the data-driven aerodynamic module and the one based on the Krylov ROM, respectively, which

already gives us an insight of the larger error of the latter model. As our controlled system we employ again the nonlinear aeroelasticity simulation host SHARPy, which communicates with our control framework using the UDP network mentioned in § 6.1 and described with more detail in [14] .

Disturbance Rejection in Gust Encounters

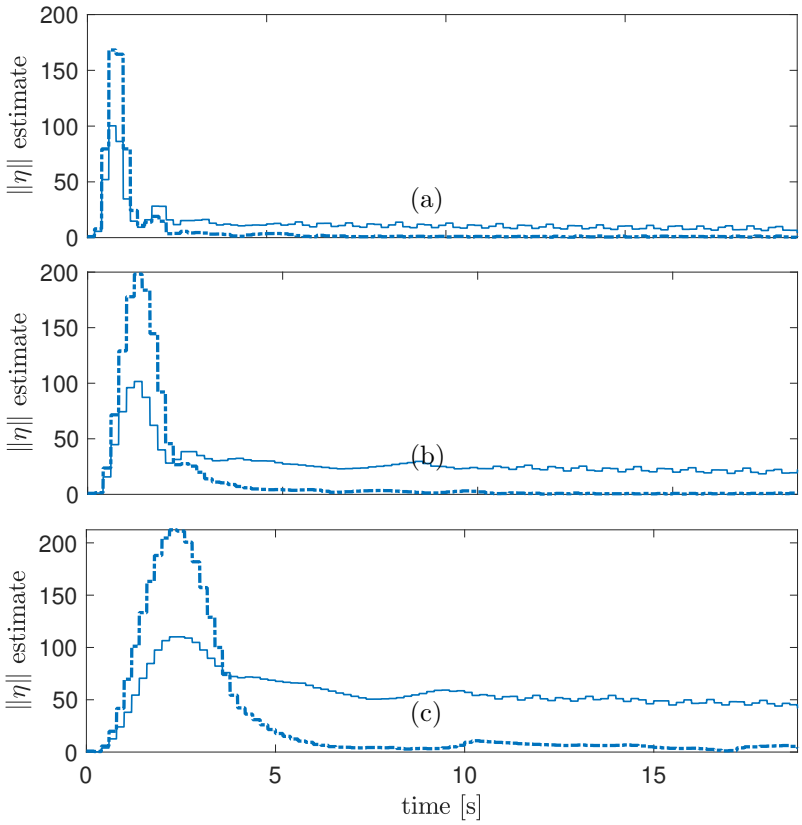


Figure 6.22: Estimates of the disturbance magnitude for gust perturbations of span (a) 10 m (b) 20 m and (c) 40 m. MPC closed-loop responses with the data-driven (▪▪▪▪▪) and linear ROM (——) UVLM models.

Here, three different gust profiles are considered as perturbations to the system and are simulated in SHARPy. All are *1-cos* shaped gusts, as described by Eq. (6.1), with a vertical velocity amplitude of $W = 2\,\mathrm{m/s}$ (that is, an intensity of 20%), reaching the leading edge of the aircraft at time $t_g = 0.25\,\mathrm{s}$ and with increasing spans $H_g = \{10, 20, 40\}\,\mathrm{m}$.

An outline of the presented results, gathered in four different figures, is given next, prior to its discussion. First, we show in Fig. 6.22 and Fig. 6.23 the results of the estimation: the first gathers the magnitude (norm) of the estimated external forcing vector (which has 9 components in total, for each longitudinal mode), $\boldsymbol{\eta}$, due to the gust perturbations.

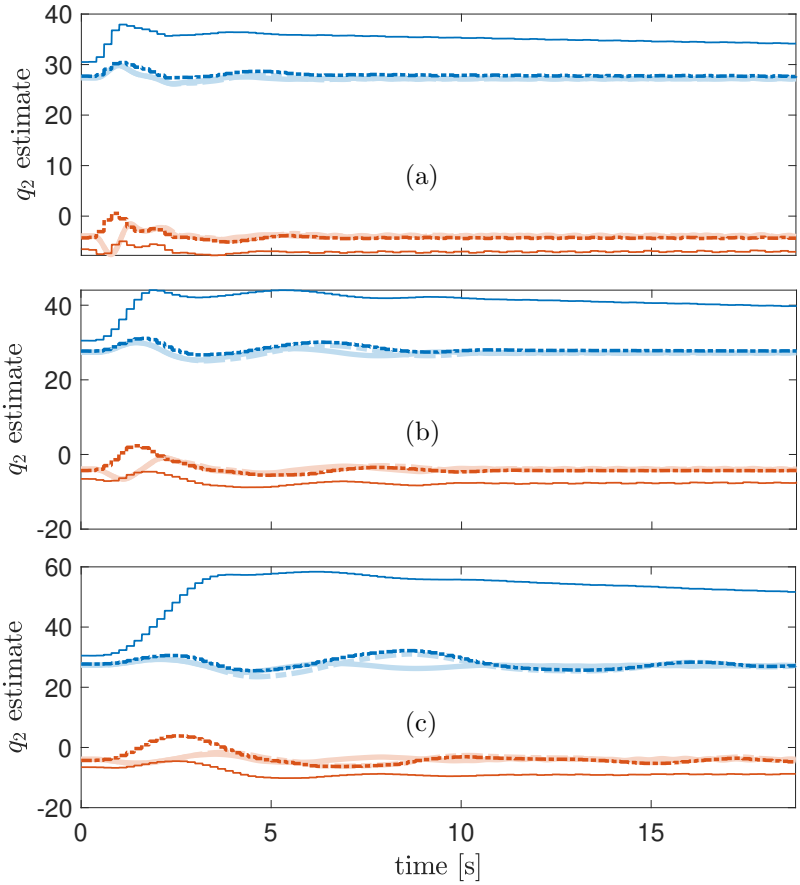


Figure 6.23: Estimates of the $\boldsymbol{q}_2$ state components (first bending in colour ■, second bending in ■) for gust perturbations of span (a) 10 m (b) 20 m and (c) 40 m for the data-driven (▪▪▪▪▪) and linear ROM (——) UVLM internal models. Actual components from SHARPy closed-loop MPC simulations corresponding to the data-driven (▪▪▪▪) and linear ROM (▬▬) UVLM internal models.

The second shows the two first components of the force/moment state $\boldsymbol{q}_2$ (which has 6 components in total, for each elastic longitudinal mode). These results should give us an idea of the effect of model-accuracy on the estimation problems (note that estimation of the velocity state $\boldsymbol{q}_1$ is rather uninteresting, since it is easily recovered by the estimator as all the considered measurements are velocities). The results obtained using the internal model employing data-driven aerodynamics are represented with dash-dotted lines (▪▪▪▪▪), and the one using the UVLM ROM, with thin solid line (——). Since we can easily obtain the components of $\boldsymbol{q}_2$ from post-process of the closed-loop simulations in SHARPy, we include them in thick shaded lines in Fig. 6.23 for reference, similarly with dash-dotted (▪▪▪▪) for those corresponding to the MPC closed-loop using the data-driven UVLM model and solid (▬▬) for those corresponding to the MPC closed-loop using the linear ROM UVLM model. The third figure, Fig. 6.24, shows the flight mechanics variables (flight velocity, U, angle of attack, α, and pitch, θ) of the open-loop responses, shown

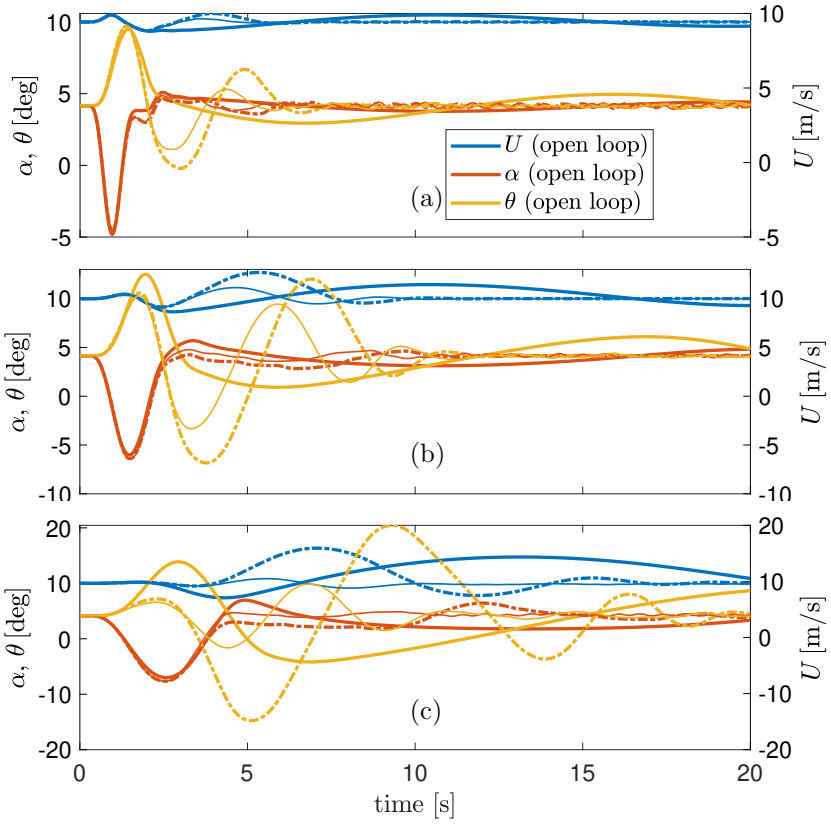


Figure 6.24: U, α and θ for gust perturbations of span (a) 10 m (b) 20 m and (c) 40 m, with open loop (——) and MPC closed-loop responses using the data-driven (- - - -) and the linear ROM (——) UVLM models.

with thick solid lines (——), for the different gust perturbations together with the MPC closed-loop responses using the previously described *line style* notation, which has been employed consistently throughout all the figures in this section. Finally, the generated control inputs of both controllers are shown in Fig. 6.25, where the displayed signals are the normalised increments of control commands from the trim values.

We start the discussion inspecting the outcomes of the estimator. A first observation is that the controller equipped with the data-driven aerodynamic model is seen to produce much more accurate predictions of the system. As we observe in Fig. 6.22, the magnitude of the disturbances seems to be correctly captured by the data-driven-aero controller across all gust spans, showing a bump which eventually tends to zero once the aircraft leaves the gusty region behind. Note that the external force caused by a *1-cos* gust does not follow exactly the same temporal distribution, due to the aerodynamic unsteadiness. Conversely, we observe that the ROM-based internal model shows some difficulties in estimating correctly the external forcing, showing a residual offset once the gust is no longer present. The magnitude of this error seems to correlate with the length of the gust.

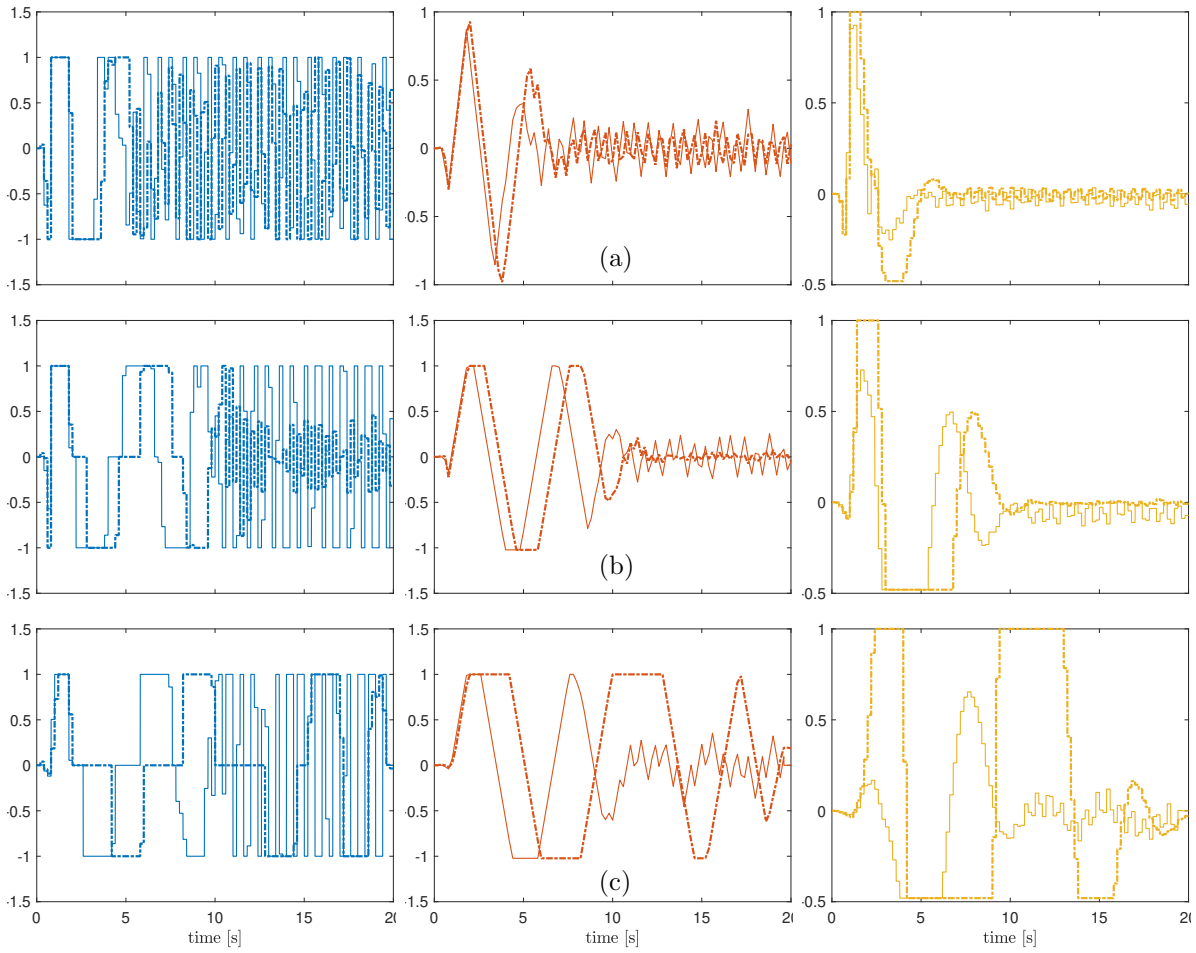


Figure 6.25: Normalised control inputs: elevator rate $\dot{\delta}$ (—), deflection δ (—) and thrust T (—) for gust perturbations of span (a) 10 m (b) 20 m and (c) 40 m. MPC closed-loop responses with the data-driven (▪▪▪▪▪) and linear ROM (——) UVLM models.

This might be explained by the larger excursions of the state space away from the region of validity of the UVLM ROM for more prolonged times. The results in Fig. 6.23 seem to corroborate the increase in accuracy of the data-driven-aero model, which consistently finds estimates of the $\boldsymbol{q}_2$ state with very good agreement with the post-processed closed-loop solution of SHARPy. The first two components, which correspond to the physically more significant first and second bending modes of the aircraft, are seen to match almost perfectly the values retrieved from SHARPy, with the second (red lines) deviating slightly during the main excitation however rapidly coalescing with the reference. On the contrary, the internal model employing the UVLM ROM, which already starts from trim values with noticeable discrepancies, produces estimations with errors that grow in time and with increasing gust spans.

We now focus on the control outcomes. By observing the flight variables response in

Fig. 6.24, we see that both controllers are capable of stabilising the system consistently across the different explored gust spans. We note that since the gusts are all of the same intensity, greater spans H_g translate into more prolonged excitations to the system, which is observed by larger-amplitude responses of the open-loop dynamics. Another observation is that the internal model employing the linear ROM model of the aerodynamics appears to produce more effective stabilisation when compared to the one equipped with the data-driven model, dampening the system faster (i.e., with shorter settling time) and producing a less oscillatory response. This is further supported by the control inputs shown in Fig. 6.25, where the control effort of the UVLM-ROM-based internal controller appears to be consistently lower for all the tested cases. As a matter of fact, the ROM-based control effort is roughly half that of the data-driven-aero for the first two cases, and a sixth for the third case (where the control effort is computed by adding up the weighted norm $\hat{\boldsymbol{u}}^\top R_c \hat{\boldsymbol{u}} + 10^{-3} \hat{\boldsymbol{\delta}}_e^{\ 2}$ over all time steps of the control input signals displayed in Fig. 6.25); the data-driven based internal model produces inputs with longer settling times but in general smoother than the ROM-based counterpart, especially in the thrust setting input (top-right column in Fig. 6.25).

An explanation of these apparent contradictory results may lie in the fact that the posed MPC problem is rather benign, since the control objective is to penalise deviations in the velocity of the frame A while using velocity measurements for the estimation. Therefore, even with poorly estimated values of the disturbances (which might compensate for inaccuracies in the predicted aerodynamic forces), the ROM-based internal model accurately estimates the velocity states $\boldsymbol{q}_1$ and the controller is able to produce more efficient control laws. Note that inputs on control surfaces are very well approximated by the linear UVLM (deflections are usually kept within the linear regime), and it is large variations in elastic deformation, orientation or rigid-body velocities which are known important sources of error in the linearised UVLM. Therefore, the linear-aerodynamics-based controller could benefit from a better prediction of the effect of elevator inputs on the aerodynamic forces, while the data-driven input-output mappings might see a deterioration along the closed-loop solution (possibly due to unexplored combination of inputs in the data-acquisition simulations).

Payload Drop Stabilisation

In this case, the nonlinear aeroelastic simulations of the HALE vehicle in SHARPy are set up so that at $t = 0.25\,\mathrm{s}$ a fraction of the aircraft payload is released, which introduces a sudden perturbation to the trim flight conditions. Three different magnitudes of the

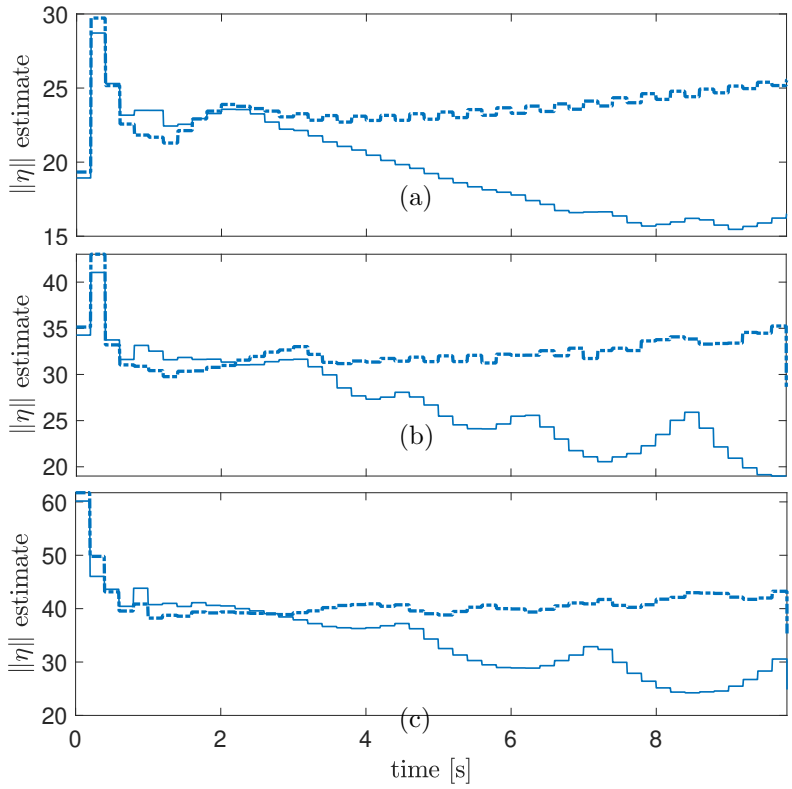


Figure 6.26: Estimates of the disturbance magnitude for the payload mass releases of (a) 25 kg (b) 35 kg and (c) 45 kg. MPC closed-loop responses with the data-driven (▪▪▪▪▪) and linear ROM (——) UVLM models.

dropped payload are considered, $m_l = -25, -35, -45\,\text{kg}$, with the first one giving the same problem setup that has been explored in the example of the previous section.

The results we show in this case are the same as those presented in the previous gust-rejection scenario, with the estimated values of the external forcing magnitude and the first two components of the modal force/moment state $\boldsymbol{q}_2$ presented in Fig. 6.26 and Fig. 6.27, the response in flight mechanics variables (flight velocity, U, angle of attack, α, and pitch, θ) shown in Fig. 6.28 and the generated control inputs of both controllers gathered in Fig. 6.29. The employed line style in the figures below is consistent with the one used in the previous gust-rejection setting.

The superior model accuracy provided by the data-driven aerodynamic model is also observed here in both the external force $\boldsymbol{\eta}$ and the modal force state $\boldsymbol{q}_2$ estimation. As seen in Fig. 6.26, the magnitude of the estimated external force by the data-driven aerodynamic model is seen to reach a roughly constant value after a reasonable settling time, which is in agreement with the nature of the disturbance (note that after stabilisation, the dropped mass would add a constant forcing input to the equations of motion as given by Eq. (6.4)). Moreover, the magnitude seems to scale correspondingly with the increase in

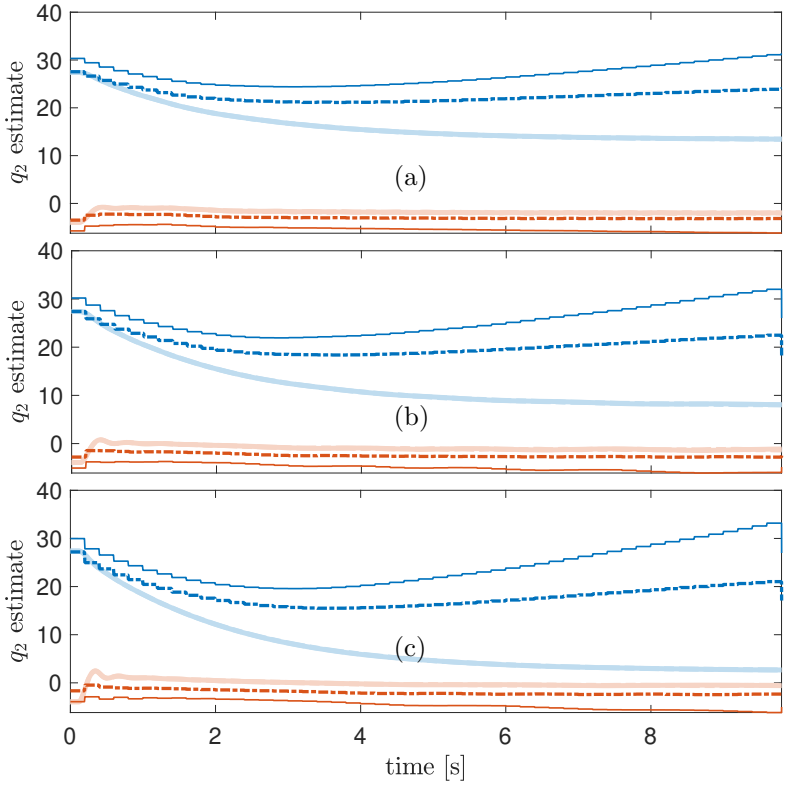


Figure 6.27: Estimates of the $\boldsymbol{q}_2$ state components (first bending in colour ■, second bending in ■) for the payload mass releases of (a) 25 kg (b) 35 kg and (c) 45 kg for the data-driven (▪▪▪▪▪) and linear ROM (——) UVLM internal models. Actual components from SHARPy closed-loop MPC simulations corresponding to the data-driven (▪▪▪▪) and linear ROM (▬) UVLM internal models.

the mass being released. Conversely, the estimated values by the linear-aerodynamics-based internal model are seen, in the same figure, to either diverge or oscillate. The slight divergence, observable with both internal models, is due to a drift in the the projection onto the first bending mode of the external forcing (η_7). This deviation is related to the corresponding first bending mode component of $\boldsymbol{q}_2$, shown in blue in Fig. 6.27, which is also seen to drift with time in the estimates provided by both internal models. This can be caused by the MHE reaching an alternative local minimum which compensates bending deformation with external forcing in the bending component and/or by the non-negligible model mismatch between both models and SHARPy nonlinear simulations. To overcome this difficulty, additional measurements (e.g., root moments or strains) could be considered. Nevertheless, the rest of estimated components of $\boldsymbol{q}_2$ produced by the data-driven-aero model (Fig. 6.27 only shows the two first modes, for clarity) are very good and enable successful stabilisation of the system.

The flight variables in Fig. 6.28 show us the challenge of the posed control case, where the open-loop simulations see the angle of attack and pitch increase rapidly, which could

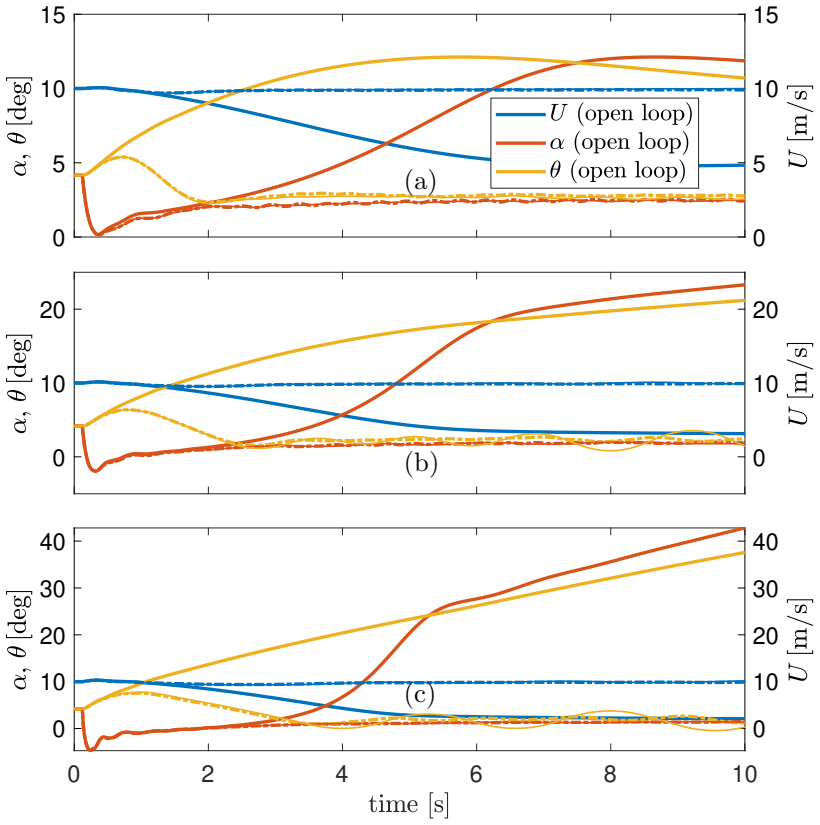


Figure 6.28: U, α and θ for the payload mass releases of (a) 25 kg (b) 35 kg and (c) 45 kg with open loop (——) and MPC closed-loop responses using the data-driven (- - - -) and the linear ROM (——) UVLM models.

possibly lead to stall in a realistic scenario. As a matter of fact, the two last cases yield angles of attack higher than 20 deg for which the validity of the UVLM is compromised (note that no stall effects are modelled). A first compelling observation is that both tested internal models achieve very effective stabilisation of the aircraft. And in contrast to the gust-rejection scenario portrayed above, the linear-aerodynamics-based controller shows worse performance than the data-driven-aero counterpart, illustrated by growing oscillations in the flight variables (principally pitch) of the two heaviest release cases. This deterioration on the performance is seen with greater ease in the resulting input commands shown in Fig. 6.29, which show divergent oscillations in both the elevator and thrust setting inputs. The control effort of the signals displayed in Fig. 6.29 (computed as before) are roughly the same for both internal models for the two first payload releases (where the cost of the larger-amplitude elevator and thrust oscillations of the ROM-based controller are balanced by the higher oscillatory response of the elevator rate for the data-driven-aero model), however for the heaviest release case the ROM-based internal model requiring 33.5% more effort than the data-driven counterpart.

Therefore, it is suggested that, in this more complex control case, where the system has to be stabilised around a notably different deformed configuration (precisely where the linearised UVLM is known to produce less accurate predictions) the internal model based on data-driven aerodynamics can exploit the improved accuracy of the model to better stabilise the system against the considered range of disturbances showing better performance than the ROM-based counterpart.

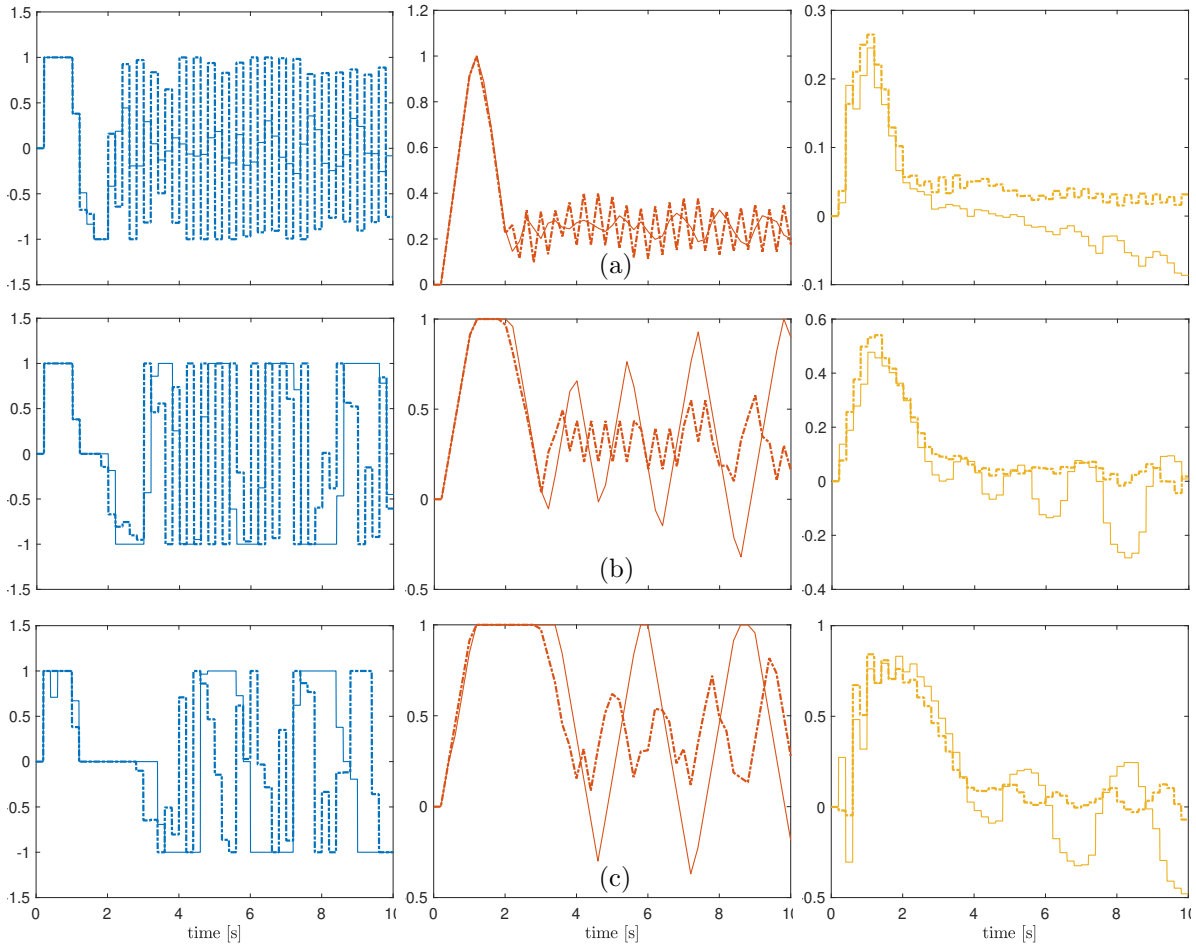


Figure 6.29: Normalised control inputs: elevator rate $\dot{\delta}$ (—), deflection δ (—) and thrust T (—) for the payload mass releases of (a) 25 kg (b) 35 kg and (c) 45 kg. MPC closed-loop responses with the data-driven (▪▪▪▪▪) and linear ROM (——) UVLM models.

Chapter 7

Conclusions

7.1 Summary of Achievements

The overall novel contribution of this dissertation is on the construction of nonlinear low-order models of geometrically-nonlinear very flexible aircraft suitable for control. These must characterise the complex dynamics of such vehicles efficiently using the smallest possible number of degrees of freedom. The key achievements of the presented work that make up this general contribution are outlined below.

7.1.1 Structural Damping for Geometrically-Nonlinear Beams

The infinite-dimensional geometrically-exact beam formulation, from which the proposed internal models for control stem, has been equipped with a generalised form of Kelvin-Voigt structural damping. This development is facilitated by the intrinsic formulation, which describes the beam three-dimensional dynamics using velocities and strains as primary variables. The result is a compact set of partial differential equations that provides a general framework to incorporate measured damping characteristics into the dynamics of beam structures with arbitrary cross sections (including anisotropic materials) with geometrically-nonlinear effects. We note that analytical models to include damping mechanisms are scarce in the literature and very often limited to much simpler configurations and small amplitude dynamics. The proposed formulation builds on the intrinsic theory of beams, and therefore the equations of motions are written in a material frame of reference. This naturally maintains the structural linear constitutive relations into the

geometrically-nonlinear dynamics, and in particular, allows the current formulation to identify the coefficients in the damping model from small-amplitude experimental tests.

A theoretical insight on the decay rates and the equilibrium solutions arising from damping has been given for the resulting model and for one where a first order approximation to the damping terms has been taken. For simplicity, the latter is the one selected to build the modal-based low-order models. However, it is observed that linearisation of the damping terms leads to increased dissipation which eventually removes rotary rigid-body motions from the set of equilibrium solutions. Hence, despite of the increased complexity of the fully-damped model with respect to the linearised one, its use is considered essential for accurate and physically sensible modelling of highly flexible structures with considerable structural damping, and especially so for those subject to rigid-body motions involving rotations (e.g., wind turbine or helicopter rotor blades). The resulting models have been validated through numerical investigation and several simulations are finally given which support and exemplify the theoretical findings.

Finally, we stress that both the nonlinear intrinsic equations and the Kelvin-Voigt damping model have independently been validated in the literature against experimental evidence for the description of geometrically-exact beam dynamics and structural damping, respectively. As geometrically-nonlinear beam theory still uses linear constitutive relations, we expect that the combination of both models would result in an equally well-founded formulation. Nevertheless, nonlinear experimental validation of the proposed model would be highly valuable to support the theoretical contributions presented in Chapter 2, and hence it is regarded as a subsequent natural step in the investigation.

7.1.2 Theoretical MPC Results for the Intrinsic Description of Geometrically Nonlinear Structures

As has been stressed throughout the dissertation, the intrinsic geometrically-exact beam equations offer notable advantages towards the construction of control-oriented models. Importantly, the full equations are written compactly as two coupled sets of partial differential equations with quadratic nonlinearities (semi-linear) and first-order spatial and temporal derivatives. This characteristic structure can be exploited for efficient model-order reduction using a few structural modes of vibration as a solution basis, which as shown, retains the inherent nonlinearity of the dynamics while filtering out higher-order frequency motions. This allows us to capture nonlinear, low-frequency behaviour typical of very flexible structures undergoing large deformations. Nonetheless, due to the

selection of velocities and sectional forces as the main variables of the intrinsic formulation, the state-space needs to be augmented with a chosen parametrisation of the finite rotations if external forcing, dependent on the local orientation, needs to be accounted for (e.g., gravity forces). Since rotations are derived variables, the linearisation of any finite-dimensional representation of the augmented state-space will present unstabilisable modes, as shown in § 4.1. In particular, this prevents us from using conventional MPC theoretical results to guarantee convergence and stability using our low-order internal models for control.

In order to equip our framework with provable, theoretical results on convergence and stability of the closed-loop MPC dynamics using our proposed low-order models a novel MPC setup has been proposed. This involves a redefinition of the MPC stage and terminal costs, which form the cost function of the optimal control problem, used as a Lyapunov candidate to prove stability of the closed-loop MPC dynamics. We have shown that under appropriate construction of this cost function, whose weighing matrices can be obtained solving linear matrix inequalities, provable bounds on the decay of the controllable states and convergence of the MPC closed loop can be established when the linearly unstabilisable modes are brought to a small, bounded subset by the control action. Moreover, it has been shown in numerical examples that, in practice, this is feasible and the effect of the unstabilisable modes can be made insignificant resulting in successful stabilisation of the controlled system.

7.1.3 Nonlinear Low-Order Internal Models for Control

The proposed modal-based low-order aeroelastic models for control have allowed us to condense the physically relevant nonlinear dynamics of very flexible aircraft in very concise systems, which are used to underpin MPC/MHE strategies for these complex vehicles at a much lower computational cost.

The key to the formulation is that it retains the structural geometrically-nonlinear effects, characteristic of structures that undergo large deformations, and are inherited from the intrinsic geometrically-exact beam equations. The coupled low-order aeroelastic models employ a linearisation of unsteady vortex lattice models, projected onto the structural modal expansion and further reduced using efficient bespoke model-order reduction techniques. This yields a very compact model, with quadratic nonlinearities, decidedly amenable to model-based estimation and control strategies. Despite the use of linearised aerodynamics, the nonlinear follower force effect is retained thanks to the use of the geometrically-exact

beam formulation. This is considered to be significantly more relevant than the variation in the relative distance between the different aerodynamic lattice points (which is effectively neglected in the linearisation) which would lead to changing aerodynamic influence coefficients. Further, numerical examples have shown that, at least in the clamped wing scenario, this claim is valid. In the context of free-flying very flexible aircraft, second order effects (missing in these linearised versions of UVLM and negligible in the case of clamped structures) such as variation in the dynamic pressure due to changes in flight velocity or induced drag, lead to discrepancies with full nonlinear simulations that only become obvious in the long-term dynamics.

To parametrise finite rotations within the intrinsic description we have introduced rotation quaternions. Two approximations of different fidelities have been introduced to couple the quaternion dynamics with the low-order aeroelastic models. Properties of the two quaternion approximations, which ensure that the nature of the associated rotation transformation is preserved, have been also investigated. Importantly, both approaches yield systems with identical structure (i.e., quadratic nonlinearities), which facilitates the use of computationally advantageous analytical differentiation.

When these internal models are used as part of the estimation and control framework, it has been shown that it unequivocally exploits the nonlinearity in the system to achieve stabilisation. Moreover, as shown by the extensive numerical evidence, the first few modes are found sufficient to stabilise higher dimensional representations of the controlled systems, implying that the relevant nonlinear dynamics of the system are accurately accounted for by the internal models and highlighting the inherent robustness of the framework in the considered regimes.

7.1.4 Application of Data-Driven Methods in Aeroelasticity Modelling

Data-driven regression tools have proved successful in the task of obtaining closed models of the gravity forcing and the unsteady aerodynamics in terms of the modal intrinsic variables. On the one hand, data-driven identification of the gravity forcing avoids the necessity to introduce approximations to the entire quaternion field. Instead, only the quaternion at one single spatial coordinate needs to be tracked. This yields a reduction of the the state-space vector of the order of the number of retained modes $\mathcal{O}(N_m)$. On the other hand, when stable identified models of the unsteady aerodynamic models have been obtained, these have been shown to be more accurate, accounting for varying dynamic

pressure and induced drag. These improvements with respect linear aerodynamic models are clear in comparisons of the long-time open-loop simulations against full nonlinear solutions. However, when the data-driven enhanced models are used within the MPC/MHE framework the effect on the closed loop performance has been found slightly inconclusive. It has been observed that the increased accuracy of the internal models yields better estimation performance, however a control case where these improvements are highlighted further is yet a matter of future investigation.

7.1.5 Applications of the Framework

Successful application examples of the framework have been obtained, where this has been shown to exploit its knowledge of the controlled system inherent nonlinearity to produce novel stabilisation mechanisms.

The flutter suppression mechanism shown in § 6.1 is particularly compelling. The controller knowledge of the stability properties around different nonlinear equilibria is leveraged to produce a novel stabilisation mechanism, where the wing is brought from an unstable equilibrium point to a stable one, that completely suppresses flutter. This is an application example that is only attainable by control laws based on fully nonlinear information of the controlled system. The examples on stabilisation of a HALE aircraft after a sudden payload drop of § 6.2 and § 6.3 are other particular application examples where information of the nonlinear dynamics of the system is crucial for successful estimation and control. The change in the aircraft overall inertia distribution after the release effectively alters the stability and equilibrium properties of the aircraft, which have to be correctly captured by the internal controllers for successful performance. Remarkably, this can be achieved with very concise system descriptions. For instance, the last example employing the data-driven improvements on the HALE model uses a system constructed with only 30 states.

The presented control framework is generic and is meant to be applied to very flexible aircraft displaying dynamics principally driven by low-frequency large-deflection motions. These include, but not limit to, typical HALE or HAPS aircraft concepts, which, by virtue of their optimised aerodynamic efficiency using extremely slender wings and lightweight composite materials, they display increased flexibility.

As already mentioned in the introduction, the most notable effect of flexibility in the aircraft dynamics is the tightening of the frequency gap between rigid flight mechanics modes and the first elastic modes of vibration. Under certain disturbances or configura-

tions, these modes are known to couple and produce nontrivial dynamics characterised by large-amplitude low-frequency motions, which are highly reproducible by our internal models. Besides, it is thought that, with the typical time scales involved in these problems (as in the HALE example in § 6.2), real-time deployment of our current implementation, written in MATLAB, is essentially possible.

In the context of very flexible aircraft, general vibration suppression mechanisms, characterised by high-frequency and low-amplitude dynamics, or long-horizon objectives (e.g., trajectory tracking) are problems that are not considered to be within the scope of our control framework. We note that the proposed framework is ideal for transient motions characterised by low-frequency markedly nonlinear behaviour, with potential applications in manoeuvre or gust load alleviation suppression. We note that for the first, higher-frequency control problems linear control methods are commonly employed and the long-term aircraft behaviour requirements can be addressed by construction of appropriate outer loops (e.g., reference governors).

7.2 Recommendations for Future Work

In the following lines, the possible future lines of investigation that have been identified as potential improvements to the work presented in this dissertation are discussed.

7.2.1 Improvements to the Nonlinear Low-Order Control Models

As described in Chapter 3, the low-order modal-based models are built from the nonlinear intrinsic beam equations with linearised damping, for simplicity. However, as seen in the theoretical results in § 2.1.3 and backed by the numerical evidence in § 5.1 using the full and highly resolved implementations of the PDEs, linearised damping terms lead to an overestimation of dissipation and can lead to inaccurate predictions. Notwithstanding, the importance and effect of retaining the full nonlinear damping terms on the overall dynamics have not been studied in the modal space. The considered numerical examples employ rather low values of structural damping, for which the discrepancy between full nonlinear and linearised damping terms is assumed to be negligible. However, for application examples where structural damping is moderate-to-high and large rotary rigid-body motions are expected (e.g., in wind turbine applications) the role of the full damping terms in the

modal-based nonlinear structural dynamics should be analysed if the proposed low-order nonlinear models are to be employed for control.

The truncation of the modal basis used to construct approximations to the solution, as shown in Chapter 3, is typically performed based on the frequencies of the structural natural modes of vibration. Hence, after a cutoff frequency is chosen the modes with lower natural frequencies, together with the rigid-body modes, are employed to construct the solution approximation (3.31). This is done as it is expected that the large-amplitude, low-frequency motions, characteristic of very flexible aircraft dynamics, are adequately captured by the first few modes. However, an *ad hoc* mode selection could be considered to improve convergence and accuracy of the modal solution, similarly to the strategy followed in the convergence analysis of 5.2.1, where axial and bending modes are added to the solution regardless of the associated frequencies. In such example, with axial stiffness much larger than bending stiffness, if only the few first modes ordered by ascending frequency are chosen, no axial modes are included in the expansion and hence any inherent nonlinearity in the problem dynamics (in the problem at hand, gyroscopic effects, geometrical stiffening) is unaccounted for. Another strategy to enhance the approximation basis could involve a linear transformation of all the normal modes of vibration (i.e., a sufficiently large set) into a smaller subset in order to compress the relevant dynamics in a certain application case using fewer degrees of freedom. Investigation on suitable or optimal (in some sense) linear transformations should be performed, studying the implications of using such transformation in the properties of the resulting low-order models (e.g., stability or energy preservation properties).

Another interesting line of investigation with potential applications in gust-load alleviation of aircraft with very flexible wings involves construction of low-order modal-based nonlinear aeroelastic models able to reproduce the dynamics of hinged joints; Airbus' Albatross proof-of-concept displays freely-flapping wing tips aiming to alleviate wing root loads [6] during gust encounters. As it has been shown in Chapter 3, normal modes of vibration for joints allowing rotations can be obtained, however they only remain valid for small angular perturbations around the reference linearisation angle. It is thought that construction of a library of nonlinear low-order models employing modes around different joint reference angles to then interpolate according to the instantaneous joint angle could offer an advantageous low-order modelling framework for control of these novel wing designs. This can be regarded as an extension to the nonlinear domain of linear parameter-varying systems, where each of the models in the library would retain nonlinear information of the individual structures composing the network (elastic, gyroscopic and inertial nonlinear effects) yet satisfying linearised joint constraints, where the

interpolation would be performed.

Finally, testing the control framework in a three-dimensional dynamics case of very flexible aircraft would be a natural subsequent step in the investigation. This would only require further work in obtaining a suitable UVLM model, where the developed data-driven tools can be employed too. However, this is thought to be a rather more complex exercise since the number of structural degrees of freedom would be doubled (to account for lateral/asymmetric modes) leading to a substantial increase in the data-driven UVLM model parameters.

7.2.2 Algorithmic Improvements Towards Real-Time Deployment

The main focus of the presented work has been placed on deriving compact models that characterise the nontrivial dynamics of very flexible aircraft, using the fewest possible degrees of freedom to make them suitable for control applications. However, recent efforts by the control community have been directed at conceiving advanced algorithms to accelerate MPC/MHE in order to make real-time application feasible. One significant contribution is the *real-time iteration* scheme [47], where one iteration of the SQP procedure (4.12) is performed at each sampling time (instead of solving the full NLP until convergence tolerance is reached) to then feed back to the controlled system the control inputs available at that iteration. It is shown that, using these procedure, stability and convergence can be guaranteed despite using *unconverged* or *sub-optimal* solutions in the feedback loop. Despite our efforts to reduce the size of our internal models for control, their size is considerably higher to those used to demonstrate the performance of these unconverged MPC strategies, where plant model mismatch is not considered either. Then, it remains of interest to further study (note that § 5.3 already tests a *real-time iteration* implementation [47] on the simpler, purely structural problem) the feasibility of employing these advanced techniques in our framework and analyse its performance in the presence of model uncertainty in the more complex scenario posed by free-flying very flexible aircraft.

The current implementation of the control framework is in MATLAB, since this is a programming platform that facilitates rapid prototyping and eases code testing and debugging. However, to achieve maximum performance, compiled programming languages such as C++ should be considered instead. With regards to the ultimate goal of real application deployment of the control framework, dedicated-software or embedded sys-

tems should be used, due to the typical severe payload limitations of very flexible aircraft (HALE or HAPS) which make the use of general-purpose computers impossible.

7.2.3 Physics-Informed Data-Driven Modelling

A known difficulty of system identification methods to obtain mathematical models of physical dynamical systems is to obtain globally stable models. Unconstrained regression algorithms, such as the one proposed in § 3.3, usually yield unstable models that diverge in finite time and hence are of no use for control purposes. The latest trend in machine learning research is physics-constrained or physics-informed machine learning, so called because the optimal problems that underpin these strategies are modified to benefit from, or to ensure that the resulting identified models satisfy *a priori* known physical properties. An example is the sparsity-promoting algorithm of [84], which by construction of the regression problem ensures global boundedness of the resulting models.

Our modelling framework would certainly benefit from further investigation on these lines, to ensure that the identified reduced-order models of the UVLM are globally stable, since this is a crucial requirement for an adequate functioning of the MPC/MHE strategies. Besides, the structure imposed by the added constraints should be physically sensible, which is a matter that remains unclear with our choice. The selection of the projector operator used to obtain concise state-space representations of the UVLM variables, to which the stability of the obtained data-driven models has shown increased sensitivity, opens another compelling exploration route.

Finally, to overcome the limitation of potential flow assumptions (i.e., infinite Reynolds number), introduced by the use of UVLM, data-driven models of the unsteady aerodynamics, based on higher-fidelity data from Computational Fluid Dynamics simulations, could alternatively be sought. With this, viscosity-driven effects such as flow separation and stall, which can be of significance in highly deformed configurations, could be naturally captured in the formulation. This approach is especially relevant in the context of physics-informed machine-learning modelling, since the known properties of the Navier-Stokes equations can be exploited.

Bibliography

[1] "Climate Emergency Declarations in 1,933 Jurisdictions and Local Governments Cover 826 Million Citizens," 2021. Available online: https://climateemergencydeclaration.org/climate-emergency-declarations-cover-15-million-citizens/ [Accessed on 04/05/2021].

[2] Adhikari, S., *Structural Dynamic Analysis with Generalized Damping Models: Analysis*, John Wiley and Sons, Ltd, 2014.

[3] Adhikari, S., *Structural Dynamic Analysis with Generalized Damping Models: Identification*, John Wiley and Sons, Ltd, 2014.

[4] Adhikari, S., and Woodhouse, J., "Quantification of Non-Viscous Damping in Discrete Linear Systems," *Journal of Sound and Vibration*, Vol. 260, No. 3, 2003, pp. 499 – 518. doi: 10.1016/S0022-460X(02)00952-5.

[5] Ahmadi, A. R., and Widnall, S. E., "Unsteady Lifting-Line Theory as a Singular Perturbation Problem," *Journal of Fluid Mechanics*, Vol. 153, 1985, p. 59–81. doi: 10.1017/S0022112085001148.

[6] Airbus, "The Albatross is Inspiring Tomorrow's Aircraft Wings," 2019. Available online: https://www.airbus.com/newsroom/stories/the-albatross-is-inspiring-tomorrows-next-generation-of-aircraft-wings.html [Accessed on 28/06/2021].

[7] Airbus, "Airbus Reveals New Zero-Emission Concept Aircraft," 2020. Available online: https://www.airbus.com/newsroom/press-releases/en/2020/09/airbus-reveals-new-zeroemission-concept-aircraft.html [Accessed on 11/05/2021].

[8] Airbus, "First A350-1000 Successfully Completes First Flight," 2021. Available online: https://www.airbus.com/newsroom/press-releases/en/2016/11/first-a350-1000-successfully-completes-first-flight.html [Accessed on 18/01/2021].

[9] Al-Jiboory, A. K., Zhu, G., Swei, S. S.-M., Su, W., and Nguyen, N. T., "LPV Modeling of a Flexible Wing Aircraft Using Modal Alignment and Adaptive Gridding Methods,"

Aerospace Science and Technology, Vol. 66, 2017, pp. 92–102. doi: 10.1016/j.ast.2017.03.009.

[10] Albano, E., and Rodden, W., "A Doublet-Lattice Method for Calculating Lift Distributions on Oscillating Surfaces in Subsonic Flows." *AIAA Journal*, Vol. 7, No. 2, 1969, pp. 279–285. doi: 10.2514/3.5086.

[11] Amsallem, D., and Farhat, C., "An Online Method for Interpolating Linear Parametric Reduced Order Models," *SIAM Journal on Scientific Computing*, Vol. 33, No. 5, 2011, pp. 2169–2198. doi: 10.1137/100813051.

[12] Artola, M., Goizueta, N., Wynn, A., and Palacios, R., "Modal-Based Nonlinear Estimation and Control for Highly Flexible Aeroelastic Systems," *AIAA Scitech 2020 Forum*, Orlando, FL, 2020. doi: 10.2514/6.2020-1192.

[13] Artola, M., Goizueta, N., Wynn, A., and Palacios, R., "Aeroelastic Control and Estimation with a Minimal Nonlinear Modal Description," *AIAA Journal*, Vol. 59, No. 7, 2021, pp. 2697–2713. doi: 10.2514/1.J060018.

[14] Artola, M., Goizueta, N., Wynn, A., and Palacios, R., "Proof of Concept for a Hardware-in-the-Loop Nonlinear Control Framework for Very Flexible Aircraft," *AIAA Scitech 2021 Forum*, Nashville, TN, 2021. doi: 10.2514/6.2021-1392.

[15] Artola, M., Wynn, A., and Palacios, R., "A Nonlinear Modal-Based Framework for Low Computational Cost Optimal Control of 3D Very Flexible Structures," *2019 European Control Conference*, Naples, Italy, 2019, pp. 3836–3841. doi: 10.23919/ECC.2019.8796151.

[16] Artola, M., Wynn, A., and Palacios, R., "A Modal-Based Nonlinear Model Predictive Control for 3D Very Flexible Structures," *IEEE Transactions on Automatic Control*, Vol. 67, No. 5, 2022. doi: 10.1109/TAC.2021.3071326.

[17] Ascher, U. M., Ruuth, S. J., and Spiteri, R. J., "Implicit-Explicit Runge-Kutta Methods for Time-Dependent Partial Differential Equations," *Applied Numerical Mathematics*, Vol. 25, No. 2, 1997, pp. 151 – 167. doi: 10.1016/S0168-9274(97)00056-1.

[18] Aurora Flight Sciences, "ODYSSEUS," 2019. Available online: https://www.aurora.aero/odysseus-high-altitude-pseudo-satellite-haps/ [Accessed on 18/01/2021].

[19] Avin, O., Drachinsky, A., Ben-Shmuel, Y., and Raveh, D. E., "Design of an Experimental Benchmark of a Highly Flexible Wing," *60th Israel Annual Conference on Aerospace Sciences*, 2020.

[20] Banks, H., and Inman, D., "On Damping Mechanisms in Beams," Tech. Rep. CR-181904, NASA, Dec. 1989.

[21] Banks, H., and Wang, Y., "Damping Modeling in Timoshenko Beams," *1992 American Control Conference*, IEEE, Chicago, IL, USA, 1992, pp. 2139–2143. doi: 10.23919/ACC.1992.4792509.

[22] Bird, H. J., Otomo, S., Ramesh, K. K., and Viola, I. M., "A Geometrically Non-Linear Time-Domain Unsteady Lifting-Line Theory," *AIAA Scitech 2019 Forum*, San Diego, CA, 2019. doi: 10.2514/6.2019-1377.

[23] Bock, H., and Krämer-Eis, P., "A Multiple Shooting Method for Numerical Computation of Open and Closed Loop Controls in Nonlinear Systems," *IFAC Proceedings Volumes*, Vol. 17, No. 2, 1984, pp. 411–415. doi: 10.1016/S1474-6670(17)61005-X.

[24] Boeing, "Boeing 787 Dreamliner Completes First Flight," 2021. Available online: https://boeing.mediaroom.com/2009-12-15-Boeing-787-Dreamliner-Completes-First-Flight [Accessed on 18/01/2021].

[25] Boyd, J. P., *Chebyshev and Fourier Spectral Methods*, 2nd ed., Dover, New York, 2001.

[26] Brunton, S. L., Noack, B. R., and Koumoutsakos, P., "Machine Learning for Fluid Mechanics," *Annual Review of Fluid Mechanics*, Vol. 52, No. 1, 2020, pp. 477–508. doi: 10.1146/annurev-fluid-010719-060214.

[27] Brunton, S. L., Proctor, J. L., and Kutz, J. N., "Discovering Governing Equations from Data by Sparse Identification of Nonlinear Dynamical Systems," *Proceedings of the National Academy of Sciences*, Vol. 113, No. 15, 2016, pp. 3932–3937. doi: 10.1073/pnas.1517384113.

[28] Capsoni, A., Viganò, G. M., and Bani-Hani, K., "On Damping Effects in Timoshenko Beams," *International Journal of Mechanical Sciences*, Vol. 73, 2013, pp. 27 – 39. doi: 10.1016/j.ijmecsci.2013.04.001.

[29] Cardona, A., and Geradin, M., "A Beam Finite Element Non-Linear Theory with Finite Rotations," *International Journal for Numerical Methods in Engineering*, Vol. 26, No. 11, 1988, pp. 2403–2438. doi: 10.1002/nme.1620261105.

[30] Cartraud, P., and Messager, T., "Computational Homogenization of Periodic Beam-Like Structures," *International Journal of Solids and Structures*, Vol. 43, No. 3, 2006, pp. 686 – 696. doi: 10.1016/j.ijsolstr.2005.03.063.

[31] Caughey, T. K., and O'Kelly, M. E. J., "Classical Normal Modes in Damped Linear Dynamic Systems," *Journal of Applied Mechanics*, Vol. 32, No. 3, 1965, pp. 583–588. doi: 10.1115/1.3627262.

[32] Cesnik, C. E. S., and Hodges, D. H., "Variational-Asymptotical Analysis of Initially Curved and Twisted Composite Beams," *Applied Mechanics Reviews*, Vol. 46, No. 11S, 1993, pp. S211–S220. doi: 10.1115/1.3122638.

[33] Cesnik, C. E. S., and Hodges, D. H., "VABS: A New Concept for Composite Rotor Blade Cross-Sectional Modeling," *Journal of the American Helicopter Society*, Vol. 42, No. 1, 1997, pp. 27–38. doi: 10.4050/JAHS.42.27.

[34] Cesnik, C. E. S., Senatore, P. J., Su, W., Atkins, E. M., and Shearer, C. M., "X-HALE: A Very Flexible Unmanned Aerial Vehicle for Nonlinear Aeroelastic Tests," *AIAA Journal*, Vol. 50, No. 12, 2012, pp. 2820–2833. doi: 10.2514/1.J051392.

[35] Chang, C.-S., Hodges, D. H., and Patil, M. J., "Flight Dynamics of Highly Flexible Aircraft," *Journal of Aircraft*, Vol. 45, No. 2, 2008, pp. 538–545. doi: 10.2514/1.30890.

[36] Chen, L. H., Zhang, W., and Liu, Y. Q., "Modeling of Nonlinear Oscillations for Viscoelastic Moving Belt Using Generalized Hamilton's Principle," *ASME. J. Vib. Acoust.*, Vol. 129, No. 1, 2006, pp. 128–132. doi: 10.1016/j.ijmecsci.2013.04.001.

[37] Cosserat, E., and Cosserat, F., *Théorie des Corps Déformables*, Hermann, Paris, 1909.

[38] Crisfield, M. A., and Jelenić;, G., "Objectivity of Strain Measures in the Geometrically Exact Three-Dimensional Beam Theory and its Finite-Element Implementation," *Proceedings of the Royal Society of London. Series A: Mathematical, Physical and Engineering Sciences*, Vol. 455, No. 1983, 1999, pp. 1125–1147. doi: 10.1098/rspa.1999.0352.

[39] de F.V. Pereira, M., Kolmanovsky, I., and Cesnik, C. E. S., "Model Predictive Control with Constraint Aggregation Applied to Conventional and Very Flexible Aircraft," *2019 IEEE 58th Conference on Decision and Control (CDC)*, 2019, pp. 431–437. doi: 10.1109/CDC40024.2019.9029769.

[40] de F.V. Pereira, M., Kolmanovsky, I., Cesnik, C. E. S., and Vetrano, F., "Model Predictive Control Architectures for Maneuver Load Alleviation in Very Flexible Aircraft," *AIAA Scitech 2019 Forum*, San Diego, CA, 2019. doi: 10.2514/6.2019-1591.

[41] del Carre, A., Muñoz-Simón, A., Goizueta, N., and Palacios, R., "SHARPy: A Dynamic Aeroelastic Simulation Toolbox for Very Flexible Aircraft and Wind Turbines," *Journal of Open Source Software*, Vol. 4, No. 44, 2019, p. 1885. doi: 10.21105/joss.01885.

[42] del Carre, A., and Palacios, R., "Efficient Time-Domain Simulations in Nonlinear Aeroelasticity," *AIAA Scitech 2019 Forum*, San Diego, CA, 2019. doi: 10.2514/6.2019-2038.

[43] del Carre, A., Teixeira, P. C., Palacios, R., and Cesnik, C. E. S., "Nonlinear Response of a Very Flexible Aircraft Under Lateral Gust," *2019 International Forum on Aeroelasticity and Structural Dynamics (IFASD)*, Savannah, Georgia, 2019.

[44] Deskos, G., del Carre, A., and Palacios, R., "Assessment of Low-Altitude Atmospheric Turbulence Models for Aircraft Aeroelasticity," *Journal of Fluids and Structures*, Vol. 95, 2020, p. 102981. doi: 10.1016/j.jfluidstructs.2020.102981.

[45] Devinant, P., "An Approach for Unsteady Lifting-Line Time-Marching Numerical Computation," *International Journal for Numerical Methods in Fluids*, Vol. 26, No. 2, 1998, pp. 177–197. doi: 10.1002/(SICI)1097-0363(19980130)26:2⟨177::AID-FLD633⟩3.0.CO;2-P.

[46] Devinant, P., and Gallois, T., "Swept and Curved Wings: a Numerical Approach Based on Generalized Lifting-Line Theory," *Computational Mechanics*, Vol. 29, No. 4, 2002, pp. 322–331. doi: 10.1007/s00466-002-0345-8.

[47] Diehl, M., Bock, H., and Schlöder, J., "A Real-Time Iteration Scheme for Nonlinear Optimization in Optimal Feedback Control," *SIAM Journal on Control and Optimization*, Vol. 43, No. 5, 2005, pp. 1714–1736. doi: 10.1137/S0363012902400713.

[48] Dillsaver, M., Cesnik, C. E. S., and Kolmanovsky, I., "Gust Load Alleviation Control for Very Flexible Aircraft," *AIAA Atmospheric Flight Mechanics Conference*, Portland, OR, 2011. doi: 10.2514/6.2011-6368.

[49] Dillsaver, M., Cesnik, C. E. S., and Kolmanovsky, I., "Trajectory Control of Very Flexible Aircraft with Gust Disturbance," *AIAA Atmospheric Flight Mechanics (AFM) Conference*, Boston, MA, 2013. doi: 10.2514/6.2013-4745.

[50] Dizy, J., Palacios, R., and Pinho, S. T., "Homogenisation of Slender Periodic Composite structures," *International Journal of Solids and Structures*, Vol. 50, No. 9, 2013, pp. 1473 – 1481. doi: 10.1016/j.ijsolstr.2013.01.017.

[51] dos Santos, C. R., Marques, F. D., and Taha, H. E., "Onera-Type Corrections into the Unsteady Vortex Lattice Method for Dynamic Stall Representation," *International Forum on Aeroelasticity and Structural Dynamics*, Savannah, GA, 2019.

[52] Drela, M., "Integrated Simulation Model for Preliminary Aerodynamic, Structural, and Control-Law Design of Aircraft," *40th Structures, Structural Dynamics, and Materials Conference and Exhibit*, St. Louis, MO, 1999. doi: 10.2514/6.1999-1394.

[53] Duan, M., Cesnik, C. E. S., Kolmanovsky, I. V., and Vetrano, F., "Nonlinear Control-Oriented Modeling for Very Flexible Aircraft," *AIAA Scitech 2021 Forum*, Nashville, TN, 2021. doi: 10.2514/6.2021-1501.

[54] Eng, J., "Google's Solar-Powered Internet Drone Crashes During Test Flight," 2015. NBC News. Available online: https://www.nbcnews.com/tech/innovation/googles-solar-powered-internet-drone-crashes-during-test-flight-n366831 [Accessed on 11/05/2021].

[55] Falkner, V. M., "The Calculations of Aerodynamic Loading on Surfaces of any Shape," Tech. rep., British A.R.C., 1943.

[56] Ferreres, G., "Computation of a Flexible Aircraft LPV/LFT Model Using Interpolation," *IEEE Transactions on Control Systems Technology*, Vol. 19, No. 1, 2011, pp. 132–139. doi: 10.1109/TCST.2010.2078510.

[57] Fonzi, N., Brunton, S. L., and Fasel, U., "Data-Driven Nonlinear Aeroelastic Models of Morphing Wings for Control," *Proceedings of the Royal Society A: Mathematical, Physical and Engineering Sciences*, Vol. 476, No. 2239, 2020, p. 20200079. doi: 10.1098/rspa.2020.0079.

[58] Geradin, M., and Cardona, A., *Flexible Multibody Dynamics: a Finite Element Approach*, 3rd ed., John Wyley and Sons, Chichester, UK, 2015.

[59] Gibson, T., Annaswamy, A., and Lavretsky, E., "Modeling for Control of Very Flexible Aircraft," *AIAA Guidance, Navigation, and Control Conference*, Portland, OR, 2011. doi: 10.2514/6.2011-6202.

[60] Giesing, J. P., Kalman, T. P., and Rodden, W. P., "Subsonic Steady and Oscillatory Aerodynamics for Multiple Interfering Wings and Bodies," *Journal of Aircraft*, Vol. 9, No. 10, 1972, pp. 693–702. doi: 10.2514/3.59066.

[61] Gill, P., Murray, W., and Wright, M., *Numerical Linear Algebra and Optimization*, 1st ed., Addison-Wesley, 1991.

[62] Glover, K., "All Optimal Hankel-Norm Approximations of Linear Multivariable Systems and their L_∞ -Error Bounds," *International Journal of Control*, Vol. 39, No. 6, 1984, pp. 1115–1193. doi: 10.1080/00207178408933239.

[63] Goizueta, N., Wynn, A., and Palacios, R., "Parametric Krylov-Based Order Reduction of Aircraft Aeroelastic Models," *AIAA Scitech 2021 Forum*, Nashville, TN, 2021. doi: 10.2514/6.2021-1798.

[64] Goizueta, N., Wynn, A., Palacios, R., Drachinksy, A., and Raveh, D. E., "Flutter Predictions for Very Flexible Wing Wind Tunnel Test," *AIAA Scitech 2021 Forum*, Nashville, TN, 2021. doi: 10.2514/6.2021-1711.

[65] González, P. J., Silvestre, F. J., Pereira, M. d. F. V., Pang, Z. Y., and Cesnik, C. E. S., "Loop-Separation Control for Very Flexible Aircraft," *AIAA Journal*, Vol. 58, No. 9, 2020, pp. 3819–3834. doi: 10.2514/1.J058692.

[66] Griewank, A., "A Mathematical View of Automatic Differentiation," *Acta Numerica*, Vol. 12, 2003, pp. 321–398. doi: 10.1017/CBO9780511550157.005.

[67] Guendel, R. E., "Unsteady Aerodynamics for Aeroelastic Applications Using the Impulse Response Method," Master's thesis, Massachusetts Institute of Technology, 2000.

[68] Guermond, J.-L., "A Generalized Lifting-Line Theory for Curved and Swept Wings," *Journal of Fluid Mechanics*, Vol. 211, 1990, p. 497–513. doi: 10.1017/S0022112090001665.

[69] Gupta, M., Sarkar, K., and Hodges, D. H., "Dynamic Analysis of Nonlinear Composite Beams with 3-D Structural Damping," *AIAA Scitech 2019 Forum*, San Diego, CA, USA, 2019, pp. 2139–2143. doi: 10.2514/6.2019-0211.

[70] Géradin, M., and Rixen, D., *Mechanical Vibrations: Theory and Application to Structural Dynamics*, 2nd ed., Wiley, 1997.

[71] Haghighat, S., T. Liu, H. H., and R. A. Martins, J. R., "Model-Predictive Gust Load Alleviation Controller for a Highly Flexible Aircraft," *Journal of Guidance, Control, and Dynamics*, Vol. 35, No. 6, 2012, pp. 1751–1766. doi: 10.2514/1.57013.

[72] Hanson, A., *Visualizing quaternions*, Elsevier, 2005.

[73] Hesse, H., Palacios, R., and Murua, J., "Consistent Structural Linearization in Flexible-Body Dynamics with Large Rigid-Body Motion," *AIAA Journal of Computers and Structures*, Vol. 52, No. 3, 2012, pp. 528–538. doi: 10.2514/1.J052316.

[74] Hodges, D. H., "A Mixed Variational Formulation Based on Exact Intrinsic Equations for Dynamics of Moving Beams," *International Journal of Solids and Structures*, Vol. 26, No. 11, 1990, pp. 1253 – 1273. doi: 10.1016/0020-7683(90)90060-9.

[75] Hodges, D. H., "Geometrically Exact, Intrinsic Theory for Dynamics of Curved and Twisted Anisotropic Beams," *AIAA Journal*, Vol. 41, No. 6, 2003, pp. 1131–1137. doi: 10.2514/2.2054.

[76] Holten, T. V., "Some Notes on Unsteady Lifting-Line Theory," *Journal of Fluid Mechanics*, Vol. 77, No. 3, 1976, p. 561–579. doi: 10.1017/S0022112076002255.

[77] Howcroft, C., Cook, R. G., Neild, S. A., Lowenberg, M. H., Cooper, J. E., and Coetzee, E. B., "On the Geometrically Exact Low-Order Modelling of a Flexible Beam: Formulation and Numerical Tests," *Proceedings of the Royal Society A: Mathematical, Physical and Engineering Sciences*, Vol. 474, No. 2216, 2018, p. 20180423. doi: 10.1098/rspa.2018.0423.

[78] Iannelli, A., Fasel, U., Yogarajah, N., and Smith, R. S., "A Balanced Mode Decomposition Approach for Equation-Free Reduced-Order Modeling of LPV Aeroservoelastic Systems," *AIAA Scitech 2021 Forum*, Nashville, TN, 2021. doi: 10.2514/6.2021-1796.

[79] Izraelevitz, J. S., Zhu, Q., and Triantafyllou, M. S., "State-Space Adaptation of Unsteady Lifting Line Theory: Twisting/Flapping Wings of Finite Span," *AIAA Journal*, Vol. 55, No. 4, 2017, pp. 1279–1294. doi: 10.2514/1.J055144.

[80] James, E. C., "Lifting-Line Theory for an Unsteady Wing as a Singular Perturbation Problem," *Journal of Fluid Mechanics*, Vol. 70, No. 4, 1975, p. 753–771. doi: 10.1017/S0022112075002339.

[81] Jiffri, S., Fichera, S., Mottershead, J. E., and Da Ronch, A., "Experimental Nonlinear Control for Flutter Suppression in a Nonlinear Aeroelastic System," *Journal of Guidance, Control, and Dynamics*, Vol. 40, No. 8, 2017, pp. 1925–1938. doi: 10.2514/1.G002519.

[82] Jones, J. R., and Cesnik, C. E. S., "Preliminary Flight Test Correlations of the X-HALE Aeroelastic Experiment," *The Aeronautical Journal*, Vol. 119, No. 1217, 2015, p. 855–870. doi: 10.1017/S0001924000010952.

[83] Kalman, T. P., Rodden, W. P., and Giesing, J. P., "Application of the Doublet-Lattice Method to Nonplanar Configurations in Subsonic Flow," *Journal of Aircraft*, Vol. 8, No. 6, 1971, pp. 406–413. doi: 10.2514/3.59117.

[84] Kaptanoglu, A. A., Callaham, J. L., Hansen, C. J., Aravkin, A., and Brunton, S. L., "Promoting Global Stability in Data-Driven Models of Quadratic Nonlinear Dynamics," 2021.

[85] Karkehabadi, R., "Thick Wings in Steady and Unsteady Flows," *Journal of Aircraft*, Vol. 41, No. 4, 2004, pp. 964–967. doi: 10.2514/1.4589.

[86] Katz, J., and Plotkin, A., "Unsteady Incompressible Potential Flow," *Low Speed Aerodynamics*, Cambridge University Press, 2001, Chap. 13, 2nd ed., pp. 369–433.

[87] Kennedy, G. J., and Martins, J. R., "A Homogenization-Based Theory for Anisotropic Beams with Accurate Through-Section Stress and Strain Prediction," *International Journal of Solids and Structures*, Vol. 49, No. 1, 2012, pp. 54 – 72. doi: 10.1016/j.ijsolstr.2011.09.012.

[88] Keys, R. G., "Cubic Convolution Interpolation for Digital Image Processing," *IEEE Transactions on Acoustics, Speech, and Signal Processing*, Vol. 29, No. 6, 1981, pp. 1153–1160. doi: 10.1109/TASSP.1981.1163711.

[89] LaSalle, J., and Lefschetz, S., *Stability by Lyapunov's Direct Method*, Academic Press, 1961.

[90] Lazan, B., *Damping of Materials and Members in Structural Mechanics*, Pergamon Press, 1968.

[91] Le Clainche, S., Rodríguez, D., Theofilis, V., and Soria, J., "Flow Around a Hemisphere-Cylinder at High Angle of Attack and Low Reynolds Number. Part II: POD and DMD Applied to Reduced Domains," *Aerospace Science and Technology*, Vol. 44, 2015, pp. 88–100. doi: 10.1016/j.ast.2014.10.009.

[92] Leishman, J. G., "Unsteady Lift of a Flapped Airfoil by Indicial Concepts," *Journal of Aircraft*, Vol. 31, No. 2, 1994, pp. 288–297. doi: 10.2514/3.46486.

[93] Levine, J., "Highly Flexible Wings Tested," 2017. NASA Armstrong Flight Research Center. Available online: https://www.nasa.gov/centers/armstrong/features/highly_flexible_wings_tested.html [Accessed on 11/05/2021].

[94] Lisitano, D., Bonisoli, E., and Mottershead, J. E., "Experimental Direct Spatial Damping Identification by the Stabilised Layers Method," *Journal of Sound and Vibration*, Vol. 437, 2018, pp. 325 – 339. doi: 10.1016/j.jsv.2018.08.055.

[95] Loiseau, J.-C., and Brunton, S. L., "Constrained Sparse Galerkin Regression," *Journal of Fluid Mechanics*, Vol. 838, 2018, p. 42–67. doi: 10.1017/jfm.2017.823.

[96] Love, M., Zink, P., Wieselmann, P., and Youngren, H., "Body Freedom Flutter of High Aspect Ratio Flying Wings," *46th AIAA/ASME/ASCE/AHS/ASC Structures, Structural Dynamics and Materials Conference*, Austin, TX, 2005. doi: 10.2514/6.2005-1947.

[97] Macchelli, A., "Stabilisation of a Nonlinear Flexible Beam in Port-Hamiltonian Form," *IFAC Proceedings Volumes*, Vol. 46, No. 23, 2013, pp. 412–417. doi: 10.3182/20130904-3-FR-2041.00115, 9th IFAC Symposium on Nonlinear Control Systems.

[98] Macchelli, A., Melchiorri, C., and Stramigioli, S., "Port-Based Modeling of a Flexible Link," *IEEE Transactions on Robotics*, Vol. 23, No. 4, 2007, pp. 650–660. doi: 10.1109/TRO.2007.898990.

[99] Malcolm, D. J., and Laird, D. L., "Extraction of Equivalent Beam Properties from Blade Models," *Wind Energy*, Vol. 10, No. 2, 2007, pp. 135–157. doi: 10.1002/we.213.

[100] Maraniello, S., and Palacios, R., "Optimal Vibration Control and Co-design of Very Flexible Actuated Structures," *Journal of Sound and Vibration*, Vol. 377, No. 2016, 2016, pp. 1–21. doi: 10.1016/j.jsv.2016.05.018.

[101] Maraniello, S., and Palacios, R., "State-Space Realizations and Internal Balancing in Potential-Flow Aerodynamics with Arbitrary Kinematics," *AIAA Journal*, Vol. 57, No. 6, 2019, pp. 1–14. doi: 10.2514/1.J058153.

[102] Maraniello, S., and Palacios, R., "Parametric Reduced-Order Modeling of the Unsteady Vortex-Lattice Method," *AIAA Journal*, Vol. 58, No. 5, 2020, pp. 2206–2220. doi: 10.2514/1.J058894.

[103] Mardanpour, P., Hodges, D. H., Neuhart, R., and Graybeal, N., "Engine Placement Effect on Nonlinear Trim and Stability of Flying Wing Aircraft," *Journal of Aircraft*, Vol. 50, No. 6, 2013, pp. 1716–1725. doi: 10.2514/1.C031955.

[104] Mardanpour, P., Hodges, D. H., and Rezvani, R., "Nonlinear Aeroelasticity of High-Aspect-Ratio Wings Excited by Time-Dependent Thrust," *Nonlinear Dynamics*, Vol. 75, No. 3, 2014, pp. 475–500. doi: 10.1007/s11071-013-1079-1.

[105] Mardanpour, P., Richards, P. W., Nabipour, O., and Hodges, D. H., "Effect of Multiple Engine Placement on Aeroelastic Trim and Stability of Flying Wing Aircraft," *Journal of Fluids and Structures*, Vol. 44, 2014, pp. 67–86. doi: 10.1016/j.jfluidstructs.2013.09.018.

[106] Mignolet, M. P., Przekop, A., Rizzi, S. A., and Spottswood, S. M., "A Review of Indirect/Non-Intrusive Reduced Order Modeling of Nonlinear Geometric Structures," *Journal of Sound and Vibration*, Vol. 332, No. 10, 2013, pp. 2437–2460. doi: 10.1016/j.jsv.2012.10.017.

[107] Mook, D., and Nayfeh, A., "Numerical Simulations of Dynamic/Aerodynamic Interactions," *Computing Systems in Engineering*, Vol. 1, No. 2, 1990, pp. 461–482. doi: 10.1016/0956-0521(90)90030-O.

[108] Murua, J., Palacios, R., and Graham, J. M. R., "Applications of the Unsteady Vortex-Lattice Method in Aircraft Aeroelasticity and Flight Dynamics," *Progress in Aerospace Sciences*, Vol. 55, 2012, pp. 46 – 72. doi: 10.1016/j.paerosci.2012.06.001.

[109] NASA, "Past Projects: Helios Prototype Solar-Powered Aircraft," 2009. Available online: https://www.nasa.gov/centers/dryden/history/pastprojects/Helios/index.html [Accessed on 18/01/2021].

[110] Nocedal, J., and Wright, S. J., *Numerical Optimization*, 2nd ed., Springer, 2006.

[111] Noor, A. K., Anderson, M. S., and Greene, W. H., "Continuum Models for Beam- and Platelike Lattice Structures," *AIAA Journal*, Vol. 16, No. 12, 1978, pp. 1219–1228. doi: 10.2514/3.61036.

[112] Palacios, R., "Nonlinear Normal Modes in an Intrinsic Theory of Anisotropic Beams," *Journal of Sound and Vibration*, Vol. 330, No. 8, 2011, pp. 1772–1792. doi: 10.1016/j.jsv.2010.10.023.

[113] Palacios, R., and Cesnik, C. E. S., "Cross-Sectional Analysis of Nonhomogeneous Anisotropic Active Slender Structures," *AIAA Journal*, Vol. 43, No. 12, 2005, pp. 2624–2638. doi: 10.2514/1.12451.

[114] Palacios, R., Murua, J., and Cook, R., "Structural and Aerodynamic Models in Nonlinear Flight Dynamics of Very Flexible Aircraft," *AIAA Journal*, Vol. 48, No. 11, 2010, pp. 2648–2659. doi: 10.2514/1.J050513.

[115] Parenteau, M., Plante, F., Laurendeau, E., and Costes, M., "Unsteady Coupling Algorithm for Lifting-Line Methods," *55th AIAA Aerospace Sciences Meeting*, Gravepine, TX, 2017. doi: 10.2514/6.2017-0951.

[116] Patil, M., "Nonlinear Gust Response of Highly Flexible Aircraft," *48th AIAA/ASME/ASCE/AHS/ASC Structures, Structural Dynamics, and Materials Conference*, Honolulu, HI, 2007. doi: 10.2514/6.2007-2103.

[117] Patil, M. J., and Hodges, D. H., "Output Feedback Control of the Nonlinear Aeroelastic Response of a Slender Wing," *Journal of Guidance, Control, and Dynamics*, Vol. 25, No. 2, 2002, pp. 302–308. doi: 10.2514/2.4882.

[118] Patil, M. J., and Hodges, D. H., "Flight Dynamics of Highly Flexible Flying Wings," *Journal of Aircraft*, Vol. 43, No. 6, 2006, pp. 1790–1799. doi: 10.2514/1.17640.

[119] Peters, D., "Two-Dimensional Incompressible Unsteady Airfoil Theory — An Overview," *Journal of Fluids and Structures*, Vol. 24, No. 3, 2008, pp. 295–312. doi: 10.1016/j.jfluidstructs.2007.09.001.

[120] Peters, D. A., Karunamoorthy, S., and Cao, W.-M., "Finite State Induced Flow Models. I - Two-Dimensional Thin Airfoil," *Journal of Aircraft*, Vol. 32, No. 2, 1995, pp. 313–322. doi: 10.2514/3.46718.

[121] Poussot-Vassal, C., and Roos, C., "Generation of a Reduced-Order LPV/LFT Model from a Set of Large-Scale MIMO LTI Flexible Aircraft Models," *Control Engineering Practice*, Vol. 20, No. 9, 2012, pp. 919–930. doi: 10.1016/j.conengprac.2012.06.001.

[122] Prandtl, L., "Applications of Modern Hydrodynamics to Aeronautics," Tech. rep., NACA, 1923.

[123] Rawlings, J. B., Mayne, D. Q., and Diehl, M. M., *Model Predictive Control: Theory, Computation and Design*, 2nd ed., Nob Hill Publishing, 2018.

[124] Rayleigh, L., *Theory of Sound*, 2nd ed., Dover Publications, 1945 (re-issue).

[125] Reissner, E., "On One-Dimensional Large-Displacement Finite-Strain Beam Theory," *Studies in Applied Mathematics*, Vol. 52, No. 2, 1973, pp. 87–95. doi: 10.1002/sapm197352287.

[126] Reissner, E., "On Finite Deformations of Space-Curved Beams," *Zeitschrift für angewandte Mathematik und Physik ZAMP*, Vol. 32, 1981, pp. 734– 744. doi: 10.1007/BF00946983.

[127] Riso, C., and Cesnik, C. E. S., "Correlations Between UM/NAST Nonlinear Aeroelastic Simulations and the Pre-Pazy Wing Experiment," *AIAA Scitech 2021 Forum*, Nashville, TN, 2021. doi: 10.2514/6.2021-1712.

[128] Ritter, M., Cesnik, C. E. S., and Krüger, W. R., "An Enhanced Modal Approach for Large Deformation Modeling of Wing-Like Structures," *56th AIAA/ASCE/AHS/ASC Structures, Structural Dynamics, and Materials Conference*, Kissimmee, FL, 2015. doi: 10.2514/6.2015-0176.

[129] Rodriguez, C., and Leugering, G., "Boundary Feedback Stabilization for the Intrinsic Geometrically Exact Beam Model," *SIAM Journal on Control and Optimization*, Vol. 58, No. 6, 2020, pp. 3533–3558. doi: 10.1137/20M1340010.

[130] Rugh, W. J., and Shamma, J. S., "Research on Gain Scheduling," *Automatica*, Vol. 36, No. 10, 2000, pp. 1401–1425. doi: 10.1016/S0005-1098(00)00058-3.

[131] Schlegel, M., and Noack, B. R., "On Long-Term Boundedness of Galerkin Models," *Journal of Fluid Mechanics*, Vol. 765, 2015, p. 325–352. doi: 10.1017/jfm.2014.736.

[132] Schmid, P. J., "Dynamic Mode Decomposition of Numerical and Experimental Data," *Journal of Fluid Mechanics*, Vol. 656, 2010, p. 5–28. doi: 10.1017/S0022112010001217.

[133] Shahruz, S. M., "Stability of a Nonlinear Axially Moving String With the Kelvin–Voigt Damping," *ASME. J. Vib. Acoust.*, Vol. 131, No. 1, 2009, pp. 014501–1–4. doi: 10.1115/1.3025835.

[134] Silvestre, F. J., Guimarães Neto, A. B., Bertolin, R. M., da Silva, R. G. A., and Paglione, P., "Aircraft Control Based on Flexible Aircraft Dynamics," *Journal of Aircraft*, Vol. 54, No. 1, 2017, pp. 262–271. doi: 10.2514/1.C033834.

[135] Simo, J., "A Finite Strain Beam Formulation. The Three-Dimensional Dynamic Problem. Part I," *Computer Methods in Applied Mechanics and Engineering*, Vol. 49, No. 1, 1985, pp. 55 – 70. doi: 10.1016/0045-7825(85)90050-7.

[136] Simo, J., and Vu-Quoc, L., "A Three-Dimensional Finite-Strain Rod Model. Part II: Computational aspects," *Computer Methods in Applied Mechanics and Engineering*, Vol. 58, No. 1, 1986, pp. 79 – 116. doi: 10.1016/0045-7825(86)90079-4.

[137] Simo, J., and Vu-Quoc, L., "On the Dynamics in Space of Rods Undergoing Large Motions — A Geometrically Exact Approach," *Computer Methods in Applied Mechanics and Engineering*, Vol. 66, No. 2, 1988, pp. 125 – 161. doi: 10.1016/0045-7825(88)90073-4.

[138] Simo, J. C., and Vu-Quoc, L., "On the Dynamics of Flexible Beams Under Large Overall Motions—The Plane Case: Part II," *Journal of Applied Mechanics*, Vol. 53, 1986, pp. 855–863. doi: 10.1115/1.3171871.

[139] Simpson, R. J., Palacios, R., Hesse, H., and Goulart, P., "Predictive Control for Alleviation of Gust Loads on Very Flexible Aircraft," *55th AIAA/ASME/ASCE/AHS/ASC Structures, Structural Dynamics, and Materials Conference*, National Harbour, MD, 2014. doi: 10.2514/6.2014-0843.

[140] Simpson, R. J. S., and Palacios, R., "Numerical Aspects of Nonlinear Flexible Aircraft Flight Dynamics Modeling," *54th AIAA/ASME/ASCE/AHS/ASC Structures, Structural Dynamics, and Materials Conference*, Boston, Massachusetts, 2013. doi: 10.2514/6.2013-1634.

[141] Simsek, M., and Kocatürk, T., "Nonlinear Dynamic Analysis of an Eccentrically Prestressed Damped Beam Under a Concentrated Moving Harmonic Load," *Journal of Sound and Vibration*, Vol. 320, No. 2009, 2009, pp. 235–253. doi: 10.1016/j.jsv.2008.07.012.

[142] Sotoudeh, Z., Hodges, D. H., and Chang, C.-S., "Validation Studies for Aeroelastic Trim and Stability of Highly Flexible Aircraft," *Journal of Aircraft*, Vol. 47, No. 4, 2010, pp. 1240–1247. doi: 10.2514/1.46974.

[143] Steger, S., "Facebook's Airbus Zephyr Drone 'Crashes' in Kimberley Test," 2019. The West Australian. Available online: https://thewest.com.au/news/kimberley/facebooks-airbus-zephyr-drone-crashes-in-kimberley-test-ng-b881165181z [Accessed on 11/05/2021].

[144] Su, W., and Cesnik, C. E. S., "Nonlinear Aeroelasticity of a Very Flexible Blended-Wing-Body Aircraft," *Journal of Aircraft*, Vol. 47, No. 5, 2010, pp. 1539–1553. doi: 10.2514/1.47317.

[145] Su, W., and Cesnik, C. E. S., "Strain-Based Geometrically Nonlinear Beam Formulation for Modeling Very Flexible Aircraft," *International Journal of Solids and Structures*, Vol. 48, No. 16, 2011, pp. 2349 – 2360. doi: 10.1016/j.ijsolstr.2011.04.012.

[146] Su, W., and Cesnik, C. E. S., "Strain-Based Analysis for Geometrically Nonlinear Beams: A Modal Approach," *Journal of Aircraft*, Vol. 51, No. 3, 2014, pp. 890–903. doi: 10.2514/1.C032477.

[147] Su, W., Zhang, J., and Cesnik, C. E. S., "Correlations Between UM/NAST Nonlinear Aeroelastic Simulations and Experiments of a Cantilever Slender Wing," *Proceedings of International Forum on Aeroelasticity and Structural Dynamics (IFASD 2009)*, 2019.

[148] Tibshirani, R., "Regression Shrinkage and Selection via the Lasso," *Journal of the Royal Statistical Society. Series B (Methodological)*, Vol. 58, No. 1, 1996, pp. 267–288.

[149] Tu, J. H., Rowley, C. W., Luchtenburg, D. M., Brunton, S. L., and Kutz, J. N., "On Dynamic Mode Decomposition: Theory and Applications," *Journal of Computational Dynamics*, Vol. 1, 2014, p. 391. doi: 10.3934/jcd.2014.1.391.

[150] van Zyl, L. H., and Mathews, E. H., "Quadratic Mode Shape Components From Linear Finite Element Analysis," *Journal of Vibration and Acoustics*, Vol. 134, No. 1, 2011, p. 014501. doi: 10.1115/1.4004681, 014501.

[151] Verschueren, R., Frison, G., Kouzopis, D., van Duijkeren, N., Zanelli, A., Quirynen, R., and Diehl, M., "Towards a Modular Software Package for Embedded Optimization," *IFAC Papers OnLine*, Vol. 51, No. 20, 2018, pp. 374–380. doi: 10.2514/1.27606.

[152] Wagner, N., and Adhikari, S., "Symmetric State-Space Method for a Class of Nonviscously Damped Systems," *AIAA Journal*, Vol. 41, No. 5, 2003, pp. 951–956. doi: 10.2514/2.2032.

[153] Wang, Q., and Yu, W., "Sensitivity Analysis of Geometrically Exact Beam Theory (GEBT) Using the Adjoint Method with Hydra," *52nd AIAA/ASME/ASCE/AHS/ASC Structures, Structural Dynamics and Materials Conference*, Denver, 2011. doi: 10.2514/6.2011-1897.

[154] Wang, Y., "Aeroelastic Modelling and Control of Very Flexible Air Vehicles Using a Nonlinear Modal Formulation," Ph.D. thesis, Imperial College London, 2015.

[155] Wang, Y., Palacios, R., and Wynn, A., "A Method for Normal-Mode-Based Model Reduction in Nonlinear Dynamics of Slender Structures," *Computers and Structures*, Vol. 159, 2015, pp. 26 – 40. doi: 10.1016/j.compstruc.2015.07.001.

[156] Wang, Y., Wynn, A., and Palacios, R., "Nonlinear Model Reduction for Aeroelastic Control of Flexible Aircraft Described by Large Finite-Element Models," *55th AIAA/ASME/ASCE/AHS/ASC Structures, Structural Dynamics, and Materials Conference*, AIAA, National Harbor, Maryland, 2014. doi: 10.2514/6.2014-0842.

[157] Wang, Y., Wynn, A., and Palacios, R., "Nonlinear Modal Aeroservoelastic Analysis Framework for Flexible Aircraft," *AIAA Journal*, Vol. 54, No. 10, 2016, pp. 3075–3090. doi: 10.2514/1.J054537.

[158] Wang, Y., Wynn, A., and Palacios, R., "Nonlinear Aeroelastic Control of Very Flexible Aircraft Using Model Updating," *Journal of Aircraft*, Vol. 55, No. 4, 2018, pp. 1551–1563. doi: 10.2514/1.C034684.

[159] Wang, Z., Chen, P. C., Liu, D. D., and Mook, D. T., "Nonlinear-Aerodynamics/Nonlinear-Structure Interaction Methodology for a High-Altitude Long-Endurance Wing," *Journal of Aircraft*, Vol. 47, No. 2, 2010, pp. 556–566. doi: 10.2514/1.45694.

[160] Wei, X., and Mottershead, J. E., "Aeroelastic Systems with Softening Nonlinearity," *AIAA Journal*, Vol. 52, No. 9, 2014, pp. 1915–1927. doi: 10.2514/1.J052712.

[161] Wilson, T., Castrichini, A., Azabal, A., Cooper, J., Ajaj, R., and Herring, M., "Aeroelastic Behaviour of Hinged Wing Tips," *2017 International Forum on Aeroelasticity and Structural Dynamics (IFASD)*, 2017.

[162] Woodbury, M. A., *Inverting Modified Matrices*, Statistical Research Group, Memo. Rep. no. 42, Princeton University, Princeton, N. J., 1950.

[163] Wright, S. J., Nowak, R. D., and Figueiredo, M. A. T., "Sparse Reconstruction by Separable Approximation," *IEEE Transactions on Signal Processing*, Vol. 57, No. 7, 2009, pp. 2479–2493. doi: 10.1109/TSP.2009.2016892.

[164] Wynn, A., Wang, Y., Palacios, R., and Goulart, P. J., "An Energy-Preserving Description of Nonlinear Beam Vibrations in Modal Coordinates," *Journal of Sound and Vibration*, Vol. 332, No. 21, 2013, pp. 5543 – 5558. doi: 10.1016/j.jsv.2013.05.021.

Appendix A

NMPC Convergence Proofs

The purpose of this appendix is to prove the diverse Lemmas and the Theorem involved in the theoretical control discussion of § 4.1.

Proof of Lemma 3

Since (A_w, B_w) is a stabilisable pair, there exists $0 < \beta < 1, P_w \in \mathcal{S}^{n_1}_{++}$ and $K_w \in \mathbb{R}^{m \times n_1}$ such that $(A_w + B_w K_w)^\top P_w (A_w + B_w K_w) - P_w \preceq -\beta P_w$. Now, by a Schur complement argument $X \succeq 0$ is equivalent to

$$\begin{pmatrix} \hat{A}_w^\top P_w \hat{A}_w & \hat{A}_w^\top P_w \hat{A}_d \\ [*] & \hat{A}_d^\top P_w \hat{A}_d \end{pmatrix} \preceq \begin{pmatrix} (1-\beta) P_w & 0 \\ 0 & P_d \end{pmatrix},$$

where $\hat{A}_w = A_w + B_w K_w$ and $\hat{A}_d = A_d + B_w K_d$. Consequently, for β, P_w, K_w as above and fixed K_d, it is clear that there exists $P_d \in \mathcal{S}^{n_2}_{++}$ sufficiently large and $R \in \mathcal{S}^{m}_{++}$ sufficiently small such that $X \succeq 0$ and $Y \succeq 0$. □

Proof of Lemma 5

Letting $\hat{\boldsymbol{f}} = \begin{pmatrix} \hat{\boldsymbol{f}}_w \\ \hat{\boldsymbol{f}}_d \end{pmatrix}$ and $\boldsymbol{x}^+ = \begin{pmatrix} \boldsymbol{w}^+ \\ \boldsymbol{d}^+ \end{pmatrix}$ we have that

$$\begin{aligned} \|\boldsymbol{w}^+\|^2_{P_w} = \|\hat{A}_w \boldsymbol{w} + \hat{A}_d \boldsymbol{d}\|^2_{P_w} + \|\hat{\boldsymbol{f}}_w\|^2_{P_w} \\ + 2(\hat{A}_w \boldsymbol{w} + \hat{A}_d \boldsymbol{d})^\top P_w \hat{\boldsymbol{f}}_w(\boldsymbol{x}, K\boldsymbol{x}), \end{aligned} \tag{A.1}$$

and

$$\|\boldsymbol{d}^+\|_{P_d}^2 = \|\boldsymbol{d}\|_{P_d}^2 + \|\hat{\boldsymbol{f}}_d(\boldsymbol{x}, K\boldsymbol{x})\|_{P_d}^2 + 2\boldsymbol{d}^\top P_d \hat{\boldsymbol{f}}_d(\boldsymbol{x}, K\boldsymbol{x}). \tag{A.2}$$

Now, since $\hat{\boldsymbol{f}}$ contains higher-than-linear terms, there exist sufficiently small $\omega, \delta > 0$ such that both

$$\begin{aligned} \|\hat{\boldsymbol{f}}_w(\boldsymbol{x}, K\boldsymbol{x})\|_{P_w}^2 + 2(\hat{A}_w\boldsymbol{w} + \hat{A}_d\boldsymbol{d})^\top P_w \hat{\boldsymbol{f}}_w(\boldsymbol{x}, K\boldsymbol{x}) \\ \leq \frac{\beta}{2}\|\boldsymbol{w}\|_{P_w}^2 + \frac{1}{2}\|\boldsymbol{d}\|_{P_d}^2 \end{aligned} \tag{A.3}$$

and

$$\|\hat{\boldsymbol{f}}_d(\boldsymbol{x}, K\boldsymbol{x})\|_{P_d}^2 + 2\boldsymbol{d}^\top P_d \hat{\boldsymbol{f}}_d(\boldsymbol{x}, K\boldsymbol{x}) \leq \eta, \tag{A.4}$$

hold for any $\boldsymbol{x} \in \chi(\omega, \delta)$.

Now, using (4.8) from Lemma 4 gives

$$\begin{aligned} V_f(\boldsymbol{x}^+) - V_f(\boldsymbol{x}) &= \|\hat{A}_w\boldsymbol{w} + \hat{A}_d\boldsymbol{d}\|_{P_w}^2 - \|w\|_{P_w}^2 + \|\hat{\boldsymbol{f}}_w\|_{P_w}^2 \\ &\quad + 2(\hat{A}_w\boldsymbol{w} + \hat{A}_d\boldsymbol{d})^\top P_w \hat{\boldsymbol{f}}_w(\boldsymbol{x}, K\boldsymbol{x}) \\ &\leq -\frac{\beta}{2}\|\boldsymbol{w}\|_{P_w}^2 + \frac{3}{2}\|\boldsymbol{d}\|_{P_d}^2. \end{aligned}$$

Equation (4.10) then follows from (4.9) of Lemma 4.

We now show that $\boldsymbol{x}^+ \in \chi(\omega, \delta + \eta)$, given that $\boldsymbol{x} \in \chi(\omega, \delta)$. From (A.2) and (A.4),

$$\|\boldsymbol{d}^+\|_{P_d}^2 \leq \|\boldsymbol{d}\|_{P_d}^2 + \eta \leq \delta + \eta.$$

Finally, using (A.1), (A.3) and (4.8),

$$\begin{aligned} \|\boldsymbol{w}^+\|_{P_w}^2 = V_f(\boldsymbol{x}^+) &\leq \left(1 - \frac{\beta}{2}\right)\|\boldsymbol{w}\|_{P_w}^2 + \frac{3}{2}\|\boldsymbol{d}\|_{P_d}^2 \\ &\leq \left(1 - \frac{\beta}{2}\right)\omega + \frac{3\delta}{2} \leq \omega \end{aligned}$$

where the final inequality holds with the additional assumption $\delta \leq \frac{\beta\omega}{3}$.

Proof of Lemma 6

Let $\epsilon > 0$. First note that since V_N is continuously differentiable and $\chi(\omega_0, \delta_0)$ is compact, there exists $L_V > 0$ such that

$$|V_N(\boldsymbol{y}, \boldsymbol{u}) - V_N(\boldsymbol{y}, \boldsymbol{v})| \leq L_V \|\boldsymbol{u} - \boldsymbol{v}\|_{U^N} \tag{A.5}$$

for $\boldsymbol{u}, \boldsymbol{v} \in U^N, \boldsymbol{y} \in \chi(\omega_0, \delta_0)$. By Assumption 2 there exists $\eta > 0$ such that

$$d_H\left(\mathcal{U}_{N,\omega,\delta}(\boldsymbol{y}), \mathcal{U}_{N,\omega,\delta+\eta}(\boldsymbol{y})\right) \leq \frac{\epsilon}{L_V}, \tag{A.6}$$

for any $\omega < \omega_0, \delta < \delta_0$ and $\boldsymbol{y} \in X_{N,\omega,\delta}$.

Next, pick $\omega < \omega_0$ and $\delta < \omega\beta/3$ such that the consequences of Lemma 5 are true for $\eta > 0$. Let $\boldsymbol{x} \in X_{N,\omega,\delta}$ and let $\boldsymbol{u}^* = (\boldsymbol{u}_*^0, \ldots, \boldsymbol{u}_*^{N-1})$ be an optimizing sequence for $V^*_{N,\omega,\delta}(\boldsymbol{x})$. Let $\boldsymbol{x}_*^k = \boldsymbol{\phi}(k; \boldsymbol{x}, \boldsymbol{u}^*)$ be the associated state trajectory. Then $\boldsymbol{x}_*^N \in \chi(\omega, \delta)$ and, by the assumption of control invariance,

$$\boldsymbol{x}_*^1 = f(\boldsymbol{x}, \boldsymbol{\kappa}_{N,\omega,\delta}(\boldsymbol{x})) \in X_{N,\omega,\delta}.$$

Now, since $\boldsymbol{x}_*^N \in \chi(\omega, \delta)$, Lemma 5 implies that $\boldsymbol{f}(\boldsymbol{x}_*^N, K\boldsymbol{x}_*^N) \in \chi(\omega, \delta + \eta)$ and

$$V_f(f(\boldsymbol{x}_*^N, K\boldsymbol{x}_*^N)) - V_f(\boldsymbol{x}_*^N) + \ell(\boldsymbol{x}_*^N, K\boldsymbol{x}_*^N) \leq 2\|\boldsymbol{d}_*^N\|_{P_d}^2. \tag{A.7}$$

Furthermore, since $\boldsymbol{f}(\boldsymbol{x}_*^N, K\boldsymbol{x}_*^N) \in \chi(\omega, \delta + \eta)$, it follows that the input sequence $\tilde{\boldsymbol{u}} = (\boldsymbol{u}_*^1, \ldots, \boldsymbol{u}_*^{N-1}, K\boldsymbol{x}_*^N)$ satisfies

$$\tilde{\boldsymbol{u}} \in \mathcal{U}_{N,\omega,\delta+\eta}(\boldsymbol{x}_*^1).$$

By (A.6), there exists $\boldsymbol{v} \in \mathcal{U}_{N,\omega,\delta}(\boldsymbol{x}_*^1)$ such that $\|\tilde{\boldsymbol{u}} - \boldsymbol{v}\|_{U^N} \leq \epsilon/L_V$. By (A.5),

$$|V_N(\boldsymbol{x}_*^1, \boldsymbol{v}) - V_N(\boldsymbol{x}_*^1, \tilde{\boldsymbol{u}})| \leq \epsilon.$$

By optimality and the above inequality,

$$V^*_{N,\omega,\delta}(\boldsymbol{x}_*^1) \leq V_N(\boldsymbol{x}_*^1, \boldsymbol{v}) \leq V_N(\boldsymbol{x}_*^1, \tilde{\boldsymbol{u}}) + \epsilon.$$

Using the definitions of $\tilde{\boldsymbol{u}}$ and $V^*_{N,\omega,\delta}(\boldsymbol{x})$,

$$V_N(\boldsymbol{x}_*^1, \tilde{\boldsymbol{u}}) = \sum_{k=1}^{N-1} \ell(\boldsymbol{x}_*^k, \boldsymbol{u}_*^k) + \ell(\boldsymbol{x}_*^N, K\boldsymbol{x}_*^N) + V_f(f(\boldsymbol{x}_*^N, K\boldsymbol{x}_*^N))$$

$$
\begin{aligned}
&= \left(\sum_{k=0}^{N-1} \ell(\boldsymbol{x}_*^k, \boldsymbol{u}_*^k) + V_f(\boldsymbol{x}_*^N)\right) - \ell(\boldsymbol{x}, \boldsymbol{u}_*^0) - V_f(\boldsymbol{x}_*^N) \\
&+ V_f(f(\boldsymbol{x}_*^N, K\boldsymbol{x}_*^N)) + \ell(\boldsymbol{x}_*^N, K\boldsymbol{x}_*^N) \\
&= V_{N,\omega,\delta}^*(\boldsymbol{x}) - \ell(\boldsymbol{x}, \boldsymbol{u}_*^0) - V_f(\boldsymbol{x}_*^N) + V_f(\boldsymbol{f}(\boldsymbol{x}_*^N, K\boldsymbol{x}_*^N)) + \ell(\boldsymbol{x}_*^N, K\boldsymbol{x}_*^N) \\
\text{(by (A.7))} &\leq V_{N,\omega,\delta}^*(\boldsymbol{x}) - \ell(\boldsymbol{x}, \boldsymbol{\kappa}_{N,\omega,\delta}(\boldsymbol{x})) + 2\|\boldsymbol{d}_*^N\|_{P_d}^2 \\
(\boldsymbol{x}_*^N \in \chi(\omega,\delta)) &\leq V_{N,\omega,\delta}^*(\boldsymbol{x}) - \ell(\boldsymbol{x}, \boldsymbol{\kappa}_{N,\omega,\delta}(\boldsymbol{x})) + 2\delta \\
\text{(by def. of } \ell) &\leq V_{N,\omega,\delta}^*(\boldsymbol{x}) - \frac{\beta}{4}\|\boldsymbol{w}\|_{P_w}^2 + 2\delta.
\end{aligned}
$$

Hence, since $\boldsymbol{x}_*^1 = \boldsymbol{f}(\boldsymbol{x}, \boldsymbol{\kappa}_{N,\omega,\delta}(\boldsymbol{x})) = \boldsymbol{x}^+$ it follows that

$$
V_{N,\omega,\delta}^*(\boldsymbol{x}^+) \leq V_{N,\omega,\delta}^*(\boldsymbol{x}) - \frac{\beta}{4}\|\boldsymbol{w}\|_{P_w}^2 + 2\delta + \epsilon.
$$

Proof of Theorem 7

By Lemma 6, there exist $\omega < \omega_0, \delta < \delta_0$ such that for any $k \in \mathbb{N}$,

$$
V_{N,\omega,\delta}^*(\boldsymbol{x}^k) \leq V_{N,\omega,\delta}^*(\boldsymbol{x}^0) - \frac{\beta}{4}\sum_{i=0}^{k-1}\|\boldsymbol{w}^i\|_{P_w}^2 + k(2\delta + \epsilon).
$$

Now, suppose that there exists $\rho > 0$ such that $\|\boldsymbol{w}^k\|_{P_w}^2 \geq (4/\beta)(2\delta + \epsilon) + \rho$ for all $k \in \mathbb{N}$. Then

$$
0 \leq V_{N,\omega,\delta}^*(\boldsymbol{x}^k) \leq V_{N,\omega,\delta}^*(\boldsymbol{x}^0) - \rho k, \qquad k \in \mathbb{N},
$$

which is a contradiction. Hence, there exists $k_0 \in \mathbb{N}$ such that $\|\boldsymbol{w}^{k_0}\|_{P_w}^2 \leq \frac{4}{\beta}(2\delta + \epsilon)$. The eventual bound follows from estimating the maximum increase in $\|w^k\|_{P_w}$ after the first time its value is less than $(4/\beta)(2\delta + \epsilon)$. □

Appendix B

Relation of Intrinsic Equations to Standard Beam Formulations

This section is devoted to describe how two classic beam formulations are contained in and can be obtained from our general nonlinear intrinsic beam formulation, namely the two-dimensional Euler-Bernoulli and Timoshenko beams. This is useful for the first numerical example in § 5.1, since the damping model in the intrinsic equations is validated against an Euler-Bernoulli test case [141].

We start with the Euler-Bernoulli beam. Given the two-dimensional nature of the case we restrict our attention to variables participating in the motion contained in the 1–3 plane, that is v_1, v_3, ω_2 and f_1, f_3, κ_2 with the corresponding inertial and structural properties μ, i_2, EA, EI_2, GA_3 (i.e., mass per unit length, rotary inertia and axial, bending and shear stiffness, respectively) and equal damping coefficient η for each degree of freedom. The nonlinear equations (2.13)–(2.14) restricted to this 2D case become

$$\mu\dot{v}_1 - (f_1 + \eta\dot{f}_1)' + \omega_2\mu v_3 - (f_3 + \eta\dot{f}_3)\tfrac{1}{EI_2}m_2 = f_{e1}, \tag{B.1a}$$

$$\mu\dot{v}_3 - (f_3 + \eta\dot{f}_3)' - \omega_2\mu v_1 + (f_1 + \eta\dot{f}_1)\tfrac{1}{EI_2}m_2 = f_{e3}, \tag{B.1b}$$

$$i_2\dot{\omega}_2 - (m_2 + \eta\dot{m}_2)' + (f_3 + \eta\dot{f}_3) + (f_3 + \eta\dot{f}_3)\tfrac{1}{EA}f_1 - (f_1 + \eta\dot{f}_1)\tfrac{1}{GA_3}f_3 = m_{e2}, \tag{B.1c}$$

$$\tfrac{1}{EA}\dot{f}_1 - v_1' - v_3\tfrac{1}{EI_2}m_2 + \omega_2\tfrac{1}{GA_3}f_3 = 0, \tag{B.1d}$$

$$\tfrac{1}{GA_3}\dot{f}_3 - v_3' - \omega_2 + v_1\tfrac{1}{EI_2}m_2 - \omega_2\tfrac{1}{EA}f_1 = 0, \tag{B.1e}$$

$$\tfrac{1}{EI_2}\dot{m}_2 - \omega_2' = 0. \tag{B.1f}$$

Now, the Euler-Bernoulli hypotheses assume that $i_2 \to 0$ and $GA_3 \to \infty$ for finite f_3 (i.e., shear strain tends to zero) and hence damping terms associated to shear strain also

vanish $\eta \dot{f}_3 \to 0$. In practice, and in order to avoid the appearance of algebraic expressions, we select i_2 small enough and GA_3 high enough which asymptotically lead us to an Euler-Bernoulli solution (typically a convergence study would be performed to determine appropriate values). Introducing u and w as the axial and transverse displacements, and considering the following kinematic relationships

$$v_1 = \frac{\partial u}{\partial t}, \quad v_3 = \frac{\partial w}{\partial t}, \tag{B.2}$$

we recover the well-known linear Euler-Bernoulli model by removing all nonlinear terms in (B.1). Then,

$$\begin{aligned}
&\text{from (B.1e)} \qquad \omega_2 = -\frac{\partial}{\partial t}\frac{\partial w}{\partial s},\\
&\text{from (B.1f)} \qquad m_2 = EI_2\frac{\partial^2 w}{\partial s^2},\\
&\text{from (B.1d)} \qquad f_1 = EA\frac{\partial u}{\partial s},\\
&\text{from (B.1c)} \qquad f_3 = \frac{\partial}{\partial s}\left(m_2 + \eta\frac{\partial m_2}{\partial t}\right),
\end{aligned}$$

and finally substituting in (B.1a) and (B.1b) we arrive at

$$\mu\frac{\partial^2 u}{\partial t^2} - \frac{\partial}{\partial s}\left(EA\frac{\partial u}{\partial s} + \eta EA\frac{\partial^2 u}{\partial t \partial s}\right) = f_{e1}, \tag{B.3a}$$

$$\mu\frac{\partial^2 w}{\partial t^2} - \frac{\partial^2}{\partial s^2}\left(EI_2\frac{\partial^2 w}{\partial s^2} + \eta EI_2\frac{\partial^3 w}{\partial t \partial s^2}\right) = f_{e3}. \tag{B.3b}$$

This set of results obtained with the intrinsic formulation can be compared to [141], where von-Kármán's nonlinear strain–displacement relationship is assumed. The model in [141] results in a hybrid between the full nonlinear (B.1) and the linear Euler-Bernoulli model (B.3). It can be obtained by removing all nonlinear terms in (B.1) except for the most relevant one in (B.1d) ($v_3\frac{1}{EI_2}m_2$, linked to the geometrical nonlinear inextension effect), which is replaced by an approximate expression resulting in an axial force

$$f_1 = EA\left(\frac{\partial u}{\partial s} + \frac{1}{2}\left(\frac{\partial w}{\partial s}\right)^2\right). \tag{B.4}$$

For the sake of completeness we also describe how the Timoshenko beam model would be obtained. The hypotheses differ from the Euler-Bernoulli in that GA_3 is finite and $i_2 \neq 0$, hence (B.1) would already provide a nonlinear Timoshenko beam model. The linear model would be similarly obtained by neglecting all nonlinear terms in (B.1) but

introducing now the rotation angle ϕ and defining the following kinematic equivalences

$$v_1 = \frac{\partial u}{\partial t}, \quad v_3 = \frac{\partial w}{\partial t}, \quad \omega_2 = \frac{\partial \phi}{\partial t}. \tag{B.5}$$

Then

$$\begin{aligned} \text{from (B.1e)} \qquad & f_3 = GA_3 \left(\frac{\partial w}{\partial s} + \phi \right), \\ \text{from (B.1f)} \qquad & m_2 = EI_2 \frac{\partial \phi}{\partial s}, \\ \text{from (B.1d)} \qquad & f_1 = EA \frac{\partial u}{\partial s}, \end{aligned}$$

and substituting in (B.1a), (B.1b) and (B.1c) we get to

$$\mu \frac{\partial^2 u}{\partial t^2} - \frac{\partial}{\partial s} \left(EA \frac{\partial u}{\partial s} + \eta EA \frac{\partial^2 u}{\partial t \partial s} \right) = f_{e1}, \tag{B.6a}$$

$$\mu \frac{\partial^2 w}{\partial t^2} - \frac{\partial}{\partial s} \left(GA_3 \left(\frac{\partial w}{\partial s} + \phi \right) + \eta GA_3 \left(\frac{\partial^2 w}{\partial t \partial s} + \frac{\partial \phi}{\partial t} \right) \right) = f_{e3}. \tag{B.6b}$$

$$i_2 \frac{\partial^2 \phi}{\partial t^2} - \frac{\partial}{\partial s} \left(EI_2 \frac{\partial \phi}{\partial s} + \eta EI_2 \frac{\partial^2 \phi}{\partial t \partial s} \right) + GA_3 \left(\frac{\partial w}{\partial s} + \phi \right) + \eta GA_3 \left(\frac{\partial^2 w}{\partial t \partial s} + \frac{\partial \phi}{\partial t} \right) = m_{e2}. \tag{B.6c}$$

Appendix C

FE Implementation of the Damped Intrinsic Beam Equations

The aim of this section is to describe the finite element implementation used to simulate the two proposed damping models for the intrinsic beam equations. We first show the implementation for the undamped equations and later we proceed to describe how this is modified to account for the two different damping models and its associated distinct boundary conditions.

For the sake of completeness we rewrite here the undamped form of the intrinsic equations

$$M\dot{\boldsymbol{x}}_1 - \boldsymbol{x}_2' - E\boldsymbol{x}_2 + \mathcal{L}_1(\boldsymbol{x}_1)M\boldsymbol{x}_1 + \mathcal{L}_2(\boldsymbol{x}_2)C\boldsymbol{x}_2 = \boldsymbol{f}_e, \tag{C.1}$$

$$C\dot{\boldsymbol{x}}_2 - \boldsymbol{x}_1' + E^\top \boldsymbol{x}_1 - \mathcal{L}_1^\top(\boldsymbol{x}_1)C\boldsymbol{x}_2 = \boldsymbol{0}, \tag{C.2}$$

with boundary conditions that we express now as

$$G_0 \begin{pmatrix} \boldsymbol{x}_1 \\ \boldsymbol{x}_2 \end{pmatrix}\Bigg|_0 = \boldsymbol{g}_0(t), \quad G_L \begin{pmatrix} \boldsymbol{x}_1 \\ \boldsymbol{x}_2 \end{pmatrix}\Bigg|_L = \boldsymbol{g}_L(t), \tag{C.3}$$

where $G_0, G_L \in \mathbb{R}^{6\times 12}$ are constant full-rank matrices, $\boldsymbol{g}_0(t), \boldsymbol{g}_L(t) : \mathbb{R}_{\geq 0} \to \mathbb{R}^6$ and the evaluation symbol $(\bullet)|$ is used here to alleviate notation and refers to the spatial coordinate s.

Weak formulation

We start by defining the sets of trial solutions $\mathcal{V}$ and weighting functions $\mathcal{W}$ as

$$\mathcal{V} = \left\{ \boldsymbol{v} = \begin{pmatrix} \boldsymbol{v}_1 \\ \boldsymbol{v}_2 \end{pmatrix} : \boldsymbol{v}_1, \boldsymbol{v}_2 \in H^1\left([0,L];\mathbb{R}^6\right),\ G_0\,\boldsymbol{v}|_0 = \boldsymbol{g}_0(t),\, G_L\,\boldsymbol{v}|_L = \boldsymbol{g}_L(t) \right\}, \tag{C.4}$$

$$\mathcal{W} = \left\{ \boldsymbol{w} = \begin{pmatrix} \boldsymbol{w}_1 \\ \boldsymbol{w}_2 \end{pmatrix} : \boldsymbol{w}_1, \boldsymbol{w}_2 \in H^1\left([0,L];\mathbb{R}^6\right),\ G_0\,\boldsymbol{w}|_0 = \boldsymbol{0},\, G_L\,\boldsymbol{w}|_L = \boldsymbol{0} \right\}, \tag{C.5}$$

for a beam of length L, noting that we require the defined functions and its spatial derivatives to be, at least, square-integrable in the interval $[0, L]$. Substitution of $\left(\boldsymbol{x}_1^\top, \boldsymbol{x}_2^\top\right)^\top = \boldsymbol{v}$ in (C.2), pre-multiplying by the transposed trial functions vector $\boldsymbol{w}^\top$ and integrating along the spatial domain (i.e., imposing the minimum weighted error) yields the weak formulation of the problem

$$\begin{aligned} \int_0^L \boldsymbol{w}_1^\top \left(M\dot{\boldsymbol{v}}_1 - \boldsymbol{v}_2' - E\boldsymbol{v}_2 + \mathcal{L}_1(\boldsymbol{v}_1)M\boldsymbol{v}_1 + \mathcal{L}_2(\boldsymbol{v}_2)C\boldsymbol{v}_2\right)ds \\ + \int_0^L \boldsymbol{w}_2^\top \left(C\dot{\boldsymbol{v}}_2 - \boldsymbol{v}_1' + E^\top \boldsymbol{v}_1 - \mathcal{L}_1^\top(\boldsymbol{v}_1)C\boldsymbol{v}_2\right)ds = \int_0^L \boldsymbol{w}_1^\top \boldsymbol{f}_e ds. \end{aligned} \tag{C.6}$$

Spatial Discretisation

Next, we consider the discrete subsets of the previously defined sets, respectively $\mathcal{V}^h$ and $\mathcal{W}^h$, where the spatial domain has been split into a uniform grid with $N+1$ nodes, with coordinates $s_{j+1} = s_j + h$, $j = 0, \ldots, N$ and $h = \frac{L}{N}$

$$\mathcal{V}^h = \left\{ \boldsymbol{v}^h = \sum_{j=0}^{N} \varphi_j(s)\boldsymbol{v}_j^h(t) : \varphi \in H^1\left([0,L];\mathbb{R}\right),\, G_0\boldsymbol{v}_0^h = \boldsymbol{g}_0(t),\, G_L\boldsymbol{v}_N^h = \boldsymbol{g}_L(t) \right\}, \tag{C.7}$$

$$\mathcal{W}^h = \left\{ \boldsymbol{w}^h = \sum_{j=0}^{N} \psi_j(s)\boldsymbol{w}_j^h(t) : \psi \in H^1\left([0,L];\mathbb{R}\right),\, G_0\boldsymbol{w}_0^h = \boldsymbol{0},\, G_L\boldsymbol{w}_N^h = \boldsymbol{0} \right\}, \tag{C.8}$$

where φ, ψ are the *interpolating* or *shape* functions and $\boldsymbol{v}^h, \boldsymbol{w}^h : \mathbb{R}_{\geq 0} \to \mathbb{R}^{12}$ are the nodal values of the trial solution and weighting functions. By choosing $\varphi_j = \psi_j$ a Galerkin projection results, and they are further selected to be quadratic interpolating functions which satisfy $\varphi_i(s_j) = \delta_{ij}$. That is, they are the identity at their corresponding node and zero at any other node. A representation of this shape functions can be seen in Fig. C.1. Using these quadratic interpolating functions, the domain is divided in N_{el}

elements, where each one of them has three associated nodes: two nodes are shared with the adjacent elements (big nodes in Fig. C.1) and another node is defined at the centre. Then, the number of elements and the total number of nodes is related by $N = 2N_{el} + 1$. Moreover, each of the interpolating functions has compact support: for the odd nodes, i.e., the nodes shared by adjacent elements, the functions are defined over those two elements; for the even, their support is only the element they belong to.

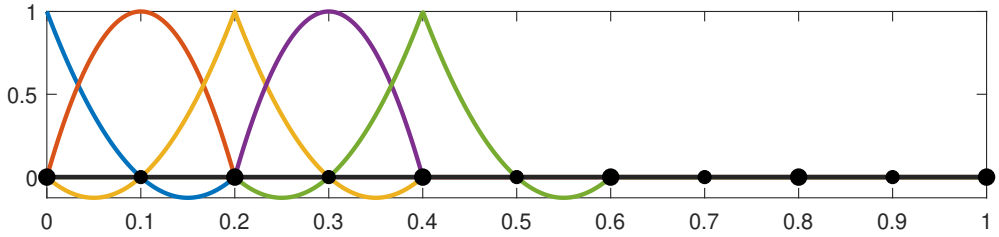


Figure C.1: Five first interpolating quadratic shape functions for a beam discretisation of $L = 1$ using 10 nodes (5 elements).

By inserting the discrete solutions $\boldsymbol{v}^h$ and $\boldsymbol{w}^h$ into (C.6) and realising that the resulting expression needs to be satisfied for any choice of $\boldsymbol{w}_j^h$, the result is a system of ordinary differential equations in terms of the nodal values $\boldsymbol{v}_j^h$. The i*th* system of equations reads

$$\sum_{j=0}^{N}\left(\int_0^L \varphi_i M\varphi_j \dot{\boldsymbol{v}}_{1j}^h ds - \int_0^L \varphi_i\left(\varphi_j' I_6 + \varphi_j E\right)\boldsymbol{v}_{2j}^h ds + \int_0^L \varphi_i \mathcal{L}_1\left(\sum_{l=0}^{N}\varphi_l \boldsymbol{v}_{1l}^h\right) M\varphi_j \boldsymbol{v}_{1j}^h ds \right.$$
$$\left. + \int_0^L \varphi_i \mathcal{L}_2\left(\sum_{l=0}^{N}\varphi_l \boldsymbol{v}_{2l}^h\right) C\varphi_j \boldsymbol{v}_{2j}^h ds\right) = \int_0^L \varphi_i \boldsymbol{f}_e ds.$$
$$\sum_{j=0}^{N}\left(\int_0^L \varphi_i C\varphi_j \dot{\boldsymbol{v}}_{2j}^h ds - \int_0^L \varphi_i\left(\varphi_j' I_6 - \varphi_j E\right)\boldsymbol{v}_{1j}^h ds - \int_0^L \varphi_i \mathcal{L}_1^\top\left(\sum_{l=0}^{N}\varphi_l \boldsymbol{v}_{1l}^h\right) C\varphi_j \boldsymbol{v}_{2j}^h ds\right) = \boldsymbol{0}. \tag{C.9}$$

Gathering all the nodal coefficients in a column vector $\boldsymbol{V}^h = \left(\boldsymbol{v}_{10}^{h\top}, \boldsymbol{v}_{20}^{h\top}, \ldots, \boldsymbol{v}_{1N}^{h\top}, \boldsymbol{v}_{2N}^{h\top}\right)^\top$, we can write the above equation as a matrix-vector expression

$$\mathcal{M}\dot{\boldsymbol{V}}^h + \overline{\mathcal{K}}\boldsymbol{V}^h + \mathcal{K}(\boldsymbol{V}^h)\boldsymbol{V}^h = \boldsymbol{\mathcal{F}}^h. \tag{C.10}$$

Taking advantage of the fact that shaping functions have compact support, the integrals required to get to (C.10) can be performed over each of the elements to then add up (assemble) each of the nodes contribution into the global matrices $\mathcal{M}$, $\overline{\mathcal{K}}$ and $\mathcal{K}$ in (C.10). Therefore, the participating nodes within an element *el* are located at global coordinates $s_{2(el-1)}$, $s_{2(el-1)+1}$ and $s_{2(el-1)+2}$, and the shape functions, using the *local* spatial coordinate

$\sigma = \frac{1}{\Delta s}(s - s_{2(el-1)})$, with $\Delta s = s_{2(el-1)+2} - s_{2(el-1)}$, are

$$\varphi_1(\sigma) = 2\left(\sigma - \tfrac{1}{2}\right)(\sigma - 1)\,, \tag{C.11}$$

$$\varphi_2(\sigma) = -4\sigma\,(\sigma - 1)\,, \tag{C.12}$$

$$\varphi_3(\sigma) = 2\sigma\left(\sigma - \tfrac{1}{2}\right), \tag{C.13}$$

where the subscripts $1, 2, 3$ refer to the local node numbering within the element (where the order is for increasing spatial coordinate s), as seen in Fig.C.2.

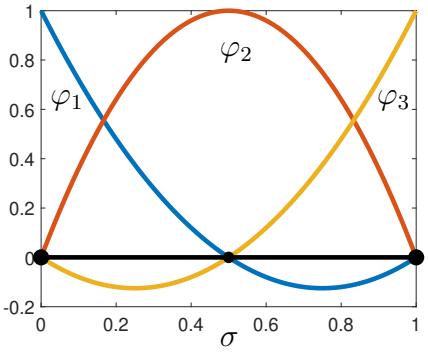


Figure C.2: Local nodes and shape functions within an element.

Then, assuming constant property matrices M, C and E, the element *mass* matrix $\mathcal{M}_{el} \in \mathbb{R}^{36\times 36}$ is

$$\mathcal{M}_{el} = \frac{h}{15}\begin{pmatrix} 4M & 0 & 2M & 0 & -M & 0 \\ 0 & 4C & 0 & 2C & 0 & -C \\ 2M & 0 & 16M & 0 & 2M & 0 \\ 0 & 2C & 0 & 16C & 0 & 2C \\ -M & 0 & 2M & 0 & 4M & 0 \\ 0 & -C & 0 & 2C & 0 & 4C \end{pmatrix}. \tag{C.14}$$

The stiffness matrix, as shown in (C.10), has been split into constant $\overline{\mathcal{K}}$ and solution-dependent $\mathcal{K}(\boldsymbol{V}^h)$ contributions. The corresponding element matrices $\overline{\mathcal{K}}_{el}, \mathcal{K}_{el}(\boldsymbol{V}^h) \in \mathbb{R}^{36\times 36}$ are

$$\overline{\mathcal{K}}_{el} = -\frac{h}{15}\begin{pmatrix} 0 & 4E & 0 & 2E & 0 & -E \\ -4E^\top & 0 & -2E^\top & 0 & E^\top & 0 \\ 0 & 2E & 0 & 16E & 0 & 2E \\ -2E^\top & 0 & -16E^\top & 0 & 2E^\top & 0 \\ 0 & -E & 0 & 2E & 0 & 4E \\ E^\top & 0 & -2E^\top & 0 & -4E^\top & 0 \end{pmatrix} - \frac{1}{6}\begin{pmatrix} 0 & -3I_6 & 0 & 4I_6 & 0 & -I_6 \\ -3I_6 & 0 & 4I_6 & 0 & -I_6 & 0 \\ 0 & -4I_6 & 0 & 0 & 0 & 4I_6 \\ -4I_6 & 0 & 0 & 0 & 4I_6 & 0 \\ 0 & 1I_6 & 0 & -4I_6 & 0 & 3I_6 \\ I_6 & 0 & -4I_6 & 0 & 3I_6 & 0 \end{pmatrix}, \tag{C.15}$$

$$\mathcal{K}_{el} = \frac{h}{210}\begin{pmatrix} \mathcal{L}_1\left(39\boldsymbol{v}_{11}^h + 20\boldsymbol{v}_{12}^h - 3\boldsymbol{v}_{13}^h\right) M & \mathcal{L}_2\left(39\boldsymbol{v}_{21}^h + 20\boldsymbol{v}_{22}^h - 3\boldsymbol{v}_{23}^h\right) C & \mathcal{L}_1\left(20\boldsymbol{v}_{11}^h + 16\boldsymbol{v}_{12}^h - 8\boldsymbol{v}_{13}^h\right) M & \dots \\ 0 & -\mathcal{L}_1^\top\left(39\boldsymbol{v}_{11}^h + 20\boldsymbol{v}_{12}^h - 3\boldsymbol{v}_{13}^h\right) C & 0 & \\ \mathcal{L}_1\left(20\boldsymbol{v}_{11}^h + 16\boldsymbol{v}_{12}^h - 8\boldsymbol{v}_{13}^h\right) M & \mathcal{L}_2\left(20\boldsymbol{v}_{21}^h + 16\boldsymbol{v}_{22}^h - 8\boldsymbol{v}_{23}^h\right) C & \mathcal{L}_1\left(16\boldsymbol{v}_{11}^h + 192\boldsymbol{v}_{12}^h + 16\boldsymbol{v}_{13}^h\right) M & \dots \\ 0 & -\mathcal{L}_1^\top\left(20\boldsymbol{v}_{11}^h + 16\boldsymbol{v}_{12}^h - 8\boldsymbol{v}_{13}^h\right) C & 0 & \\ \mathcal{L}_1\left(-3\boldsymbol{v}_{11}^h - 8\boldsymbol{v}_{12}^h - 3\boldsymbol{v}_{13}^h\right) M & \mathcal{L}_2\left(-3\boldsymbol{v}_{21}^h - 8\boldsymbol{v}_{22}^h - 3\boldsymbol{v}_{23}^h\right) C & \mathcal{L}_1\left(-8\boldsymbol{v}_{11}^h + 16\boldsymbol{v}_{12}^h + 20\boldsymbol{v}_{13}^h\right) M & \\ 0 & -\mathcal{L}_1^\top\left(-3\boldsymbol{v}_{11}^h - 8\boldsymbol{v}_{12}^h - 3\boldsymbol{v}_{13}^h\right) C & 0 & \end{pmatrix}$$

$$\begin{pmatrix} \mathcal{L}_2\left(20\boldsymbol{v}_{21}^h + 16\boldsymbol{v}_{22}^h - 8\boldsymbol{v}_{23}^h\right) C & \mathcal{L}_1\left(-3\boldsymbol{v}_{11}^h - 8\boldsymbol{v}_{12}^h - 3\boldsymbol{v}_{13}^h\right) M & \mathcal{L}_2\left(-3\boldsymbol{v}_{21}^h - 8\boldsymbol{v}_{22}^h - 3\boldsymbol{v}_{23}^h\right) C \\ -\mathcal{L}_1^\top\left(20\boldsymbol{v}_{11}^h + 16\boldsymbol{v}_{12}^h - 8\boldsymbol{v}_{13}^h\right) C & 0 & -\mathcal{L}_1^\top\left(-3\boldsymbol{v}_{11}^h - 8\boldsymbol{v}_{12}^h - 3\boldsymbol{v}_{13}^h\right) C \\ \dots \quad \mathcal{L}_2\left(16\boldsymbol{v}_{21}^h + 192\boldsymbol{v}_{22}^h + 16\boldsymbol{v}_{23}^h\right) C & \mathcal{L}_1\left(-8\boldsymbol{v}_{11}^h + 16\boldsymbol{v}_{12}^h + 20\boldsymbol{v}_{13}^h\right) M & \mathcal{L}_2\left(-8\boldsymbol{v}_{21}^h + 16\boldsymbol{v}_{22}^h + 20\boldsymbol{v}_{23}^h\right) C \\ -\mathcal{L}_1^\top\left(16\boldsymbol{v}_{11}^h + 192\boldsymbol{v}_{12}^h + 16\boldsymbol{v}_{13}^h\right) C & 0 & -\mathcal{L}_1^\top\left(-8\boldsymbol{v}_{11}^h + 16\boldsymbol{v}_{12}^h + 20\boldsymbol{v}_{13}^h\right) C \\ \mathcal{L}_2\left(-8\boldsymbol{v}_{21}^h + 16\boldsymbol{v}_{22}^h + 20\boldsymbol{v}_{23}^h\right) C & \mathcal{L}_1\left(-3\boldsymbol{v}_{11}^h + 20\boldsymbol{v}_{12}^h + 39\boldsymbol{v}_{13}^h\right) M & \mathcal{L}_2\left(-3\boldsymbol{v}_{21}^h + 20\boldsymbol{v}_{22}^h + 39\boldsymbol{v}_{23}^h\right) C \\ -\mathcal{L}_1^\top\left(-8\boldsymbol{v}_{11}^h + 16\boldsymbol{v}_{12}^h + 20\boldsymbol{v}_{13}^h\right) C & 0 & -\mathcal{L}_1^\top\left(-3\boldsymbol{v}_{11}^h + 20\boldsymbol{v}_{12}^h + 39\boldsymbol{v}_{13}^h\right) C \end{pmatrix}, \tag{C.16}$$

where the second subscript i in $\boldsymbol{v}_{1i}^h, \boldsymbol{v}_{2i}^h$, $i = 1, 2, 3$ refers to the local node numbering as in Fig. C.2. Finally the elemental contribution of the forcing term, $\mathcal{F}_{el} \in \mathbb{R}^{36}$, is obtained by computing the following spatial integrals

$$\mathcal{F}_{el} = \begin{pmatrix} \int_0^1 \varphi_1(\sigma)\boldsymbol{f}_e(s(\sigma))\frac{ds}{d\sigma}d\sigma \\ \int_0^1 \varphi_2(\sigma)\boldsymbol{f}_e(s(\sigma))\frac{ds}{d\sigma}d\sigma \\ \int_0^1 \varphi_3(\sigma)\boldsymbol{f}_e(s(\sigma))\frac{ds}{d\sigma}d\sigma \end{pmatrix}. \tag{C.17}$$

Time-Integration Scheme

A midpoint-rule time-integration scheme is chosen, with which the continuous-time expression (C.10) is approximated by

$$\mathcal{M}\frac{\boldsymbol{V}^{n+1} - \boldsymbol{V}^n}{\Delta t} + \overline{\mathcal{K}}\boldsymbol{V}^{n+\frac{1}{2}} + \mathcal{K}\left(\boldsymbol{V}^{n+\frac{1}{2}}\right)\boldsymbol{V}^{n+\frac{1}{2}} = \boldsymbol{\mathcal{F}}^{n+\frac{1}{2}}, \tag{C.18}$$

for time steps $t^{n+1} = t^n + \Delta t$, where the superscript $n + \frac{1}{2}$ denotes evaluation at time $t^{n+\frac{1}{2}} = t^n + \frac{\Delta t}{2}$ with $\boldsymbol{V}^{n+\frac{1}{2}} = \frac{1}{2}\left(\boldsymbol{V}^{n+1} + \boldsymbol{V}^n\right)$. As seen, this constitutes an implicit equation in terms of the unknown $\boldsymbol{V}^{n+1}$ which has to be solved iteratively at each time step, for instance, with a Newton-Raphson algorithm.

Boundary conditions are enforced in (C.10) by solving only for the set of equations resulting from pre-multiplying the first and last 12 equations (corresponding to the nodes at $s = 0$ and $s = L$, respectively) by $G_0^\perp$ and $G_L^\perp$ and substituting the relationships $G_0\boldsymbol{v}_0^h = \boldsymbol{g}_0(t)$, $G_L\boldsymbol{v}_N^h = \boldsymbol{g}_L(t)$ in the resulting set of equations. The rows of the matrices $G_0^\perp$ and $G_L^\perp$ span the orthogonal complement of the subspaces defined by G_0 and G_L, which effectively remove the equations as dictated by the definition of the discrete

trial functions space (C.8). For instance, a pinned end at $s = 0$ (where linear velocities are constrained and all three rotations are allowed) would be expressed by means of $G_0 = \left(\begin{smallmatrix} I_3 & 0 & 0 & 0 \\ 0 & 0 & 0 & I_3 \end{smallmatrix}\right)$ and $\boldsymbol{g}_0 = \mathbf{0}$, while $G_0^{\perp} = \left(\begin{smallmatrix} 0 & I_3 & 0 & 0 \\ 0 & 0 & I_3 & 0 \end{smallmatrix}\right)$.

Damped Intrinsic Beam Equations

The previously described finite element implementation is easily adapted to the intrinsic beam equations with full nonlinear damping terms (2.13)–(2.14) by slight modification of the stiffness terms (C.15)–(C.16). Since the midpoint rule is used to approximate time derivatives, damping terms are substituted accordingly by $C_\tau \dot{\boldsymbol{x}}_2 \approx \frac{1}{\Delta t} C_\tau (\boldsymbol{x}_2^{n+1} - \boldsymbol{x}_2^n) = \frac{2}{\Delta t} C_\tau (\boldsymbol{x}_2^{n+\frac{1}{2}} - \boldsymbol{x}_2^n)$. Therefore the implementation accounting for full nonlinear damping terms is obtained

$$\mathcal{M} \frac{\boldsymbol{V}^{n+1} - \boldsymbol{V}^n}{\Delta t} + \overline{\mathcal{K}}^{n+\frac{1}{2}} \boldsymbol{V}^{n+\frac{1}{2}} + \overline{\mathcal{K}}^n \boldsymbol{V}^n + \mathcal{K}\left(\boldsymbol{V}^{n+\frac{1}{2}}, \boldsymbol{V}^n\right) \boldsymbol{V}^{n+\frac{1}{2}} = \boldsymbol{\mathcal{F}}^{n+\frac{1}{2}}, \tag{C.19}$$

where the modified constant stiffness matrices $\overline{\mathcal{K}}^{n+\frac{1}{2}}$ and $\overline{\mathcal{K}}^n$ of each element are computed by

$$\begin{aligned} \overline{\mathcal{K}}_{el}^{n+\frac{1}{2}} = &-\frac{h}{15} \begin{pmatrix} 0 & 4(E + \frac{2}{\Delta t} C_\tau) & 0 & 2(E + \frac{2}{\Delta t} C_\tau) & 0 & -(E + \frac{2}{\Delta t} C_\tau) \\ -4E^\top & 0 & -2E^\top & 0 & E^\top & 0 \\ 0 & 2(E + \frac{2}{\Delta t} C_\tau) & 0 & 16(E + \frac{2}{\Delta t} C_\tau) & 0 & 2(E + \frac{2}{\Delta t} C_\tau) \\ -2E^\top & 0 & -16E^\top & 0 & 2E^\top & 0 \\ 0 & -(E + \frac{2}{\Delta t} C_\tau) & 0 & 2(E + \frac{2}{\Delta t} C_\tau) & 0 & 4(E + \frac{2}{\Delta t} C_\tau) \\ E^\top & 0 & -2E^\top & 0 & -4E^\top & 0 \end{pmatrix} \\ &-\frac{1}{6} \begin{pmatrix} 0 & -3(I_6 + \frac{2}{\Delta t} C_\tau) & 0 & 4(I_6 + \frac{2}{\Delta t} C_\tau) & 0 & -(I_6 + \frac{2}{\Delta t} C_\tau) \\ -3I_6 & 0 & 4I_6 & 0 & -I_6 & 0 \\ 0 & -4(E + \frac{2}{\Delta t} C_\tau) & 0 & 0 & 0 & 4(E + \frac{2}{\Delta t} C_\tau) \\ -4I_6 & 0 & 0 & 0 & 4I_6 & 0 \\ 0 & 1(E + \frac{2}{\Delta t} C_\tau) & 0 & -4(E + \frac{2}{\Delta t} C_\tau) & 0 & 3(E + \frac{2}{\Delta t} C_\tau) \\ I_6 & 0 & -4I_6 & 0 & 3I_6 & 0 \end{pmatrix} \end{aligned} \tag{C.20}$$

and

$$\begin{aligned} \overline{\mathcal{K}}_{el}^{n} = &\frac{h}{15} \begin{pmatrix} 0 & 4\frac{2}{\Delta t} C_\tau & 0 & 2\frac{2}{\Delta t} C_\tau & 0 & -\frac{2}{\Delta t} C_\tau \\ 0 & 0 & 0 & 0 & 0 & 0 \\ 0 & 2\frac{2}{\Delta t} C_\tau & 0 & 16\frac{2}{\Delta t} C_\tau & 0 & 2\frac{2}{\Delta t} C_\tau \\ 0 & 0 & 0 & 0 & 0 & 0 \\ 0 & -\frac{2}{\Delta t} C_\tau & 0 & 2\frac{2}{\Delta t} C_\tau & 0 & 4\frac{2}{\Delta t} C_\tau \\ 0 & 0 & 0 & 0 & 0 & 0 \end{pmatrix} \\ &+\frac{1}{6} \begin{pmatrix} 0 & -3\frac{2}{\Delta t} C_\tau & 0 & 4\frac{2}{\Delta t} C_\tau & 0 & -\frac{2}{\Delta t} C_\tau \\ 0 & 0 & 0 & 0 & 0 & 0 \\ 0 & -4\frac{2}{\Delta t} C_\tau & 0 & 0 & 0 & 4\frac{2}{\Delta t} C_\tau \\ 0 & 0 & 0 & 0 & 0 & 0 \\ 0 & \frac{2}{\Delta t} C_\tau & 0 & -4\frac{2}{\Delta t} C_\tau & 0 & 3\frac{2}{\Delta t} C_\tau \\ 0 & 0 & 0 & 0 & 0 & 0 \end{pmatrix}, \end{aligned} \tag{C.21}$$

while the solution-dependent stiffness matrix is obtained evaluating expression (C.16) using $\mathcal{K}_{el}(\boldsymbol{V}^h) = \mathcal{K}_{el}\left(\boldsymbol{v}_{1i}^{n+\frac{1}{2}}, \left(I_6 + \frac{2}{\Delta t}C_\tau\right)\boldsymbol{v}_{2i}^{n+\frac{1}{2}} - \frac{2}{\Delta t}C_\tau \boldsymbol{v}_{2i}^{n}\right)$. We also note that boundary conditions are now

$$G_0 \begin{pmatrix} \boldsymbol{x}_1 \\ \boldsymbol{x}_2 + C_\tau \dot{\boldsymbol{x}}_2 \end{pmatrix}\Bigg|_0 = \boldsymbol{g}_0(t), \quad G_L \begin{pmatrix} \boldsymbol{x}_1 \\ \boldsymbol{x}_2 + C_\tau \dot{\boldsymbol{x}}_2 \end{pmatrix}\Bigg|_L = \boldsymbol{g}_L(t), \tag{C.22}$$

which, by using the midpoint scheme

$$G_0^{n+\frac{1}{2}} \begin{pmatrix} \boldsymbol{x}_1^{n+\frac{1}{2}} \\ \boldsymbol{x}_2^{n+\frac{1}{2}} \end{pmatrix}\Bigg|_0 = \boldsymbol{g}_0(t^{n+\frac{1}{2}}) + G_0^n \begin{pmatrix} \boldsymbol{0} \\ \boldsymbol{x}_2^n \end{pmatrix}\Bigg|_0, \quad G_L^{n+\frac{1}{2}} \begin{pmatrix} \boldsymbol{x}_1^{n+\frac{1}{2}} \\ \boldsymbol{x}_2^{n+\frac{1}{2}} \end{pmatrix}\Bigg|_L = \boldsymbol{g}_L(t^{n+\frac{1}{2}}) + G_L^n \begin{pmatrix} \boldsymbol{0} \\ \boldsymbol{x}_2^n \end{pmatrix}\Bigg|_L, \tag{C.23}$$

with new matrices

$$G_0^{n+\frac{1}{2}} = G_0 \begin{pmatrix} I_6 & 0 \\ 0 & I_6 + \frac{2}{\Delta t}C_\tau \end{pmatrix}, \qquad G_0^n = G_0 \begin{pmatrix} 0 & 0 \\ 0 & \frac{2}{\Delta t}C_\tau \end{pmatrix}, \tag{C.24}$$

$$G_L^{n+\frac{1}{2}} = G_L \begin{pmatrix} I_6 & 0 \\ 0 & I_6 + \frac{2}{\Delta t}C_\tau \end{pmatrix}, \qquad G_L^n = G_L \begin{pmatrix} 0 & 0 \\ 0 & \frac{2}{\Delta t}C_\tau \end{pmatrix}, \tag{C.25}$$

and hence the procedure to enforce boundary conditions is analogously done here with matrices $G_0^{n+\frac{1}{2}}$ and $G_L^{n+\frac{1}{2}}$.

Intrinsic Beam Equations with Linearised Damping

For the case of linearised damping terms, an alternative approach is taken, which involves obtaining a new weak form of the equations. We commence by writing the previously described intrinsic beam equations with linearised damping (2.22)–(2.23) without expanding the terms that lead to the matrices D_0, D_1 and D_2:

$$M\dot{\boldsymbol{x}}_1 - \left(\boldsymbol{x}_2 + C_d\left(\boldsymbol{x}_1' - E^\top \boldsymbol{x}_1\right)\right)' - E\left(\boldsymbol{x}_2 + C_d\left(\boldsymbol{x}_1' - E^\top \boldsymbol{x}_1\right)\right) \tag{C.26}$$

$$+\mathcal{L}_1(\boldsymbol{x}_1)M\boldsymbol{x}_1 + \mathcal{L}_2(\boldsymbol{x}_2)C\boldsymbol{x}_2 = \boldsymbol{f}_e, \tag{C.27}$$

$$C\dot{\boldsymbol{x}}_2 - \boldsymbol{x}_1' + E^\top \boldsymbol{x}_1 - \mathcal{L}_1^\top(\boldsymbol{x}_1)C\boldsymbol{x}_2 = \boldsymbol{0}, \tag{C.28}$$

with boundary conditions that we express now as

$$G_0 \begin{pmatrix} \boldsymbol{x}_1 \\ \boldsymbol{x}_2 + C_d\left(\boldsymbol{x}_1' - E^\top \boldsymbol{x}_1\right) \end{pmatrix}\Bigg|_0 = \boldsymbol{g}_0(t), \quad G_L \begin{pmatrix} \boldsymbol{x}_1 \\ \boldsymbol{x}_2 + C_d\left(\boldsymbol{x}_1' - E^\top \boldsymbol{x}_1\right) \end{pmatrix}\Bigg|_L = \boldsymbol{g}_L(t), \tag{C.29}$$

where we split $G_0 = \left((G_0^1, 0)^\top, G_0^{2\top}\right)^\top$ and $G_L = \left((G_L^1, 0)^\top, G_L^{2\top}\right)^\top$, where G_0^2 and G_L^2 are the rows of G_0 and G_L, respectively, that have nonzero entries in the six last columns, that is, the entries corresponding to $\boldsymbol{x}_2 + C_d\left(\boldsymbol{x}_1' - E^\top \boldsymbol{x}_1\right)$. This is done since the boundary conditions affecting only the velocity states will be enforced as Dirichlet conditions while the ones linked to the force distribution will be enforced as natural boundary conditions. Correspondingly, we split $\boldsymbol{g}_0(t) = \left(\boldsymbol{g}_0^{1\top}, \boldsymbol{g}_0^{2\top}\right)^\top$ and $\boldsymbol{g}_L(t) = \left(\boldsymbol{g}_L^{1\top}, \boldsymbol{g}_L^{2\top}\right)^\top$. Hence, we define the new sets of trial and weighting functions

$$\mathcal{V} = \left\{ \boldsymbol{v} = \begin{pmatrix} \boldsymbol{v}_1 \\ \boldsymbol{v}_2 \end{pmatrix} : \boldsymbol{v}_1, \boldsymbol{v}_2 \in H^1\left([0, L]; \mathbb{R}^6\right),\ G_0^1\, \boldsymbol{v}_1|_0 = \boldsymbol{g}_0^1(t),\ G_L^1\, \boldsymbol{v}_1|_L = \boldsymbol{g}_L^1(t) \right\}, \quad \text{(C.30)}$$

$$\mathcal{W} = \left\{ \boldsymbol{w} = \begin{pmatrix} \boldsymbol{w}_1 \\ \boldsymbol{w}_2 \end{pmatrix} : \boldsymbol{w}_1, \boldsymbol{w}_2 \in H^1\left([0, L]; \mathbb{R}^6\right),\ G_0^1\, \boldsymbol{w}_1|_0 = \boldsymbol{0},\ G_L^1\, \boldsymbol{w}_1|_L = \boldsymbol{0} \right\}. \quad \text{(C.31)}$$

The weak form is now obtained performing integration by parts on $\left(\boldsymbol{x}_2 + C_d\left(\boldsymbol{x}_1' - E^\top \boldsymbol{x}_1\right)\right)'$, so that the boundary conditions involving this force term can be naturally imposed in the resulting boundary term

$$\begin{aligned} &\int_0^L \boldsymbol{w}_1^\top \left(M\dot{\boldsymbol{v}}_1 - E\left(\boldsymbol{v}_2 + C_d\left(\boldsymbol{v}_1' - E^\top \boldsymbol{v}_1\right)\right) + \mathcal{L}_1(\boldsymbol{v}_1) M \boldsymbol{v}_1 + \mathcal{L}_2(\boldsymbol{v}_2) C \boldsymbol{v}_2\right) ds \\ &- \int_0^L \boldsymbol{w}_1'^\top \left(\boldsymbol{v}_2 + C_d\left(\boldsymbol{v}_1' - E^\top \boldsymbol{v}_1\right)\right) ds + \boldsymbol{w}_1^\top \left(\boldsymbol{v}_2 + C_d\left(\boldsymbol{v}_1' - E^\top \boldsymbol{v}_1\right)\right)\Big|_0^L \\ &+ \int_0^L \boldsymbol{w}_2^\top \left(C\dot{\boldsymbol{v}}_2 - \boldsymbol{v}_1' + E^\top \boldsymbol{v}_1 - \mathcal{L}_1^\top(\boldsymbol{v}_1) C \boldsymbol{v}_2\right) ds = \int_0^L \boldsymbol{w}_1^\top \boldsymbol{f}_e ds. \end{aligned} \quad \text{(C.32)}$$

The corresponding discrete subsets are

$$\mathcal{V}^h = \left\{ \boldsymbol{v}^h = \sum_{j=0}^{N} \varphi_j(s) \boldsymbol{v}_j^h(t) : \varphi \in H^1\left([0, L]; \mathbb{R}\right),\ G_0^1 \boldsymbol{v}_{10}^h = \boldsymbol{g}_0^1(t),\ G_L^1 \boldsymbol{v}_{1N}^h = \boldsymbol{g}_L^1(t) \right\}, \quad \text{(C.33)}$$

$$\mathcal{W}^h = \left\{ \boldsymbol{w}^h = \sum_{j=0}^{N} \psi_j(s) \boldsymbol{w}_j^h(t) : \psi \in H^1\left([0, L]; \mathbb{R}\right),\ G_0^1 \boldsymbol{w}_{10}^h = \boldsymbol{0},\ G_L^1 \boldsymbol{w}_{1N}^h = \boldsymbol{0} \right\}. \quad \text{(C.34)}$$

The discrete set of equations is obtained similarly to (C.9): weighting and shape functions are chosen to be equal and the discrete versions of trial solutions and weighting functions defined by (C.33)–(C.34) are substituted in (C.32), giving raise to a set of linear ordinary differential equations. Boundary conditions are imposed now by pre-multiplying the first six and the second-to-last six equations (equations corresponding to the velocity states

at nodes $s = 0$ and $s = L$) by the orthogonal complement of G_0^1 and G_L^1 ($G_0^{1\perp}$ and $G_L^{1\perp}$, respectively) and substituting in the resulting set of equations the relationships $G_0^1 \boldsymbol{v}_{10}^h = \boldsymbol{g}_0(t)$ and $G_L^1 \boldsymbol{v}_{1N}^h = \boldsymbol{g}_L(t)$. The boundary conditions concerning the force distribution, defined by $G_0^2 \boldsymbol{v}_0^h = \boldsymbol{g}_0^2(t)$ and $G_L^2 \boldsymbol{v}_L^h = \boldsymbol{g}_L^2(t)$ would be directly substituted in the boundary term $\boldsymbol{w}_1^\top \left(\boldsymbol{v}_2 + C_d \left(\boldsymbol{v}_1' - E^\top \boldsymbol{v}_1\right)\right)\Big|_0^L$ in (C.32), giving only contribution to the equations corresponding to the first and last nodes.

Recovering the example of a pinned end at $s = 0$, the associated constraint matrices would be $G_0^1 = \left(\begin{smallmatrix} I_3 & 0 \end{smallmatrix}\right)$, hence $G_0^{1\perp} = \left(\begin{smallmatrix} 0 & I_3 \end{smallmatrix}\right)$, with $\boldsymbol{g}_0^1(t) = \boldsymbol{0}$ and $G_0^2 = \left(\begin{smallmatrix} 0 & 0 & 0 & I_3 \end{smallmatrix}\right)$ with $\boldsymbol{g}_0^2(t) = \boldsymbol{0}$.

Using similarly a midpoint rule as a time-integration scheme, the resulting finite element implementation has the same form as (C.18) with identical mass and solution-dependent stiffness matrices (since damping here does not modify the nonlinear terms), but slightly different constant stiffness matrix

$$
\begin{aligned}
\overline{\mathcal{K}}_{el} = &-\frac{h}{15}\begin{pmatrix}
-4EC_dE^\top & 4E & -2EC_dE^\top & 2E & EC_dE^\top & -E \\
-4E^\top & 0 & -2E^\top & 0 & E^\top & 0 \\
-2EC_dE^\top & 2E & -16EC_dE^\top & 16E & -2EC_dE^\top & 2E \\
-2E^\top & 0 & -16E^\top & 0 & 2E^\top & 0 \\
EC_dE^\top & -E & -2EC_dE^\top & 2E & -4EC_dE^\top & 4E \\
E^\top & 0 & -2E^\top & 0 & -4E^\top & 0
\end{pmatrix} \\
&-\frac{1}{6}\begin{pmatrix}
-3(C_dE^\top + EC_d) & 3I_6 & -4(C_dE^\top - EC_d) & 4I_6 & (C_dE^\top - EC_d) & -I_6 \\
-3I_6 & 0 & 4I_6 & 0 & -I_6 & 0 \\
4(C_dE^\top - EC_d) & -4I_6 & 0 & 0 & -4(C_dE^\top - EC_d) & 4I_6 \\
-4I_6 & 0 & 0 & 0 & 4I_6 & 0 \\
-(C_dE^\top - EC_d) & 1I_6 & 4(C_dE^\top - EC_d) & -4I_6 & 3(C_dE^\top + EC_d) & -3I_6 \\
I_6 & 0 & -4I_6 & 0 & 3I_6 & 0
\end{pmatrix} \\
&-\frac{1}{6h}\begin{pmatrix}
-7C_d & 0 & 8C_d & 40 & -C_d & 0 \\
0 & 0 & 0 & 0 & 0 & 0 \\
8C_d & 0 & -16C_d & 0 & 8C_d & 0 \\
0 & 0 & 0 & 0 & 0 & 0 \\
-C_d & 0 & 8C_d & 0 & -7C_d & 0 \\
0 & 0 & 0 & 0 & 0 & 0
\end{pmatrix},
\end{aligned}
\tag{C.35}
$$

where we note that all extra damping terms in (C.35) add positive semidefinite contributions ($C_d \succeq 0$) to $\overline{\mathcal{K}}$, which sits on the left hand side of equation (C.18), and hence has a dissipative effect.